Symmetry Breaking and Spin-Orbit Interaction on the Triangular Lattice

Dissertation zur Erlangung des naturwissenschaftlichen Doktorgrades
der Julius-Maximilians-Universität Würzburg

vorgelegt von

Philipp Eck
aus Würzburg

Würzburg 2023

Eingereicht am: 07.07.2023

bei der Fakultät für Physik und Astronomie

1. Gutachter: Prof. Dr. Giorgio Sangiovanni

2. Gutachter: Prof. Dr. Björn Trauzettel

3. Gutachter: Prof. Dr. Roser Valentí

der Dissertation

Vorsitzende(r) _____

1. Prüfer: Prof. Dr. Giorgio Sangiovanni

2. Prüfer: Prof. Dr. Björn Trauzettel

3. Prüfer: Prof. Dr. Ralph Claessen

im Promotionskolloquium

Tag des Promotionskolloquiums: 08.03.2024

Doktorurkunde ausgehändigt am: _____

Supervisor: Prof. Dr. Giorgio Sangiovanni
Co-Supervisor: Prof. Dr. Domenico Di Sante

In any case, it is a very good symmetry...

Bogdan Andrei Bernevig, 20. January 2021, SPICE-SPIN+X seminar on "Moiré Samples: The twisted bilayer graphene scenario".

Acronyms

0D zero-dimensional

1D one-dimensional

2D two-dimensional

ARPES Angle-Resolved Photoelectron Spectroscopy

BZ Brillouin Zone

CD Circular Dichroism

DFT Density Functional Theory

DOS Density of States

EBR Elementary Band Representation

GGA Generalized-Gradient Approximation

HOTI Higher-Order Topological Insulator

HSE06 Heyd-Scuseria-Ernzerhof Functional (2006)

irreps Irreducible Representations

ISB Inversion Symmetry Breaking

LCAO Linear Combination of Atomic Orbitals

LD Linear Dichroism

LDA Local-Density Approximation

LG Layer Group

MLWF Maximally Localized Wannier Functions

MTP Modern Theory of Polarization

OAM Orbital Angular Momentum

ONB Orthonormal Basis

PBE Perdew-Burke-Ernzerhof Functional

QSHI Quantum Spin Hall Insulator

SOC Spin-Orbit Coupling

STM Scanning Tunneling Microscopy

STS Scanning Tunneling Spectroscopy

TRIM Time-Reversal Invariant Momentum

UC Unit Cell

VASP Vienna Ab Initio Simulation Package

WCC Wannier-Charge Center

WP Wyckoff Position

Abstract

Since the prediction of the quantum spin Hall effect in graphene by Kane and Mele, $\mathbb{Z}_2$-topology in hexagonal monolayers is indissociably linked to high-symmetric honeycomb lattices. This thesis breaks with this paradigm by focusing on topological phases in the fundamental two-dimensional hexagonal crystal, the triangular lattice. In contrast to Kane-Mele-type systems, electrons on the triangular lattice profit from a sizable, since local, spin-orbit coupling (SOC) and feature a non-trivial ground state only in the presence of inversion symmetry breaking. This tends to displace the valence charge form the atomic position. Therefore, all non-trivial phases are real-space obstructed.

Inspired by the contemporary conception of topological classification of electronic systems, a comprehensive lattice and band symmetry analysis of insulating phases on the triangular lattice is presented. This reveals not only the mechanism at the origin of band topology, the competition of SOC and symmetry breaking, but also the electric polarization arising from a displacement of the valence charge centers from the nuclei. The latter is defined as real-space obstruction and can stabilize in the bulk gap fractionally filled zero-dimensional corner states. If the one-dimensional edges are insulating, this constitutes a higher-order topological insulator (HOTI).

In particular, a p-shell (or $l = 1$ sub-shell) on the triangular lattice has symmetry protected in-plane Dirac fermions at the valley momenta and can host a nodal line resulting from the intersection of the p_z and the in-plane bands. These features are gapped by SOC and also by horizontal and vertical reflection symmetry breaking, which gives rise to four topologically distinct insulating phases. The two disconnected quantum spin Hall insulators (QSHIs) can be transformed into each other via two different atomic limits, a high symmetric SOC-dominated and a strongly inversion symmetry broken insulator. The $\mathbb{Z}_2$-trivial phases are distinguishable by their valence charge localization as only the symmetry broken insulator is a real-space obstructed HOTI: vertical mirror symmetry breaking discriminates between the two void sites in the triangular unit cell (the honeycomb Wyckoff position) and displaces the electronic charge to one of the them. However, such a classification is not available for $\mathbb{Z}_2$-non-trivial bands, as they lack a proper Wannier representation by definition. Upon releasing the protecting internal symmetry, time-reversal violating Wannier functions are constructed for the two QSHIs, which extends the concept of real-space obstruction to $\mathbb{Z}_2$-non-trivial systems: a dominant vertical reflection symmetry breaking enforces a HOTI-like localization on only one of the voids of the triangular lattice. Instead the

presence of vertical reflection symmetry yields Wannier centers on both void sites, i.e., a honeycomb lattice. This analogy to the Kane-Mele model is not coincidental as the valence band representation is identical for both systems.

The thesis concludes with state-of-the-art first principles calculations and experiments on trigonal monolayer adsorbate systems. This validates and complements the preceding theoretical analysis by establishing the connection to real materials, paving the way towards technological application. The chapter starts unveiling the fundamental interplay of SOC and inversion symmetry breaking in the binary honeycomb compound AgTe on Ag(111). The symmetry breaking promotes orbital angular momentum polarization resulting in a sizable spin-splitting, the so-called orbital orbital-driven Rashba effect and has been published in Ref. *Ünzelmann* et al. (2020). The centerpiece of this thesis is the conception of *indenene*, a triangular monolayer of indium atoms on silicon carbide. It is the first in literature reported real-space obstructed QSHI. The material features a valence band symmetry identical to graphene, i.e., the time-reversal violating Wannier centers localize in the void positions between the indium sites, forming a honeycomb lattice, as shown by *Eck* et al. (2022). In contrast to other QSHIs, its non-trivial $\mathbb{Z}_2$-topology has been determined by addressing the bulk wave function symmetry instead of relying on transport experiments. In analogy to the Kane-Mele model, the valence states of the valley Dirac cone display a honeycomb charge localization indicative for a SOC opened gap as presented by *Bauernfeind* et al. (2021). Upon reducing the SOC interaction, achieved in practice by considering light Group 3 adsorbates (B, Al, Ga), a real-space obstructed HOTI phase can be stabilized. The charge of the $\mathbb{Z}_2$-trivial bands localizes in one of the voids of the triangular lattice and fractionally filled in-gap corner states have been predicted by *Eck* et al. (2023). As an outlook beyond topology in the independent particle picture, triangular monolayers of Group V elements on SiC are investigated. The doping by two electrons compared to Group III shifts the chemical potential to the in-plane bands and gives rise to a compensated Fermi surface. The orbital contribution of the associated electron and hole pockets is dictated by the reflection mirror planes of the triangular lattice, which in turn is also reflected in the orbital channels of the Lindhard function.

Zusammenfassung

Seit der Vorhersage des Quanten-Spin-Hall-Effekts in Graphen von Kane und Mele wird $\mathbb{Z}_2$-Topologie in hexagonalen Monolagen untrennbar mit hoch-symmetrischen Honigwaben Gittern in Verbindung gebracht. Diese Doktorarbeit bricht mit diesem Paradigma und rückt topologische Phasen im fundamentalen zweidimensionalen hexagonalen Kristall, dem Dreiecksgitter, in den Fokus. Im Gegensatz zu Kane-Mele-artigen Systemen profitieren Elektronen im Dreiecksgitter von einer lokalen, daher auch starken, Spin-Bahn Wechselwirkung. Außerdem erfordert die Stabilisierung einer nicht-trivialen Phase zwangsläufig die Abwesenheit von Inversionssymmetrie. Des Weiteren führt der Symmetriebruch im Dreiecksgitter zu einer Verschiebung der Valenzladungsträgerdichte weg von der atomaren Position, alle nicht-trivialen Phasen sind ortsraumobstruiert.

Inspiriert vom gegenwärtigen Verständnis der topologischen Klassifizierung von elektronischen Systemen präsentiert diese Arbeit eine fundierte Gitter- und Bandsymmetrieanalyse von isolierenden Phasen auf dem Dreiecksgitter. Dies offenbart nicht nur den Bandtopologie definierenden Mechanismus, nämlich die Konkurrenz von Spin-Bahn Wechselwirkung und Symmetriebruch, sondern auch die elektronische Polarisierung, welche auf eine Verschiebung der Ladungszentren weg von den Atomrümpfen zurückzuführen ist. Letzteres wird als Ortsraumobstruktion bezeichnet und kann in der Volumenbandlücke null-dimensionale fraktional besetzte Eckzustände[1] hervorrufen. Sind die eindimensionalen Kanten ebenfalls isolierend, so handelt es sich um einen topologischen Isolator höherer Ordnung.

Im speziellen wird in dieser Arbeit eine p-Schale (oder $l = 1$ Unterschale) auf dem Dreiecksgitter behandelt. Dort bilden die horizontal orientierten Orbitale symmetriegeschützte Dirac Fermionen an den Ecken der Brillouin Zone aus. Des Weiteren führt die Überschneidung des p_z-Bandes mit den Bändern der horizontal ausgerichteten Orbitale zu einer nodalen Linie. Diese Bandschnittpunkte können entweder durch die Spin-Bahn Kopplung oder durch horizontalen und vertikalen Symmetriebruch aufgehoben werden, sodass vier topologisch unterschiedliche isolierende Phasen existieren. Die zwei voneinander getrennten Quanten-Spin-Hall Isolatoren sind über zwei unterschiedliche atomare Limes ineinander überführbar, entweder über einen Spin-Bahn dominierten oder einen stark inversionssymmetriegebrochenen Isolator. Die $\mathbb{Z}_2$-trivialen Phasen unterscheiden sich anhand der Lokalisierung der Valenzelektronen. Der Sym-

[1] Die Namensgebung bezieht sich auf die Geometrische Anordnung, dem Schnittpunkt zweier Kanten. Die glückliche Übereinstimmung mit dem Namen des Authoren ist zufälliger Natur.

metriebruch führt zu einem ortsraumobstruierten topologischen Isolator höherer Ordnung: Durch den Bruch der vertikalen Spiegelsymmetrie werden die beiden Leerstellen im Dreiecksgitter unterscheidbar (Honigwaben Wyckoffposition) und die elektronische Ladung wird zu einer der beiden Leerstellen verschoben. Solch eine direkte Ortsraum Klassifizierung fehlt hingegen für $\mathbb{Z}_2$-nicht-triviale Phasen, da sie definitionsgemäß keine Wannierrepräsentation besitzen. Unter der Aufgabe der schützenden internen Symmetrie können jedoch zeitumkehrbrechende Wannierfunktionen für die zwei genannten Quanten-Spin-Hall Isolatoren konstruiert werden. Dies erweitert das Konzept der Ortsraumobstruktion um $\mathbb{Z}_2$-nicht-triviale Phasen: Ein dominierender vertikaler Symmetriebruch erzwingt eine Ladungsträgerlokalisierung wie in der topologischen Phase höherer Ordnung auf nur einer der Leerstellen im Dreiecksgitter. Der Erhalt der vertikalen Spiegelebene resultiert hingegen in Wannierzentren auf beiden Leerstellen, einem Honigwabengitter. Diese Analogie zum Kane-Mele Modell ist kein Zufall, beide Systeme besitzen gleiche Valenzbandrepräsentationen.

Den Abschluss der Arbeit bilden hochmoderne *ab initio* Rechnungen und Experimente zu trigonalen einschichtigen Adsorbatsystemen. Diese betonen die Relevanz der vorhergehenden theoretischen Betrachtung und etablieren eine Verbindung zu echten Materialien, ein wichtiger Meilenstein hin zur technologischen Anwendung. Zu Beginn des Kapitels wird auf das fundamentale Zusammenspiel von Spin-Bahn Kopplung und Inversionssymmetriebruch in der binären Honigwabenstruktur AgTe auf Ag(111) eingegangen. Der Symmetriebruch erzeugt eine orbitale Drehimpulspolarisierung, welche eine beträchtliche Spin-Aufspaltung zur Folge hat, der sogenannte orbitalgetriebene Rashba Effekt, welcher in Ref. *Ünzelmann* et al. (2020) publiziert wurde. Ein zentraler Aspekt dieser Dissertation ist die Konzeption von *indenene*, eine dreieckige Monolage aus Indium Atomen auf Siliziumcarbid. Es ist der erste in der Literatur genannte und experimentell nachgewiesene ortsraumobstruierte Quanten-Spin-Hall Isolator. Die Valenzbandsymmetrie ist identisch zu Graphen, d.h., die zeitumkehrverletzenden Wannierzentren lokalisieren auf den Leerstellen zwischen den Indium Atomen und bilden dabei ein Honigwabengitter aus wie in Ref. *Eck* et al. (2022) gezeigt. Im Gegensatz zu anderen Quanten-Spin-Hall Isolatoren wurde die nicht-triviale $\mathbb{Z}_2$-Topologie anhand der Symmetrie der Volumenwellenfunktionen bestimmt, anstatt auf Transportexperimente zurückzugreifen. Dies ermöglicht die Analogie zum Kane-Mele Modell: Die Valenzzustände des Dirac-Kegels weisen eine Honigwabengeometrie auf, welche einer Spin-Bahn Kopplung geöffneten Bandlücke zuzuordnen ist und von *Bauernfeind* et al. (2021) gezeigt wurde. Werden hingegen leichte Gruppe III Adsorbate (B, Al, Ga) mit schwächerer Spin-Bahn Wechselwirkung betrachtet, so stellt sich eine ortsraumobstruierte Isolierende Phase höherer Ordnung ein. Die Ladungsträgerdichte der $\mathbb{Z}_2$-trivialen Bänder lokalisiert auf nur einer der Leerstellen. Ausgehend hiervon wurden fraktional gefüllte Eckzustände von *Eck* et al. (2023) vorhergesagt. Als Ausblick über die Topologie im Einteilchenbild hinaus werden dreieckige Monolagen aus Gruppe V Atomen untersucht. Im Vergleich zu Gruppe III verschieben die zwei zusätzlichen Elektronen das chemische Potential zu den Energien der Bänder der horizontal orientierten Orbitale, was eine kompensierte Fermi Fläche zur Folge hat. Die orbitalen Beiträge der

involvierten Elektronen- und Lochtaschen wird durch die Spiegelsymmetrie des Gitters bestimmt. Dies drückt sich ebenfalls in den orbitalen Kanälen der Lindhard-Funktion aus.

Contents

1. Introduction **1**

2. Basic Theory and Concepts **7**
2.1. Topological Insulators and Electric Polarization 7
2.1.1. Topological Insulators 7
2.1.2. Electric Polarization, Berry Phase and topological invariants . . 9
2.1.3. Kane-Mele model 10
2.2. *ab initio* Theory 13
2.2.1. The Many-Body Problem in Solid State Physics 13
2.2.2. Density Functional Theory (DFT) 14
2.2.2.1. Hohenberg-Kohn Theorems 14
2.2.2.2. Kohn-Sham Ansatz 15
2.2.2.3. Exchange-Correlation Functionals 17
2.2.2.4. DFT Implementation in VASP 18
2.3. Tight-Binding and LCAO Basis Functions 19
2.3.1. Slater-Koster Parametrization: Two center-approximation . . . 21
2.3.2. Wannier Functions 22
2.4. Group Theoretical Analysis of the Triangular Lattice 25
2.4.1. Group Theory in the context of Crystals 25
2.4.1.1. Point Groups 26
2.4.1.2. Translation Group 26
2.4.1.3. Band Representations and Topological Classification . 28
2.4.2. Symmetry breaking in the Hexagonal Bravais Lattice 30
2.4.2.1. Hexagonal and Trigonal Layer Groups 31
2.4.2.2. Site-Symmetry and Little Co-Group Analysis 32
2.4.3. Inversion Symmetry Breaking Induced Chiral Wave Functions . 34

3. Dirac Fermions in Trigonal and Hexagonal Space Groups **37**
3.1. Symmetry-Protected Dirac States 37
3.2. Equivalence of Honeycomb and Triangular Dirac Fermions 40
3.3. Emergent Honeycomb Connectivity on the Triangular Lattice 43
3.4. Transformation between Triangular and Honeycomb Dirac Fermions . . 46
3.5. Sublattice Polarization around the Valley Momenta 47
3.6. Summary 49

4. The p-Shell on the Triangular Lattice **51**
4.1. p6/mmm Lattice Hamiltonian . . . 51
4.2. σ_v-Symmetry-Breaking . . . 54
4.2.1. Group-Theoretical Derivation . . . 54
4.2.2. Microscopic Ansatz . . . 55
4.2.3. Explicit Ansatz . . . 56
4.3. σ_h-Symmetry Breaking . . . 58
4.4. Atomic Spin-Orbit Coupling . . . 60
4.5. Summary . . . 62

5. Symmetry-Breaking Stabilized Topological Phases on the Triangular Lattice **63**
5.1. Overview . . . 63
5.2. $\mathbb{Z}_2$-Topology and Wilson-Loops . . . 66
5.3. Orbital Angular Momentum Polarization . . . 70
5.4. Band Representations and Real-Space Obstruction . . . 71
5.5. Symmetry-Breaking Driven Electric Polarization . . . 77
5.6. Finite-Size Geometries and Edge States . . . 80
5.7. Symmetry-Breaking stabilized HOTI phase . . . 82
5.8. OAM-Driven Real-Space Obstruction . . . 87
5.9. Real-Space Obstructed QSHIs . . . 89
5.10. Graphene-like QSHI on the Triangular Lattice . . . 93
5.11. Summary . . . 95

6. Symmetry-Breaking and Topology in Adatom Monolayers **97**
6.1. Orbital-Driven Rashba Effect in AgTe . . . 98
6.1.1. Orbital Polarization and Band-Dependent Rashba-Splitting . . . 99
6.1.2. Inversion Symmetry-Breaking Promoted OAM Polarization . . . 100
6.1.3. Band Symmetries from Polarized Light ARPES . . . 102
6.1.4. Conclusion and Outlook . . . 105
6.2. Indenene on SiC . . . 105
6.2.1. Unit Cell Characterization and Electronic Structure . . . 106
6.2.2. $\mathbb{Z}_2$-classification . . . 111
6.2.3. Orbital Symmetry as an Indicator for Real-Space Obstruction . . . 113
6.2.4. DFT-Functional and Structural Details . . . 114
6.2.5. Edge States . . . 118
6.2.6. Conclusion and Outlook . . . 123
6.3. HOTIs on SiC, the Lightweight Siblings of Indenene . . . 124
6.3.1. Unit Cell and Bulk Electronic Structure . . . 124
6.3.2. Band Symmetry Driven Electronic Multipoles . . . 126
6.3.3. Edge States of Al . . . 127
6.3.4. Quadrupole Promoted Corner Charge . . . 128
6.3.5. Conclusion and Outlook . . . 130

6.4. The Generically Compensated Fermi Surface of Group V Adsorbates on SiC . . . 132
6.4.1. Unit Cell and Electronic Structure . . . 132
6.4.2. Minimal Tight-Binding Hamiltonian . . . 134
6.4.3. Static Electronic Susceptibility . . . 135
6.4.4. Robustness of the Compensated Fermi Surface . . . 139
6.4.5. Conclusion and Outlook . . . 139
6.5. Summary and Outlook . . . 140

7. Conclusion and Outlook **143**

A. Appendix **149**
A.1. Kane-Mele model . . . 149
A.2. Coulomb-Sturmians . . . 150
A.3. Coulomb-Sturmians based Transformation between Honeycomb and Triangular Lattice Basis Set . . . 151
A.4. Berry curvature of Dirac Fermions and Nodal lines in 2D . . . 153
A.4.1. Berry Charge of a Dirac Cone . . . 153
A.4.2. Berry Charge of a Nodal Ring . . . 154
A.5. Sublattice Polarization and Non-Local Overlap Matrix . . . 154
A.5.1. Honeycomb Sublattice Polarization . . . 155
A.5.2. Non-Local Overlap Matrix . . . 155
A.5.3. Valley Expansion of the Triangular and the Kane-Mele Model . . . 156
A.6. Bulk OAM Polarization . . . 158
A.7. OAM and Spin Polarization in Finite Size Geometries . . . 159
A.8. Trial Basis Overlaps . . . 161
A.9. AgTe: Comparison of the Minimal Tight-Binding Model and DFT . . . 162

1. Introduction

In the last century, progress in different fields of condensed matter such as in band theory of solids [5–8] as well as in crystal growth [9–11] and characterization [12–14] have paved the way for today's semiconductor devices. They form the basis for modern communication, encryption, simulation, controlling, etc., which have decisively shaped present society and economics. Focusing on current advances, profound outcome from the application of the mathematical concept of topology in the context of electronic structure of crystalline solids may be expected. It revolutionizes the conception of band structure theory as it comes with fundamental implications on electronic properties, as recognized by the awarding of the Nobel Prize to Thouless, Haldane and Kosterlitz in 2016. The concept introduces a topological classification, all systems which can be *adiabatically transformed* into each other belong to the same class [15]. Consequently, a topological phase transition occurs at interfaces between materials of different classes. This guarantees for topologically protected interface states with exciting properties, e.g., dissipationless transport and spin-momentum locking [16–20].

The thesis mainly focuses on band insulators, which are characterized by a global gap separating the valence and the conduction states. However, only some of them have *trivial* valence bands, which can be adiabatically connected to the energy spectrum of an isolated atom, the *atomic limit* [21, 22]. As shown by Altland and Zirnbauer [23], time-reversal symmetric insulators are classified by a $\mathbb{Z}_2$-invariant [18, 24, 25]. In two dimensions (2D) the associated *non-trivial* phases are so-called quantum spin Hall insulators (QSHI) [18, 26, 27]. They possess on their edges dissipationless metallic spin-momentum locked helical edge states, potential candidates for spintronics and quantum computing[18, 28–31]. The key ingredient is the interplay of spin-orbit coupling (SOC) and spin-independent hybridizations. The presence of both can result in an *inverted* bulk gap [27]: the symmetry of the valence bands varies in momentum space between a SOC- and a hybridization-dominated atomic limit. Hence, these systems lack a localized basis, which is capable of describing the bands in the full Brillouin zone (BZ) [32–34]. The *Wannier obstruction* is a physical consequence of the non-trivial geometric phase and the related Berry curvature [35, 36].

This highlights also the importance of spatial symmetries, which introduce side conditions on band structure and momentum space Berryology. The presence of time-reversal and inversion symmetry guarantees for spin-degenerate bands with total vanishing chirality [37]. An insulating state can be stabilized by gapping all low-energy band crossings by SOC. Instead, inversion-symmetry breaking (ISB) promotes chiral

wave functions on the level of the orbital degrees of freedom, i.e., even in the absence of SOC [38, 39]. Therefore, the low-energy states in non-inversion symmetric insulators can be either gapped by SOC or ISB. Further, if ISB dominates in the whole BZ, the valence bands can be adiabatically connected to a time-reversal symmetric spinless model. Consequently, these bands must be necessarily $\mathbb{Z}_2$-trivial. Therefore ISB has been historically anticipated as detrimental to $\mathbb{Z}_2$-topology and the focus was primarily on high symmetric crystals with large SOC [24].

The importance of lattice symmetries is also reflected in the main driving forces for the discovery of new QSHIs, which are (I) efficient classification schemes [40–47], (II) theoretical models [18, 27, 48] and (III) material realizations [31, 49–52]. The topological classification (I) can be either obtained by directly addressing the geometrical phase emerging from Berry curvature sources [42, 43], i.e., (avoided) band crossings such as Dirac and Weyl cones as well as nodal lines, or from a symmetry analysis, which considers only states at certain momenta [40, 41, 44–47]. The latter approach underlines further the notion that spatial symmetries, especially inversion symmetry, are in support of the stabilization of QSHI phases. Recently, under the name of *topological quantum chemistry*, a scheme relying on the wave function symmetry at all high symmetry momenta has been established [44–47]. The classification is based on the comparison of the valence band representation to band representations of all atomic limits. Despite its efficiency and simplicity, it is important to note that in low-symmetric space groups, non-trivial bands can be identified as *false-trivial* and a fallback to a direct calculation of the geometrical phase is unavoidable.

From the model (II) and material side (III), in 2006 mercury telluride quantum wells have been proposed and swiftly confirmed at ultra low temperature as QSHIs resulting from a band inversion at the Γ point, which profits from atomic SOC [27, 49]. However, historically, the search for topological models originated from a one-orbital basis on the honeycomb lattice starting with the Chern insulator by Haldane in 1988 [53] and the first QSHI model by Kane and Mele in 2005 [18, 24]. The non-trivial insulating state is stabilized by a non-local SOC term, which renders the valley Dirac fermions massive, and inversion symmetry breaking favors a trivial gap. Up to now, several attempts of a material realization of the Kane-Mele model have been pursued. As the SOC interaction in graphene is orders of magnitude to weak even for low-temperature experiments [54], heavier Group IV derivatives have been considered [55]. They require a supporting substrate, which breaks inversion symmetry [56, 57]. A seminal breakthrough has been achieved by the discovery of the large-gap QSHI *bismuthene* [52], a honeycomb lattice of bismuth atoms on a silicon carbide substrate in 2017. Its Dirac fermions arise from the multi-orbital in-plane p-subspace and are rendered massive by a sizable, since local, SOC. Furthermore, the substrate is indispensable as it not only promotes structural stability, but it is also relevant for achieving the characteristic low-energy band structure. Still, the relatively small flake sizes owing to the adsorption geometry prevent the measurement of the quantized edge channel transport. Recently, the research on topology in hexagonal crystals has been further stimulated as the

scientific community has been attracted by kagome systems [48, 58–60].

Taking up the intrinsic interest in hexagonal QSHIs, this thesis breaks with the paradigm of inversion symmetric multi-site basis sets. It focuses instead on their elementary symmetry equivalent, namely the triangular lattice, which is the predominant surface arrangement on technologically relevant trigonal substrate surfaces (see also supplemental material to Ref. [3]). Furthermore, monoatomic basis sets come with the advantage of a sizable atomic SOC interaction. Still, it remains to be seen how a triangular basis can host metallic band crossings, such as Dirac fermions and nodal lines. It is also worth mentioning that local SOC dominates when taking these systems to their atomic limit. Hence, a non-local counterpart, which induces the phase winding, is required for the stabilization of a QSHI ground state. This inevitably leads to the task of determining the necessary conditions for non-trivial $\mathbb{Z}_2$-topology on the triangular lattice. In particular, is spatial symmetry in support of or detrimental to the QSHI phase? What are the consequences of horizontal and vertical mirror reflection symmetry on electrons on the triangular lattice? As a well established phenomenon in Rashba systems [1], ISB promotes chiral wave functions, i.e., by promoting orbital angular momentum polarization. Can symmetry breaking serve as the desired complementary non-local antagonist to the atomic SOC? If so, how do triangular QSHI phases compare to non-trivial phases on hexagonal multi-site basis sets, such as the honeycomb? Are there fundamental differences and to which extent can they be regarded as equivalent? Can symmetry indicators unambiguously identify the band topology in these low-symmetric space groups, i.e., are their non-trivial phases lurking in a blind spot of the high-throughput studies? Finally, are these considerations solely limited to the theoretical discourse or can we propose non-trivial insulating phases in realistic triangular material realizations?

Motivated by such an intriguing perspective, this thesis presents a thorough analysis of symmetry-breaking stabilized topological insulating phases of p-electrons on the triangular lattice. The main focus is on group theoretical aspects, minimal tight-binding modeling including mirror reflection symmetry-breaking terms and the investigation of material realizations based on *ab initio* methods, substantiated if possible, with comparison to experiments. This unveils the underlying physics of indenene [3, 61] and its general key aspects such as the relation between inversion symmetry breaking and chiral wave functions. The comparison of valley Dirac fermions from honeycomb and from triangular multi-orbital basis sets is also discussed. Equipped with the minimal p-shell model, the full topological phase space arising from the interplay of horizontal and vertical reflection symmetry breaking and atomic SOC is explored. The analysis of the wave function symmetry in terms of irreducible band representations and OAM polarization demonstrates the intricate impact of real-space symmetry on band symmetry and topology.

Beyond band topology, symmetry indicators have been recently also proposed for a topological distinction of insulators with trivial bands on the level of their valence

charge localization. Considering also the positions of the atomic nuclei, these insulators can be sub-classified as trivial atomic limits, if the valence charge centers are aligned with the atomic lattice, and as *real-space obstructed* atomic limits, where at least one electron is displaced from the nuclei position [44, 46, 47, 62–64]. The latter results in finite electric multipoles. These have been put forward as a driving force for higher-order topological insulators (HOTIs) in two dimensions, which are characterized by insulating edges and fractionally filled in-gap corner states [65–72]. Hence this raises the question of the relation between real-space obstruction and triangular lattice symmetries. Can we propose a higher-order topological insulator with insulating 1D edges and fractionally filled in-gap corner states [4]. Obviously, it is compelling to extend the concept of real-space obstruction to QSHIs. However, since these insulators lack a Wannier representation, the definition of a charge center localization is not straightforward as symmetry indicators are not directly applicable. To tackle this challenge, we follow the proposed time-reversal violating Wannier construction for $\mathbb{Z}_2$-non-trivial bands by Soluyanov and Vanderbilt [73]. With this charge center locator, all QSHI phases of the triangular model are examined and the importance of real-space obstruction as a discriminator between disconnected non-trivial phases is highlighted. This addresses not only the relation between mirror symmetry breaking and the localization of the non-Kramers degenerate Wannier centers, but elucidates also the full extent of the equivalence and difference between a Kane-Mele and indenene-type QSHI.

The thesis concludes with a discussion on triangular monolayer adsorbates on trigonal substrate surfaces, where horizontal and vertical mirror reflection symmetry breaking is present. Combining adatom species and various substrates gives access to a rich parameter space of symmetry breaking and SOC strength as well as electron filling. This allows to inspect the fundamental physics of the minimal p-shell model in real materials and validates the applicability of our theoretical edifice, including also the discovery of indenene. The chapter profits substantially from experiments sensitive to the wave function symmetry, such as linear polarized angle-resolved photoemission measurements and spatially resolved scanning tunneling microscopy data. A preliminary discussion on the orbital-driven Rashba effect in the binary honeycomb AgTe on Ag (111) illustrates the interplay of SOC and inversion symmetry breaking [1]. As a central aspect, the first realized triangular QSHI indenene on SiC is analyzed in all its facets [3]. Another crowning moment is the classification of its topology by the direct probe of the bulk wave function symmetry, instead of relying on signatures in transport experiments. Extending this analysis to the full Brillouin zone, we will assess whether indenene constitutes also the first real-space obstructed QSHI [2]? By reducing the SOC strength, i.e., considering the lighter Group III elements, a real-space obstructed HOTI phase is proposed. The section is concluded by an outlook beyond single particle physics focusing on Group V adsorbates on SiC. They possess a compensated Fermi surface formed by the in-plane p bands The Lindhard function is investigated in the light of band symmetry mediated long-range multi-orbital instabilities.

The thesis is structured as follows: chapter 2 is devoted to an introduction to the rel-

evant theory and concepts applied in this thesis including the symmetry discussion of triangular lattices in hexagonal and trigonal environments. In chapter 3 the symmetry and real-space localization of valley Dirac fermions from multi-orbital basis sets on the triangular lattice are analyzed, which comprises also the comparison to the honeycomb basis set. The lattice-periodic tight-binding description is derived in Chapter 4. In particular, horizontal reflection-symmetry breaking as well as the local SOC term are introduced. For the full phase space of this model, the resulting $\mathbb{Z}_2$-topology and real-space obstruction are discussed in Chapter 5. The thesis concludes with Chapter 6, where the aforementioned phenomena are investigated in triangular monolayer adsorbates on trigonal substrate surfaces. The *ab initio* study is complemented by results from collaborations with the experiment.

2. Basic Theory and Concepts

2.1. Topological Insulators and Electric Polarization

This section provides a compact overview on topological insulators with the focus on quantum spin Hall insulators (QSHI). Further, it gives a short introduction to higher-order topology in 2D. The connection between the geometrical phase and the electric polarization will be established. Lastly the Kane-Mele model is briefly discussed as the paradigmatic hexagonal QSHI. The interested reader is referred to excellent Refs. [18–20, 24, 74, 75].

2.1.1. Topological Insulators

The mathematical concept of topology introduces a classification scheme, all systems that can be *adiabatically transformed* into each other belong to the same class [15]. As a result, a topological phase transition must occur at interfaces where materials of different classes meet. In solid state physics, crystals can be distinguished at the level of their band structure, which is either metallic, semi-metallic or insulating. The latter is characterized by the absence of states at the Fermi energy, i.e., a global gap, which divides the bands in the subsets of valence and conduction states. Considering all possible types of valence bands, there exist indeed several topological classes ranging from the ordinary insulator to exotic phases, which are still insulating in the bulk, but possess metallic surface states [19, 20, 23]. The former group falls into the class of the *atomic limits*. Their *trivial* valence bands can be adiabatically connected to the states of an isolated atom [22]. The band structure remains insulating by taking slowly[1] the lattice constant to infinity, which rescales the non-local terms of the Hamiltonian. This does not hold for topological insulators [21]. The transformation into an atomic limit involves necessarily a gap reopening under the exchange of valence and conduction states. Hence, metallic states must exist at interfaces of insulators belonging to different topological classes and at surfaces[2] of non-trivial insulators. Their existence is topologically protected against all perturbations, which leave the bulk properties invariant and explains the particular scientific interest in these exciting phases [19, 20].

[1] "slow" with respect to the energy scale of the gap.
[2] Interface to the topologically trivial vacuum.

The first topological lattice model has been conceived by Haldane [53], which falls into the class of Chern insulators in 2D [36]. A staggered magnetic field with vanishing total flux breaks time-reversal symmetry. It results in a (anti-) clockwise propagating 1D helical edge state. This is called quantum anomalous Hall effect in analogy to the quantum Hall effect [76], which arises from an external magnetic field. Time-reversal symmetric systems are instead classified by a $\mathbb{Z}_2$-invariant with the QSHI as the non-trivial phase in 2D [18, 23, 26, 27]. The presence of spin-orbit coupling (SOC) and spin-independent orbital hybridizations defines two disconnected atomic limits: the former interaction promotes a splitting with respect to the total angular momentum J, the latter may be represented by a crystal field or covalent bonding. Hence, the interplay of SOC and orbital hybridizations can stabilize an *inverted* bulk gap[18, 26, 27]: the variation of the valence band symmetry in momentum space results in at least two momenta, of which one represents a SOC-dominated limit, while the states at the other momentum are adiabatically connected to a hybridization-driven atomic limit. As a result, the occupied bands in the whole BZ lack an atomic limit. The quantum spin Hall effect occurs in finite size geometries of 2D $\mathbb{Z}_2$-non-trivial systems. Time-reversal symmetry enforces the presence of two dissipationless counter-propagating edge states with anti-parallel spin alignment[18, 26, 27]. As a pedagogical approach to 2D spin-diagonal QSHIs, their spin-blocks may be regarded as time-reversal partners of Chern insulators. However, this oversimplifies drastically the situation in real crystals and excludes non-trivial $\mathbb{Z}_2$-phases based on off-diagonal SOC terms, an example will be given in Chap. 5. This fact is often swept under the rug in the contemporary discussion of topological systems, when it comes to the comparison of condensed matter realizations to the flourishing fields of ultra cold atoms [77] as well as bosonic [78, 79] and classical analogues [80–84].

The formerly described d-dimensional topological insulators have $d-1$-dimensional surface states (codimension 1), i.e., they relate to first-order topology. Recently higher-order topological phases have been discovered [65, 69]. A second-order topological insulator in 2D is characterized by an insulating bulk and 1D edges, but 0D metallic in-gap corner states. Therefore, such a phase must be $\mathbb{Z}_2$-trivial. A finite electric quadrupole moment of the bulk has been put forward as a driving mechanism for corner charge. Electric multipoles imply real-space obstruction, at least one of the Wannier charge centers of the valence bands is located on a non-atomic lattice position. The band structure of such an *obstructed atomic limit* is not adiabatically connected to the ordinary atomic limit with charge centers only on the atomic sites if the lattice symmetries are preserved. This introduces a topological classification scheme in the class of $\mathbb{Z}_2$-trivial bands at the level of the electronic and atomic charge localization. Further it raises the question, if these phases are comprised by the terminology "topological insulator", which is historically exclusively reserved for isolated subsets of bands lacking a Wannier representation. In this thesis, we follow the modern and inclusive interpretation of Refs. [65, 85–93]. Further insights on the relation between real-space obstruction, electronic multipoles and corner states on the triangular lattice are discussed in Secs. 5.5 and 5.7.

2.1.2. Electric Polarization, Berry Phase and topological invariants

While the previous section has established the fundamental properties of topological insulators, the origin of the exotic transport characteristics remains still elusive. Also the connection to a mathematical geometric object carrying the topological invariant is missing. Here we will discuss the relation between the geometric phase of the wave function and the electronic polarization in the presence of time-reversal symmetry. As will be shown in Sec. 2.3.2, the real-space representation of a cell-periodic Bloch wave function $u_n(\mathbf{k})$ of an isolated band n, i.e., its Wannier function, can be constructed in the unit cell at Bravais vector $\mathbf{R}$ by

$$|w_{n\mathbf{R}}\rangle = \frac{V}{(2\pi)^3}\int \mathrm{d}\mathbf{k}^3 e^{i\mathbf{k}\cdot(\mathbf{r}-\mathbf{R})}\,|u_n(\mathbf{k})\rangle\,. \tag{2.1}$$

Invoking the definition of the Wannier center expectation value formulated in real and momentum space in Eq. 2.59

$$\langle\mathbf{r}\rangle_n = \langle w_{n0}|\mathbf{r}|w_{n0}\rangle = i\frac{V}{(2\pi)^3}\int \mathrm{d}\mathbf{k}\,\langle u_n(\mathbf{k})|\nabla_{\mathbf{k}}|u_n(\mathbf{k})\rangle\,, \tag{2.2}$$

highlights the connection between real-space localization and the geometric phase of the cell-periodic Bloch wave function in momentum space. As will be discussed in Sec. 2.3.2, the Wannier charge centers are gauge-dependent and must obey the lattice periodicity. Therefore, a closed path s in parameter space λ leaves the charge center position invariant up to a Bravais vector. The change in the electric polarization $\mathbf{P} = -e\mathbf{r}$ is given by

$$\begin{aligned}\Delta\mathbf{P} &= \oint_s \mathrm{d}\lambda \frac{\partial\mathbf{P}}{\partial\lambda}\\ &= -|e|\frac{2}{(2\pi)^3}\mathrm{Im}\int_{\mathrm{BZ}}\mathrm{d}\mathbf{k}\int_{\lambda_i}^{\lambda_f}\mathrm{d}\lambda\sum_n^{\mathrm{occ}}\left\langle\frac{\partial u_n(\lambda,\mathbf{k})}{\partial k_\alpha}\middle|\frac{\partial u_n(\lambda,\mathbf{k})}{\partial\lambda}\right\rangle\\ &= -e\mathbf{R}.\end{aligned} \tag{2.3}$$

Hence the accumulated polarization is equivalent to the Berry phase γ and the integrated Berry curvature flux Ω through the enclosed surface S

$$\gamma = \oint \mathrm{d}\lambda\,\langle u(\lambda)|i\partial_\lambda u(\lambda)\rangle = \int_S \Omega(\lambda)\mathrm{d}S, \tag{2.4}$$

which can be of course generalized to a multi band formalism [75]. The adiabatic pumping parameter λ will be in the following a closed path in momentum space for determining the topology of an Hamiltonian of a periodic system. Non trivial bands are characterized by an adiabatic charge pump of the Wannier centers by a lattice vector $\mathbf{R}$, i.e., a quantized Berry phase of multiples of 2π. Tracing the adiabatic evolution, also called the Wilson-loop, is mathematically identical to the integration of the Berry curvature. The former is numerically more stable.

The topological invariant of Chern insulators $C \in \mathbb{Z}$ can be immediately identified with this formalism. However, time-reversal symmetry impedes the direct calculation of the $\mathbb{Z}_2$-invariant $\nu = \{0, 1\}$ [40]. The Bloch functions come in time-reversal partners, which must carry an opposed phase. Hence, the total phase vanishes irrespective of the invariant. On the other hand, time-reversal symmetry relates states at $\mathbf{k}$ and $-\mathbf{k}$. Therefore, sampling half of the BZ in combination with geometric arguments is sufficient for determining the $\mathbb{Z}_2$-invariant [42, 43]. Albeit tremendous progress in symmetry-based classification schemes, this is up to date the method of choice for a flawless computation of the $\mathbb{Z}_2$-invariant of non-inversion symmetric systems.

Let us relate this discussion to our initial definition of topological bands: the absence of a localized band representation is reflected in a charge center flow in momentum space. The latter is a consequence of the non-trivial winding of the geometric phase, the mathematical object which carries the topological information. This relation will be briefly discussed for the Kane-Mele model in the next section.

2.1.3. Kane-Mele model

This section is devoted to a brief introduction of the *the hexagonal* QSHI model on the honeycomb lattice [18, 24]. It will serve as a reference system for the proposed QSHIs on the triangular lattice in Chaps. 5 and 6. The model was inspired by mapping symmetry-derived Dirac cones onto a crystal lattice. This reveals illustratively the impact of symmetry breaking and SOC on the low-energy states and the associated topology. Here we will consider only spin-diagonal terms, which allows for the interpretation of the QSHI phase as a time-reversal symmetric combination of Chern insulators defined on the separated spin blocks.

As will be discussed in detail in Sec. 2.4, the presence of inversion symmetry in a honeycomb lattice results in Dirac cones at the opposed corners K and K' in the hexagonal BZ [18][3]. Expressed in a spin-full honeycomb basis $\{\mathrm{A}, \mathrm{B}\} \otimes \{\uparrow, \downarrow\}$, the Dirac Hamiltonian reads in the presence of SOC and inversion symmetry breaking (ISB) [18, 24]

$$H^{K/K'}(\mathbf{k}) = v_F \left(\pm k_x \tau_x + k_y \tau_y\right) \otimes \mathbb{1}_{2,2} \pm \lambda_{\mathrm{SOC}} \tau_z \otimes \sigma_z + \lambda_{\mathrm{ISB}} \tau_z \otimes \mathbb{1}_{2,2}. \tag{2.5}$$

The Pauli matrices τ_i and σ_i act on the orbital and spin degrees of freedom, respectively. The group velocity is denoted by v_F. The SOC and ISB interaction are diagonal in orbital and spin space, they scale with λ_{SOC} and λ_{ISB}, while the "$\pm$" discriminates K and K'. Hence, each spin block is described by an effective two band model

$$H^{K/K',\sigma}(\mathbf{k}) = \mathbf{d}(\mathbf{k}) \cdot \boldsymbol{\tau} = v_F \left(\pm k_x \tau_x + k_y \tau_y\right) + m(K/K', \sigma)\tau_z. \tag{2.6}$$

[3] For illustrations of the UC and BZ see Figs. 2.4.2 and 3.2.1 (a).

The **d**-vector covers either the upper or lower hemisphere depending on the sign of $m(K/K', \sigma)$. In 2D, its integrated Berry curvature accumulates to a Berry charge of $\pm\pi$ [74, 75]. If SOC dominates the mass term, the total Berry charge of both valley momenta is $\pm 2\pi$, which results in a spin Chern number of $C_{\uparrow/\downarrow} = \pm 1$. In turn also the $\mathbb{Z}_2$-invariant $\nu = |(C_\uparrow - C_\downarrow)/2| = 1$[4] is non-trivial. Instead, if ISB dominates, the total Berry charge vanishes in each spin block and the $\mathbb{Z}_2$-invariant is trivial.

Upon embedding the continuous model given in Eq. 2.5 in a lattice Hamiltonian, Kane and Mele unveiled that this results the low-energy description of the π electrons in graphene [18, 24]

$$\hat{H}^{\mathrm{KM}} = t \sum_{\langle ij \rangle} c_i^\dagger c_j + i \frac{\lambda_{\mathrm{SOC}}}{3\sqrt{3}} \sum_{\langle\langle ij \rangle\rangle} \nu_{ij} c_i^\dagger \sigma_z c_j + \lambda_{\mathrm{ISB}} \sum_i \xi_i c_i^\dagger c_i . \tag{2.7}$$

The first term is the first neighbor hopping term, which promotes the lattice symmetry enforced Dirac Fermions at the valley momenta as shown in Fig. A.1.1. The next-nearest neighbor spin-orbit interaction is given by the second term and preserves the lattice symmetries. Its prefactor has been chosen such that the valley Hamiltonian in Eq. 2.5 is retrieved and ν_{ij} is the sign of z-component of the Dzyaloshinskii–Moriya vector $(2/\sqrt{3})(\mathbf{d}_1 \times \mathbf{d}_2)_z$. It is defined by a two step hopping process along the connecting first neighbor bonds [see also Sec. 4.2.2 and Fig. 4.2.1 (c)]. The last term breaks inversion symmetry, as it introduces a staggered potential ($\xi = \pm 1$), which renders the the two sublattices inequivalent [94]. A formulation of the Hamiltonian in momentum space can be found in App. A.5.3.

The competition of ISB and SOC defines the symmetry character of the valence band at K, which in turn is imperative for the topological phase as shown in Fig. 2.1.1 (a). A dominant ISB term results in a strong localization of the valence bands on only one of the sublattice sites in the whole BZ. This band structure is $\mathbb{Z}_2$trivial, as it represents an atomic limit. In the $\nu = 1$ phase, the sizable SOC promotes a sublattice polarization which alternates between the two states of the valence doublet at K. This band symmetry prohibits an adiabatic connection to an atomic limit.

In the following, we will analyze the impact of the gap at the valley momenta on the geometric phase. This will also serve as an introduction to the method of choice for the calculation of the $\mathbb{Z}_2$-invariant in this thesis: the analysis of the Wilson loop integral given Eq. 2.3. The $\mathbb{Z}_2$-invariant is encoded in the Wannier charge center movement of the two phases shown in Fig. 2.1.1 (b). The vertical axis denotes the Wannier center position in units of the second Bravais vector and the horizontal axis is the pumping momentum [parameter λ in Eqs. 2.3 and 2.4] in units of the first reciprocal vector[5]. The WCCs of the trivial phase split gently during the pumping cycle and recombine

[4] Definition via spin-Chern numbers is only possible for spin-diagonal Hamiltonians [75].

[5] Time-reversal symmetry enforces a symmetric Wannier charge center flow with respect to the time-reversal invariant pumping momenta 0 and 1/2. Therefore the pumping interval $[0, 0.5]$ is representative for the closed Wilson Loop $[0, 1]$.

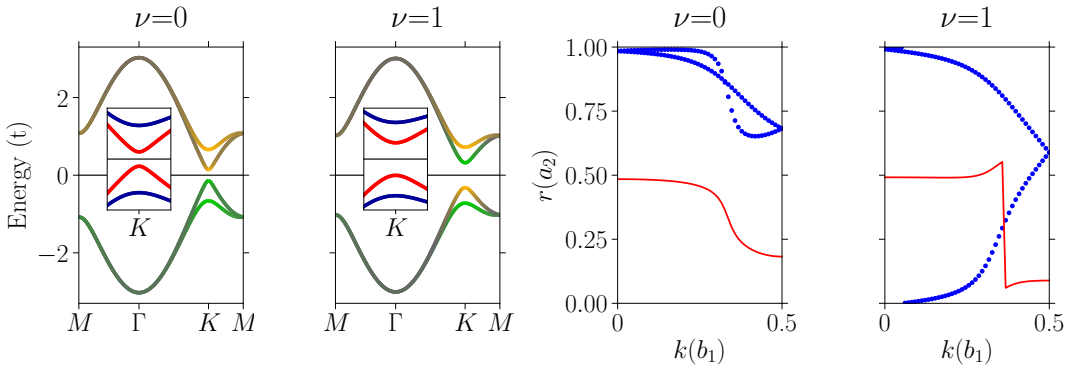

(a) (b)

Figure 2.1.1.: (a) Representative band structure for the $\nu = 0(1)$ phase of the Kane-Mele model for $\lambda_{\mathrm{SOC}} = 0.1(0.2)t$ and $\lambda_{\mathrm{ISB}} = 0.4(0.2)t$. The orange-green color code denotes the sublattice character and the red-blue color scheme in the inset shows the $\langle S_z \rangle$ polarization at valley momentum K. The BZ and the position of the high-symmetry points is illustrated in Figs. 2.4.2 (b).
(b) Corresponding Wannier charge center (blue) movement and their largest gap (red) to the band structures shown in (a).

without carrying a net polarization. This is qualitatively different for the $\nu = 1$ bands, the WCC of the two spin blocks traverse the UC in opposite direction, i.e., they acquire a Berry phase of $\pm 2\pi$. As a consequence of the interplay of SOC and first neighbor hybridizations, the WCCs and hence the valence band subspace cannot be localized in real space. This insulating phase lacks an atomic limit.

In finite size geometries[6], the reduced coordination at the surfaces enforces the connection to an atomic limit. For $\nu = 1$ bands, this can only be established by re-opening the bulk gap under the exchange of valence and conduction bands, i.e., the presence of helical edge states. As shown in Fig. A.1.2, only the $\nu = 1$ bulk phase possesses four metallic edge states connecting the valence and conduction bands. The presence of time-reversal symmetry forbids back-scattering between two anti-parallel spin-polarized and counter propagating states at each edge [19]. The edge localization and interaction between opposed edges is mediated by the bulk gap [16]. Further, their existence is topologically protected against any perturbation acting at the edges. The $\nu = 0$ phase of the Kane-Mele has instead insulating finite size geometries. In general, they can be also rendered from insulating to metallic and *vice versa* by applying an appropriate edge potential, which modifies the electronic polarization at the edges[7].

To summarize, the Kane-Mele model describes a minimal one orbital basis on a

[6] See Fig. 5.6.1 for an illustration of the fundamental edge terminations and corresponding BZs.
[7] A bulk polarized insulator with $\nu = 0$ bands will be discussed in Chap. 5. It has metallic edges and their band structures can be found in Sec. 5.6.

honeycomb lattice. This results in inversion symmetry protected Dirac cones at the valley momenta. Upon including SOC, a QSHI phase is stabilized. It highlights the detrimentality of ISB to non-trivial $\mathbb{Z}_2$-topology: a staggered potential is in favor of a trivial insulator. Hence the $\mathbb{Z}_2$invariant of the Kane-Mele model is not only encoded in the geometrical phase, it can be straightforwardly derived from the real-space localization of the valley valence states. In this thesis, the comparison of the Kane-Mele model with triangular systems will allow us to highlight intuitively their similarities and fundamental differences. As a prerequisite, Dirac fermions expressed in both basis sets will be discussed in Chap. 3.

2.2. *ab initio* Theory

This section is devoted to a short introduction to a self-consistent description of electrons in solids within the framework of density functional theory (DFT). In the context of this thesis, DFT will be applied for determining the topological character of the insulating ground state. Hence a qualitative, but symmetry-correct description of the band structure may be acceptable as long as the gapping of the low-energy bands is properly described. This is however an intrinsic weakness of standard DFT functionals, which can be either overcome by improved methods and, if applicable, the comparison to the experiment, as highlighted in Chap. 6. In the following, fundamental concepts and the applied DFT theory in this thesis will be introduced based on the implementation in the Vienna *ab initio* simulation package (VASP) [95–98]. This is by no means comprehensive, the interested reader is referred to standard literature such as Refs. [99, 100].

2.2.1. The Many-Body Problem in Solid State Physics

In this thesis, the crystal structure formed by the atomic nuclei serves as an external potential. It defines the electronic ground state via the imposed symmetries and the properties of the involved atomic species. However, in the most general situation, where the atomic nuclei are also treated as independent particles, the whole system is described by the kinetic energy of the electrons and the nuclei as well as by the interaction between the charged particles via the Coulomb potential. The corresponding Hamiltonian may be formulated as[100]:

$$\hat{H} = -\frac{\hbar^2}{2m_e}\sum_i \nabla_i^2 - \sum_I \frac{\hbar^2}{2M_I}\nabla_I^2 \tag{2.8}$$

$$+\frac{1}{4\pi\epsilon_0}\left(\frac{1}{2}\sum_{i\neq j}\frac{e^2}{|\mathbf{r}_i-\mathbf{r}_j|}+\frac{1}{2}\sum_{I\neq J}\frac{Z_I Z_J e^2}{|\mathbf{R}_I-\mathbf{R}_J|}-\sum_{i,I}\frac{Z_i e^2}{|\mathbf{r}_i-\mathbf{R}_J|}\right). \tag{2.9}$$

Upper and lower case notation denotes nuclei and electrons, respectively. A theory is called *ab initio*[8], if it is defined self-consistently based on fundamental laws by considering the natural constants. These are for Eq. 2.9 the electron mass m_e, the reduced Planck constant $\hbar$ and the vacuum permittivity ϵ_0 as well as the mass M_I and charge Z_I of the nuclei. A general mathematical and numerical solution to this many-body problem is however challenging owed to the non-locality and locality of the kinetic and Coulomb terms, respectively, and the large number of degrees of freedom. This has stimulated the search for effective theories and reasonable approximations. As sketched in the beginning and proposed by Born and Oppenheimer, the atomic positions may be considered as fixed as their mass is three orders of magnitude larger than the electron mass [101]. The fundamental description simplifies to:

$$\hat{H} = -\frac{\hbar^2}{2m_e}\sum_i \nabla_i^2 + \frac{1}{8\pi\epsilon_0}\sum_{i\neq j}\frac{e^2}{|\mathbf{r}_i - \mathbf{r}_j|} + \sum_{i,I} V_I(|\mathbf{r}_i - \mathbf{R}_I|) + E_{II} \tag{2.10}$$

$$= \hat{T} + \hat{V}_{\text{int}} + \hat{V}_{\text{ext}} + E_{II}. \tag{2.11}$$

Hence, the electron-nuclei interaction enters as a single particle term. It considers electrons in an "external" potential $\hat{V}_{\text{ext}}$ and the nucleus-nucleus repulsion contributes with a constant value E_{II} [100]. The interacting nature of the electron system is instead retained and the solution of the Schrödinger equation requires a fermionic many-body ansatz.

2.2.2. Density Functional Theory (DFT)

The success of DFT relies on the proof of the existence of a unique functional which relates the many-body ground state density $n_0(r)$ to the total energy, as derived by Hohenberg and Kohn [7]. Hence, all properties of an interacting electron system can be derived from the density. This functional is however unknown, but reasonable results can be obtained from the Kohn-Sham ansatz, which maps the interacting system onto a single-particle auxiliary model [8].

2.2.2.1. Hohenberg-Kohn Theorems

Starting from the Born-Oppenheimer approximation given in Eqs. 2.10 and 2.11, Hohenberg and Kohn have proven that a system of electrons in an external potential $V_{\text{ext}}(\mathbf{r})$ is uniquely defined by the ground state density $n_0(\mathbf{r})$. This manifests in two theorems [7, 100]:

I *For any system of electrons in an external potential $V_{\text{ext}}(\mathbf{r})$, that potential is determined uniquely, except for a constant, by the ground state density $n_0(\mathbf{r})$.*

[8]Latin: From the beginning, fig. from first principles.

II *A **universal functional** for the energy $E[n(\mathbf{r})]$ of the density $n(\mathbf{r})$ can be defined for all electron systems. The exact ground state energy is the global minimum for a given $V_{\text{ext}}(\mathbf{r})$, and the density $n(r)$ which minimizes the functional is the exact ground state density $n_0(r)$.*

From the first theorem can be derived that the Hamiltonian is fully defined by $V_{\text{ext}}(\mathbf{r})$ and the many-body wave function as well as all other properties are completely determined. The second theorem implies that the functional $E[n(\mathbf{r})]$ is sufficient to obtain the ground state energy and density via a variational principle [99, 100]. This constitutes an exact and solvable many-body theory and the existence of such a functional has been proven formally. However, its formulation remains elusive.

2.2.2.2. Kohn-Sham Ansatz

Kohn and Sham proposed a mapping of the full many-body problem onto a *non-interacting* auxiliary system with many-body corrections [8]. This allows the reformulation of the functional $E[n(\mathbf{r})]$ in the single-particle picture and has paved the way for modern DFT functionals. They operate under the assumption, that the many-body ground state density can be represented by the ground state density of an auxiliary system of non-interacting particles, the so called Kohn-Sham wave orbitals $\phi_i(\mathbf{r})$ [100]. They are the eigenfunctions of a Schrödinger-like equation

$$\left(\hat{H}_{\text{KS}}(\mathbf{r}) - \epsilon_i\right) \phi_i(\mathbf{r}) = 0, \tag{2.12}$$

with the eigenvalues ϵ_i of the effective Kohn-Sham Hamiltonian H_{KS}. It is defined by the kinetic energy of the auxiliary independent electrons and the Kohn-Sham potential

$$\hat{H}_{\text{KS}}(\mathbf{r}) = -\frac{\hbar^2}{2m_e}\nabla^2 + V_{\text{KS}}(\mathbf{r}). \tag{2.13}$$

The subtle many-body correction is contained in the Kohn-Sham potential. It is derived from the Kohn-Sham ground state functional E_{KS}, which treats correctly the Hartree contribution of the Coulomb interaction $E_{\text{Hartree}}[n]$. All other many-body effects are incorporated in the exchange-correlation functional $E_{\text{xc}}[n]$

$$E_{\text{KS}}[n] = T[n] + E_{\text{ext}}[n] + E_{\text{Hartree}}[n] + E_{\text{xc}}[n] + E_{II}. \tag{2.14}$$

The ground state energy is obtained by minimizing the functional with respect to the density by a variational approach under the assumption of orthonormal Kohn-Sham wave orbitals

$$\frac{\delta E_{\text{KS}}}{\delta \phi_i^*(\mathbf{r})} = \frac{\delta T}{\delta \phi_i^*(\mathbf{r})} + \left[\frac{\delta E_{\text{ext}}}{\delta n(\mathbf{r})} + \frac{\delta E_{\text{Hartree}}}{\delta n(\mathbf{r})} + \frac{\delta E_{\text{xc}}}{\delta n(\mathbf{r})}\right] \frac{\delta n(\mathbf{r})}{\delta \phi_i^*(\mathbf{r})}. \tag{2.15}$$

The functional derivative acting on the kinetic functional yields immediately the free-electron term. Similarly, the Kohn-Sham eigenvalues enter as Lagrange multipliers

$$\frac{\delta T}{\delta \phi_i^*(r)} = \frac{\hbar}{2m_e} \sum_j^N \int \mathrm{d}^3\mathbf{r}' \frac{|\nabla \phi_j(\mathbf{r}')|^2}{\delta \phi_i^*(\mathbf{r})} = -\frac{\hbar^2}{2m_e} \nabla^2 \phi_i(\mathbf{r}), \tag{2.16}$$

$$\frac{\delta E_{\mathrm{KS}}}{\delta \phi_i^*(\mathbf{r})} = \sum_j^N \epsilon_j \frac{\delta |\phi_j(\mathbf{r})|^2}{\delta \phi_i^*(\mathbf{r})} = \epsilon_i \phi_i(\mathbf{r}). \tag{2.17}$$

With the functional derivative of the density

$$\frac{\delta n(\mathbf{r})}{\delta \phi_i^*(\mathbf{r})} = \sum_{j=1}^N \frac{\delta |\phi_j(\mathbf{r})|^2}{\delta \phi_i^*(\mathbf{r})} = \phi_i(\mathbf{r}), \tag{2.18}$$

the external and the Hartree potential are derived by [8]

$$\frac{\delta E_{\mathrm{ext}}}{\delta n(\mathbf{r})} = \int \mathrm{d}\mathbf{r}' V_{\mathrm{ext}}(\mathbf{r}') \frac{\delta n(\mathbf{r}')}{\delta n(\mathbf{r})} = V_{\mathrm{ext}}(\mathbf{r}), \tag{2.19}$$

$$\begin{aligned} \frac{\delta E_{\mathrm{Hartree}}}{\delta n(\mathbf{r})} &= \frac{e^2}{8\pi\epsilon_0} \int\int \mathrm{d}\mathbf{r}' \mathrm{d}\mathbf{r}'' \frac{1}{|\mathbf{r}' - \mathbf{r}''|} \frac{\delta n(\mathbf{r}') n(\mathbf{r}'')}{\delta n(\mathbf{r})} \\ &= \frac{1}{4\pi\epsilon_0} \int \mathrm{d}\mathbf{r}' \frac{n(\mathbf{r}')}{|\mathbf{r} - \mathbf{r}'|} = V_{\mathrm{Hartree}}(\mathbf{r}), \end{aligned} \tag{2.20}$$

$$\frac{\delta E_{\mathrm{xc}}}{\delta n(\mathbf{r})} = V_{\mathrm{xc}}(\mathbf{r}), \tag{2.21}$$

$$\tag{2.22}$$

The last term denotes the exchange-correlation potential, which is the remaining undetermined parameter. Hence, the Kohn-Sham potential of the Kohn-Sham Hamiltonian in Eq. 2.13 is given by:

$$V_{\mathrm{KS}}(\mathbf{r}) = V_{\mathrm{ext}}(\mathbf{r}) + V_{\mathrm{Hartree}}(\mathbf{r}) + V_{\mathrm{xc}}(\mathbf{r}). \tag{2.23}$$

Before discussing parametrizations of the exchange-correlation functional, let us briefly comment on the advantages of the Kohn-Sham ansatz and the interpretation of the Kohn-Sham eigenvalues and orbitals. The many-body Hamiltonian was mapped onto first-order differential equations which can be solved with standard minimization procedures and appropriate basis sets. In principal, if the correct exchange-correlation functional is known and if the densities of the many-body ground state and of the auxiliary single-particle system are identical, the solution will be exact. *Vice versa*, the Kohn-Sham ansatz is obviously incapable of describing strongly correlated ground states such as Mott phases, Kondo-physics and super conductivity. Further, the Kohn-Sham eigenvalues ϵ_i are formally only Lagrange multipliers, which lack any physical meaning, e.g., Koopmans' theorem [102] does not hold [99]. Nevertheless, a good up to an excellent agreement between the DFT and band structure with the experiment

is often achieved upon an appropriate functional choice. Examples can be found in Chap. 6. This however highlights also an important deficiency of DFT as standard functionals tend to underestimate the hybridization gap in semiconductors and insulators. This might even result in the prediction of a metallic ground state. In the context of topological insulators, this can lead to a wrong band hierarchy, i.e., it favors a band inversion and predicts *false non-trivials* [103–105]. A robust solution to this problem is presented for the case of indenene in Sec. 6.2.2, which bases on the comparison of the wave function symmetry in theory and experiment.

2.2.2.3. Exchange-Correlation Functionals

As pointed out in the previous section, the Kohn-Sham ansatz is under certain conditions exact. However the delicate many-body contributions are to be embedded in the exchange-correlation functional. As a first intuitive attempt, Kohn and Sham proposed the local-density approximation (LDA) based on the exchange-correlation functional of a uniform interacting electron gas [8]

$$E_{\mathrm{xc}}^{\mathrm{LDA}}[n] = \int \mathrm{d}^3\mathbf{r}\epsilon_{\mathrm{xc}}[n(\mathbf{r})]n(\mathbf{r}). \tag{2.24}$$

It has been soon extended to spin-dependent systems under the name of local spin density approximation [106–108],

$$E_{\mathrm{xc}}^{\mathrm{LSDA}}[n^{\uparrow}, n^{\downarrow}] = \int \mathrm{d}^3\mathbf{r}\epsilon_{\mathrm{xc}}[n^{\uparrow}(\mathbf{r}), n^{\downarrow}(\mathbf{r})]n(\mathbf{r}). \tag{2.25}$$

These approximations have a tendency towards the underestimation of the gap, but are justified in systems with reasonably slowly varying spatial electronic densities [99]. Further improvement has been achieved by the generalized-gradient approximation (GGA) by considering also derivatives of the density [100, 109, 110]

$$E_{\mathrm{xc}}^{\mathrm{GGA}}[n^{\uparrow}, n^{\downarrow}] = \int \mathrm{d}^3\mathbf{r} f[n^{\uparrow}(\mathbf{r}), n^{\downarrow}(\mathbf{r}), |\nabla n^{\uparrow}(\mathbf{r})|, |\nabla n^{\downarrow}(\mathbf{r})|, ...]n(\mathbf{r}), \tag{2.26}$$

Within the framework of certain physical conditions [111], a broad spectrum of GGA functional f parametrizations has been developed. In the context of electronic band structures in crystals, the functional proposed by Perdew, Burke and Ernzerhof (PBE) has proven its efficiency and reasonable accuracy, which qualifies it as the method of choice in this thesis.

Still PBE tends to underestimate band gaps owed to the improper incorporation of the Fock-exchange

$$E_{\mathrm{x}}^{\mathrm{F}} = -\frac{e^2}{8\pi\epsilon_0}\sum_{i,j}^{N}\int \mathrm{d}^3\mathbf{r}'\mathrm{d}^3\mathbf{r}\phi_j^*(\mathbf{r}')\phi_i^*(\mathbf{r})\frac{1}{|\mathbf{r}-\mathbf{r}'|}\phi_j(\mathbf{r})\phi_i(\mathbf{r}'). \tag{2.27}$$

The calculation of the Fock potential comes at an significant increase of the computational cost as it scales with $\mathcal{O}(N^3)$ compared to the Hartree-like Kohn-Sham ansatz scaling $\mathcal{O}(N^2)$. Substantial improvement in the DFT eigenvalues has been achieved by hybrid functionals, where the exchange contribution E_x of a standard LDA/GGA functional is corrected by the Fock-exchange [112]

$$E_{\mathrm{xc}} = E_{\mathrm{xc}}^{\mathrm{LDA/GGA}} + a(E_{\mathrm{x}}^{\mathrm{HF}} - E_{\mathrm{x}}^{\mathrm{LDA/GGA}}), \quad a = (0, 1]. \tag{2.28}$$

Again, various flavors exist. In this thesis an updated version of the Heyd-Scuseria-Ernzerhof functional HSE06 is employed. It corrects the PBE exchange term by a screened Coulomb interaction [113, 114].

An improved estimation of the screening can be obtained within the *GW* approximation. A comparison of PBE, HSE06 and *GW* results is shown in Sec. 6.2.4 for the triangular QSHI indenene on SiC.

2.2.2.4. DFT Implementation in VASP

In this section, the remaining ingredients required for performing DFT calculations are discussed based on their implementation in the Vienna *ab initio* simulation package (VASP). The most important technical details, which discriminate between various DFT codes, are the chosen basis set for the Kohn-Sham wave functions and approximations made to the atomic potential. They influence greatly the performance as well as the accuracy in energy and in the spatial distribution of the wave function.

VASP uses a plane wave basis set, the maximum wave vector $\mathbf{G}$ and the number of coefficients is defined by the size of the unit cell and the plane wave cutoff

$$E_{\mathrm{cut}} \geq \frac{\hbar^2}{2m_e}|\mathbf{G} + \mathbf{k}|^2. \tag{2.29}$$

This is a well-suited basis choice for weakly bound states. However deep atomic potentials resulting in a strong wave function localization require an extensive plain wave basis set, i.e., a large energy cutoff.

The high efficiency of VASP relies mainly on softened potentials, so-called pseudo potentials. Inside the atomic spheres, the potential is smoothed with the boundary condition, that the wave function at and beyond the boundary is identical to the one of the initial potential. As a consequence, the number of nodes in the radial part of the wave functions is reduced or vanishes. In this thesis, VASP's projector augmented wave pseudo potentials are used [98, 115]. The plane wave functions are mapped inside the atomic spheres via a projector scheme on spherical Bessel functions centered at the atomic sites. The pseudo potentials are further smoothed within the frozen core approximation, where the core electrons have been integrated out. This softens the core potential by Coulomb screening and reduces also the number of electrons in the DFT calculation.

Before concluding the section on *ab initio* theory, it should be noted that the here presented concepts are also valid for non-collinear calculations, which are required for the proper description of $\mathbb{Z}_2$-non-trivial phases. Relativistic terms such asSOC can be included self-consistently based on the expansion of the Dirac equation. In particular, the projector augmented wave basis allows for a straightforward formulation in terms spherical harmonics [116, 117].

2.3. Tight-Binding and LCAO Basis Functions

This chapter is devoted to a short introduction to tight-binding methods. Based on these, the triangular p-shell Hamiltonian is derived in Chap. 4. Further, the creation of minimal models from *ab initio* simulations is introduced. All tight-binding calculations in this thesis have been performed with the python library *post_wan* [118], which has been developed during my PhD project.

The fundamental problem of electrons on a crystal lattice can be addressed in two basis function limits: in the case of weakly bound electrons, the nearly free electron picture applies. This is the realm of the plane-wave expansion, as discussed in the previous section for the DFT code VASP. However for tightly-bound electrons, Bloch proposed a linear combination of atomic orbitals (LCAO) with finite hopping strengths between neighboring sites [5]. The strength of tight-binding resides in the efficient and symmetry-correct model description in small basis sets. This allows for a direct analysis of the symmetry of the Bloch wave function. Further, it is the method of choice for the simulation of large unit cells, e.g., for the calculation of surface states in finite size geometries. As highlighted in the second section of this chapter, the construction of Wannier-Hamiltonians from DFT-wave functions interfaces *ab-initio* methods and tight-binding descriptions [34, 119]. This introduces also realistic single-electron basis sets to all-electron methods.

The Hamiltonian of an independent electron reads in real space

$$\hat{H}(\mathbf{r}) = \left(-\frac{h^2}{2m}\nabla^2_{\mathbf{r}} + V(\mathbf{r}) \right), \tag{2.30}$$

with the lattice periodic potential

$$V(\mathbf{r}) = \sum_{\mathbf{R},\alpha} V_\alpha(\mathbf{r} - \boldsymbol{\tau}_\alpha - \mathbf{R}), \tag{2.31}$$

where $\mathbf{R}$ denotes the lattice vector of the unit cell and α labels the atom-specific potentials centered at the Wyckoff position $\boldsymbol{\tau}_\alpha$.

Following the lines and adapting the notation of [75], we define the orthonormal basis (ONB) set of local orbitals $\phi_{j\mathbf{R}}$ obeying

$$\langle \phi_{i\mathbf{R}} | \phi_{j\mathbf{R}'} \rangle = \delta_{i,j}\delta_{\mathbf{R},\mathbf{R}'}. \tag{2.32}$$

It is noteworthy to mention, that the finite overlap of atomic orbitals on a lattice excludes them of being a ONB. However, an atomic-like ONB can be obtained by applying a Löwdin orthogonalization, which preserves the symmetries of the wave functions [6, 34]. In the local basis, the elements of the Hamiltonian of Eq. 2.30 read

$$H_{ij}(\mathbf{R}) = \langle \phi_{i\mathbf{R}'} | \hat{H} | \phi_{j,\mathbf{R}'+\mathbf{R}} \rangle = \langle \phi_{i0} | \hat{H} | \phi_{j\mathbf{R}} \rangle \,, \tag{2.33}$$

where $\mathbf{R}$ is the relative distance between the orbitals i and j.

In the "Bloch-gauge", i.e., assigning the same Bloch phase to all orbitals belonging to the same unit cell, the trial Bloch basis reads

$$|\psi_j(\mathbf{k})\rangle = \sum_{\mathbf{R}} e^{i\mathbf{k}\cdot\mathbf{R}} \, |\phi_{j\mathbf{R}}\rangle \,, \tag{2.34}$$

with the Hamiltonian in momentum space

$$H_{ij}(\mathbf{k}) = \langle \psi_i(\mathbf{k}) | H | \psi_j(\mathbf{k}) \rangle = \sum_{\mathbf{R}} e^{i\mathbf{k}\cdot\mathbf{R}} H_{ij}(\mathbf{R}). \tag{2.35}$$

By solving the eigenvalue equation

$$H(\mathbf{k})\mathbf{C}_n(\mathbf{k}) = E_n(\mathbf{k})\mathbf{C}_n(\mathbf{k}), \tag{2.36}$$

the coefficients of the Bloch wave eigenfunction

$$|\Psi_n(\mathbf{k})\rangle = \sum_{\mathbf{R}j} e^{i\mathbf{k}\cdot\mathbf{R}} c_{nj}(\mathbf{k}) \, |\phi_{\mathbf{R},j}\rangle \,, \tag{2.37}$$

can be obtained. They are connected to the "lattice gauge" by a momentum-dependent gauge transformation $U(\mathbf{k})$

$$c_{nj}(\mathbf{k}) = e^{i\mathbf{k}\cdot\boldsymbol{\tau}_j} \tilde{c}_{nj}(\mathbf{k}), \tag{2.38}$$

where $\boldsymbol{\tau}_j$ denotes the Wyckoff position of the orbital j. The Hamiltonian in momentum space is given by

$$\tilde{H}_{ij}(\mathbf{k}) = \langle \tilde{\phi}_i(\mathbf{k}) | H | \tilde{\phi}_j(\mathbf{k}) \rangle = \sum_{\mathbf{R}} e^{i\mathbf{k}\cdot(\mathbf{R}+\boldsymbol{\tau}_j-\boldsymbol{\tau}_i)} H_{ij}(\mathbf{R}). \tag{2.39}$$

The lattice gauge is often the natural choice for analytic tight-binding models. However, for multi-site basis sets, the fractional translations $\boldsymbol{\tau}_j - \boldsymbol{\tau}_i$ result in a momentum space Hamiltonian, which is not invariant under the translation of a reciprocal lattice vector $\mathbf{G}$ [74]:

$$\tilde{H}_{\mathbf{k}+\mathbf{G}} \neq \tilde{H}(\mathbf{k}). \tag{2.40}$$

The Bloch gauge respects this translational invariance which expresses itself in the simple Fourier transformation in Eq. 2.35. This simplifies the numerical implementation

and is the chosen gauge in *wannier90* [120, 121] and in the *post_wan* package [118]. The former has been used for obtaining minimal models from DFT for the systems presented in Chap. 6, while the latter was used for all tight-binding calculations presented in this thesis.

This links the tight-binding wave function to the cell-periodic wave functions $u_n(\mathbf{k})$

$$\Psi_n(\mathbf{k}) = e^{i\mathbf{k}\cdot\mathbf{r}} u_n(\mathbf{k}), \tag{2.41}$$

which play a decisive role in the modern theory of polarization introduced in Sec. 2.1.2. The connection is given by

$$|\Psi_n(\mathbf{k})\rangle = \sum_{\mathbf{R}} \int_{\mathrm{uc}} \mathrm{d}^3\mathbf{r}\, u_n(\mathbf{k}) e^{i\mathbf{k}\cdot(\mathbf{R}+\mathbf{r})} \,|\mathbf{R}+\mathbf{r}\rangle\,, \tag{2.42}$$

$$= \sum_{\mathbf{R}} \sum_{j} \tilde{c}_{nj}(\mathbf{k}) e^{i\mathbf{k}\cdot(\mathbf{R}+\boldsymbol{\tau}_j)} \,|\phi_{j\mathbf{R}}\rangle\,. \tag{2.43}$$

In the following, an overview is given on the construction of tight-binding models based on lattice symmetries (Slater-Koster) and from first-principles (Wannier functions).

2.3.1. Slater-Koster Parametrization: Two center-approximation

Slater and Koster introduced an efficient formalism for calculating tight-binding hopping elements by considering only one- and two-center transfer integrals [6]. This allows for a simple qualitative model description, the discrete symmetries of the lattice enter via the real-space interaction elements of the Hamiltonian.

Bloch's initial proposal of the LCAO-method [5] is in principle an accurate single-particle description. However, the Hamiltonian given in Eq. 2.33

$$H_{ij}(\mathbf{R}) = \int \mathrm{d}^3\mathbf{r} \phi_i^*(\mathbf{r}) H \phi_j(\mathbf{r}+\mathbf{R}), \tag{2.44}$$

involves complicated three-center integrals where electrons from two different sites interact with the lattice potential (see Eq. 2.31) of a third site. By considering only two-center contributions, Eq. 2.44 simplifies to the defining equation of the Slater-Koster integrals

$$H_{ij}^{\mathrm{SK}}(\mathbf{R}) = \int \mathrm{d}^3\mathbf{r} \phi_i^*(\mathbf{r}) H_{\mathbf{R},ij}^{2c} \phi_j(\mathbf{r}+\mathbf{R}). \tag{2.45}$$

Here, $H_{R,ij}^{2c}$ is the Dimer-version of Eq. 2.30 or, if $i = j$, a mono-atomic on-site integral [122][9]. As s, p-orbital tight-binding basis sets will be considered in this thesis, the

[9] Interestingly, the SK approximation is per construction incapable to generate crystal field splittings, unless the ligand orbitals are explicitly included. This is addressed in [123, 124].

geometric dependence of their Slater-Koster integrals is given hereinafter [6]:

$$E_{s,s} = V_{ss}^{\sigma}, \tag{2.46}$$
$$E_{s,p_i} = n_i V_{sp}^{\sigma}, \tag{2.47}$$
$$E_{p_i,p_i} = n_i^2 V_{pp}^{\sigma} + \left(1 - n_i^2\right) V_{pp}^{\pi}, \tag{2.48}$$
$$E_{p_i,p_j} = n_i n_j \left(V_{pp}^{\sigma} - V_{pp}^{\pi}\right). \tag{2.49}$$

Here $i, j \in \{x, y, z\}$ with $i \neq j$ denote the alignment of the p-orbitals with respect to the cartesian coordinate axes. For a given dimer Hamiltonian $H_{\mathbf{R},ij}^{2c}$, V^{σ} and V^{π} denote the Slater-Koster parameters for σ and π transmission, which depend on the distance and the atomic species. n_i and n_j are direction cosines of the displacement vector and reflect the relative alignment of the orbitals.

2.3.2. Wannier Functions

Driven by the vision of reconciling the plane-wave and localized wave function picture in solids, Wannier proved that any Bloch wave function can be represented by localized orbitals $w_{\mathbf{R}j}$ full-filling Eq. 2.32 [125]. This decomposition is however not unique owed to a gauge freedom. Hence, various Wannier construction approaches based on wave function symmetries have been proposed [34, 126, 127]. Instead, Marzari and Vanderbilt have put forward the concept of maximally localized Wannier functions (MLWF) by minimizing their spread. This allows for the down-folding of ab-initio wave functions onto minimal Wannier basis sets [119, 128] and provides realistic tight-binding parameters for model calculations and advanced all-electron methods. Furthermore, the localized Wannier functions allow for a rigorous definition of the position operator in solids, the central property in the "modern theory of polarization" (MTP) [129, 130].

Here we review briefly the construction of Wannier functions and their gauge-freedom. We introduce the definition of the position operator and give an overview on the construction of MLWFs as implemented in *wannier90*. It is the applied software package for the creation of Wannier models in this thesis.

According to Bloch's theorem [5], the translational invariance in a solid implies

$$\Psi_n(\mathbf{r} + \mathbf{a}, \mathbf{k}) = \hat{T}_{\mathbf{a}} \Psi_n(\mathbf{r}, \mathbf{k}) = e^{i\mathbf{k}\cdot\mathbf{a}} \Psi_n(\mathbf{r}, \mathbf{k}). \tag{2.50}$$

In analogy to Eq. 2.34 we can define the Bloch wave function in the continuous lattice gauge

$$\Psi_n(\mathbf{r}, \mathbf{k}) = e^{i\mathbf{k}\cdot\mathbf{r}} u(\mathbf{r}), \tag{2.51}$$

as the product of the Bloch phase and its cell-periodic function $\hat{T}_{\mathbf{R}} u(\mathbf{r}) = u(\mathbf{r})$. Wannier functions $|w_{n\mathbf{R}}\rangle$ located in the unit cell $\mathbf{R}$ can be constructed by an integration over

the first BZ

$$\begin{aligned} |w_{n\mathbf{R}}\rangle &= \frac{V}{(2\pi)^3}\int \mathrm{d}^3\mathbf{k}\hat{T}_{-\mathbf{R}}\,|\Psi_n(\mathbf{k})\rangle \\ &= \frac{V}{(2\pi)^3}\int \mathrm{d}^3\mathbf{k}e^{-i\mathbf{k}\cdot\mathbf{R}}\,|\Psi_n(\mathbf{k})\rangle \\ &= \frac{V}{(2\pi)^3}\int \mathrm{d}^3\mathbf{k}e^{i\mathbf{k}\cdot(\mathbf{r}-\mathbf{R})}\,|u_n(\mathbf{k})\rangle\,, \end{aligned} \tag{2.52}$$

with V being the volume of the unit cell and $\mathbf{r}$ denotes the position coordinate in the home unit cell ($\mathbf{R} = 0$). Further, the equations above make evidently clear, that Wannier functions depend on the chosen gauge of the Bloch wave function

$$|\tilde{\Psi}_n(\mathbf{k})\rangle = e^{i\tilde{\gamma}_n(\mathbf{k})}\,|\Psi_n(\mathbf{k})\rangle\,, \quad |\tilde{u}_n(\mathbf{k})\rangle = e^{i\tilde{\gamma}_n(\mathbf{k})}\,|u_n(\mathbf{k})\rangle\,. \tag{2.53}$$

The gauge phase $\tilde{\gamma}_n(\mathbf{k})$ is required to be smooth such that $\nabla_{\mathbf{k}}\,|u_n(\mathbf{k})\rangle$ is well-defined and periodic in momentum space [34]:

$$\tilde{\gamma}_n(\mathbf{k}+\mathbf{G}) = \tilde{\gamma}_n(\mathbf{k}) + \mathbf{G}\cdot\mathbf{R} = \tilde{\gamma}_n(\mathbf{k}) + 2\pi n, \quad n \in \mathbb{N}. \tag{2.54}$$

This condition highlights two fundamental points:

- A given wave function may be expressed in different gauges, however phase differences arising from shifts by a reciprocal lattice vector $\mathbf{G}$ are quantized to $2\pi n$.
- The phase difference is directly related to a translation in real space by a Bravais lattice vector $\mathbf{R}$.

This is of great importance for wave functions obtained from numerical simulations. Their gauge may depend on the implementation and diagonalization procedure.

To control the gauge-dependency, we can introduce a momentum-dependent unitary transformation $U_{mn}(\mathbf{k})$ in Eq.2.52

$$|w_{n\mathbf{R}}\rangle = \frac{V}{(2\pi)^3}\int \mathrm{d}^3\mathbf{k}e^{-i\mathbf{k}\cdot\mathbf{R}}U_{mn}(\mathbf{k})\,|\Psi_n(\mathbf{k})\rangle\,. \tag{2.55}$$

The initial gauge can be controlled by projecting onto a localized trial basis $|g_n\rangle$ [34, 119, 131]

$$|\phi_n(\mathbf{k})\rangle = \sum_m |\Psi_m(\mathbf{k})\rangle\,\langle\Psi_m(\mathbf{k})|g_n\rangle\,. \tag{2.56}$$

A smooth gauge $U_{mn}(\mathbf{k})$ can be then obtained from the Löwdin orthogonalization of the overlap matrix $S_{mn}(\mathbf{k}) = \langle\phi_m(\mathbf{k})|\phi_n(\mathbf{k})\rangle$

$$|\tilde{\Psi}_n(\mathbf{k})\rangle = \sum_m |\phi_m(\mathbf{k})\rangle\,(S(\mathbf{k})^{-1/2})_{mn}, \tag{2.57}$$

which can be used to generate Wannier functions following Eq. 2.55.

Another ansatz are MLWFs, which are obtained by minimizing the spread functional [119]

$$\Omega = \sum_n \left[\langle \mathbf{r}^2 \rangle_n - \langle \mathbf{r} \rangle_n^2 \right], \tag{2.58}$$

By following Blount's definition of the position operator for periodic functions [132], it becomes evident that the localization of a Wannier function is directly related to the phase gauge of the corresponding cell-periodic wave functions [119]

$$\langle \mathbf{r} \rangle_n = \langle w_{n0} | \mathbf{r} | w_{n0} \rangle = i \frac{V}{(2\pi)^3} \int \mathrm{d}^3\mathbf{k} \, \langle u_n(\mathbf{k}) | \nabla_{\mathbf{k}} | u_n(\mathbf{k}) \rangle \, . \tag{2.59}$$

Consequently, the second moment is given by

$$\langle \mathbf{r}^2 \rangle_n = \frac{V}{(2\pi)^3} \int \mathrm{d}^3\mathbf{k} \, \langle u_n(\mathbf{k}) | \nabla_{\mathbf{k}}^2 | u_n(\mathbf{k}) \rangle^2 \, . \tag{2.60}$$

As demonstrated by Marzari and Vanderbilt, the spread defined in Eq. 2.58 can be decomposed into a gauge-independent and a gauge-dependent contribution. The minimization of the latter allows for the construction of a unique MLWF basis set [119] by optimizing $U_{mn}(\mathbf{k})$.

The software package *wannier90* combines the two aforementioned approaches in a three-step procedure [119–121, 128]:

- The initial gauge is obtained via the projection onto an atomic-like trial basis g_n: $\rightarrow U_{mn}(\mathbf{k})^g$
- Disentanglement of non-isolated bands via minimization of the spread: $\rightarrow U_{mn}(\mathbf{k})^{\mathrm{dis}}$
- Maximally localization of the disentangled subspace : $\rightarrow U_{mn}(\mathbf{k})^{\mathrm{loc}}$

It is worth mentioning that the symmetries inherited from the trial basis projection (e.g., atomic s, p, d, f orbitals) of the Wannier functions and of the Wannier Hamiltonian are not necessarily preserved throughout the disentanglement and the localization procedure. Further, $U_{mn}(\mathbf{k})^{\mathrm{dis}}$ and $U_{mn}(\mathbf{k})^{\mathrm{loc}}$ optimize the spread by mixing orbital- and, if SOC is included, spin-degrees of freedom. The constructed Wannier functions may differ significantly from the initial trial basis. Especially for systems with dominant atomic SOC, a L, S trial basis may be rotated into a J Wannier basis. As the thesis focuses on symmetry-driven phenomena, the symmetries of the tight-binding wave functions have to be well-defined. Therefore, the Wannier models are constructed by avoiding the disentanglement and the localization procedure. For entangled bands, this comes at the expense of enlarged trial and Wannier basis sets.

2.4. Group Theoretical Analysis of the Triangular Lattice

The strength of group theory resides on its qualitative predictive power, based on the symmetry analysis of the system. In this section, the basic concepts of group theory applied to solid state physics will be reviewed. It is followed by a profound symmetry analysis of hexagonal and trigonal layer groups, which will be of fundamental importance for the understanding of the electronic properties of the discussed models and materials in this thesis.

2.4.1. Group Theory in the context of Crystals

A crystal is defined by the combination of a Bravais lattice, spanned by the primitive vectors $\{\mathbf{a}_i\}$ and the unit cell (UC), i.e., the basis positions of the atoms. This results in discrete crystal symmetries, which are reflected in the invariance under a set of translations $\mathbf{t}$ and point group operations α, such as rotations C_n, reflections σ_i, improper rotations S_n and inversion $\mathcal{I}$. The combinations of all these symmetry operations define the elements g

$$g = \{\alpha|\mathbf{t}\}\,, \tag{2.61}$$

of the space group G [133]. They are defined as a point group operation followed by a translation:

$$g\mathbf{r} = \{\alpha|\mathbf{t}\}\,\mathbf{r} = \mathbf{r}' = R_\alpha\mathbf{r} + \mathbf{t}, \tag{2.62}$$

with the matrix representation R_α of α. Consequently, the Hamiltonian H commutes with the elements of G and the Bloch wave function must be an *irreducible representation* of G and H.

Special symmetry operations are [133]:

- $\{\epsilon|0\}$=identity
- $\{\alpha|0\}$=pure point group operations
- $\{\epsilon|\mathbf{t}\}$=pure translations

The elements of the latter two constitute the point group of the crystal and the translation group which are both subgroups of G. In the following, we will briefly elaborate on these two important groups establishing also fundamental concepts of group theory based on references [133–136].

2.4.1.1. Point Groups

Besides the identity, the elements of the point groups can be rotations C_n, reflections σ, inversion $\mathcal{I}$ and roto-reflections. They can be grouped into classes and two elements g_i and g_j belong to the same class if there exists another element $\tilde{g}$ in G fulfilling

$$g_i = \tilde{g} \circ g_j \circ \tilde{g}^{-1}. \tag{2.63}$$

For instance, the C_n rotations of a group form a class, if there exists another point group operation, that transforms the C_n rotations into each other. The identity operation ϵ forms its own class. If all elements of a group commute ($g_i = \tilde{g} \circ g_i \circ \tilde{g}^{-1}$), the group is *abelian* and has as many classes as elements and all *irreducible representations* (irreps) are one-dimensional.

A *representation* T of a group G assigns to each element $g \in G$ a linear operator $T(g)$ such that

$$g_1 \circ g_2 = g_3 \quad \Rightarrow \quad T(g_1)T(g_2) = T(g_3), \tag{2.64}$$

and *characters* χ of operations are defined as

$$\chi_T(g) = \mathrm{trace}(T(g)). \tag{2.65}$$

Hence, we can define a scalar product of two representations T_i and T_j of group G based on their characters

$$(\chi_i, \chi_j) = \frac{1}{N} \sum_{g \in G} \chi_i^*(g)\chi_j(g), \tag{2.66}$$

with N being the total number of elements of G. This allows for the definition of *irreducible representations* which we denote by τ. These are representations, whose subspaces are (block-) diagonal with respect to their characters.

$$(\chi_i, \chi_j) = \delta_{ij}. \tag{2.67}$$

Further the number of these elementary building blocks is equal to the number of classes in a group. A *character table* lists the characters of the (irreducible) representations under the symmetry operations (usually grouped in classes) for a given point group and can be found in standard literature.

2.4.1.2. Translation Group

As the translations commute with each other, the translation group is abelian and all irreducible representations are one dimensional. By defining the reciprocal lattice vectors $\{\mathbf{b}_j\}$ as the inverse of the primitive vectors $\{\mathbf{a}_i\}$ [133],

$$\mathbf{a}_i \cdot \mathbf{b}_j = 2\pi\delta_{ij}, \tag{2.68}$$

the translation by a lattice vector $\mathbf{R}$ can be represented by plane waves with lattice momentum $\mathbf{k}$

$$\hat{P}_{\{\epsilon|\mathbf{R}\}} = T^{\mathbf{k}}(\mathbf{R}) = e^{i\mathbf{k}\cdot\mathbf{R}}. \tag{2.69}$$

The Bloch wave function can be written as

$$\psi(\mathbf{r},\mathbf{k}) = e^{i\mathbf{k}\cdot\mathbf{r}}u(\mathbf{r}), \tag{2.70}$$

with the cell-periodic wave function $u(\mathbf{r})$ invariant under the lattice translations of the crystal:

$$\begin{aligned}\hat{P}_{\{\epsilon|\mathbf{R}\}}\psi(\mathbf{r},\mathbf{k}) &\overset{!}{=} \psi(\mathbf{r}+\mathbf{R},\mathbf{k}) = e^{i\mathbf{k}\cdot(\mathbf{r}+\mathbf{R})}u(\mathbf{r}+\mathbf{R}) \\ &= e^{i\mathbf{k}\cdot\mathbf{R}}\left[e^{i\mathbf{k}\cdot\mathbf{r}}u(\mathbf{r})\right] = e^{i\mathbf{k}\cdot\mathbf{R}}\psi(\mathbf{r},\mathbf{k}).\end{aligned} \tag{2.71}$$

Hence, the Bloch wave functions are the basis functions of the translation group in solids. This periodicity implies, that translations by integer linear combinations of reciprocal lattice vectors $\mathbf{G}$

$$\mathbf{k}+\mathbf{G} \equiv \mathbf{k}, \quad \mathbf{G} = n_i\mathbf{b}_i, \quad n_i \in \mathbb{Z}, \tag{2.72}$$

have the same representations. For a given crystal, we define the momenta $\mathbf{k}$ of the first BZ as a set of non-equivalent irreducible representations of the translation group. Further, we can directly relate real- and reciprocal-space symmetries as scalar products must be invariant under the symmetry operations of the point group:

$$2\pi N_\alpha = (\hat{P}_\alpha\mathbf{R})\cdot\mathbf{G} \overset{\hat{P}_\alpha^{-1}}{=} \mathbf{R}\cdot(\hat{P}_\alpha^{-1})\mathbf{G}, \quad N_\alpha \in \mathbb{Z}. \tag{2.73}$$

Therefore, the effect of a symmetry operator $\hat{P}_\alpha$ on a real space translation is equivalent to the effect of the inverse symmetry operation in momentum space. This establishes the connection between real space and reciprocal space symmetries. All crystal momenta in the BZ transforming under

$$h\mathbf{k} = \{\alpha|\mathbf{G}\}\mathbf{k} = \mathbf{k}, \quad h \in G_{\mathbf{k}} \subset G, \tag{2.74}$$

form the *star* k^* of momentum $\mathbf{k}$. The elements h give rise to the *little co-group* $G_{\mathbf{k}}$, and $\mathbf{k}$ is a high-symmetry point, if $G_{\mathbf{k}}$ is not trivial (i.e., consists not only of the reciprocal translations). Special points are the time-reversal invariant momenta (TRIM)

$$\mathcal{T}\mathbf{k} = -\mathbf{k} = \mathbf{k} \mod \mathbf{G}, \tag{2.75}$$

which host in Kramers degenerate eigenstates in the presence of time-reversal symmetry (see also Sec. 2.4.3).

The real space equivalents of the star are *Wyckoff* positions $\boldsymbol{\tau}$ which are similarly defined by the *site-symmetry group* by

$$g\boldsymbol{\tau} = \{\alpha|\mathbf{R}\}\boldsymbol{\tau} = \boldsymbol{\tau}, \quad g \in G_{\mathbf{r}} \subset G, \tag{2.76}$$

and the set of the symmetry operations g define the *orbit* of position $\boldsymbol{\tau}$. The multiplicity of a Wyckoff positions denotes the number of inequivalent positions in the primitive UC, which transform into each other under symmetry operations of G [135]

$$g\boldsymbol{\tau}_i = \boldsymbol{\tau}_j, \quad i \neq j. \tag{2.77}$$

2.4.1.3. Band Representations and Topological Classification

Having established the fundamental concepts and definitions of group theory, we will apply it to band structure theory. The one electron Hamiltonian in solids given in Eq. 2.30 considers the electron's free-motion in a periodic potential $V(\mathbf{r})$ (see Eq. 2.31). While the kinetic energy term preserves the continuous SO(3) symmetry, the crystal potential introduces discrete symmetries and defines the space group. In turn, the Hamiltonian has to commute with the symmetry operators of the space group. The Bloch functions provide the representation of the eigenfunctions of the momentum space Hamiltonian and can be decomposed into irreducible representations of the little group at wave vector $\mathbf{k}$.

Defining the basis Bloch wave functions ψ_j in a local orbital basis (see also Sec. 2.3)

$$|\psi_j\rangle = \sum_{\mathbf{R}} e^{i\mathbf{k}\cdot\mathbf{R}} |\phi_{j\mathbf{R}}\rangle \,, \tag{2.78}$$

allows for a straightforward group theoretical analysis profiting from the well-defined symmetries of the local orbitals ϕ_j. The character of such a Bloch state under an element $h = \{\alpha|\mathbf{t}\}$ of the little group of the momentum $G_{\mathbf{k}}$ is given by

$$\chi_{\psi_j}(h, \mathbf{k}) = e^{i\mathbf{k}\cdot\mathbf{t}} \chi_{\phi_j}(\alpha), \tag{2.79}$$

where $e^{i\mathbf{k}\cdot\mathbf{t}}$ represents the translation eigenvalue. $\chi_{\phi_j}(\alpha)$ is the character of the local orbital under the symmetry operation, i.e., it is the point group character of ϕ under α. Therefore, at $\mathbf{k} = 0$, the Γ-point, the character of the Bloch wave basis function is identical to the one of the local orbital ϕ_j.

Having established the character of a single Bloch wave function (e.g., from a one band tight-binding model), we will consider a general multi-orbital tight-binding basis in the following. As a space group is defined by the Bravais lattice and the point group symmetries, a tight-binding basis for a given space group must obey:

- the point group symmetry of the basis position. The local orbital representations $\mathcal{T}$ must be built from irreducible representations of the site-symmetry group. For instance, a pair of $p_\pm = 1/\sqrt{2}(p_x \pm ip_y)$ orbital is an irreducible representation of the point group $C_{3\nu}$. A single in-plane orbital would break the point group symmetry, as it is not an irreducible representation of the point group (see also Tab. 3.1.1).

- the UC symmetries, i.e., the local orbital sets of basis sites belonging to the same Wyckoff position must be identical. To give an example, in an inversion symmetric honeycomb lattice, both sublattice sites must have identical local basis sets.

The character formula of a general Bloch wave function representation T formed by

the local representation $\mathcal{T}$ reads [136]

$$\chi_T(g, \mathbf{k}) = \sum_i \Delta_i(g, \mathbf{k})\theta_i(g)\chi_{\mathcal{T}}(g), \tag{2.80}$$

where the index i labels all basis positions and Δ_i denotes the Bloch phase difference. $\theta_i(g)$ equals 1, if the basis site is invariant under g, 0 otherwise. This is important for Wyckoff positions with higher multiplicity, as the symmetry operation may map on different, but equivalent basis positions. This is for instance the case for the honeycomb Wyckoff position in hexagonal space groups: vertical mirror reflections and C_6 rotations result in a mapping onto the other sublattice[10]. The character of the local representation at site i is given by $\chi_{\mathcal{T}}(g)$. Therefore the character of the Bloch wave function is given by the product of the character of the transformation of the basis site and the local representation.

To express the Bloch wave function representation T in irreducible representations τ_j of the little group $G_{\mathbf{k}}$

$$T = \sum_j m_j \tau_j, \tag{2.81}$$

we can define scalar product of characters given in Eq. 2.66:

$$m_j = \frac{1}{N} \sum_{g \in G_{\mathbf{k}}} \chi_T^*(g)\chi_j(g), \tag{2.82}$$

which allows for decomposition of the full Bloch wave function of a subset of bands into irreducible representations.

Equipped with this basic, but powerful knowledge, profound qualitative properties of the band structure of electronic orbitals on a lattice in a given space group can be derived [137, 138]. (I) At each momentum, the Bloch wave function must be an irreducible representation of the little group. Hence, the set of irreducible representations and their dimensionality define all possible Bloch wave function symmetries and their degeneracies, respectively. (II) Shared symmetries between high-symmetry momenta impose connectivity relations between their irreps. The irreducible representation of a band can change discontinuously, but must be compatible with the irreps at the surrounding momenta. (III) Extending this concept to the full BZ, the qualitative band structure induced by an orbital representation on a Wyckoff position is given, which goes under the name elementary band representation (EBR). To give an example, the band structure of the inversion symmetric Kane-Mele model shown in Fig. A.1.1 is an EBR induced by the orbitals on the honeycomb Wyckoff positions. The two orbitals give rise to two bands, which are formed by two one-dimensional irreps at the high-symmetry momenta Γ and M and one two-dimensional representation at K. As

[10] See also Figs. 2.4.2 and 3.2.1.

will be discussed in the next chapter, the path Γ-K-M is located in a mirror plane. This imposes a connectivity relation based on the mirror symmetry eigenvalue: at Γ the one dimensional irreps in conduction and valence have different eigenvalues, which remain preserved along Γ-K. At the valley, the two bands intersect and the symmetry values in valence and conduction along K-M are reversed compared to Γ-K. Hence the qualitative band structure and the symmetry of the Bloch wave functions can be solely derived from group theory. However, the assignment of valence and conduction bands requires a Hamiltonian and a given fixed electron number. In the case of the Kane-Mele model, the energy hierarchy of the bands is defined by the sign of the hopping parameter t in Eq. 2.7.

Despite of symmetry protected degeneracies, accidental band crossings can occur in more evolved models at non-high-symmetric momenta. These intersections happen mostly for bands with different irreps living in separate Blocks of the Hamiltonian. Instead, bands with identical irreps can hybridize which makes crossings of bands with identical symmetry characters unlikely. Nevertheless, all of these degeneracies will occur in the p-shell model introduced in Chap. 4 and are relevant for the topological phase transitions in Chap. 5.

Particular interest in band representations has been stimulated by the development of a criterion for the $\mathbb{Z}_2$ classification [44–47, 62, 135]: statements (I-III) allow for a determination of all possible insulating band structures formed by EBRs, which are by definition $\mathbb{Z}_2$-trivial atomic limits. *Vice versa* the non-trivial topology of any insulating subset of bands can be determined with Eq. 2.82, i.e., testing if it can be decomposed in EBRs. If not, the subset of bands is necessarily $\mathbb{Z}_2$-non-trivial. However the results must be taken with care in low-symmetric space groups, as *false-trivials* can occur and will be discussed in Chap. 5. Recently, the classification of $\mathbb{Z}_2$-trivial insulators has been further refined based on the relative alignment of the EBRs and the atoms in real space [44, 46, 47, 62–64]. In trivial atomic limits the positions of the charge centers and the nuclei are in unison. However, for some crystals, at least one EBR of the valence bands is displaced from the atomic lattice. This goes along with finite electric bulk multipoles, which can stabilize charge at interfaces and surfaces of finite-size geometries.

It should be appreciated, that up to this point, all implications on the crystal's electronic band structure have been drawn without solving the Hamiltonian [133]. Of course, the quantitative band dispersion remains elusive. The partition into conduction and valence states requires a minimal model or *ab initio* treatment.

2.4.2. Symmetry breaking in the Hexagonal Bravais Lattice

After having established theoretical framework of group theory, we will analyze in the following the impact of symmetry breaking in the hexagonal lattice. It is the Bravais

lattice of the tight-binding model in Chaps. 4 and 5 and of the adatom monolayers in Chap. 6.

2.4.2.1. Hexagonal and Trigonal Layer Groups

The hexagonal Bravais lattice is shown in Fig. 2.4.1 (a) which has the inversion symmetric wallpaper group[11] $p6mm$. Its 2D point group $6mm$ comprises one C_2, two C_6 and two C_3 in-plane rotations, three in-plane reflection lines σ_v spanned by the first neighbors of Bravais points and three in-plane reflection lines σ_d defined by the connecting line spanned by second neighbors. The angle spanned by the Bravais vectors is $2\pi/3$ (or $\pi/3$ depending on the chosen convention), importantly the reciprocal lattice is rotated by $\pi/6$ against the real space lattice as shown in Fig. 2.4.1 (b). This has the consequence that a vertical reflection σ_v (σ_d) in real space translates into σ_d (σ_v) in reciprocal space. If a crystal lacks one of the in-plane reflections, the real and reciprocal layer groups differ, as their point groups are rotated by $\pi/6$ against each other.

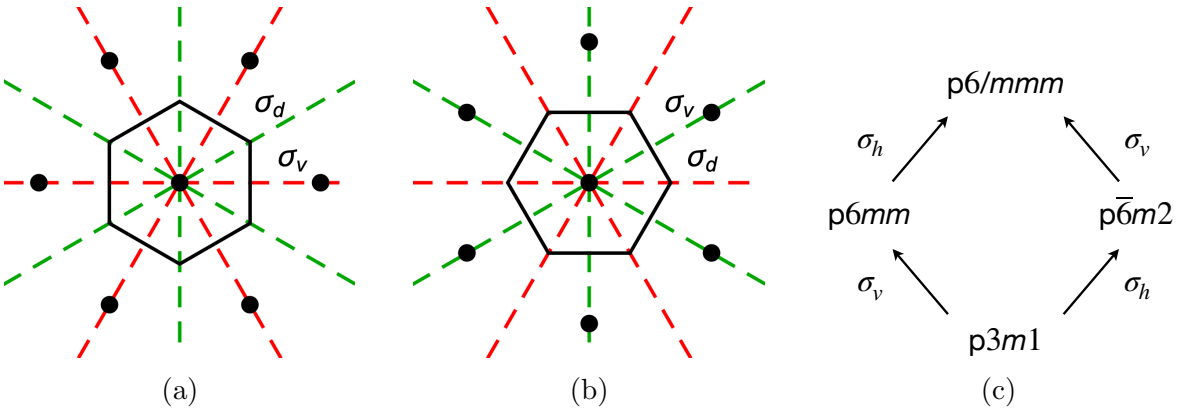

Figure 2.4.1.: Real (a) and reciprocal (b) hexagonal lattice and Wigner-Seitz primitive UC and BZ. The in-plane reflection symmetry lines σ_v (red) and σ_d (green) and the C_6 symmetry of the hexagonal lattice generate the 2D point group $6mm$. (c) Genealogical relation between the hexagonal layer groups $p6/mmm$, $p6mm$ and $p\bar{6}m2$ and the trigonal layer group $p3m1$. In the reading direction bottom to top, the introduced reflection symmetry is written next to the connecting line.

Including the third spatial dimension, the hexagonal Bravais lattice is also invariant under reflections at the horizontal mirror plane σ_h and under the three C_2' and the three C_2'' rotations with rotation axes in the σ_d and σ_v planes, respectively. Its elements comprise also two roto-reflections $S_i = \sigma_h C_i$, namely two S_3 and two S_6. The point group is $6/mmm$ resulting in the layer group p$6/mmm$, where the "/" indicates the rotation axis perpendicular to the σ_h mirror plane. The presence of the out-of-plane

[11] Analogue of the space group in two dimensions.

Hexagonal and trigonal point groups and their symmetry operations

$6/mmm$	E	$2C_6$	$2C_3$	C_2	$3C_2'$	$3C_2''$	I	$2S_3$	$2S_6$	σ_h	$3\sigma_d$	$3\sigma_v$
$6mm$	E	$2C_6$	$2C_3$	C_2							$3\sigma_d$	$3\sigma_v$
$\overline{6}m2$	E		$2C_3$		$3C_2'$			$2S_3$		σ_h	$3\sigma_d$	
$3m1$	E		$2C_3$								$3\sigma_d$	

Table 2.4.1.: Summary of the symmetry operations of the most important point groups in this thesis.

symmetries distinguishes the irreducible representations with respect to their even or odd symmetry under σ_h, e.g., orbitals with different reflection eigenvalues will live in decoupled subspaces of the Hamiltonian.

We will turn now to the consequences of in-plane inversion symmetry breaking, i.e., $(x, y) \not\to (-x, -y)$, which directly forbids C_2 and C_6. As there are pairs of orthogonal σ_v and σ_d reflection lines [see again Fig. 2.4.1 (a,b)], an inversion can be also achieved by the operation $\sigma_v\sigma_d$. Therefore one of the reflection symmetries must be broken. For the systems of interest in this thesis, the absence of σ_v plays a decisive role and reduces the point group from $6/mmm$ to $\overline{6}m2$. Further, the real and reciprocal space are characterized by different layer groups as given in Tab. 2.4.2, which has important consequences for the site-symmetry little co-groups discussed in Sec. 2.4.2.2.

Upon releasing inversion symmetry of layer group p$6/mmm$ by breaking σ_v and/or σ_h, three different layer groups can be stabilized as illustrated in Fig. 2.4.1 (c). In the absence of σ_h, the layer group is p$6mm$. Further releasing σ_v results in the trigonal layer group p$3m1$. If only σ_v is broken, the hexagonal layer group is p$\overline{6}m2$. The corresponding reciprocal layer groups can be found in Tab. 2.4.2. A full overview of the point group elements of the aforementioned real space layer groups is given in Tab. 2.4.1. The elements of $\overline{6}2m$ and $31m$ can be obtained by exchanging σ_v and σ_d.

2.4.2.2. Site-Symmetry and Little Co-Group Analysis

In the following, we will analyze the impact of in-plane inversion symmetry breaking on the site-symmetry groups in real space and the little co-groups in momentum space. For the Wyckoff position $1a$ and the high-symmetry point Γ, i.e., the center of the hexagonal lattice, the point group is the crystallographic point group (see also Tab. 2.4.2). In this section we will focus on the corners and the centers of the sides of the Wigner-Seitz cell of the UC and the BZ, namely the Wyckoff positions $2b$ and $3c$ and the high-symmetry momenta K and M shown in Fig. 2.4.2.

In the inversion symmetric layer group (LG) p$6/mmm$, the multiplicity of Wyckoff

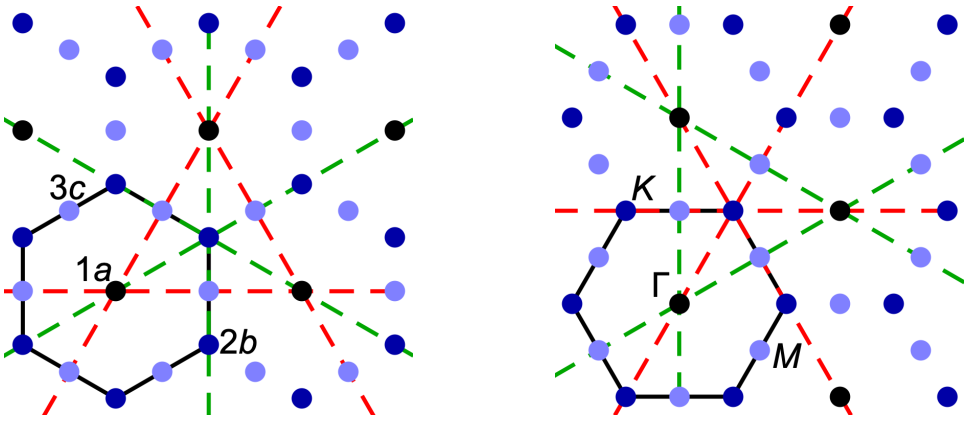

Figure 2.4.2.: Site-symmetry group (a) and little co-group (b) analysis of the Wyckoff positions $2b$ and $3c$ and the high-symmetry points K and M, respectively. The red and green dashed lines denote σ_v (σ_d) and σ_d (σ_v) in real (reciprocal) space, respectively.

position $2b$ is protected by σ_v, as it maps the two inequivalent sites onto each other. If σ_v and σ_d are both present, the point groups are identical in real and reciprocal space as shown in Tab.2.4.2. Figure 2.4.2 illustrates the site-symmetry of the Wyckoff position $2b$: the three-fold coordination of the $1a$ and the $3c$ position and the intersection with one of the σ_d mirror planes results in the point group $\bar{6}m$. The absence of σ_v (red dashed line in Fig. 2.4.2) in real space renders the former two sites belonging to $2b$ inequivalent. In reciprocal space, this translates into the absence of σ_d, the point group of the valley momenta K lacks the in-plane reflection as shown in Figs. 2.4.2 (b) and 2.4.1 (b). The remaining symmetry operations are the C_3 rotation and, if present σ_h. As they both commute, the point group is abelian. Hence, breaking σ_v in real space has two important effects: it reduces the multiplicity of the Wyckoff position on $2b$ in real space and lowers the symmetry of the little group of the valley momenta in reciprocal space.

The multiplicity of the Wyckoff position $3c$ is insensitive to σ_v breaking as it is protected by the three-fold rotation around the $1a$ position of the trigonal and hexagonal layer groups. However, only in the presence of σ_v and σ_d, its in-plane position is fixed by the intersection point of the two reflections (see Fig. 2.4.2). In the presence of only one reflection, its in-plane position is defined to be located along the remaining reflection line and must be C_3 symmetric with respect to $1a$. The point groups of $3c$ and of the high-symmetry momentum M are identical with the subtle detail that σ_v and σ_d exchange as shown in Tab. 2.4.2. Further, as a time-reversal invariant momentum, the position in of the three M points remains symmetry protected by time reversal symmetry, even in the absence of spatial reflections.

From the site-symmetry analysis, two important facts about the in-plane inversion

Real Space				Reciprocal Space			
LG	$1a$	$2b$	$3c$	LG	Γ	K	M
p6/mmm	6/mmm	$\bar{6}m2$	mmm	p6/mmm	6/mmm	$\bar{6}m2$	mmm
p6mm	6mm	3m.	2mm	p6mm	6mm	3m.	2mm
p$\bar{6}m2$	$\bar{6}m2$	$\bar{6}m2$	$mm2$	p$\bar{6}2m$	$\bar{6}m2$	$\bar{6}$..	$m2m$
p3$m1$	3m.	3m.	.m.	p31m	3.m	3..	..m

Table 2.4.2.: Site-symmetry groups of the Wyckoff positions $1a$, $2b$ and $3c$ in real space and little co-groups of the high-symmetry momenta of the corresponding layer group. The real space Wyckoff positions are labeled following the convention given in Fig. 2.4.2. It should be noted that the multiplicity of b is reduced to 1, if the layer group lacks σ_v. The symmetry axes are given with respect to the crystallographic point group orientation.

symmetry breaking driven by the absence of σ_v can be derived:

1. In real space, σ_v can be broken by either placing identical atoms on position $3c$ followed by a translation along σ_d towards one of the $2b$ sites or by explicitly rendering the positions of the $2b$ site inequivalent by placing different atoms on the two sites (or only one atom at one site).

2. In momentum space, the little group of K becomes abelian which results in one-dimensional irreducible representations. Former symmetry protected band degeneracies will be lifted.

The first point gives a clear description for relevant material realizations. In this thesis, systems will be considered where the positions of the $2b$ sites host different atoms. However, this may be also achieved by weak distortions on atoms on $3c$. Further, we will see in Sec. 3.3, how σ_v-breaking will manifest itself in the real-space localization of the Bloch wave function. The second point has profound implications for the electronic band structure and the wave function symmetry as we will be discussed in the following section. In Chap. 5, the mutual connection of real space lattice and Bloch wave function symmetries will play the decisive role resulting in symmetry-breaking stabilized topological phases.

2.4.3. Inversion Symmetry Breaking Induced Chiral Wave Functions

This section concludes the chapter on the group theoretical analysis by elaborating on direct physical consequences for the Bloch wave function arising from inversion symmetry breaking. One of them is, that the Bloch wave function *can* become chiral.

As speculated in the introduction, an angular momentum promoting mechanism may act as the required non-local antagonist to the atomic SOC interaction on the triangular lattice, indispensable for stabilizing topological phases.

To have a well-defined angular momentum operator for the Bloch wave function, we recall from Sec.2.3, that the Bloch wave function at momentum $\mathbf{k}$ can be written as

$$|\psi(\mathbf{k})\rangle = \sum_{\mathbf{R}} e^{i\mathbf{k}\cdot\mathbf{R}} |\phi_{\mathbf{R}}\rangle \,. \tag{2.83}$$

ϕ shall be a local orbital, which can be described by a linear combination of Coulomb-Sturmians (see also Sec. A.2). This allows the definition of a local angular momentum operator and can be seen as a *spectral decomposition* of the Bloch wave function in terms of local wave functions with well-defined angular momentum. If the center of the Coulomb-Sturmians is chosen to be located at the $1a$ Wyckoff position, the "local OAM" is equivalent to the angular momentum of the Bloch wave function which defines its character under rotations in Eq. 2.79.

Being equipped with a proper angular momentum operator we can define its expectation value

$$\langle \hat{L}_z(\mathbf{k})\rangle = \langle \psi(\mathbf{k})|\hat{L}_z|\psi(\mathbf{k})\rangle \,. \tag{2.84}$$

Applying the time-reversal operator $\mathcal{T}$ to the Bloch wave function takes $\mathbf{k} \to -\mathbf{k}$ and the spherical harmonics transform as $Y^l_m \to Y^l_{-m}$.

$$\begin{aligned} \langle \hat{L}_z(-\mathbf{k})\rangle &= \langle \psi(-\mathbf{k})|\hat{L}_z|\psi(-\mathbf{k})\rangle = \langle \mathcal{T}\psi(\mathbf{k})|\hat{L}_z|\mathcal{T}\psi(\mathbf{k})\rangle \\ &= \langle \psi(\mathbf{k})|\mathcal{T}\hat{L}_z\mathcal{T}|\psi(\mathbf{k})\rangle = -\langle \hat{L}_z\rangle(\mathbf{k}). \end{aligned} \tag{2.85}$$

Spatial inversion $\mathcal{I}\mathbf{r} = -\mathbf{r}$ and $\mathcal{I}\mathbf{k} = -\mathbf{k}$ leaves the spherical harmonics invariant

$$\begin{aligned} \langle \hat{L}_z(-\mathbf{k})\rangle &= \langle \psi(-\mathbf{k})|\hat{L}_z|\psi(-\mathbf{k})\rangle = \langle \mathcal{I}\psi(\mathbf{k})|\hat{L}_z|\mathcal{I}\psi(\mathbf{k})\rangle \\ &= \langle \psi|\mathcal{I}\hat{L}_z\mathcal{I}|\psi\rangle = +\langle \hat{L}_z\rangle \,, \end{aligned} \tag{2.86}$$

the OAM polarization is a pseudo vector. It is clear, that the combination $\mathcal{T}\mathcal{I}$ implies

$$\langle \hat{L}_z(\mathbf{k})\rangle = \langle \mathcal{T}\mathcal{I}\psi(\mathbf{k})|\hat{L}_z|\mathcal{T}\mathcal{I}\psi(\mathbf{k})\rangle = \langle \hat{L}_z(-\mathbf{k})\rangle \,. \tag{2.87}$$

Hence we find the following energy-momentum relation for crystals with time reversal symmetry

$$E_{L_z}(\mathbf{k}) = E_{-L_z}(-\mathbf{k}), \tag{2.88}$$

with inversion symmetry

$$E_{L_z}(\mathbf{k}) = E_{L_z}(-\mathbf{k}), \tag{2.89}$$

and with inversion and time reversal symmetry

$$E_{L_z}(\mathbf{k}) = E_{-L_z}(\mathbf{k}). \tag{2.90}$$

In the presence of both symmetries, the spinless Bloch wave function of a non degenerate band must be non-chiral [37]. However $2n$-degenerate bands can come in chiral pairs with vanishing total chirality. If only time reversal symmetry is broken, the Bloch wave functions at $\mathbf{k}$ and $-\mathbf{k}$ have the same chirality according to Eq. 2.89. In the absence of inversion symmetry, the chirality of the Bloch wave function is odd under $\mathbf{k} \to -\mathbf{k}$. From a physical perspective, chiral wave functions from broken time-reversal symmetry can be expected. Instead, chiral wave functions from inversion symmetry breaking (ISB) are more surprising, as the broken $\mathcal{I}$ does not necessarily imply a chiral crystal structure. In fact, this is reconciled by a vanishing BZ-integrated OAM polarization arising from the anti-symmetric structure of Eq.2.88. Further, it should be noted, that time-reversal symmetry can be broken on the spin- and orbital-degrees of freedom of the Bloch wave function, while ISB, as a spatial symmetry breaking. It solely affects the orbital/spatial degrees of freedom of the wave function. Nevertheless, ISB can also affect the spin-splitting via a strong SOC-interaction as it is the case in the Rashba systems [1, 38, 39] and will be discussed in Sec. 6.1. Of course, it will also play a fundamental role in the stabilization of the topological phases in Chaps. 5 and 6.

3. Dirac Fermions in Trigonal and Hexagonal Space Groups

Based on the symmetry analysis of the valley momenta in Sec. 2.4, the presence of Dirac fermions in hexagonal and trigonal space groups will be discussed in the following. These Dirac fermions become massive in the presence of spin-orbit coupling (SOC) and inversion symmetry breaking (ISB) and their competition will determine the associated Berry charge [18]. Historically, Dirac fermions in hexagonal and trigonal space groups have been mainly investigated in Kane-Mele-type [24, 53] and in Kagome systems [48, 139], however they can also exist on the fundamental space group representative, the triangular lattice [2–4]. As the thesis focuses on the latter, the Dirac Hamiltonian in a triangular basis in the presence of SOC and ISB will be established based on group theoretical arguments as elaborated by Eck *et al.* in Ref. [2]. Further, the Dirac fermions in the three aforementioned bases have identical irreps at the valley momenta. This is related to the fact, that the representations of a given crystal momentum, i.e., the little groups, are solely determined by the space group. Therefore a Bloch wave function representation of a given space group may be expressed in multiple LCAO basis sets, located on different Wyckoff positions. If so, there must be a transformation between the basis sets. In the final part of this chapter, we will establish such a transformation between triangular and honeycomb basis sets. This unveils fundamental differences on the level of the locality of the SOC and ISB interaction: the mapping between both basis sets transforms local terms into non-local terms and vice-versa [2]. It should be noted, that the hereinafter drawn conclusions and the derived mapping consider only the valley momenta. This allows for a systematic analysis of the Dirac fermions and their impact on lattice systems. However, for a complete periodic model characterization, the whole BZ must be examined to determine the topological properties and the charge localization. This will be discussed in Chap. 5.

3.1. Symmetry-Protected Dirac States

In the high symmetric layer group p6/mmm, the little group of the K/K' points is given by D_{3h} [140]. As illustrated in Sec. 2.4.2.2, this group comprises one threefold vertical rotation axis, three twofold horizontal rotation axes, three vertical reflection planes, and the horizontal reflection plane. Since the vertical reflections and the C_3

Two-dimensional representations of D_{3h}

representation	I	$2C_3$	$3C_2'$	σ_h	$2S_3$	$3\sigma_v$	orbital basis
E'	2	-1	0	2	-1	0	(p_+, p_-), (d_{+2}, d_{-2}), (f_+, f_-)
E''	2	-1	0	-2	1	0	(d_+, d_-), (f_{+2}, f_{-2})

Chiral one-dimensional representations of C_{3h}

representation	I	C_3^1	C_3^2	σ_h	S_3^1	S_3^5	orbital basis
E'	1	ω	ω^*	1	ω	ω^*	p_+, d_{-2}, f_+
	1	ω^*	ω	1	ω^*	ω	p_-, d_{+2}, f_-
E''	1	ω	ω^*	-1	$-\omega$	$-\omega^*$	d_+, f_{-2}
	1	ω^*	ω	-1	$-\omega^*$	$-\omega$	d_-, f_{+2}

Table 3.1.1.: Character table of the two-dimensional representations of point group D_{3h} and the corresponding complex-conjugate paired one-dimensional representation of its subgroup C_{3h} [141]. With $\omega = e^{i\frac{2\pi}{3}}$. The last column shows the Bloch wave function symmetry expressed in atomic-like complex spherical harmonics, the index denotes the magnetic quantum number m. Reprinted table with permission from Eck, P. *et al.* "Real-space obstruction in quantum spin Hall insulators". *Physical Review B* **106,** 195143 (2022). © 2022 by the American Physical Society.

rotation do not commute, D_{3h} is non-abelian and multi-dimensional representations must exist. This results in the two two-dimensional representations E' and E'' which are even and odd under σ_h, respectively, as shown in their character Tab. 3.1.1. The last column denotes the resulting symmetry of the Bloch wave function expressed in pairs of atomic-like complex spherical harmonics, which fall into the two representations. Let us recall the character formula of the Bloch wave function given in Eq. 2.80 for a single-site basis: since the Bloch phase remains invariant under local transformations, the character of the Bloch wave is fully determined by the local representation. Hence, the pairs of chiral orbitals of Tab. 3.1.1 can be seen as the building blocks for symmetry-protected two-fold degenerate Dirac states on the triangular lattice.

In the following, we will discuss the impact of symmetry breaking on the Dirac fermions. The absence of the vertical reflections σ_v results in the little group C_{3h} [142] (see also Sec. 2.4.2.2). As its symmetry operations commute, the group is abelian and has only one-dimensional representations. The above-mentioned twofold representations split up into pairs of chiral representations (see C_{3h} in Tab. 3.1.1). This is a perfect example of chiral wave functions induced by ISB, as introduced in Sec. 2.4.3. The group theoretical analysis indicates the Bloch wave as being an orbital angular momen-

tum (OAM) eigenstate. Again, in the presence of time-reversal symmetry, the Bloch wave function at K and K' has opposite OAM, the BZ-integrated OAM polarization vanishes. Further, we can infer, that a σ_v-breaking interaction on the triangular lattice couples to the $\hat{L}_z$-component of the atomic OAM operator. Hence, the low-energy Hamiltonian is given by:

$$\hat{H}^{\not{\sigma}_v}(K/K') = \pm\lambda_{\not{\sigma}_v}\hat{L}_z. \tag{3.1}$$

The $\pm$ sign in Eq. 3.1 is a consequence of K and K' being time-reversal partners and $\lambda_{\not{\sigma}_v}$ denotes the strength of the σ_v-breaking. Here, we have introduced a strike-out notation for symmetry-breaking terms and their strength parameters. As it has been shown by Haldane [53], Kane and Mele [18, 24] for honeycomb Dirac fermions, a gap opened by inversion symmetry breaking at the valley momenta results in a total trivial Berry charge: the monopoles at K and K' have opposite winding numbers.

The other important symmetry in this thesis is σ_h. If broken, the point group of the valley momenta reduces to the non-abelian group C_{3v} (see also Sec. 2.4.2.2). Hence, the degeneracy of the Dirac fermions remains protected. However, as σ_h discriminates between the representations E' and E'' of D_{3h}, they become indistinguishable in the absence of σ_h and collapse into the representation E of C_{3v}. While this effect has no consequences for the p-orbitals, it is relevant for d- and f-shells on the triangular lattice. As shown in Tab. 2.4.2, each of the $m = \pm 1$ and $m = \pm 2$ chiral pairs gives rise to a Dirac cone. If the horizontal reflection symmetry is released, all d- and f-type Dirac cones have identical irreps, indicating that there will be a finite hybridization and orbital mixing between the $m = \pm 1$ and ± 2 subspaces. If σ_h and σ_v are broken, the C_3 symmetry of the valley momenta allows for the hybridization of orbitals with commensurate m quantum numbers $m_i \bmod(3) = m_j \bmod(3)$ which are the, i.e., the $m = -2(-1)$ and $m = 1(2)$ orbitals.

Having established the impact of symmetry breaking on the valley Bloch states, in the following we introduce SOC. In this case, the little group of K/K' is the double group D_{3h}^D of D_{3h}, which contains only two-dimensional spinor representations. Assuming local atomic SOC $\hat{\vec{L}} \cdot \hat{\vec{S}}$ acting on any pair of basis functions D_{3h} (Tab. 3.1.1), the SOC interaction becomes diagonal and the valley Hamiltonian is given by

$$\hat{H}^{\mathrm{SOC}} = \lambda_{\mathrm{SOC}}\hat{\vec{L}} \cdot \hat{\vec{S}} = \lambda_{\mathrm{SOC}}\hat{L}_z \otimes \hat{S}_z, \tag{3.2}$$

with $\hat{\vec{L}}$ and $\hat{\vec{S}}$ denoting the orbital and spin angular momentum operator, respectively. The coupling of spin and orbital angular momenta results in states with total angular momentum quantum number $j_z = m + m_s$ and the twofold degenerate valence and conduction eigenstates of Eq. 3.2 read for $\lambda_{\mathrm{SOC}} > 0$

$$E_v: \qquad |\Psi_v\rangle = \left| j_z = \mp|m| \pm \frac{1}{2} \right\rangle, \tag{3.3}$$

$$E_c: \qquad |\Psi_c\rangle = \left| j_z = \pm|m| \pm \frac{1}{2} \right\rangle. \tag{3.4}$$

As this term preserves time-reversal and inversion symmetry, the Dirac fermions are non-trivially gapped indicating a finite total (=summed over both valley momenta) spin-Berry charge [18, 24]. As the Hamiltonian is spin-diagonal, a Chern number can be assigned to each spin-block. Similarly, the time-reversal-symmetry-violating Haldane mass Hamiltonian can be formulated as

$$\hat{H}^{\mathrm{Chern}} = \lambda_{\mathrm{Chern}} \hat{L}_z. \tag{3.5}$$

In the presence of time-reversal symmetry, the combined Hamiltonian of $\not{\sigma}_v$-breaking and SOC acting on a pair of chiral orbitals is given by

$$\begin{aligned} \hat{H}^{\mathrm{triang}}(K/K') =& \hat{H}^{\mathrm{SOC}} + \hat{H}^{\mathrm{ISB}}(K/K') \\ =& \hat{L}_z \otimes \left(\lambda_{\mathrm{SOC}} \hat{S}_z \pm \lambda_{\mathrm{ISB}} \hat{S}_0 \right), \end{aligned} \tag{3.6}$$

where S_0 is the 2×2 identity matrix. The relative strength of $\lambda_{\not{\sigma}_v}$ and λ_{SOC} dictates the gap and, in turn also the total spin Berry charge of the valley momenta. This competition is reminiscent of the Kane-Mele model, however with an on-site non-trivial mass term and a k-dependent inversion symmetry-breaking term. This has important consequences for material realizations, as the strong local SOC will help to stabilize QSHI phases. This comparison will be further discussed in Sec. 3.4.

3.2. Equivalence of Honeycomb and Triangular Dirac Fermions

The initial claim, that a certain Bloch wave function may be expressed in more than one LCAO basis set, inevitably raises the question of the underlying mechanism and the necessary prerequisites. From a pure group theoretical point of view, this can be immediately answered by requiring that the character of the irreducible representation of the Bloch wave function can be realized by more than one local orbital basis set. As the character of the Bloch wave function is determined by the Bloch phase and the character of the local orbitals (see Eq. 2.80). The contributions to the total character can be transferred between the local orbital character and the Bloch phase by changing the local orbital basis and shifting the basis position.

To illustrate this for hexagonal systems, we will consider in the following the paradigmatic Dirac fermion system, namely the honeycomb lattice, and the triangular lattice in the wallpaper group $p6m$. The former is bipartite with orbitals located at the Wyckoff positions $2b = \{\mathrm{A} = (1/3, 2/3), \mathrm{B} = (2/3, 1/3)\}$, while the site of the triangular lattice is at $1a = (0, 0)$ [143]. Henceforth we use the Bravais and reciprocal lattice vector convention

$$\mathbf{a}_1 = a_0 \left(1, 0\right)^T, \quad \mathbf{a}_2 = a_0 \left(-1/2, \sqrt{3}/2\right)^T,$$

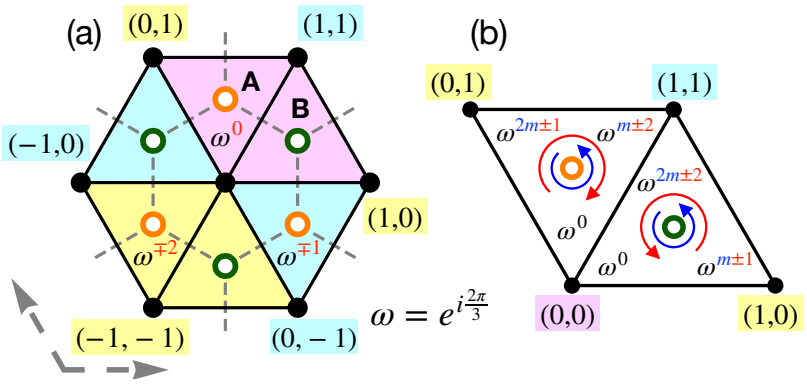

Figure 3.2.1.: (a) Wyckoff positions in the hexagonal unit cell giving rise to the triangular and honeycomb lattices. The former is made of the filled black circle at $1a$, while the latter by the orange "A" and green "B" open circles at $2b$. A different Bloch phase $\omega = \exp(i\mathbf{k}\cdot\mathbf{R})$ (purple, yellow and cyan colors) calculated at $\mathbf{k}$=K or K' is assigned to each unit cell (diamond shapes). The filled black circle in the center corresponds to $\mathbf{R} = (0,0)$ and represents the atom assigned to the purple unit cell). (b) Interference between orbital and Bloch phases. The blue arrow shows how the phase of the chiral orbitals sitting at the $\mathbf{R}$ positions of the triangular lattice winds going around the A/B points. In red we denote instead the contribution from the Bloch phases along the same path. For this specific example, we have picked an orbital with m mod $3 = 1$ at K. Reprinted figure taken and adopted with permission from Eck, P. *et al.* "Real-space obstruction in quantum spin Hall insulators". *Physical Review B* **106,** 195143 (2022). © 2022 by the American Physical Society.

$$\mathbf{b}_1 = \frac{2\pi}{a_0}\left(1, \sqrt{3}\right)^T, \quad \mathbf{b}_2 = \frac{2\pi}{a_0}\left(0, 2/\sqrt{3}\right)^T.$$

If not explicitly specified, we assume the lattice constant a_0 to be the unit of length.

Here, we will be focusing on the following comparison: the $2b$ basis site of the honeycomb with A and B sublattices [orange and green open circles in Fig. 3.2.1 (a)] on the one hand and, on the other hand, the triangular lattice with its single site (filled black circle) in the unit cell. The former has in analogy to the Kane-Mele model one orbital with magnetic quantum number $m_{hc} = 0$ per site [18], while the latter is equipped with two chiral orbitals with $m_t = \pm m$, which have been introduced in the previous section. The different dimension of the local orbital subspaces ensures the same number of degrees of freedom between the two basis sets.

To understand the equivalence of the aforementioned basis sets at the valley momenta, let us consider the Bloch wave functions in real space

$$\psi(\mathbf{k})(\mathbf{r}) = \langle \mathbf{r}|\psi(\mathbf{k})\rangle = \sum_{\mathbf{R}} e^{i\mathbf{k}\cdot\mathbf{R}}\langle \mathbf{r}|m_{\mathbf{R}}\rangle. \tag{3.7}$$

Here $|m_{\mathbf{R}}\rangle$ is an orbital with magnetic quantum number m located in the unit cell corresponding to Bravais point $\mathbf{R}$. The equivalence of different basis set choices is proven for Eq. 3.7 at the valley momenta, if the corresponding Bloch wave functions have identical characters under the symmetry classes of the little group (D_3). Focusing on the C_3 rotation, we recall the character formula of the Bloch wave function given in Eq. 2.80 and formulate it for a Bloch wave function of an orbital m at Wyckoff position $\mathbf{x}$ [2]:

$$\chi(C_3, m, \mathbf{x}, \mathbf{k}) = \Delta(C_3, \mathbf{x}, \mathbf{k})\chi_m(C_3). \tag{3.8}$$

$\Delta(C_3, \mathbf{x}, \mathbf{k})$ and $\chi_m(C_3)$ denote, respectively, the characters of the Bloch phase and of the orbital $|m\rangle$ under a C_3 rotation. As the triangular Wyckoff position $1a$ is located at the origin (black filled dot in Fig. 3.2.1), its Bloch phase remains invariant. Therefore, the character χ of the full Bloch wave function is given only by the orbital part $\chi_m(C_3) = e^{i\frac{2\pi}{3}m} = \omega^m$. For the honeycomb positions A/B (orange/green open circles), instead, a C_3 rotation around $1a$ translates A and B into the corresponding ones in neighboring unit cells, as illustrated in Fig. 3.2.1 (a). This results for the valley momenta $K = -K = (1/3, 1/3)$ in a Bloch phase difference of [2]

$$\Delta(C_3, \mathbf{x} = \mathrm{A}, \mathbf{k} = \{K/K'\}) = \omega^{\mp 2} = \omega^{\pm 1}, \tag{3.9}$$
$$\Delta(C_3, \mathbf{x} = \mathrm{B}, \mathbf{k} = \{K/K'\}) = \omega^{\mp 1}, \tag{3.10}$$

where ± 1 is determined by fixing the Wyckoff position and the valley momentum, from the clock- or anticlockwise Bloch phase rotation under a C_3 operation – see sequence of colors in Fig. 3.2.1 (a). By taking into account this additional "Bloch angular momentum" $\tilde{m}_{\mathbf{x},\mathbf{k}} = \pm 1$, we obtain the condition under which both Bloch wave functions have the same C_3 character [2]:

$$0 = (m_t - m_{hc} - \tilde{m}_{\mathbf{x},\mathbf{k}}) \mod 3. \tag{3.11}$$

This implies that any Bloch wave function of a chiral orbital $m_t \bmod 3 \neq 0$ on the triangular lattice transforms identically as one of $m_{hc} \bmod 3 = 0$ orbitals located at the A/B honeycomb sites. Further, the comparison illustrates nicely the transferability of contributions to the total character from the Bloch phase/real space position and the local orbital representation. From a more general perspective, it highlights also the chirality of Dirac states on hexagonal and trigonal lattices, which promote the helical edge states in finite size geometries of non-trivial bulk systems. While this comes naturally from the local chiral orbitals on the triangular lattice, it arises from the Bloch phase for the non-chiral orbitals in a honeycomb geometry as will be discussed and illustrated in the next section.

3.3. Emergent Honeycomb Connectivity on the Triangular Lattice

Having established the equivalence of the triangular and the honeycomb lattice on the level of the Bloch wave function symmetry, it is instructive to inspect the real space localization of the Dirac fermion Bloch wave functions. It is well established for the honeycomb lattice, that the sublattice degree of freedom is a good quantum number at the valley momenta. The wave function localizes on the sublattice sites and the charge localization pattern is indicative for the topological phase [18, 24, 53, 57]. This poses the question, if the Dirac fermions on the triangular lattice profit also from a honeycomb charge connectivity that would localize on the void position between the atoms. If so, it could be similarly used for addressing the topological phase [3] and could promote real space obstruction [2, 4]. Indeed, this concept will be of fundamental importance in Secs. 5.9, 5.10 and 6.2.2.

We investigate the charge localization at K/K' by inspecting the real space Bloch wave function at the A/B void arising from a chiral orbital m on a triangular lattice ($1a$ position). As illustrated in Fig. 3.2.1 (b), the Bloch wave at the A/B position depends on the interference of the chiral orbitals of the neighboring $1a$ sites, which contribute with their lattice and orbital phases. By exploiting the C_3 symmetry of the A/B site-symmetry group, all shells of neighbors must come in multiples of triplets and the Bloch wave function can be written as [2]:

$$\langle \mathbf{r} = \{\mathrm{A},\mathrm{B}\}|\psi(\mathbf{k})\rangle \propto \sum_{\mathbf{R}} e^{i\mathbf{k}\cdot\mathbf{R}}\langle \mathbf{r}|m_{\mathbf{R}}\rangle \tag{3.12}$$

$$= \sum_{t}\sum_{n=0}^{2}\langle \mathbf{r}|C_3^n\left(e^{i\mathbf{k}\cdot\mathbf{R}_t}|m_{\mathbf{R}_t}\rangle\right). \tag{3.13}$$

Here we have introduced the triplet index t in Eq. 3.13. All basis positions of a triplet are generated by applying C_3 rotations to one of the lattice vectors $\mathbf{R}_t$ of the triplet. As shown in Fig. 3.2.1 (b), depending on the valley momentum and the A/B position, the C_3^n rotation promotes a Bloch phase difference of $\omega^n = e^{\pm i\frac{2\pi}{3}n}$. Therefore, the valley Bloch wave function at the A/B evaluates to [2]:

$$\langle \mathbf{r} = \{\mathrm{A},\mathrm{B}\}|\psi(\mathbf{k} = \{K/K'\})\rangle = \sum_{t} e^{i\mathbf{k}\cdot\mathbf{R_t}}\langle \mathbf{r}|m_{\mathbf{R_t}}\rangle \sum_{n=0}^{2}\left[\omega^{\tilde{m}_{\mathbf{r},\mathbf{k}}}\cdot\omega^m\right]^n \tag{3.14}$$

$$= 3\delta_{(\tilde{m}_{\mathbf{r},\mathbf{k}}+m)\mathrm{mod}3,0}\sum_{t} e^{i\mathbf{k}\cdot\mathbf{R_t}}\langle \mathbf{r}|m_{\mathbf{R_t}}\rangle \tag{3.15}$$

$$\propto \delta_{(\tilde{m}_{\mathbf{r},\mathbf{k}}+m)\mathrm{mod}3,0}, \tag{3.16}$$

where $\tilde{m}_{\mathbf{r},\mathbf{k}}$ reflects the Bloch angular momentum, i.e., the winding of the Bloch phase around the considered A/B position at a given valley momentum. Assuming, that the local orbitals are sufficiently localized, the main contribution to the Bloch wave

will arise from the nearest neighbor shell and the sum over all shells in Eq. 3.15 is non-vanishing. Hence we can identify a constructive or destructive interference mechanism, which depends solely on the A/B position, the valley momentum and angular momentum of the local chiral orbital. In particular, the total angular momentum of the Bloch wave with respect to the A/B position $M = \tilde{m}_{\mathbf{r},\mathbf{k}} + m$ is the decisive property. Only if total invariance under C_3 symmetry with respect to the A/B position is achieved ($M \bmod 3 = 0$), the Bloch wave function and hence the charge is non-vanishing [2]:

$$|\psi(\mathbf{r} = \{\mathrm{A},\mathrm{B}\}, \mathbf{k} = \{K/K'\})|^2 \begin{cases} > 0, & \text{if } M \bmod 3 = 0 \\ = 0, & \text{if } M \bmod 3 \neq 0 \end{cases}. \tag{3.17}$$

Extending this simple argument to pairs of chiral orbitals (as introduced in Sec. 3.1) on the triangular site $1a$, the presence of both chiralities $\pm m$ will result in a honeycomb connectivity at the $2b$ position at K and K'. To give an example, the $p_+(p_-)$-orbital localizes at A(B) and B(A) for the valley momenta K and K', respectively.

To illustrate the localization, we compare the Bloch wave functions from $p_\pm$ orbitals on the $1a$ triangular site with a s-orbital on the A position. We choose the following non-normalized real-space parametrization for the local orbitals

$$s_{\mathbf{R}}(\mathbf{r}) = e^{-\frac{1}{a}|\mathbf{r}-\mathbf{R}|}, \tag{3.18}$$

$$p_{\pm,\mathbf{R}}(\mathbf{r}) = |\mathbf{r}-\mathbf{R}| e^{-\frac{1}{a}|\mathbf{r}-\mathbf{R}|} e^{\pm i\varphi(\mathbf{R},\mathbf{r})}, \tag{3.19}$$

with the Bohr radius a being 1/4 of a lattice constant and construct the Bloch wave function according to Eq. 2.34. Figure 3.3.1 shows $\arg[\psi(\mathbf{k})]$ with the complex phase plotted by rainbow colors and the color brightness scales with the absolute wave function value. For the crystal momentum Γ, i. e., constant Bloch phase in real-space, the maximum of the s-type Bloch wave function centers at the honeycomb position A. Instead, the $p_\pm$-Bloch wave function centers around the triangular site $1a$ with nodes at $1a$ and along the Wigner-Seitz cell boundary (hexagonal nodal line). At the valley momentum K, the s-type wave function has nodes at the unoccupied honeycomb position B and at $1a$. Importantly, the p_+-orbital realizes a qualitatively similar Bloch wave with a maximum at A and nodes at $1a$ and at B. However, it should be noted, that the s- and the p_+-type wave functions are not identical on the quantitative level. The p_- wave function has its maximum at B and a node at $1a$ and A. At K', the p_- Bloch wave is qualitatively equivalent to the s-type wave function and the p_+ wave function localizes at the B position.

The comparison illustrates nicely that,

- the equivalence of honeycomb and triangular basis sets is a momentum-dependent concept,
- the equivalence is achieved on the level of the wave function symmetries, the long-range behavior of the radial part is unimportant.

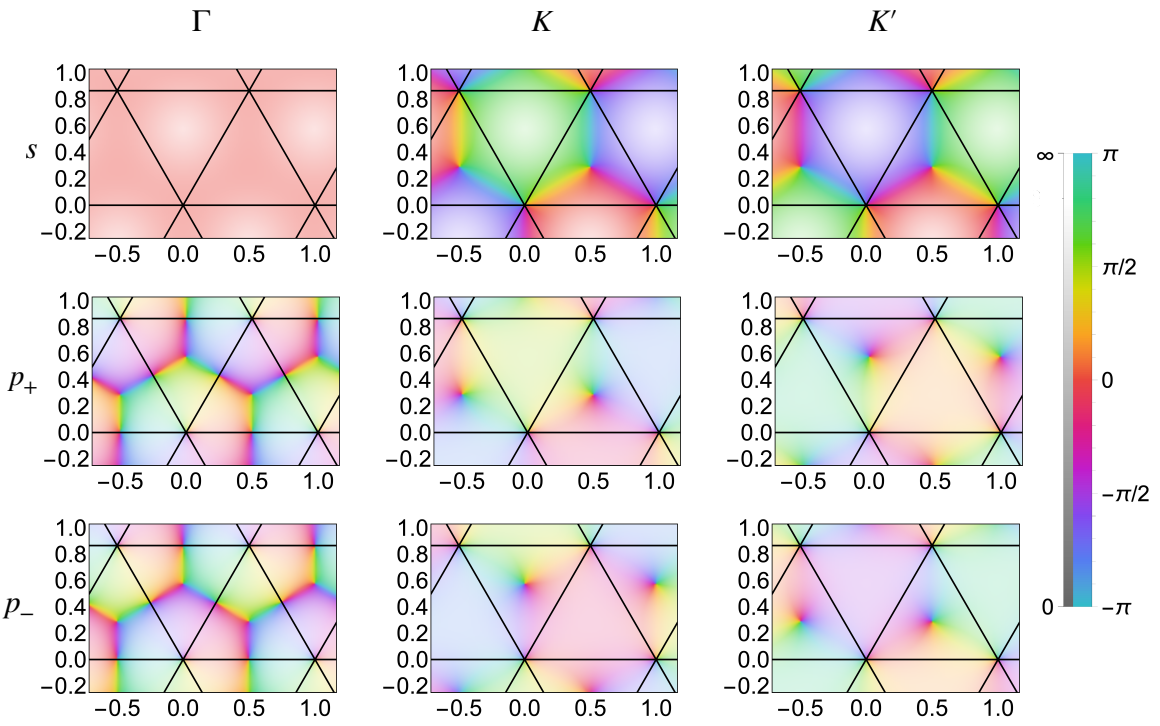

Figure 3.3.1.: Comparison of Bloch wave functions arising from an s-orbital on the A and $p_{\pm}$-orbitals on the $1a$ site (for the location of the Wyckoff positions see Fig. 3.2.1). The panels show $\arg[\psi(\mathbf{k})]$ with the complex phase visualized by a rainbow color palette, the color brightness denotes the amplitude. The x, y coordinates are given in units of the lattice constant.

The last point emphasizes further, that Bloch wave functions with identical symmetry characters may differ on the quantitative level in real-space (apart from the symmetry enforced nodes and local phase). For instance in an atomic-like picture where the local orbitals are strongly localized, i.e., when the lattice constant is very large/the Bohr radius is very short, the chiral orbitals on the triangular site will have a very small amplitude at the A/B honeycomb positions. Hence, the maximum of the wave function may still be located close to the triangular sites, even at the valley momenta. Nevertheless, as the symmetry is unaffected, the interference mechanism is at play and will promote a node or constructive interference at A/B at the valley momenta.

By recalling the symmetries of the eigenstates of the Dirac Hamiltonian in a triangular chiral basis, as introduced in Sec. 3.1, we find that

- in the non-trivial, SOC-dominated case, both m-quantum numbers are present in the valence (conduction) states. Therefore the valence (conduction) states will localize on the A and the B sublattice position, resulting in a honeycomb valence (conduction) charge distribution,

- in the trivial, σ_v-breaking dominated phase, the states of the valence (conduction) doublet have identical m-quantum numbers and will localize on the same sublattice position, either A or B. The valence charge displays a triangular motif centered at only one of the A/B position, while the conduction charge localizes around the other sublattice position.

- both, the inversion symmetry-breaking term and the Bloch phase, are odd under $K \mapsto K'$. Hence, the charge localization is independent of the valley. Therefore, the charge motif is also present in **k**-integrated properties, such as the charge density of Dirac fermions on the triangular lattice.

As a result, the charge localization of the triangular Dirac states is in analogy to the Kane-Mele model [18, 24] and can be used as an unique identifier to determine the topology of the gap at the valley momenta. Irrespective of the mass terms, Dirac fermions arising from orbitals on the triangular lattice profit from an interference mechanism in the voids of the lattice, namely at the honeycomb sublattice Wyckoff position. This will be of major importance for the topological real-space obstruction in triangular lattices discussed in Chaps 5 and 6. The mass terms dictate only the localization pattern. In line with the group theoretical analysis in Sec. 2.4.2.2, only in the presence of σ_v, the valence state is Kramers-degenerate and localizes symmetrically on A and B.

3.4. Transformation between Triangular and Honeycomb Dirac Fermions

After having established the equivalence of triangular and honeycomb Dirac fermions on the level of the wave function symmetry and the real-space localization, a unitary transformation between the two basis sets will be introduced in the following. As it has been already touched upon in the previous section, the exact transformation of the real-space representation of the local orbitals between the two basis sets is not straightforward. A formal basis function transformation is derived in appendix A.3 based on Coulomb-Sturmians, which form a spherical-harmonics-type complete basis set in $\mathbb{R}^3$ (see appendix A.2). For the sake of simplicity and in the light of a general formulation, we will derive the mapping based on the wave function symmetries. We consider chiral pairs of $\{+m_t, -m_t\} \bmod 3 = \{+1, -1\} \equiv \{-2, +2\}$ orbitals on the triangular site. On the honeycomb sites, we assume a $\{m_\mathrm{A}, m_\mathrm{B}\} = \{0, 0\}$ basis. By requiring identical Bloch wave function symmetries under the C_3 symmetry at the valley momenta K and K' (see also Secs. 3.2 and 3.3), the transformation $\{+m_t, -m_t\} \mapsto \{m_\mathrm{A}, m_\mathrm{B}\}$ reads

$$\hat{U}(K) = \begin{pmatrix} 1 & 0 \\ 0 & 1 \end{pmatrix} \otimes \hat{S}_0, \quad \hat{U}(K') = \begin{pmatrix} 0 & 1 \\ 1 & 0 \end{pmatrix} \otimes \hat{S}_0. \tag{3.20}$$

Here we assume, that the basis ordering at K remains invariant. As the localization of the chiral orbitals switches between the A/B site under $K \mapsto K'$, the transformation at K' must exchange the orbital order. The transformation maps the valley Hamiltonian from the triangular basis given in Eq. 3.6 to the Kane-Mele-type honeycomb basis:

$$\hat{H}^{\mathrm{KM}}(K/K') = \hat{U}(K/K')\hat{H}^{\mathrm{triang}}(K/K')\hat{U}(K/K')^{\dagger} \tag{3.21}$$

$$= \hat{U}(K/K')\left(\hat{H}^{\mathrm{SOC}} + \hat{H}^{\mathrm{ISB}}(K/K')\right)\hat{U}(K/K')^{\dagger} \tag{3.22}$$

$$= \hat{U}(K/K')\left(\hat{L}_z \otimes \left(\lambda_{\mathrm{SOC}}\hat{S}_z \pm \lambda_{\mathrm{ISB}}\hat{S}_0\right)\right)\hat{U}(K/K')^{\dagger} \tag{3.23}$$

$$= \pm\lambda_{\mathrm{SOC}}\tau_z \otimes \hat{S}_z + \lambda_{\mathrm{ISB}}\tau_z \otimes \hat{S}_0, \tag{3.24}$$

where τ_z denotes the third Pauli matrix representing the sublattice degree of freedom in the honeycomb basis. As the $\hat{L}_z$-operator is also represented by the third Pauli matrix in the triangular basis, the transformation at K' introduces a global "$-$", which switches the locality of the SOC and symmetry-breaking term: the local SOC interaction on the triangular lattice is transformed into the $\mathbf{k}$-dependent Kane-Mele analogue. Instead, the non-local $\not{\sigma}_v$-term transforms into a staggered potential in the honeycomb basis. To put this into context of real materials, symmetry-identical Dirac wave functions can be realized with crystals, which have either a honeycomb or a triangular atomic basis. However the Kane-Mele SOC interaction in honeycomb systems originates from an intrinsically weak second neighbor process [18, 24], while the triangular basis profits from a sizable local atomic SOC [2, 3].

Before turning to an expansion of the sublattice polarization in the vicinity of the valley momenta, let us briefly comment on the mapping of the local real-space representations. In the presence of horizontal reflection symmetry, the character under σ_h introduces a further discrimination criterion. To give specific examples, a triangular $\{p_+, p_-\}$ basis is mapped onto an $\{m_{\mathrm{A}}, m_{\mathrm{B}}\}$ basis, where the local orbitals on the honeycomb sites will be a linear combination of $s, d_z^2, ...$ wave functions (for details see appendix A.3). On the other hand, a pair of $\{d_+, d_-\}$ orbitals on $1a$ will be expanded in $p_0, f_{-3}, f_0, f_3, ...$-orbitals on the honeycomb lattice.

3.5. Sublattice Polarization around the Valley Momenta

We will conclude this chapter by extending the analysis of the triangular and honeycomb Dirac fermions to the vicinity of the valley momenta. As discussed in the previous sections and illustrated in Fig. 3.3.1, the wave functions arising from basis sets located on the two aforementioned lattices have only identical symmetries at the valley momenta, while their Bloch wave functions at Γ are qualitatively different. Hence there must be a fundamental change in the wave function symmetry along the path spanned

by Γ-K. To investigate the evolution of the Bloch states and its localization at the A/B sites, we consider a spinless Dirac Hamiltonian

$$H(\mathbf{k}) = t|\mathbf{k}|\sigma_x + m\sigma_z = \begin{pmatrix} m & tk \\ tk & -m \end{pmatrix}. \tag{3.25}$$

Without loss of generality, the term $t|\mathbf{k}|\sigma_x$ represents the in-plane-momentum-dependent hybridization with strength t [1], while $m\sigma_z$ denotes the mass term and σ_i are the Pauli matrices. In the following, we will write $|\mathbf{k}| = k$.

The Hamiltonian in Eq 3.25 has the eigenenergies $E_\pm = \pm E = \pm\sqrt{m^2 + (tk)^2}$ with eigenvectors

$$|v_-\rangle = \frac{1}{\sqrt{1 + \left(\frac{tk}{m+E}\right)^2}} \begin{pmatrix} -\frac{tk}{m+E} \\ 1 \end{pmatrix}, \quad |v_+\rangle = \frac{1}{\sqrt{1 + \left(\frac{tk}{m+E}\right)^2}} \begin{pmatrix} 1 \\ \frac{tk}{m+E} \end{pmatrix}. \tag{3.26}$$

Focusing first on the honeycomb basis $\{\mathrm{A}, \mathrm{B}\}$ and defining the sublattice projectors $\mathcal{P}_{\mathrm{A/B}} = |\mathrm{A/B}\rangle\langle\mathrm{A/B}|$, the sublattice character is given by

$$\langle v_+|\mathcal{P}_\mathrm{A}|v_+\rangle = \langle v_-|\mathcal{P}_\mathrm{B}|v_-\rangle = \frac{(m+E)^2}{(m+E)^2 + (tk)^2} = \frac{2 + \tilde{k}^2 + 2\sqrt{1+\tilde{k}^2}}{2 + 2\tilde{k}^2 + 2\sqrt{1+\tilde{k}^2}}, \tag{3.27}$$

$$\langle v_+|\mathcal{P}_\mathrm{B}|v_+\rangle = \langle v_-|\mathcal{P}_\mathrm{A}|v_-\rangle = \frac{(tk)^2}{(m+E)^2 + (tk)^2} = \frac{\tilde{k}^2}{2 + 2\tilde{k}^2 + 2\sqrt{1+\tilde{k}^2}}, \tag{3.28}$$

$$\langle v_+|\mathcal{P}_\mathrm{A}|v_+\rangle\Big|_{k=0} = \langle v_-|\mathcal{P}_\mathrm{B}|v_-\rangle\Big|_{k=0} = 1 - \frac{(\Delta\tilde{k})^2}{4} + \frac{3(\Delta\tilde{k})^4}{16} + \mathcal{O}\left((\Delta\tilde{k})^6\right), \tag{3.29}$$

$$\langle v_+|\mathcal{P}_\mathrm{B}|v_+\rangle\Big|_{k=0} = \langle v_-|\mathcal{P}_\mathrm{A}|v_-\rangle\Big|_{k=0} = \frac{(\Delta\tilde{k})^2}{4} - \frac{3(\Delta\tilde{k})^4}{16} + \mathcal{O}\left((\Delta\tilde{k})^6\right). \tag{3.30}$$

where $\tilde{k} = \frac{tk}{m}$. Hence, the sublattice character scales quadratically near the valley momenta with the generalized momentum $\tilde{k}$. Turning now to the basis of a pair of chiral orbitals on the triangular lattice $\{+m, -m\}$ we can interpret the previous result as the orbital polarization in the vicinity of the valley momenta. In analogy to Eq. 3.12, we can project the chiral orbitals located on the triangular site onto orbitals on the honeycomb sites A/B with magnetic quantum number $m = 0$

$$\mathcal{P}_{\{\mathrm{A,B}\}}|\psi(\mathbf{k})\rangle = \sum_{s\in\{\mathrm{A,B}\}} |s\rangle\langle s| \sum_R e^{i\mathbf{k}\cdot\mathbf{R}}|m(\mathbf{r})\rangle \tag{3.31}$$

$$\approx \frac{1}{3}\sum_{s\in\{\mathrm{A,B}\}} |s\rangle \sum_{n=0}^{2} e^{i\left(\mathbf{k}\cdot\mathbf{R}_{s,n} + \frac{2\pi}{3}mn\right)}. \tag{3.32}$$

[1] A general Dirac Hamiltonian in 2D momentum space (k_1, k_2) can be rotated at each momentum, such that the full momentum-dependence is absorbed into one single Pauli matrix $|\mathbf{k}|\sigma_i$.

By going from Eq. 3.31 to 3.32, we consider only contributions from the three neighboring sites of the honeycomb positions and require completeness for the projector at $\mathbf{k} = K$. Hence we can calculate the sublattice character $\langle \hat{s}(\mathbf{k}, m) \rangle$ of a pure $|m\rangle$-type Bloch wave function

$$\langle \hat{s}(\mathbf{k}, m) \rangle = \frac{1}{9} \sum_{n=0}^{2} \sum_{n'=0}^{2} e^{-i\left(\mathbf{k}\cdot\mathbf{R}_{s,n} + \frac{2\pi}{3}mn\right)} e^{i\left(\mathbf{k}\cdot\mathbf{R}_{s,n'} + \frac{2\pi}{3}mn'\right)}. \tag{3.33}$$

To expand around the valley momentum, we insert $\mathbf{k} = K + \Delta\mathbf{k}$ and recall that $K \cdot \mathbf{R}_{i,n} = \pm\frac{2\pi}{3}n$ where the sign depends on the sublattice site A/B. In the case of constructive interference, the sublattice character is given by

$$\langle \hat{s}(\mathbf{k}, m) \rangle = \frac{1}{9} \sum_{n=0}^{2} \sum_{n'=0}^{2} e^{i\Delta\mathbf{k}\cdot\mathbf{R}_{i,n}(n'-n)}. \tag{3.34}$$

Simplifying further by assuming $\Delta\mathbf{k} \cdot \mathbf{R}_{i,n} = \pm\varphi n$, i.e., evaluating the term for only the i^{th} in-plane momentum

$$\langle \hat{s}(\varphi_i) \rangle = \frac{1}{9} \sum_{n=0}^{2} \sum_{n'=0}^{2} e^{\pm i\varphi_i(n'-n)} \tag{3.35}$$

$$= \frac{1}{9} \left(3 + 4\cos(\varphi_i) + 2\cos(2\varphi_i)\right). \tag{3.36}$$

$$\langle \hat{s}(\varphi_i) \rangle \Big|_{\varphi_i=0} = 1 - \frac{2}{3}(\Delta\varphi_i)^2 + \mathcal{O}\left((\Delta\varphi_i)^4\right). \tag{3.37}$$

where the last equation denotes the expansion around $\varphi_i = 0$, while the series for destructive interference reads at $\varphi_i = \pm\frac{4\pi}{3}$

$$\langle \hat{s}(\varphi_i) \rangle \Big|_{\varphi_i=\pm\frac{4\pi}{3}} = \frac{2}{3}(\Delta\varphi_i)^2 + \mathcal{O}\left((\Delta\varphi_i)^4\right). \tag{3.38}$$

Compared to honeycomb Dirac fermions, we find that the sublattice polarization of the triangular basis is further reduced by the phase decoherence which scales likewise quadratic in the vicinity of the valley momenta. However for realistic lattice models, non-linear effects in the band dispersion, e. g., the hybridization with other orbital subspaces can profoundly change the sublattice localization, as it will be discussed in Sec. 5.10.

3.6. Summary

A pair of chiral orbitals gives rise to Dirac fermions at the valley momenta of hexagonal and trigonal space groups. The wave functions of the Dirac fermions are symmetry-identical to their honeycomb equivalents. This results in qualitatively identical physics,

however triangular basis sets profit from a sizable local SOC. Similar to the honeycomb systems, triangular Dirac fermions possess a honeycomb localization in the voids of the triangular lattice. Further the charge localization motif is driven by the competition of spin-orbit coupling and inversion symmetry breaking, i.e., it is indicative of the associated Berry charge. As a concluding remark, it should be noted that the symmetry equivalence of honeycomb and triangular Dirac fermions is only given at the valley momenta. In the next chapter, we will develop a triangular lattice model. This will allow to extend our analysis to the whole BZ.

4. The p-Shell on the Triangular Lattice

After having investigated the symmetries of Dirac fermions in hexagonal and trigonal crystal layer groups, we will develop a lattice model for Dirac fermions in the most fundamental hexagonal system, the triangular lattice. As the minimum requirement is at least one pair of chiral orbitals, we will consider a p-shell in the presence of atomic SOC as well as σ_v- and σ_h- breaking terms. The focus will be on the symmetry of the eigenstates and the momentum-dependence of the symmetry-breaking terms. The lattice formulation of the vertical-reflection symmetry-breaking term will be derived from a group theoretical and a microscopic approach to gain a broad understanding of the underlying physics of this inversion symmetry violating term. It should be noted, that the presented methods can be applied to describe general spatial symmetry-breaking phenomena in solids, hence the discussion of the σ_h-breaking term will be kept compact.

4.1. p6/mmm Lattice Hamiltonian

Let us start with the lattice Hamiltonian $\hat{H}^T$ in the maximally symmetric layer group p6/mmm. We will derive the model for a $\{p_x, p_y, p_z\}$ basis on a triangular lattice spanned by the Bravais vectors $\mathbf{a}_1 = (1, 0)$ and $\mathbf{a}_2 = (-1/2, \sqrt{3}/2)$, the reciprocal lattice vectors read $\mathbf{b}_1 = 2\pi(1, 1/\sqrt{3})$ and $\mathbf{b}_2 = (0, 4\pi/\sqrt{3})$. Their overlap integrals can be obtained by following the two-center approximation of Slater and Koster as given in App. A.2. The Slater-Koster ansatz respects by construction the site symmetry (D_{6h}) of the triangular $1a$ Wyckoff position:

$$\langle p_i(0)|\hat{H}^T|p_i(\mathbf{R})\rangle = n_i^2 V^\sigma + (1 - n_i^2)V_i^\pi, \tag{4.1}$$

$$\langle p_i(0)|\hat{H}^T|p_j(\mathbf{R})\rangle = -n_i n_j (V_{ij}^\pi - V_{ij}^\sigma). \tag{4.2}$$

With $i = x, y, z$ and $i \neq j$, the coefficients n_i incorporate the in-plane orientation ($n_x = \cos(\varphi)\sin(\theta), n_y = \sin(\varphi)\sin(\theta)$ and $n_z = \cos(\theta)$) with the azimuthal angle φ and polar angle θ. The general hopping Hamiltonian reads in momentum space:

$$\hat{H}(\mathbf{k}) = \sum_{ij} c_i^\dagger(\mathbf{k}) H_{ij}(\mathbf{k}) c_j(\mathbf{k}), \tag{4.3}$$

with the elements $H_{ij} = H^*_{ji}$:

$$H^T_{xx}(\mathbf{k}) = 2V^\sigma \cos(k_1) + \frac{V^\sigma + 3V^\pi}{2} \left(\cos(k_2) + \cos(k_1 + k_2)\right), \tag{4.4}$$

$$H^T_{yy}(\mathbf{k}) = 2V^\pi \cos(k_1) + \frac{3V^\sigma + V^\pi}{2} \left(\cos(k_2) + \cos(k_1 + k_2)\right), \tag{4.5}$$

$$H^T_{zz}(\mathbf{k}) = E_z + 2V^\pi_{p_z} \left(\cos(k_1) + \cos(k_2) + \cos(k_1 + k_2)\right), \tag{4.6}$$

$$H^T_{xy}(\mathbf{k}) = -\frac{\sqrt{3}}{2}(V^\pi - V^\sigma) \left(-\cos(k_2) + \cos(k_1 + k_2)\right), \tag{4.7}$$

$$\tag{4.8}$$

The integrals V^σ, V^π and $V^\pi_{p_z}$ are hopping strengths within the in-plane subspace and the p_z subspace, respectively. The local on-site shift of the p_z-orbital with respect to the in-plane subspace is given by E_z.

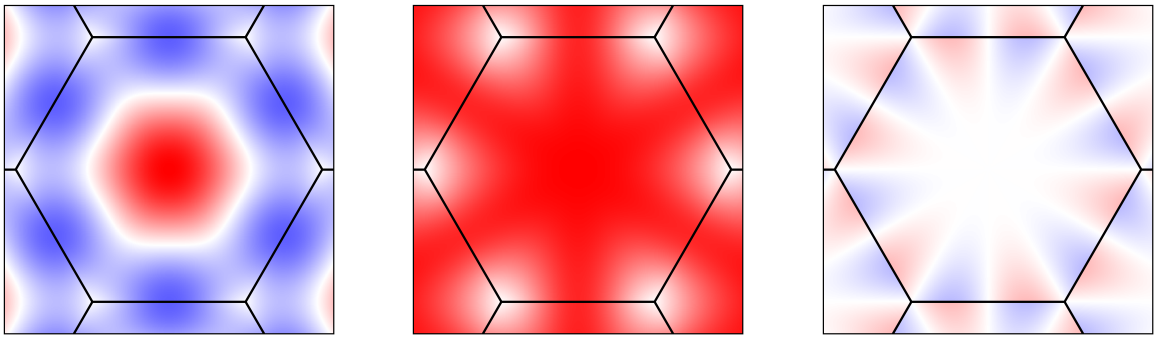

(a) (b) (c)

Figure 4.1.1.: Map plot of the matrix elements of the in-plane subspace in the $\{p_r, p_t\}$-basis in the $k_x k_y$ plane, where red(blue) denotes positive(negative) values for $1 = V^\sigma = -4V^\pi$. The plots show from (a-c) the elements $H_{p_r p_r}, H_{p_t p_t}, H_{p_r p_t}$ and the black lines show the BZ boundaries. The diagonal elements are given with respect to the Dirac point energy at the valley momenta. The corresponding band structure and orbital symmetry is illustrated in Fig. 4.1.2.

As discussed in Secs. 2.4.2.1 and 2.4.2.2, the six vertical reflection planes (σ_v, σ_d) of the layer group at p6/mmm intersect at Γ. The paths Γ-M, Γ-K and M-K are located in the vertical reflection planes. As discussed in Sec. 2.4, the Hamiltonian and the wave functions must be also (anti)-symmetric under the reflection symmetries along the high-symmetry lines. In particular, the in-plane subspace will split into two one-dimensional representations, where one representation is even (p-orbital alignment parallel to the mirror plane) and the other one is odd (alignment normal to the mirror plane) under the mirror reflection. Therefore, the intersecting mirror planes at Γ promote a radial (even) and tangential (odd) in-plane band, where the alignment is with respect to the distance vector to the nearest Γ-point. To unveil this symmetry, a

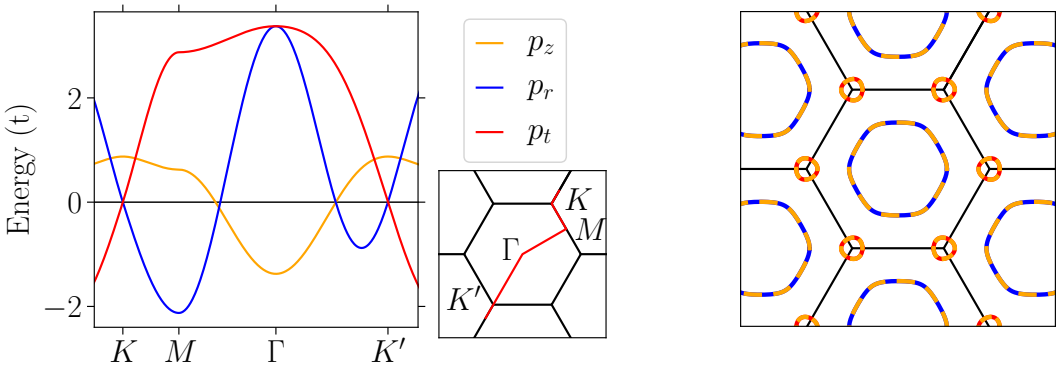

(a) (b)

Figure 4.1.2.: (a) Orbital character-resolved band structure obtained from a $p_r - p_t$ basis rotation with respect to Γ of the first BZ. The energy is given with respect to the Dirac point. The outset illustrates the path along which the band structure has been calculated. (b) Map plot of the nodal rings formed by the p_z-p_r and p_z-p_r band crossings.

momentum-dependent basis rotation can be constructed, which transforms the in-plane subspace $\{p_x, p_y\}$ into a $\{p_r, p_t\}$-basis

$$U(\varphi(\mathbf{k})) = \begin{pmatrix} \cos(\varphi(\mathbf{k})) & \sin(\varphi(\mathbf{k})) \\ -\sin(\varphi(\mathbf{k})) & \cos(\varphi(\mathbf{k})) \end{pmatrix}. \tag{4.9}$$

The transformation depends on the momentum coordinate with respect to the nearest Γ-point $\mathbf{k} = (k, \varphi(\mathbf{k}))$ and represents a continuous rotation symmetry. The rotated Hamiltonian-elements are shown in Fig. 4.1.1 for $1 = V^\sigma = -4V^\pi$. Indeed, the basis-transformation unveils the C_6-symmetry of the Hamiltonian: the off-diagonal elements vanish along the high-symmetry lines Γ-M and Γ-K, which indicates the $\{p_r, p_t\}$-orbital symmetry of the eigenstates. However, as the basis rotation assumes a continuous rotation symmetry, it yields only the eigenfunctions of the Hamiltonian along the reflection planes inside the BZ. Strong deviations can be seen at the BZ-boundary, the correct parallel/tangential alignment is only obtained at M and K. This is reflected in the small off-diagonal elements which increase with the distance to Γ. Nevertheless, as the off-diagonal elements are much smaller than the diagonal elements, we can approximately assume, that the $\{p_r, p_t\}$-basis is an eigenbasis in the full BZ and the diagonal elements can be directly related to the band energies, which reveal degeneracies at Γ and K. For the chosen tight-binding parameters, we find that the p_r band is located at lower energies than the p_t band. The corresponding band structure including the p_z-orbital is shown in Fig. 4.1.2 (a) with $V^\sigma = 4V^\pi_{p_z} = -E_{p_z}$, which displays all the aforementioned qualitative features. These tight-binding parameters reflect qualitatively the models discussed in Chap. 5 and the triangular adsorbates on SiC in Chap. 6. In the highly symmetric layer group, the model can host p_z-p_r and p_z-p_t-type metallic band crossings. These give rise to nodal rings centered around Γ

and the valley momenta as illustrated in Fig. 4.1.2 (b). In Sec. 4.3, it will be shown that the aforementioned orbital symmetry plays a significant role, when σ_h-breaking is considered.

4.2. σ_v-Symmetry-Breaking

After having established the tight-binding Hamiltonian in the presence of vertical reflection symmetry, we will discuss the lattice formulation of a σ_v violating term, which breaks the in-plane inversion symmetry. First, we will derive it from a pure group-theoretical ansatz (1), then from a hopping-process-bases argument (2), and finally from down-folding (3). While the first allows a straightforward lattice formulation, the latter two give intuitive insights into the microscopic mechanisms.

4.2.1. Group-Theoretical Derivation

As shown in Sec. 2.4.2.1, all layer groups with broken σ_v-symmetry are still symmetric under C_{3_z} and σ_d. The absence of C_{2z} symmetry allows for hoppings that are anti-symmetric under spatial inversion. Further, as σ_h remains preserved, σ_v-breaking will introduce new terms on the in-plane subspace only. Hence, by requiring C_3 symmetry, an odd behavior under C_2 and vanishing matrix elements along the σ_d reflection planes, the transfer matrix elements can be written as [4]

$$H^{\not\sigma_v}_{yx}(\mathbf{R}) = \langle p_y(\mathbf{0})|\hat{H}^{\not\sigma_v}|p_x(\mathbf{R})\rangle = +\frac{\lambda_{\not\sigma_v}}{3\sqrt{3}}\cos(3\varphi), \tag{4.10}$$

$$H^{\not\sigma_v}_{xy}(\mathbf{R}) = \langle p_x(\mathbf{0})|\hat{H}^{\not\sigma_v}|p_y(\mathbf{R})\rangle = -\frac{\lambda_{\not\sigma_v}}{3\sqrt{3}}\cos(3\varphi), \tag{4.11}$$

where $\varphi(\mathbf{R})$ is the azimuthal angle measured from $\vec{e}_x$ and $\lambda_{\not\sigma_v}$ is the interaction strength. The opposite sign in Eqs. 4.10 and 4.11 is a consequence of the broken C_2 symmetry. In momentum-space, this Hamiltonian reads in the $\{p_x, p_y\}$-subspace

$$H^{\not\sigma_v}_{xy}(\mathbf{k}) = \frac{2}{3\sqrt{3}}\lambda_{\not\sigma_v}\left[\sin(k_1) + \sin(k_2) - \sin(k_1+k_2)\right]\tau_y. \tag{4.12}$$

Upon recognizing, that the second Pauli matrix τ_y is the representation of the $\hat{L}_z$ operator in the $\{p_x, p_y\}$-basis, this interaction promotes indeed chiral wave functions. The momentum-dependence of this purely imaginary Hamiltonian is illustrated in Fig. 4.2.1 (a), which shows a vanishing amplitude along the σ_d reflection lines and an alternating behavior at K and K'. The prefactors in Eqs. 4.10 and 4.11 have been chosen such that the effective low-energy Hamiltonian at the valley momenta, introduced in Eq. 3.1, is retrieved

$$\hat{H}^{\not\sigma_v}_{xy}(K/K') = \pm\lambda_{\not\sigma_v}\hat{L}_z. \tag{4.13}$$

The band structure in the presence of vertical reflection symmetry breaking with $\lambda_{\not\sigma_v} = 0.2V^\sigma$ is shown in Fig. 4.2.1 (b). The Dirac bands at the valley momenta are massive and OAM-polarized, hence they will localize only at the A or at the B site as discussed in Sec. 3.3. The nodal-line crossings between the p_z and in-plane bands remain instead gapless. For the chosen set of tight-binding parameters, the p_z-p_r nodal-line is located in a global gap near the Fermi-level, which will play an important role for the topological phases discussed in Chap. 5.

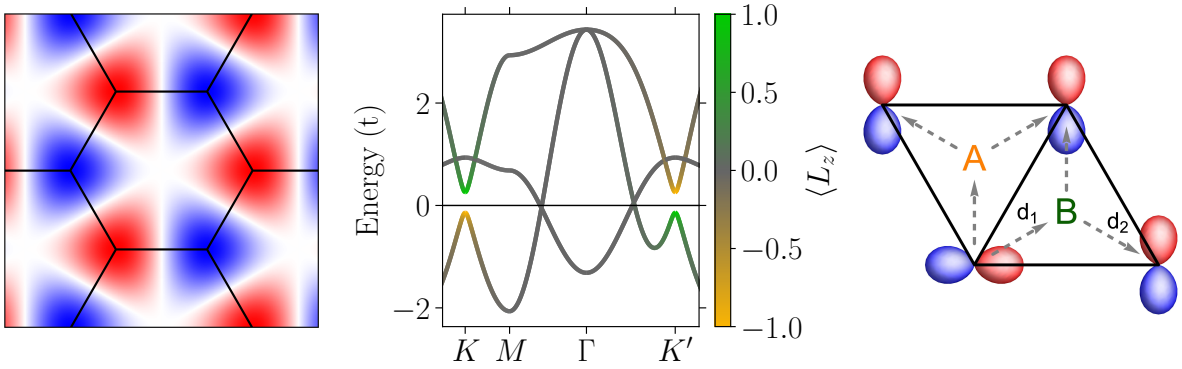

(a) (b) (c)

Figure 4.2.1.: (a) Map plot of the matrix elements of $\Im[H^{\not\sigma_v}_{xy}(\mathbf{k})]$ in units of $\lambda_{\not\sigma_v}$, where red(blue) denotes positive(negative) values. (b) Band structure with the tight-binding parameters of Fig. 4.1.2 and $\lambda_{\not\sigma_v} = 0.2V^\sigma$. The color code indicates the atomic L_z polarization. (c) Sketch of the ISB p_x-p_y interaction on the triangular lattice activated by a staggered potential peaking at the A/B voids of the triangular lattice. First neighbor hoppings can be decomposed into inequivalent second order processes via the A/B points as indicated by the gray arrows $\mathbf{d}_1$ and $\mathbf{d}_2$. Reprinted figure in (c) with permission from Eck, P. *et al.* "Real-space obstruction in quantum spin Hall insulators". *Physical Review B* **106,** 195143 (2022). © 2022 by the American Physical Society.

4.2.2. Microscopic Ansatz

The group-theoretical ansatz allows for a straightforward derivation of the interaction term, however the underlying hybridization and hopping mechanisms remain elusive. In the following, we will assume a σ_v-breaking potential in real space to investigate its impact on the hopping processes in the in-plane subspace [2]. First we decompose the nearest-neighbor interaction in a second-order hopping process from site i to A(B) and from A(B) to site j. It is illustrated by the two unit vectors $\mathbf{d}_1$ and $\mathbf{d}_2$ pointing from i to A(B) and from A(B) to j in Fig. 4.2.1 (c). This decomposition makes it evident, that such a hopping process via the A(B) site involves an overlap of wave functions

with either same or different parity. Hence its amplitude will be either positive or negative. The alternating behavior can be described by the directed angle spanned by the vectors $\mathbf{d}_1$ and $\mathbf{d}_2$. By defining the differences between the hopping strengths through the A/B sites as $\frac{\lambda_{\not\sigma_v}}{3\sqrt{3}}$, i.e., considering only the hoppings through the preferred void site, the interaction can be written as [2]:

$$\hat{H}^{\not\sigma_v}_{xy} = \frac{\lambda_{\not\sigma_v}}{3\sqrt{3}} \sum_{\langle ij \rangle} \nu_{ij} (c^{\dagger}_{p_y,i} c_{p_x,j} + \text{h.c.}). \tag{4.14}$$

As a result, an electron traveling from site i to nearest neighbor j experiences a left-right asymmetry, which is reversed when moving from j to i. This is described by the orientation of the third component of the Dzyaloshinskii-Moriya vector $\nu_{ij} = (2/\sqrt{3})(\hat{\mathbf{d}}_1 \times \hat{\mathbf{d}}_2)_z = \pm 1$. This parametrization is reminiscent of that for the second-nearest neighbor SOC interaction in the Kane-Mele model, which depends on whether the other sublattice appears on the left or the right of the hopping process [18]. Upon defining ν_{ij} in Eq. 4.14 via the azimuthal angle φ, the initial real-space definition of the σ_v-breaking term in Eqs. 4.10 and 4.11 is retrieved.

The microscopic derivation highlights explicitly the importance of:

- the parity of the involved orbitals, which promotes the direction-dependent alternating amplitude,
- the σ_v-breaking potential, which renders the hopping strengths through the A/B sites inequivalent.

4.2.3. Explicit Ansatz

In this section, we will incorporate the $\hat{H}^{\not\sigma_v}$ interaction by additionally considering orbitals on only one of the A/B positions to explicitly break the vertical reflection symmetry. This may be regarded as an explicit formulation of the σ_v-breaking potential discussed in the previous section. A low-energy Hamiltonian, i.e., an effective interaction defined in the subspace of orbitals located on the triangular lattice site can be obtained via down-folding [55]. The here presented ansatz is in close analogy to the DFT calculations in Secs. 6.2 and 6.3, where the symmetry breaking in the triangular monolayers arises from atoms of the underlying substrate.

Here we introduce a s-type orbital on site A$= (1/3, 2/3)$ and allow for a finite interaction with the in-plane p-orbitals on the triangular lattice site $1a$. The Hamiltonian reads in the $\{p_x, p_y, s\}$-basis:

$$H_{ps}(\mathbf{k}) = \begin{pmatrix} H_{p_{xy}}(\mathbf{k}) & V_{p_{xy}s}(\mathbf{k}) \\ V_{sp_{xy}}(\mathbf{k}) & H_s(\mathbf{k}) \end{pmatrix}. \tag{4.15}$$

With the 2×2 Hamiltonian of the in-plane subspace $H_{p_{xy}}(\mathbf{k})$ as introduced in Sec. 4.1, the one-dimensional Hamiltonian of the s-subspace $H_s(\mathbf{k}) = E_s$, which is given with respect to the Dirac-point of the in-plane states, and the hybridization between the two subspaces $V_{p_{xy}s}(\mathbf{k})$. By recalling the Slater-Koster integral for a s-p-overlap (see also Sec 2.3.1 and Eq. 2.47), the tight-binding interaction $V_{p_{xy}s}(\mathbf{k})$ reads:

$$V_{sx}(\mathbf{k}) = \frac{\sqrt{3}}{2} V_{\not\sigma_v} \left(e^{\frac{i}{3}(k_1 - k_2)} - e^{\frac{i}{3}(-2k_1 - k_2)} \right), \tag{4.16}$$

$$V_{sy}(\mathbf{k}) = V_{\not\sigma_v} \left[-\frac{1}{2} \left(e^{\frac{i}{3}(k_1 - k_2)} - e^{\frac{i}{3}(-2k_1 - k_2)} \right) + e^{\frac{i}{3}(k_1 + 2k_2)} \right]. \tag{4.17}$$

Here we substitute directly $V_{sp}^{\sigma} = V_{\not\sigma_v}$. By following the lines of [55], an effective low-energy model $\hat{H}^{eff}$ for the in-plane Dirac states can obtained via downfolding:

$$\hat{H}^{eff} \approx \hat{H}_{p_{xy}} - \underbrace{\hat{V}_{p_{xy}s} \cdot (\hat{H}_s)^{-1} \cdot \hat{V}_{sp_{xy}}}_{\hat{H}^{df}}. \tag{4.18}$$

This approximation considers corrections arising from second order hopping processes between the triangular in-plane orbitals via the s orbital on the A position, i.e., it is the explicit description of the microscopic ansatz given in the previous section. The correction to the in-plane Hamiltonian reads:

$$H_{xx}^{df}(\mathbf{k}) = \frac{3V_{\not\sigma_v}^2}{2E_s} \quad [1 - \cos(k_1)], \tag{4.19}$$

$$H_{yy}^{df}(\mathbf{k}) = \frac{V_{\not\sigma_v}^2}{2E_s} \quad [3 + \cos(k_1) - 2\cos(k_2) 2\cos(k_1 + k_2)], \tag{4.20}$$

$$H_{xy}^{df}(\mathbf{k}) = \frac{\sqrt{3}V_{\not\sigma_v}^2}{2E_s} [i\{\sin(k_1) + \sin(k_2) - \sin(k_1 + k_2)\} + \cos(k_2) - \cos(k_1 + k_2)]. \tag{4.21}$$

As $H_{p_{xy}}(\mathbf{k})$ vanishes at K/K', the effective Hamiltonian simplifies to the downfolded σ_v-breaking interaction:

$$H^{\not\sigma_v}(K/K') := H^{eff}(K/K') = -\frac{9}{4} \frac{V_{\not\sigma_v}^2}{E_s} (\tau_0 \mp \tau_y). \tag{4.22}$$

The broken vertical reflection symmetry promotes not only orbital angular momentum but gives also rise to a rigid band shift by τ_y and τ_0, respectively. As the latter (even with respect to $\mathbf{k}$) does not reduce the spatial symmetries of the p-shell Hamiltonian[1], it is sufficient to consider only the off-diagonal term proportional to L_z. By comparing Eqs. 4.13 and 4.22, the *ad hoc* introduced σ_v-breaking parameter is given at the valley momenta by $\lambda_{\not\sigma_v} \approx -\frac{9}{4} \frac{V_{\not\sigma_v}^2}{E_s}$.

[1]The even term can be absorbed in the p_{xy} matrix element of the p6/mmm lattice Hamiltonian given in Eq. 4.7.

Hence, we have gained a full understanding of the fundamental mechanism of vertical reflection symmetry breaking in a realistic tight-binding picture. As already stated in the previous section, it depends on the symmetries of the involved orbitals. It scales approximately quadratically with the hybridization strength and inversely with the energy separation of the triangular p and symmetry-breaking orbitals. Therefore, the interaction strength in real materials is *a priori* hard to estimate and requires state-of-the-art *ab initio* methods. Concrete examples can be found in Chap 6.

4.3. σ_h-Symmetry Breaking

Here we will derive the horizontal reflection symmetry-breaking term in real and momentum space. As in the case of $\hat{H}^{\phi_v}$, this term can be similarly derived from microscopic considerations and downfolding. This interaction is required to have complete invariance under all continuous in-plane symmetry operations, which includes the discrete in-plane symmetries of p6/mmm. However it violates σ_h ($z \mapsto\!\!\!\!\!/ \; -z$) and the C_2' and the C_2'' rotations around the main axes of the in-plane reflection planes. This activates the overlap between the in-plane and the p_z subspace and the effective transfer elements are defined in a $\{p_x, p_y, p_z\}$-basis:

$$H_{iz}^{\phi_h}(\mathbf{R}) = \langle p_i(\mathbf{0})|\hat{H}^{\phi_h}|p_z(\mathbf{R})\rangle = -\lambda_{\phi_h} n_i, \tag{4.23}$$

$$H_{zi}^{\phi_h}(\mathbf{R}) = \langle p_z(\mathbf{0})|\hat{H}^{\phi_h}|p_i(\mathbf{R})\rangle = +\lambda_{\phi_h} n_i, \tag{4.24}$$

This is in analogy to Eq. 4.2, where n_i reflects the preserved in-plane symmetries and the alternating sign in Eqs. 4.23 and 4.24 arises from the broken σ_h-symmetry. Similarly, the real-space parametrization can be obtained from a Slater-Koster Ansatz, where the symmetry-breaking is introduced by displacing the p_z-orbital. Hence the transfer integral between the in-plane and out-of-plane orbitals become finite as orbitals on neighboring sites are no-longer orthogonal to each other. According to Eq. 4.2 the interaction strength is given by $\lambda_{\phi_h} = n_z(\theta)(V_{xy,z}^{\sigma} - V_{xy,z}^{\pi})$ with $\theta \neq \pi/2$. The momentum-space formulation of the interaction read in the $\{p_x, p_z\}$- and $\{p_y, p_z\}$-subspaces

$$H_{xz}^{\phi_h}(\mathbf{k}) = \lambda_{\phi_h} \left[2\sin(k_1) - \sin(k_2) + \sin(k_1 + k_2)\right] \tau_y, \tag{4.25}$$

$$H_{yz}^{\phi_h}(\mathbf{k}) = \sqrt{3}\lambda_{\phi_h} \left[\sin(k_2) + \sin(k_1 + k_2)\right] \tau_y. \tag{4.26}$$

The components of the OAM operator are represented by the second Pauli matrix with $\hat{L}_x = \tau_y$ and $\hat{L}_y = -\tau_y$ in the $\{p_y, p_z\}$- and $\{p_x, p_z\}$-subspace, respectively. Hence, we recognize that both terms promote in-plane OAM-polarization. The Hamiltonian in the vicinity of Γ reads

$$\hat{H}^{\phi_h}(\mathbf{k}) = k_x \cdot \hat{L}_y - k_y \cdot \hat{L}_x = k_r \hat{L}_t, \tag{4.27}$$

where the labels r and t denote radial and tangential components. Hence this interaction promotes a rotating in-plane angular momentum structure around Γ. This OAM-polarization arises by coupling the radial aligned in-plane orbital to the p_z-orbital, as shown for the Hamiltonian in the $\{p_z, p_r, p_t\}$-basis (see also Sec. 4.1) in Fig. 4.3.1 (a, b). The p_r-p_z matrix elements in (a) increase with the distance to Γ and vanish at the BZ-boundary. The coupling between the p_t-p_z-orbitals in (b) vanishes in the vicinity of Γ and along the vertical reflection lines, i.e., along momenta where the applied basis transformation rotates the $\{p_x, p_y\}$ basis into eigenstates of the Hamiltonian. As this is in general not the case along the BZ-boundary, the rotated Hamiltonian yields finite off-diagonal elements at these momenta.

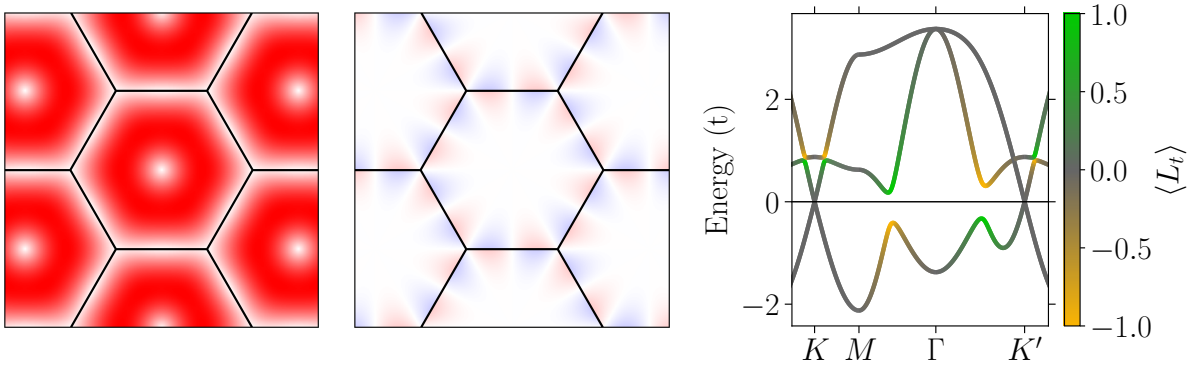

(a) (b) (c)

Figure 4.3.1.: Matrix elements of $\Im[H^{\phi_v}_{zr}(\mathbf{k})]$ (a) and $\Im[H^{\phi_v}_{zt}(\mathbf{k})]$ (b) in the $\{p_z, p_r, p_t\}$-basis in units of λ_{ϕ_h}. The saturation of the color code denotes the absolute strength. (c) Band structure with the tight-binding parameters of Fig. 4.1.2 and $\lambda_{\phi_h} = 0.1V^\sigma$. The color code denotes the tangential in-plane OAM-polarization, where the saturation is proportional to the absolute value $|\vec{L}_t|$ and the sign is proportional to L_y. The path connects momenta from $K = (-k_x, 0)$ to $K' = (k_x, 0)$.

The band structure in the presence of horizontal reflection-symmetry breaking with strength $\lambda_{\phi_h} = 0.1V^\sigma$ is shown in Fig. 4.3.1. This lifts the metallic crossing of the p_z-p_r bands by promoting in-plane OAM. However, the Dirac crossings at the valley momenta and the p_z-p_t along Γ-K are preserved. For a sufficiently large hybridization gap, as it is the case for the considered tight-binding parameters and for a filling of two electrons, the system is necessarily semimetallic with Dirac cones at the Fermi-level. Hence, the topology of the full BZ will be solely dictated by the mass term of the Dirac fermions as discussed in Chap 5. The valence band is symmetry-equivalent to the one of the Kane-Mele model, a detailed discussion can be found in Sec. 5.10.

A band-decomposed analysis of the in-plane OAM-polarization in the full BZ is illustrated in Fig. 4.3.2, which explicitly shows the chiral structure around Γ. As H^{ϕ_h} gaps-out the p_z-p_t nodal line, the involved bands must be in-plane OAM eigenstates,

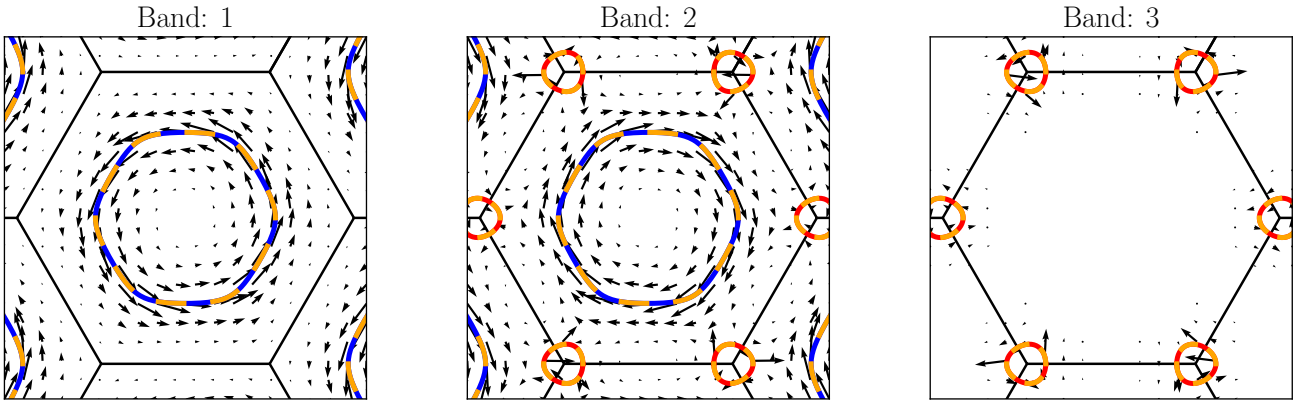

Figure 4.3.2.: (a-c) Vector field plot of the in-plane OAM-polarization with the σ_h-breaking strength of $\lambda_{\not{\sigma}_h} = 0.1V^{\sigma}$. The dashed lines show the position of the nodal lines in the p6/mmm-symmetric model (see also Fig. 4.1.2).

which is reflected in the maximum OAM-polarization at these momenta. The p_t-band carries instead vanishing OAM around Γ. It possesses a weak OAM polarization in the vicinity of the valley momenta, except along Γ-K [see also Fig.4.3.1 (c)].

4.4. Atomic Spin-Orbit Coupling

In the last section of this chapter, the atomic SOC interaction will be derived. It is given by

$$\hat{H}^{\mathrm{SOC}} = \lambda_{\mathrm{SOC}} \hat{L} \cdot \hat{S}. \tag{4.28}$$

with the interaction strength λ_{SOC}, the atomic OAM-operator $\hat{L}$ and the spin-operator $\hat{S}$. The components of the OAM-operator can be defined in terms of ladder operators

$$\hat{L}_x = \frac{1}{2}\left(\hat{L}_+ + \hat{L}_-\right), \quad \hat{L}_y = -\frac{i}{2}\left(\hat{L}_+ - \hat{L}_-\right). \tag{4.29}$$

Hence, it is convenient to express the real spherical harmonics p-basis in spherical harmonics eigenfunctions $|l, m\rangle$ with angular momentum quantum number m

$$|p_x\rangle = \frac{1}{\sqrt{2}}\left(-|1,1\rangle + |1,-1\rangle\right), \tag{4.30}$$

$$|p_y\rangle = \frac{i}{\sqrt{2}}\left(|1,1\rangle + |1,-1\rangle\right), \tag{4.31}$$

$$|p_z\rangle = |1,0\rangle, \tag{4.32}$$

where the Condon-Shortley phase convention has been applied [144, 145]. Therefore the non-zero matrix elements of the OAM-operator read in the real spherical harmonics basis

$$\begin{aligned}
&\langle p_y|\hat{L}_x|p_z\rangle = -i, && \langle p_x|\hat{L}_y|p_z\rangle = +i, && \langle p_x|\hat{L}_z|p_y\rangle = -i,\\
&\langle p_z|\hat{L}_x|p_y\rangle = +i, && \langle p_z|\hat{L}_y|p_x\rangle = -i, && \langle p_y|\hat{L}_z|p_x\rangle = +i.
\end{aligned}$$

And the SOC Hamiltonian is given in the $\{p_x, p_y, p_z\}$-basis

$$\hat{H}^{\mathrm{SOC}} = \lambda_{\mathrm{SOC}}\hat{L}\cdot\hat{S} = \frac{\lambda_{\mathrm{SOC}}}{2}\begin{pmatrix} 0 & -i\sigma_z & i\sigma_y \\ i\sigma_z & 0 & -i\sigma_x \\ -i\sigma_y & i\sigma_x & 0 \end{pmatrix}, \tag{4.33}$$

where the spin operator is expressed by the Pauli matrices $\hat{S} = \frac{1}{2}(\sigma_x, \sigma_y, \sigma_z)^T$. The band structure of the p6/*mmm*-symmetric model with $\lambda_{\mathrm{SOC}} = 0.3V^\sigma$ is shown in Fig. 4.4.1. It is insulating as the atomic SOC gaps out the Dirac cone at the valley momenta and the nodal ring formed by the crossing of the out-of-plane and radial in-plane band. The low-energy features are gapped with respect to their total angular momentum quantum number $J = L + S$.

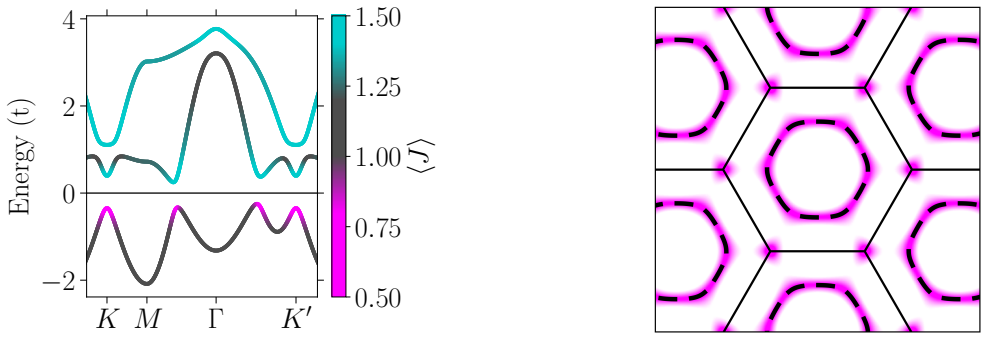

(a) (b)

Figure 4.4.1.: (a) Band structure of the p6/*mmm*-symmetric model with $\lambda_{\mathrm{SOC}} = 0.3V^\sigma$. The color code denotes the J-character. (b) Map plot J-character of the spin-degenerate valence bands with the same color code as in (a). To improve visualization, the grayish region has been set to white. The dashed lines indicate the position of the p_z-p_r-nodal-line in the absence of SOC.

We close this section by a short discussion on the dimensionality scaling of the atomic SOC. For an isolated atom in three dimension, the eigenvalue equation for the coupled spin and OAM

$$\mathbf{L}\cdot\mathbf{S} = \frac{1}{2}\left(J^2 - L^2 - S^2\right). \tag{4.34}$$

yields for a p-shell the four-fold degenerate $J = 3/2$ states with eigenvalue $11/4$ and the $J = 1/2$ states with the two-fold degenerate eigenvalue $5/4$. This results in an energy splitting of $3/2\lambda_{\mathrm{SOC}}$ for Eq. 4.33 and is 50% larger compared to the SOC-gap in the isolated $p_{\pm}$-Dirac model given in Eq. 3.2. The tight-binding model with $\lambda_{\mathrm{SOC}} = 0.3V^{\sigma}$ has a gap of $\approx 1.3\lambda_{\mathrm{SOC}}$, which is in between the two limits. This can be explained by the lifted degeneracy of the p-shell via the lattice Hamiltonian $H(\mathbf{k})$. It splits the p_z and the in-plane orbitals in energy at the valley momenta as shown in the absence of SOC in Fig. 4.1.2 (a). It is interesting to note, that this may be regarded as a dimensionality scaling of the SOC interaction: as derived in Ref. [146], the total angular momentum expectation value J^2 for a state with angular momentum j in a d-dimensional space is given by

$$J_d^2 = j(j + d - 2), \tag{4.35}$$

which yields the well-known relation in three dimensions

$$J_3^2 = j(j + 1), \tag{4.36}$$

and simplifies in two dimensions to

$$J_2^2 = j^2. \tag{4.37}$$

Hence the lattice-induced orbital splitting effectively promotes a dimensional crossover from three to two dimensions on the level of the SOC-interaction. Therefore, to maximize the SOC-opened gaps at the nodal lines and the Dirac points in our model, the in-plane and the p_z subspace should be close in energy at these momenta to converge against the 3D SOC splitting.

4.5. Summary

In this chapter, we have set the stage for the discussion of the topological phases on the triangular lattice in Chap. 5. Further it will be highlighted in Chap. 6 that it provides also an excellent qualitative description for triangular monolayer adsorbates. The important band structure features are the nodal lines and the Dirac points at the valley momenta, which are protected by the lattice symmetries and the relative alignment of the bands. In the absence of inversion symmetry, the p_z-p_r-type nodal ring and the Dirac points can be gapped by breaking the horizontal and vertical reflection symmetry, respectively. As introduced in Sec. 2.4.3, this promotes chiral wave functions. On the other hand, an insulating phase can be stabilized in the presence of atomic SOC, which results in Kramers-degenerate chiral wave functions, as inversion and time-reversal symmetry are preserved. As discussed in the next chapter, the interplay of symmetry breaking and atomic SOC will determine the topology, which is encoded in the OAM-polarization at the nodal-line and Dirac momenta.

5. Symmetry-Breaking Stabilized Topological Phases on the Triangular Lattice

After having established a minimal model describing symmetry breaking and SOC in a p-shell on the triangular lattice, this chapter is devoted to a thorough analysis of its symmetry-breaking stabilized topological phases. Here we address one of the intrinsic motivations of this work, i.e., elaborating on the question whether ISB can act as the desired antagonist to the atomic SOC for stabilizing non-trivial phases. The focus will be on the wave function symmetry, especially the OAM polarization. The chapter is structured as follows, first an overview on the topological phases and the main results will be given, followed by a detailed analysis on the level of the wave function symmetry in the spirit of topological quantum chemistry [44], including real-space obstruction and electric polarization [147]. In particular, we will extend the notion of real-space obstruction to the $\mathbb{Z}_2$ non-trivial phases on the triangular lattice. Also a higher-order topological insulator phase will be discussed in the $\mathbb{Z}_2$-trivial regime. The chapter concludes with a comparison of the triangular indenene-like QSHI to the Kane-Mele model with identical valence band symmetry.

5.1. Overview

This preliminary section compares the topological phases on the level of their qualitative band structure and on their electric polarization. This overview will guide the reader through the derivation and main discussion of the results in the following sections.

As it has been derived in Chap. 4, we will consider hereinafter the following Hamiltonian of a p-shell on a triangular lattice

$$\hat{H} = \hat{H}^T + \hat{H}^{\mathrm{SOC}}(\lambda_{\mathrm{SOC}}) + \hat{H}^{\not\sigma_h}(\lambda_{\not\sigma_h}) + \hat{H}^{\not\sigma_v}(\lambda_{\not\sigma_v}), \tag{5.1}$$

where $\hat{H}^T$ describes the symmetry allowed nearest-neighbor hoppings in the inversion symmetric layer group (LG) p6/mmm. The second term is the atomic SOC-interaction and $\hat{H}^{\not\sigma_h}$ and $\hat{H}^{\not\sigma_v}$ are the horizontal- and vertical-reflection symmetry-breaking terms,

phase	λ_{SOC}	$\lambda_{\not\sigma_h}$	$\lambda_{\not\sigma_v}$
SOC insulator	0.30	0.1/6	0.04/3
$\not\sigma_h$ QSHI	0.30	0.1	0.04/3
$\not\sigma_v$ QSHI	0.30	0.1/6	0.04·2
HOTI	0.30/2	0.1	0.04

Table 5.1.1.: Tight-binding parameters in units of t of representatives of the four topologically distinct insulating phases in this section. The Slater-Koster parameters for H^T are in all phases $E_z = -0.7$, $V^\sigma = 0.7$, $V^\pi = -0.15$ and $V^\pi_{p_z} = -0.25$.

respectively, which violate both inversion symmetry. Further it should be noted, that the last three terms scale linearly with their interaction strength λ_i and their competition can be discussed on the level of their relative strengths [4]. The chosen tight-binding parameters for all model calculations are given in Tab. 5.1.1, unless explicitly specified.

As illustrated in Fig. 5.1.1 this competition gives rise to four (I-IV) topologically distinct insulating phases for a filling of two electrons. The unit cell symmetry is schematically depicted in (a) and an exemplary band structure of the corresponding phase is shown in (b). The topological distinct phases are separated by gap-closing phase transitions either at the p_z-p_r-type nodal ring or at the valley Dirac states, as indicated by the dashed-line arrows for neighboring phases. The color code in Fig. 5.1.1 denotes the J-character and highlights that states of predominantly $J = 1/2$ and $J = 3/2$ are exchanged between valence and conduction bands at the phase transitions. The four insulating and topologically distinct phases are:

I SOC Insulator

If SOC dominates over both symmetry-breaking terms, the band structure is adiabatically connected to the p6/mmm-symmetric model. As shown in Sec. 4.4 and in Fig. 5.1.1 (b), the nodal ring and valley Dirac fermions are gapped by the atomic SOC and the valence bands can be described in terms of a J-basis. This phase must be $\mathbb{Z}_2$-trivial, as it is related to an atomic limit, which is described by atomic SOC and local crystal-field splitting. Hence its occupied bands can be represented by $|j_z = \pm 1/2\rangle$ Wannier functions on the $1a$ position. This phase is an atomic insulator.

II Indenene-like $\not\sigma_h$ QSHI

This insulating phase is stabilized, if horizontal reflection symmetry-breaking dominates over SOC and vertical reflection-symmetry breaking is small. The layer group with highest symmetry, which satisfies this condition is p6mm, e.g., as it is the case for a triangular lattice on a homogeneous substrate as illustrated in Fig. 5.1.1. This phase

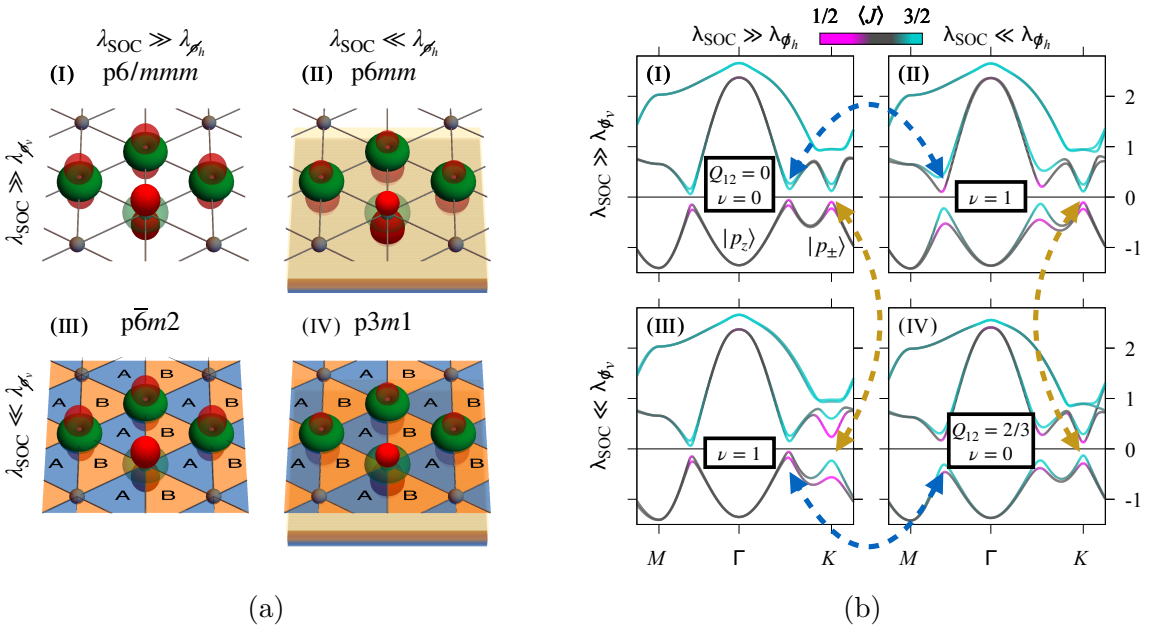

(a) (b)

Figure 5.1.1.: (a) Symbolic illustration of the maximal lattice symmetry of the four (I-IV) topological distinct phases. The red dumbbells and the green doughnuts denote p_z and $p_\pm$ orbitals, respectively, on a triangular lattice. A schematically shown substrate breaks σ_h (II, IV) and σ_v (III, IV), which renders the A/B sites inequivalent. (b) Exemplary insulating band structures of the unit cells shown in (a) with the associated $\mathbb{Z}_2$ topological invariant ν and quadrupole moment Q_{12}. The color code reflects the $\langle J \rangle$ character and the arrows indicate the relevant band inversion between neighboring phases. $\hat{H}^{\mathrm{SOC}}$, $\hat{H}^{\phi_h}$ and $\hat{H}^{\phi_v}$ are non-vanishing in all panels to lift the Kramers-degeneracy. The labels in panel (I) of (b) refer to the dominant orbital character of the valence bands. The tight-binding parameters are given in Tab. 5.1.1. Reprinted and adopted figure in (a) from Bauernfeind, M. *et al.* "Design and realization of topological Dirac fermions on a triangular lattice". *Nature Communications* **12,** 5396 (2021). CC BY 4.0. Reprinted and adopted figure in (b) with permission from Eck, P. *et al.* "Recipe for higher order topology on the triangular lattice". *Phys. Rev. B* **107,** 115130 (2023). © 2023 by the American Physical Society.

has been experimentally realized for a monolayer of indium on SiC (*indenene*), further details can be found in Sec. 6.2 and Refs. [2, 3]. As shown in Sec. 4.2, a sufficiently large σ_h-breaking pins the Dirac fermions to the Fermi level and the SOC-interaction gaps them in a $\mathbb{Z}_2$-non-trivial fashion (see also Sec.3.1). This is reflected in the angular momentum polarization of the valence bands: they have common J-character and identical tangential OAM-polarization at the valleys and at the nodal-line momenta, respectively. In Sec. 5.9, we will show that the time-reversal symmetry-violating Wan-

nier functions of the valence bands localize at the A and the B site. Therefore it may be regarded as a real-space obstructed QSHI.

III $\not\sigma_v$ QSHI

The $\not\sigma_v$ QSHI is characterized by a strong vertical reflection symmetry-breaking, intermediate SOC interaction and a weak horizontal reflection symmetry-breaking. The highest layer group, which can host this phase, is p$\bar{6}m2$. As sketched in Fig. 5.1.1, this can be achieved by a staggered potential or inequivalent orbitals on the A/B sites. The dominating σ_v-breaking gaps the valley momenta by promoting out-of-plane OAM-polarization, while the gap at the nodal-line is opened by SOC. This real-space obstructed QSHI has time-reversal symmetry-violating Wannier functions of the valence bands which are either pinned to only the A or only the B site, depending on the sign of $\lambda_{\not\sigma_v}$.

IV HOTI

In layer group p3m1, if both reflection symmetry-breaking terms dominate over SOC or if SOC is absent, the resulting band structure is necessarily $\mathbb{Z}_2$-trivial. The OAM-polarization is parallel for the valence bands doublets at the valleys and at the nodal line momenta. However, the Wannier functions of the valence bands are not localizable on the 1a position, but center at only one of the A/B sites. This promotes a finite electronic dipole and quadrupole moment, which can stabilize zero-dimensional in-gap corner states in finite-size geometries. This phase is a real-space obstructed atomic insulator.

As summarized in Tab. 5.1.2, the interplay of SOC and symmetry-breaking terms gives rise to two $\nu = 0$ and $\nu = 1$ phases. Phases with identical $\mathbb{Z}_2$-index can be discriminated by their wave function chirality at the valley momenta and the localization of the valence bands. A gap reopening involves necessarily a change in the $\mathbb{Z}_2$-index, neighboring phases have different $\mathbb{Z}_2$-indices. In contrast to symmetry protected QSHIs, either the vertical or the horizontal reflection symmetry must be broken to stabilize a QSHI-phase. Furthermore, the strongly symmetry broken layer group can host a HOTI. In the following sections, the here presented results will be derived and discussed in detail.

5.2. $\mathbb{Z}_2$-Topology and Wilson-Loops

Here we discuss the WCC movement, which reveals not only the $\mathbb{Z}_2$-invariant, but provides also insight into the electric polarization and the underlying mechanisms. Further details can be found in Sec. 2.1 and Refs. [42, 43]. The results are shown in Fig. 5.2.1, the Wilson-Loop eigenvalues indicate the SOC-dominated (I) and the strongly symmetry-broken phases (IV) as $\mathbb{Z}_2$-trivial. Instead, if only σ_h- (II) or σ_v-

Phase	Layer Group	ν	SOC vs $\not\sigma_h$	SOC vs $\not\sigma_v$	$\xi(C_3)$ at K	$\mathbf{P} = (P_1, P_2)$	Q_{12}
SOC insulator	p6/mmm	0	$\lambda_{\mathrm{SOC}} \gg \lambda_{\not\sigma_h}$	$\lambda_{\mathrm{SOC}} \gg \lambda_{\not\sigma_v}$	$\{e^{+i\pi/3}, e^{-i\pi/3}\}$	$(0,0)$ mod 2	0 mod 1
Indenene-like $\not\sigma_h$ QSHI	p6mm	1	$\lambda_{\mathrm{SOC}} \ll \lambda_{\not\sigma_h}$	$\lambda_{\mathrm{SOC}} \gg \lambda_{\not\sigma_v}$	$\{e^{+i\pi/3}, e^{-i\pi/3}\}$	-	-
$\not\sigma_v$ QSHI	p$\bar{6}m2$	1	$\lambda_{\mathrm{SOC}} \gg \lambda_{\not\sigma_h}$	$\lambda_{\mathrm{SOC}} \ll \lambda_{\not\sigma_v}$	$\{e^{\pm i\pi/3}, -1\}$	-	-
Triangular HOTI	p3$m1$	0	$\lambda_{\mathrm{SOC}} \ll \lambda_{\not\sigma_h}$	$\lambda_{\mathrm{SOC}} \ll \lambda_{\not\sigma_v}$	$\{e^{\pm i\pi/3}, -1\}$	$(\mp\frac{2}{3}, \mp\frac{2}{3})$ mod 2	$\frac{2}{3}$ mod 1

Table 5.1.2.: Classification of the four insulating phases in terms real-space symmetry and topological properties. The indicated layer group is the highest layer group that satisfies the inequalities in columns four and five. For completeness, also the C_3 rotation eigenvalues and the dipole/quadrupole moments are given. The electric multipoles in the $\nu = 1$ phases are ill defined. The corresponding irreps can be found in Tab. 5.4.4. Reprinted table with permission from Eck, P. *et al.* "Recipe for higher order topology on the triangular lattice". *Phys. Rev. B* **107,** 115130 (2023). © 2023 by the American Physical Society.

breaking (III) exceeds the SOC-interaction, the topological invariant is $\nu = 1$. By recalling the definition of the electric polarization in the MTP

$$\mathbf{r} = \frac{i}{2\pi} \oint_{\mathrm{BZ}} d\mathbf{k} \langle u(\mathbf{k}) | \nabla_{\mathbf{k}} | u(\mathbf{k}) \rangle, \tag{5.2}$$

the WCCs illustrated in Fig. 5.2.1 can be regarded as the real-space position in units of the second Bravais vector $\mathbf{a}_2$ for a given pumping-momentum along the first reciprocal vector $\mathbf{b}_1$. Hence, for the $\nu = 0$ phases, the integrated value along the pumping axis relates to the electric polarization[1]. In detail, the WCCs unveil for the four phases:

I SOC Insulator

The pair of WCCs is centered around the $1a$ position $\mathbf{r} \approx (0, 0)$ and the small asymmetry in the WCC flow arises from the weak symmetry-breaking terms. During the pumping cycle the WCCs belonging to different spin eigenvalues propagate towards the in-plane coordinates $1/3$ and $-1/3 \equiv 2/3$, but return to their initial position after the pumping momentum has passed the coordinate of the valley momentum. Hence we can conclude that the Wannier functions of the valence bands localize at the $1a$ position. The SOC-gapped nodal line, which has its main impact on the WCC positions for pumping momenta close to the Γ, and the SOC-opened Dirac cones (see also vertical dashed line and description of Fig. 5.2.1) dictate the accumulated Berry phase and the WCC movement.

[1]The polarization in Eq. 5.2 is defined by the integral over the full BZ. However, as the considered systems are time-reversal symmetric, it is sufficient to integrate over half of the BZ.

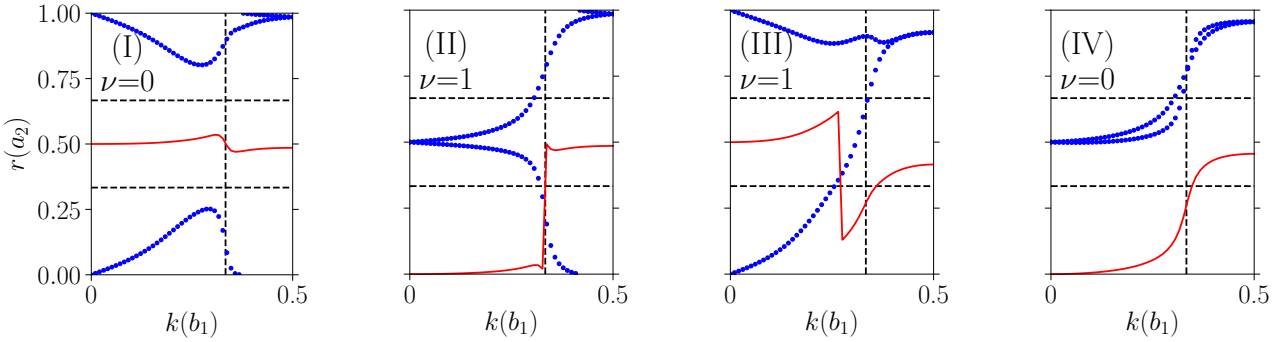

Figure 5.2.1.: WCC movement in units of the second Bravais vector of the four insulating models shown in Fig 5.1.1 (b) for pumping along the first reciprocal lattice vector b_1. The blue dots denote the WCCs of the valence bands while the red line indicates the position of the largest gap. The vertical dashed line highlights the pumping momentum which involves the integration over the valley momentum K. The horizontal dashed lines indicate $r = \{1/3, 2/3\}$. Based on the method of Soluyanov and Vanderbilt [42], the number of crossings with an odd number of WCCs indicates the $\mathbb{Z}_2$-invariant. Details can be found in Sec. 2.1 and Refs. [42, 43].This analysis yields $\nu_{\mathrm{I}} = \nu_{\mathrm{IV}} = 0$ and $\nu_{\mathrm{II}} = \nu_{\mathrm{III}} = 1$.

II Indenene-like $\not{\sigma}_h$ QSHI

The WCCs flow in a non-trivial fashion from the in-plane coordinate 1/2 to $0 \equiv 1$. The movement differs qualitatively from the one of the SOC insulator for $b_1 = [0, 1/3]$, but are equivalent for larger pumping momenta. This is a consequence of the σ_h-gapped nodal-line and the non-trivial WCC flow can be solely assigned to the SOC-opened Dirac states (see also Sec. 3.1). As time-reversal symmetric WCCs are constructed here, direct conclusions on the localization of the time-reversal symmetry-breaking Wannier functions, already mentioned in Sec 5.1, cannot be drawn.

III $\not{\sigma}_v$ QSHI

The WCC flow has qualitative similarities with the SOC insulator until the pumping momentum reaches 1/3, where the centers continue to approach each other indicating a non-trivial $\mathbb{Z}_2$-invariant. This phase is characterized by the nodal line being gapped by SOC and the Dirac points being opened by the σ_v-breaking term. Although the valence bands cannot be described with time-reversal symmetric Wannier functions, the comparison with the ndenene-like $\not{\sigma}_h$ QSHI unveils a clear difference in the **k**-dependent polarization. A first hint towards differently located time-reversal symmetry-breaking Wannier functions, as will be discussed in Sec. 5.9.

IV HOTI

The trivial WCC flow driven by σ_h- and σ_v-breaking is in qualitative agreement with

the one of the $\not{\sigma}_h$ QSHI and the one of the $\not{\sigma}_v$ QSHI for pumping momenta much smaller 1/3 and larger 1/3, respectively. Instead around the pumping momentum 1/3, the WCCs remain close to each other in a trivial fashion. In contrast to the SOC Insulator, the WCC pair centers around the $2/3 \equiv -1/3$ position. The calculated WCCs along $\mathbf{a}_1$ (not shown) center instead around 1/3. This suggests that the Wannier functions of the valence bands are located at $\mathrm{B} = (1/3, 2/3)$ which is in support of a real-space obstruction [66]. This will be thoroughly discussed in Secs. 5.4, 5.5 and 5.7.

In summary, the WCC flows of the four topological distinct phases show clear imprints of the gapping mechanisms of the low-energy band structure features: the dominating interactions at the nodal line and the valleys determine the electronic charge localization. Further, we can formulate a clear statement on the $\mathbb{Z}_2$-topology by considering separately the contributions of the low-energy states of the triangular model. As it is well-established for the valley Dirac fermions in 2D, a time-reversal symmetry-breaking mass term gives rise to a total Chern number of $C = \pm 1$ [53], while the spin-diagonal SOC interaction can be regarded as $(C_\uparrow, C_\downarrow) = (\pm 1, \mp 1)$ and the associated $\mathbb{Z}_2$-invariant is $\nu = (C_\uparrow - C_\downarrow)/2 \,\mathrm{mod} 2 = 1$ [18, 74]. In a similar fashion, we can conclude that the nodal ring carries also a non-trivial Berry charge of $C = \pm 1$ for a time-reversal symmetry-breaking mass term and $\nu = 1$ if gapped by SOC. A detailed discussion of the Berry charge of Dirac cones and nodal rings in 2D can be found in App. A.4. Hence the topology of the system may be defined as the sum over invariants of its low-energy building-blocks

$$\nu = \left(\nu^{\text{valley}} + \nu^{\text{nodal-ring}}\right) \mathrm{mod} 2, \tag{5.3}$$

which depends only on the topological invariants of the low-energy Hamiltonians of the valley momenta and of the p_z-p_r-type nodal-ring. These can be unambiguously assigned in the limits of:

$$\nu^{\text{valley}} = \begin{cases} 0, & \lambda_{\text{SOC}} \ll \lambda_{\not{\sigma}_v} \\ 1, & \lambda_{\text{SOC}} \gg \lambda_{\not{\sigma}_v} \end{cases}, \tag{5.4}$$

$$\nu^{\text{nodal-ring}} = \begin{cases} 0, & \lambda_{\text{SOC}} \ll \lambda_{\not{\sigma}_h} \\ 1, & \lambda_{\text{SOC}} \gg \lambda_{\not{\sigma}_h} \end{cases}. \tag{5.5}$$

It should be noted, that the topological invariants ν^{valley} and $\nu^{\text{nodal-ring}}$ are only well-defined in non-periodic low-energy models. They cannot be calculated from the full lattice-periodic triangular model, which is solely characterized by the $\mathbb{Z}_2$-invariant associated to the Bloch wave function in the full BZ. Nevertheless, the decomposition into contributions of the low-energy states provides a clear and comprehensible picture of the mechanism which defines the $\mathbb{Z}_2$-topology: the key interactions are SOC and symmetry breaking.

5.3. Orbital Angular Momentum Polarization

To enter the discussion of wave function symmetries, we will start with the investigation of symmetry-breaking and atomic SOC induced chirality of the wave functions. This is reflected in the local OAM in the full BZ. The analysis will allow us to rephrase the argument on the $\mathbb{Z}_2$-topology given in Eq. 5.3 in OAM-polarization patterns. Further, the C_3 rotation eigenvalues of valley Dirac fermions will be determined. It is worth mentioning, that this is the symmetry indicator which determines the real-space obstruction as will be shown in Sec. 5.5, 5.7, 5.8 and 5.9.

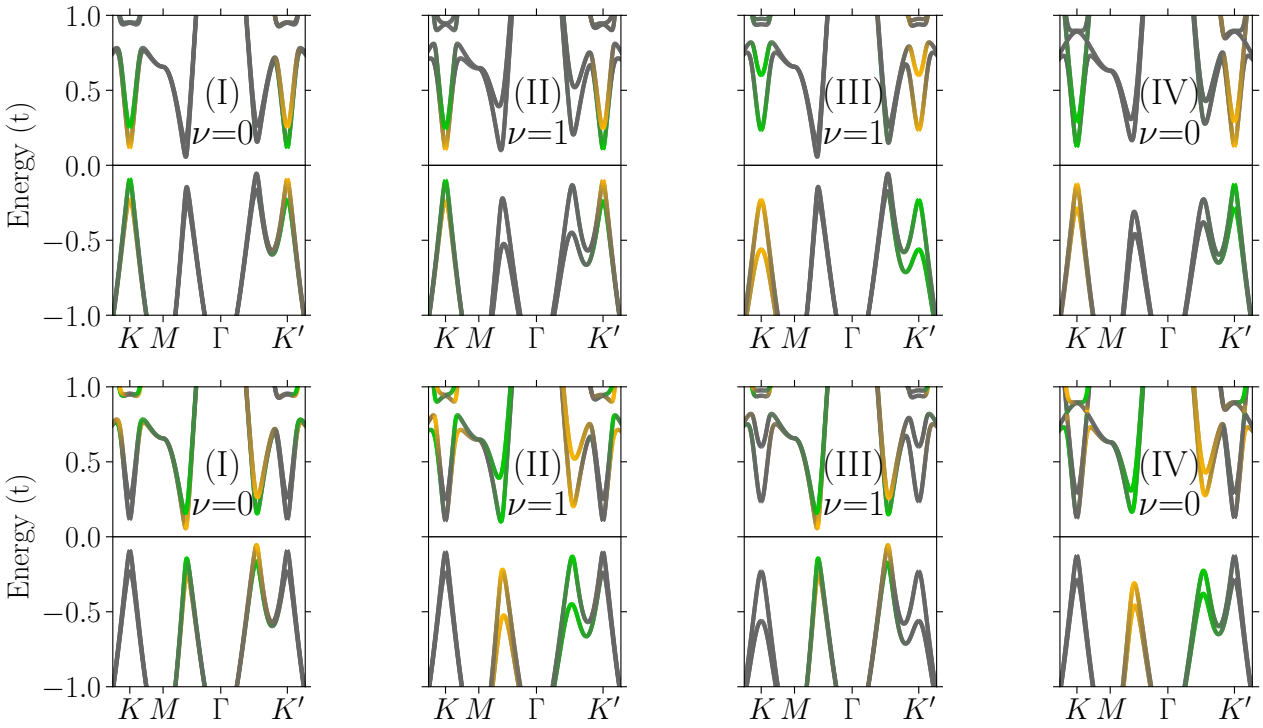

Figure 5.3.1.: Out-of plane (top row) and tangential in-plane (bottom row) OAM polarization of the four topological phases. Green and orange colors indicate positive and negative values, respectively. The tangential component of the in-plane OAM is shown similarly to Fig. 4.3.1.

The generic atomic OAM polarization of the four distinct insulating phases is shown in Fig 5.3.1[2]. It displays a strong out-of-plane polarization at the valley momenta. The valence states at K carry total angular momentum $j_z = l_z + s_z = \{-1/2, +1/2\}$ if SOC dominates over σ_v-breaking (I,II) and $j_z = \{-1/2, -3/2\}$ in the strongly reflection symmetry-broken phases (III+IV) (see also Sec. 3.1 and Tab. 3.1.1). This corresponds to the C_3 rotation characters of $(e^{+i\pi/3}, e^{-i\pi/3})$ and $(e^{-i\pi/3}, -1)$. However determining the $\mathbb{Z}_2$-invariant requires also the inspection of the p_z-p_r-type nodal line.

[2]The OAM polarization of the valence bands in the full BZ is shown in Fig. A.6.1.

Its gapping mechanisms provide in-plane OAM polarization, which is shown in the bottom row of Fig 5.3.1. The nodal ring is sensitive to the competition between SOC and horizontal reflection symmetry-breaking. Insulating phases with identical valley wave functions but different $\mathbb{Z}_2$-indices can be indeed discriminated by their in-plane OAM-polarization.

Hence, equivalently to the total angular momentum J shown in Fig. 5.1.1 (b) [4], the OAM-polarization of the valence bands at the nodal-line and the valley momenta serves a clear-cut indicator for the competition of SOC and symmetry-breaking terms, which defines the $\mathbb{Z}_2$-topology of the system. Furthermore, the OAM-induced Bloch wave function chirality and therefore the bulk topology can be addressed with experiments sensitive to the initial state. An explicit example of the experimental detection of in-plane OAM based on circular and linear dichroism ARPES techniques [148–152] will be given in Sec. 6.1. However, it should be noted, that this wave function symmetry-based $\mathbb{Z}_2$-classification is a result of a preceding analysis of the full electronic band structure. This has revealed the importance of the nodal-line and its gapping mechanisms. As we will discuss in the next section, symmetry-indicators at the high-symmetry momenta are instead insufficient for the $\mathbb{Z}_2$-classification, as the topology of the nodal ring is not captured.

5.4. Band Representations and Real-Space Obstruction

After having derived the $\mathbb{Z}_2$-invariants from a brute-force Wilson-Loop calculation and from OAM-polarization patterns, we will analyze in the following the wave function symmetries on the level of the irreps. Here we will apply the concept of symmetry indicators in the light of $\mathbb{Z}_2$-topology and real-space obstruction [44–47]. On one hand, this allows for a direct relation of real-space lattice and $\mathbf{k}$-dependent wave function symmetries to derive general ground state properties of the insulating phases. On the other hand, the considered model serves as a perfect template to highlight the strengths and weaknesses of symmetry indicators in the light of $\mathbb{Z}_2$-classification and real-space obstruction in high- and low-symmetric space groups. This section builds up on the concepts and lattice symmetry analysis presented in Sec. 2.4.

The building blocks of the model are the p-type local orbitals on the Wyckoff position $1a$. Their spinless and double-group representations in the four relevant layer groups are shown in Tab. 5.4.1. It is important to note, that the p_z and the in-plane orbitals are indistinguishable in terms of their spin-full representations: the coupling of OAM and spin splits the representation of the in-plane orbitals into two two-dimensional representations with $j_z = \pm\frac{1}{2}$ and $j_z = \pm\frac{3}{2}$. However, also the spin-full p_z-orbitals have total angular momentum $j_z = \pm\frac{1}{2}$. Hence, the orbital character can be exchanged between the p_z- and in-plane-type $j_z \pm \frac{1}{2}$ representations based on the competition of SOC and the on-site splitting. Further, also their band representations will be identical,

with profound implications on the determination of the $\mathbb{Z}_2$-topology.

Orbital-basis	p_z	(p_x, p_y)	$j_z = (-\frac{1}{2}, \frac{1}{2})$	$j_z = (-\frac{3}{2}, \frac{3}{2})$
p6/mmm	A_{2u}	E_{1u}	$\overline{E}_{1u}$	$\overline{E}_{3u}$
p6mm	A_1	E_1	$\overline{E}_1$	$\overline{E}_3$
p$\bar{6}m2$	A_2''	E_{1u}'	$\overline{E}_1$	$\overline{E}_3$
p3$m1$	A_1	E	$\overline{E}_1$	$^1\overline{E}^2\overline{E}$

Table 5.4.1.: Spinless and double-group representations of the p-shell on Wyckoff position $1a$ in hexagonal and trigonal layer groups.

As introduced in Sec. 2.4.1.3, the band representation classification bases on connectivity relations between the high-symmetry points. Therefore only the irreps at the high symmetry momenta Γ, M and K have to be considered for the triangular model. For completeness, we will also take into account the paths Γ-M represented by $\Sigma = (u, 0, 0)$ and Γ-K denoted by $\Lambda = (u, u, 0)$. The irreps of the EBRs induced by the local representations given in Tab. 5.4.1 of the p-shell on the triangular lattice are shown in Tab. 5.4.2.

Starting with the spinless model, the graph theoretical analysis of the band structures in the four relevant layer groups is shown in Fig. 5.4.1. It highlights the overall band symmetries discussed in Chap. 4 (see also Fig. 4.1.1). In the maximum symmetric layer group p6/mmm, the alternating ordering in energy of the irrep of the in-plane bands and the one of the p_z-band at Γ and K induces accidental band crossings between the two orbital-subspaces. These are the two nodal-lines discussed in Sec. 4.1.

In the absence of σ_h (p6mm), the former p_r-p_z nodal ring is gapped as both bands have identical irreps at Σ and Λ[3]. This pins the valley Dirac fermions to the Fermi level, if $\hat{H}^{\not\sigma_h}$ is sufficiently strong. If instead only σ_v is broken (p$\bar{3}m2$), the two-dimensional representation of the Dirac states splits into two one-dimensional chiral representations $\{p_+, p_-\}$ and the Fermi energy is located close to the p_r-p_z nodal ring. The only insulating phase can be stabilized, if both reflection symmetry-breaking terms are sufficiently strong (p3$m1$).

Hence the graph-theoretical analysis has unveiled the presence of nodal lines arising from accidental band crossings and two-fold in-plane degeneracies at Γ and K. By allowing for horizontal-reflection symmetry breaking and assuming a filling of two electrons, a semi-metallic band structure with Dirac fermions at the valley momenta can be stabilized. A symmetry-protected Dirac semi-metal with a Γ-centered nodal ring can be promoted by vertical-reflection symmetry breaking in LG p6mm.

A closer inspection of the isolated valence band in the p3$m1$ layer group unveils its

[3]The same mechanism gaps out the nodal line in conduction along M-K.

p6/mmm

Orbital-Rep.	p_z	(p_x, p_y)	$j_z = \pm 1/2$	$j_z = \pm 3/2$
Band-Rep.	A_{2u}	E_{1u}	$\overline{E}_{1u}$	$\overline{E}_{3u}$
Γ	$\Gamma_2^-(1)$	$\Gamma_6^-(2)$	$\overline{\Gamma}_{12}(2)$	$\overline{\Gamma}_{10}(2)$
K	$K_3(1)$	$K_5(2)$	$\overline{K}_8(2)$	$\overline{K}_7(2)$
M	$M_2^-(1)$	$M_3^-(1) \oplus M_4^-(1)$	$\overline{M}_6(2)$	$\overline{M}_6(2)$
Σ	$\Sigma_3(1)$	$\Sigma_1(1) \oplus \Sigma_2(1)$	$\overline{\Sigma}_5(2)$	$\overline{\Sigma}_5(2)$
Λ	$\Lambda_3(1)$	$\Lambda_1(1) \oplus \Lambda_4(1)$	$\overline{\Lambda}_5(2)$	$\overline{\Lambda}_5(2)$

p6mm

Orbital-Rep.	p_z	(p_x, p_y)	$j_z = \pm 1/2$	$j_z = \pm 3/2$
Band-Rep.	A_1	E_1	$\overline{E}_1$	$\overline{E}_3$
Γ	$\Gamma_1(1)$	$\Gamma_6(2)$	$\overline{\Gamma}_9(2)$	$\overline{\Gamma}_7(2)$
K	$K_1(1)$	$K_3(2)$	$\overline{K}_6(2)$	$\overline{K}_4(1) \oplus \overline{K}_5(1)$
M	$M_1(1)$	$M_3(1) \oplus M_4(1)$	$\overline{M}_5(2)$	$\overline{M}_5(2)$
Σ	$\Sigma_1(1)$	$\Sigma_1(1) \oplus \Sigma_2(1)$	$\overline{\Sigma}_3(1) \oplus \overline{\Sigma}_4(1)$	$\overline{\Sigma}_3(1) \oplus \overline{\Sigma}_4(1)$
Λ	$\Lambda_1(1)$	$\Lambda_1(1) \oplus \Lambda_2(1)$	$\overline{\Lambda}_3(1) \oplus \overline{\Lambda}_4(1)$	$\overline{\Lambda}_3(1) \oplus \overline{\Lambda}_4(1)$

p$\bar{6}m2$

Orbital-Rep.	p_z	(p_x, p_y)	$j_z = \pm 1/2$	$j_z = \pm 3/2$
Band-Rep.	$A_2''(1)$	E'	$\overline{E}_2$	$\overline{E}_3$
Γ	$\Gamma_3(1)$	$\Gamma_5(2)$	$\overline{\Gamma}_8(2)$	$\overline{\Gamma}_7(2)$
K	$K_2(1)$	$K_3(1) \oplus K_5(1)$	$\overline{K}_9(1) \oplus \overline{K}_{12}(1)$	$\overline{K}_7(1) \oplus \overline{K}_8(1)$
M	$M_3(1)$	$M_1(1) \oplus M_2(1)$	$\overline{M}_5(2)$	$\overline{M}_5(2)$
Σ	$\Sigma_3(1)$	$\Sigma_1(1) \oplus \Sigma_2(1)$	$\overline{\Sigma}_5(2)$	$\overline{\Sigma}_5(2)$
Λ	$\Lambda_2(1)$	$2\ \Lambda_1(1)$	$\overline{\Lambda}_3(1) \oplus \overline{\Lambda}_4(1)$	$\overline{\Lambda}_3(1) \oplus \overline{\Lambda}_4(1)$

p3$m1$

Orbital-Rep.	p_z	(p_x, p_y)	$j_z = \pm 1/2$	$j_z = \pm 3/2$
Band-Rep.	A_1	E	$\overline{E}_1$	${}^1\overline{E}^2\overline{E}$
Γ	$\Gamma_1(1)$	$\Gamma_3(2)$	$\overline{\Gamma}_6(2)$	$\overline{\Gamma}_4\overline{\Gamma}_5(2)$
K	$K_1(1)$	$K_2(1) \oplus K_3(1)$	$\overline{K}_5(1) \oplus \overline{K}_6(1)$	$2\ \overline{K}_4(1)$
M	$M_1(1)$	$M_1(1) \oplus M_2(1)$	$\overline{M}_3\overline{M}_4(2)$	$\overline{M}_3\overline{M}_4(2)$
Σ	$\Sigma_1(1)$	$\Sigma_1(1) \oplus \Sigma_2(1)$	$\overline{\Sigma}_3(1) \oplus \overline{\Sigma}_4(1)$	$\overline{\Sigma}_3(1) \oplus \overline{\Sigma}_4(1)$
Λ	$\Lambda_1(1)$	$2\ \Lambda_1(1)$	$2\ \overline{\Lambda}_2(1)$	$2\ \overline{\Lambda}_2(1)$

Table 5.4.2.: Elementary band representations and their irreducible representations at the high symmetry momenta and at $\Sigma = (u, 0, 0)$ and $\Lambda = (u, u, 0)$. The notation follows Ref. [153].

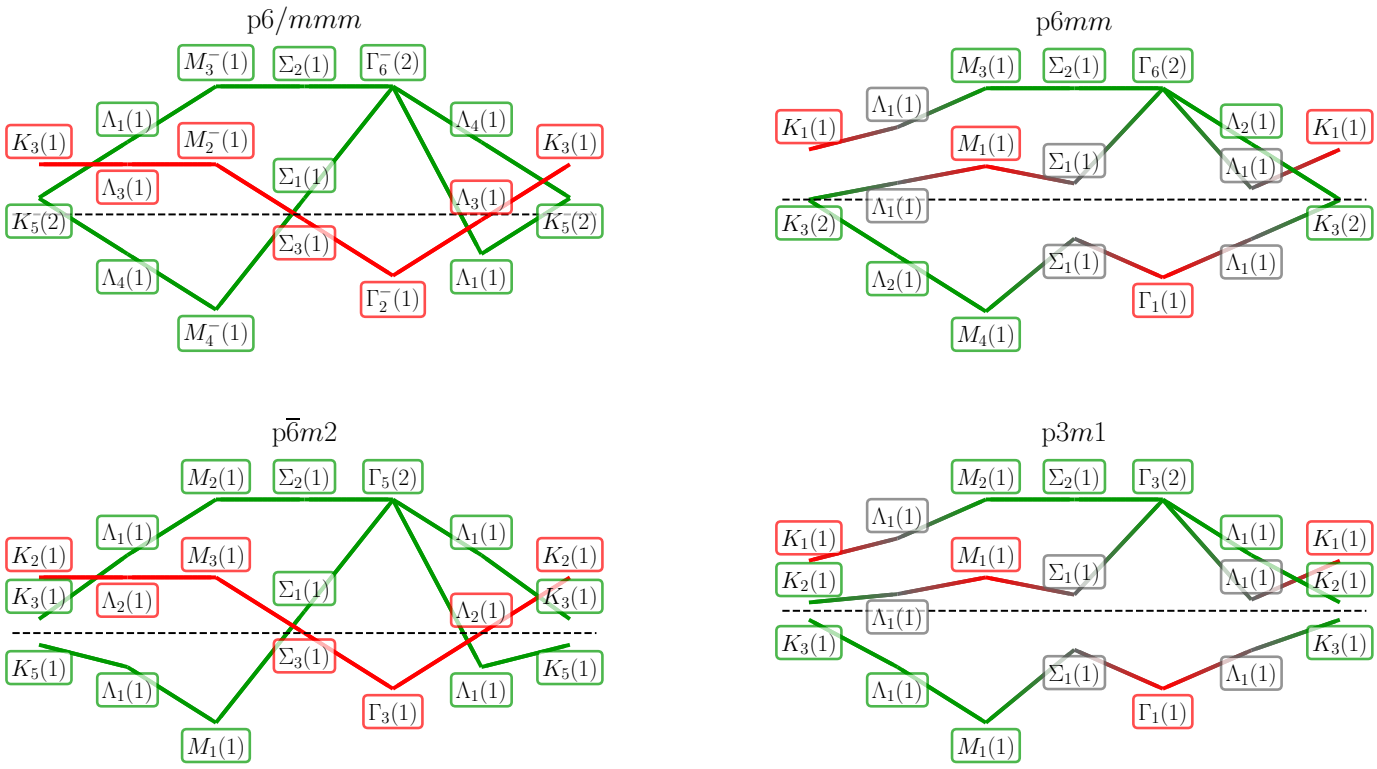

Figure 5.4.1.: Graph-symmetry analysis and irreps of the band structure of the spinless model. Red, green and grayish colors denote in-plane-, p_z- and mixed-orbital character, respectively. The dashed black line indicates the position of the Fermi level for a filling of two electrons.

non-trivial topology in terms of real-space obstruction: as SOC is not considered and time-reversal symmetry is preserved, the system is $\mathbb{Z}_2$-trivial. Therefore, its valence bands are induced by a local representation, the corresponding irreps belong to an EBR. However, it is not an EBR of the A_1 representation on Wyckoff position $1a$ given in Tab. 5.4.2 [4]. Therefore, its Wannier function cannot be located on the atomic $1a$ position indicating this phase as an obstructed-atomic limit. It is an EBR induced by the A_1 representation on WP B=$1c$(A=$1b$) as given in Tab 5.4.3. The localization is driven by the global sign of λ_{ϕ_v}, which promotes either a $K_3(p_-)$ or a $K_2(p_+)$ valence band irrep. Hence, strong vertical reflection symmetry-breaking localizes not only the Bloch wave function at the valley momenta on one of the honeycomb sites (see also Sec. 3.3), it induces in combination with the horizontal reflection symmetry breaking a real-space obstruction: the valence band Wannier function is displaced from the atomic site. The real-space obstruction and the consequences to the electric polarization will be discussed in Secs. 5.5 and 5.7.

[4]For completeness, the valence band is not an EBR of any local representations on Wyckoff position $1a$ of layer group p3m1.

LG	p3m1				p$\bar{6}m$2	
WP	1b		1c		1b	1c
Rep.	A_1	$\overline{E}_1$	A_1	$\overline{E}_1$	$\overline{E}_2$	$\overline{E}_2$
Γ	$\Gamma_1(1)$	$\overline{\Gamma}_6(2)$	$\Gamma_1(1)$	$\overline{\Gamma}_6(2)$	$\overline{\Gamma}_8(2)$	$\overline{\Gamma}_8(2)$
K	$K_2(1)$	$\overline{K}_4(1) \oplus \overline{K}_6(1)$	$K_3(1)$	$\overline{K}_4(1) \oplus \overline{K}_5(1)$	$\overline{K}_8(1) \oplus \overline{K}_{11}(1)$	$\overline{K}_7(1) \oplus \overline{K}_{10}(1)$
M	$M_1(1)$	$\overline{M}_3\overline{M}_4(2)$	$M_1(1)$	$\overline{M}_3\overline{M}_4(2)$	$\overline{M}_5(2)$	$\overline{M}_5(2)$
Σ	$\Sigma_1(1)$	$\overline{\Sigma}_3(1) \oplus \overline{\Sigma}_4(1)$	$\Sigma_1(1)$	$\overline{\Sigma}_3(1) \oplus \overline{\Sigma}_4(1)$	$\overline{\Sigma}_5(2)$	$\overline{\Sigma}_5(2)$
Λ	$\Lambda_1(1)$	$2\,\overline{\Lambda}_2(1)$	$\Lambda_1(1)$	$2\,\overline{\Lambda}_2(1)$	$\overline{\Lambda}_3(1) \oplus \overline{\Lambda}_4(1)$	$\overline{\Lambda}_3(1) \oplus \overline{\Lambda}_4(1)$

Table 5.4.3.: Selected EBRs of representations located on the Wyckoff positions A=1b and B=1c of LGs p3m1 and p$\bar{6}m$2.

We will turn now to the discussion of the band representations of the insulating phases of the spin-full model. As SOC promotes isolated bands of Kramer's pairs, a flattened graph-analysis is shown in Fig 5.4.2. In the presence of symmetry-breaking terms, the spin doublets can split at the non-TRIMs, which is indicated by the direct sum of two 1D irreps. Further, as discussed earlier, a clear assignment of in-plane and out-of plane bands as in the spinless case is impossible. Starting with the inversion symmetric layer group p6/mmm, the bands are Kramers-degenerate in the whole BZ and the p_r-p_z-derived valence band is an EBR of the $\overline{E}_{1u}$ representation on WP 1a as given in Tab 5.4.2. Hence, the SOC insulator is an atomic limit. In agreement with the discussion on the spinless model, the p3m1-symmetric graph-analysis with $j_z = (-\frac{1}{2}, -\frac{3}{2})$ states in valence at K indicates the lowest band as an EBR of the $\overline{E}_1$ representation on WP 1b, which confirms the real-space obstruction.

The band representation analysis can not only unveil the position of the Wannier centers, but allows also the determination of the $\mathbb{Z}_2$-invariant. This bases on the criterion whether the valence band is an EBR, i.e., if it has a Wannier representation at all [44–47]. However, in low-symmetric systems, this can result in false-negatives (false-trivials) as we will discuss for p6mm: it can host $\mathbb{Z}_2$-non-trivial valence bands, if horizontal reflection symmetry-breaking dominates over SOC. The topological phase transition between the SOC insulator and the $\not{m}_h$ QSHI involves the exchange of $\overline{\Sigma}_4(1)$ and $\overline{\Lambda}_4(1)$ irreps at the p_z-p_r-type nodal line. However, the irreps at the high-symmetry momenta (see Fig. 5.4.2) Γ, M and K, relevant for the band representation classification, are identical in both topological phases. For weak $\not{m}_h$-breaking, the bands are adiabatically connected to the p6/mmm-symmetric phase, i.e., the $\nu = 0$ SOC insulator with a valence band $\overline{E}_1$ EBR on WP 1a (see Tab. 5.4.2). Therefore, the symmetry analysis of the bands of the $\not{m}_h$ QSHI results in a false-trivial $\mathbb{Z}_2$-classification.

In p$\bar{6}m$2, the valence bands of the $\not{m}_v$ QSHI (shown in Fig. 5.4.2) are not identical to an EBR of WP 1a (c.f. Tab. 5.4.2). The bands are also not induced by EBRs located

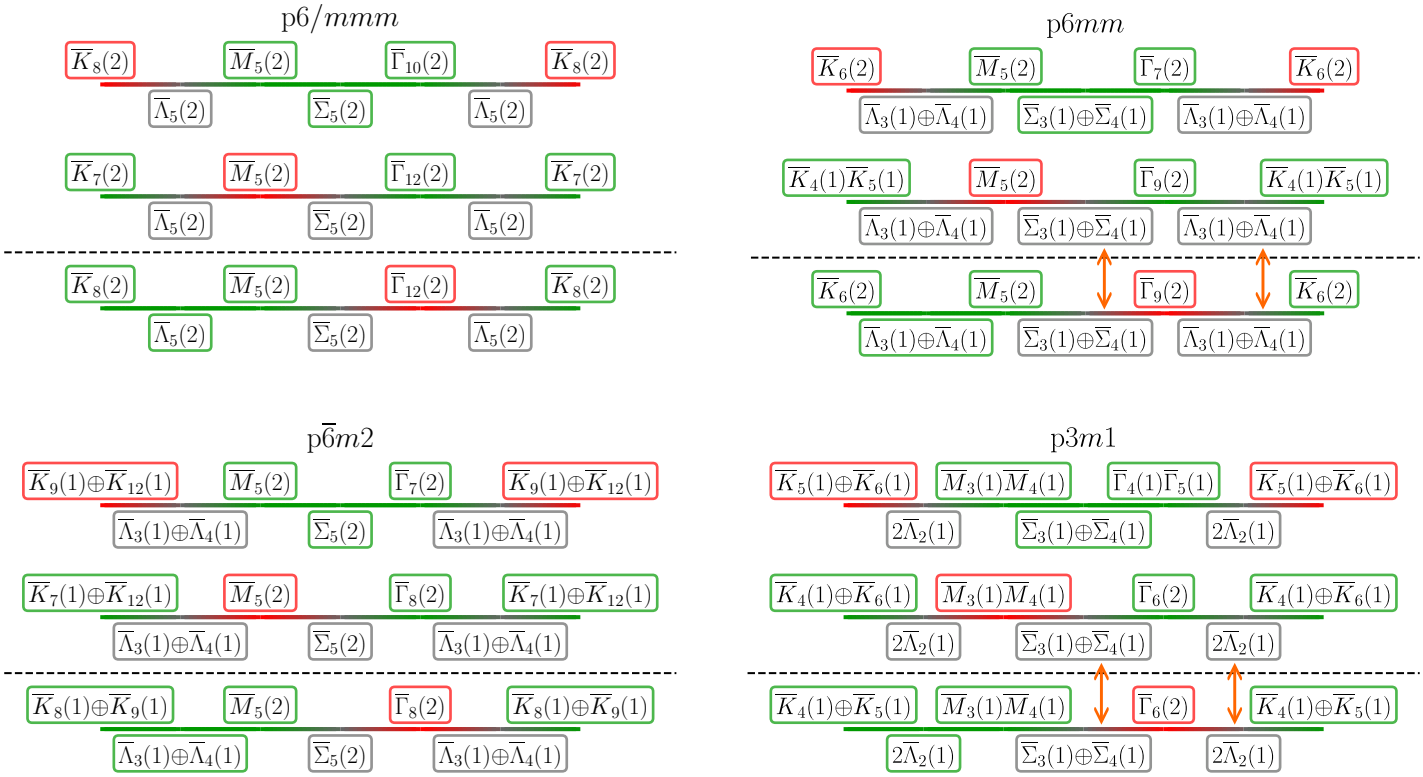

Figure 5.4.2.: Flattened graph-symmetry analysis and irreps of the band structure of the spin-full model. Red, green and grayish colors denote predominantly in-plane-, p_z- and mixed-orbital character, respectively. However, an unambiguous orbital assignment is impossible, as SOC mixes the in-plane and out-of plane orbital degrees of freedom (see text). The dashed black line indicates the position of the Fermi level for a filling of two electrons. The graphs for layer groups p$\bar{6}m2$ and p3$m1$ illustrate the model where $\hat{H}^{\phi_v}$ dominates over $\hat{H}^{\mathrm{SOC}}$ with $j_z = (-\frac{1}{2}, -\frac{3}{2})$ states in valence at K. The orange arrows indicate the exchange of identical irreps at the gap-reopening at the p_z-p_r-type nodal ring driven by the competition of $\hat{H}^{\mathrm{SOC}}$ and $\hat{H}^{\phi_h}$.

on the A/B sublattice sites at WPs 1b and 1c which have the desired $\overline{\Gamma}_8$ irrep (c.f. Tab. 5.4.3). For this layer group, the graph-analysis indicates correctly the non-trivial $\mathbb{Z}_2$-invariant. If $\hat{H}^{\mathrm{SOC}}$ dominates over $\hat{H}^{\lambda_{\phi_v}}$ at the valley momenta, the valence bands with $j_z = (-\frac{1}{2}, \frac{1}{2})$ transform as the irreps $\overline{K}_9$ and $\overline{K}_{12}$ and the lowest band is an EBR of $\overline{E}_2$ on WP 1a, the system is in the SOC insulator phase.

The aforementioned results apply also to LG p3$m1$, where all four topologically distinct phases can be realized, depending on the competition of SOC and symmetry-breaking. Owed to the insensitivity of the irreps to the gapping at the nodal ring, the $\mathbb{Z}_2$-invariant cannot be determined. However, the real-space localization in an *a priori*

Phase	Layer Group	ν	SOC vs $\not\sigma_h$	SOC vs $\not\sigma_v$	irreps Γ	irreps K	$\mathbf{P} = (P_1, P_2)$	Q_{12}
SOC insulator	p6/mmm	0	$\lambda_{\text{SOC}} \gg \lambda_{\not\sigma_h}$	$\lambda_{\text{SOC}} \gg \lambda_{\not\sigma_v}$	$\overline{\Gamma}_{12}(2)$	$\overline{K}_8(2)$	$(0,0)$ mod 2	0 mod 1
$\not\sigma_h$ QSHI	p6mm	1	$\lambda_{\text{SOC}} \ll \lambda_{\not\sigma_h}$	$\lambda_{\text{SOC}} \gg \lambda_{\not\sigma_v}$	$\overline{\Gamma}_9(2)$	$\overline{K}_6(2)$	-	-
$\not\sigma_v$ QSHI	p$\bar{6}m2$	1	$\lambda_{\text{SOC}} \gg \lambda_{\not\sigma_h}$	$\lambda_{\text{SOC}} \ll \lambda_{\not\sigma_v}$	$\overline{\Gamma}_8(2)$	$\overline{K}_8(1) \oplus \overline{K}_9(1)$	-	-
HOTI	p3$m1$	0	$\lambda_{\text{SOC}} \ll \lambda_{\not\sigma_h}$	$\lambda_{\text{SOC}} \ll \lambda_{\not\sigma_v}$	$\overline{\Gamma}_6(2)$	$\overline{K}_4(1) \oplus \overline{K}_5(1)$	$(-\frac{2}{3}, -\frac{2}{3})$ mod 2	$\frac{2}{3}$ mod 1

Table 5.4.4.: Classification of the four insulating phases in terms of their valence band irreps and topological properties. The indicated layer group is the highest symmetry group that satisfies the inequalities in columns four and five. The last two columns denote the electronic dipole and quadrupole moment, which is only well-defined for $\nu = 0$ phases. The corresponding C_3 eigenvalues can be found in Tab. 5.1.2. Reprinted table has been taken and adopted from supplemental material with permission from Eck, P. *et al.* "Recipe for higher order topology on the triangular lattice". *Phys. Rev. B* **107,** 115130 (2023). © 2023 by the American Physical Society.

identified $\nu = 0$ insulator can be classified. This is summarized in Tab. 5.4.4, which relates the irreps to the topological phases and the electronic polarization. This will be the topic of the next section.

To conclude, the thorough graph theoretical analysis has unveiled the manifestation of real-space symmetries in the electronic band structure properties. This includes symmetry driven degeneracies and band splittings as well as real-space obstruction. However, symmetry indicators fail to predict the $\mathbb{Z}_2$-topology flawlessly in non-inversion symmetric layer groups, if gap-reopenings occur at non-high-symmetry momenta. This makes the identification of the indenene-like $\not\sigma_h$-QSHI in high-throughput studies challenging and the Wilson-loop calculation becomes unavoidable (see also Sec. 5.2).

5.5. Symmetry-Breaking Driven Electric Polarization

The analysis presented in the preceding sections has unveiled the presence of two $\mathbb{Z}_2$-trivial insulating phases, which are topologically distinct on the level of the localization of the occupied bands. Here we will extend this discussion to the electric polarization arising from the displacement of the electron's charge from the lattice positions by a symmetry indicator analysis. As will be derived in the following, reflection symmetry breaking is the fundamental driving force of the electric polarization. The C_3-symmetric trigonal Bravais lattice symmetry will guarantee for well-defined quantized electric momenta.

Before turning to the symmetry indicator analysis, let us briefly recall the implications of vertical-reflection symmetry breaking on the Wyckoff positions and on the valley momenta as discussed in Sec. 2.4.2.2: the layer group is C_6-symmetric in the presence of both in-plane reflections σ_v and σ_d. Further, the only Wyckoff position with multiplicity one is $1a$. Hence, an isolated $\mathbb{Z}_2$-trivial spinless valence band of any 2D hexagonal system must be localized on $1a$. However, upon releasing σ_v-reflection symmetry, which maps the A and B positions onto each other and protects their multiplicity of two, A and B become inequivalent Wyckoff positions with multiplicity one. As a result, the Wannier center of an isolated band can be either centered at $1a$, A or B. In addition, the point group of the valley momenta is rendered abelian, former 2D representations split-up into chiral 1D representations. They must be irreps of an EBR centered on the three Wyckoff positions with multiplicity one. Therefore, there is a direct relation between reflection symmetry breaking, momentum-dependent wave function chirality and real-space localization.

This notion of real-space lattice and momentum-space wave function symmetry analysis induced charge localization has lead to the concept of symmetry indicators. As shown by Benalcazar and others [147, 154–158], the wave function symmetries of occupied $\mathbb{Z}_2$-trivial bands at the high-symmetry momenta in C_n-symmetric systems are sufficient to determine the electric bulk multipoles. In general, the dipole moment induced by the displacement of the electron's charge from the atomic lattice

$$\mathbf{P} = p_i \mathbf{a}_i, \tag{5.6}$$

can be expressed in terms of the Bravais vectors $\mathbf{a}_i$ and must obey the C_n-symmetry

$$C_n^i \mathbf{P} = \mathbf{P} + \mathbf{R}. \tag{5.7}$$

In particular this is the only defining symmetry relation of Wyckoff positions with multiplicity one in C_n-symmetric systems. For trigonal systems this relates to the aforementioned $1a$, A and B positions and the polarization forms hence a $\mathbb{Z}_3$-index [147]. Further it can be shown, that this invariant is obtained from symmetry characters of the occupied bands at high symmetry momenta by counting the appearance of the rotational eigenvalues. The eigenvalues of spinless systems (Altland-Zirnbauer class AI [23]) are defined as [147, 158]

$$\Pi_p^{(n)} = e^{2\pi i(p-1)/n}, \quad \text{for } p = 1, 2, ...n. \tag{5.8}$$

For time-reversal symmetric spin-full systems (class AII) they are given by

$$\Pi_p^{(n)} = e^{2\pi i(p-1)/n} e^{\pi i/n}, \quad \text{for } p = 1, 2, ...n. \tag{5.9}$$

Integer topological rotational invariants for C_3-symmetric systems can be defined as the difference in the total number of the rotational eigenvalue $\Pi_p^{(n)}$ at $K = (1/3, 1/3)$[5]

[5]Caution, for consistency in this thesis, the Bravais and reciprocal lattice vector convention given in Sec. 4.1 is used. Most of the references use instead the following convention: $\mathbf{a}_1 = (1, 0)$, $\mathbf{a}_2 = (1/2, \sqrt{3}/2)$ and $\mathbf{b}_1 = 2\pi(1, -1/\sqrt{3})$, $\mathbf{b}_2 = (0, 4\pi/\sqrt{3})$ and consider K=$(2/3, 1/3)$, which corresponds to K' in the here presented discussion.

and Γ

$$\left[K_p^n\right] = \#K_p^n - \#\Gamma_p^n. \tag{5.10}$$

The components of the electric polarization for the atomic lattice site on $1a$ read for class AI [4, 147]

$$p_1 = -p_2 = \frac{2e}{3}\left([K_3^3] - [K_2^3]\right) \bmod 2e = \frac{2e}{3}\left([\#e^{-i2\pi/3}] - [\#e^{i2\pi/3}]\right) \bmod 2e, \tag{5.11}$$

and for class AII

$$p_1 = -p_2 = \frac{2e}{3}\left([K_3^3] - [K_1^3]\right) \bmod 2e = \frac{2e}{3}\left([\#e^{-i\pi/3}] - [\#e^{i\pi/3}]\right) \bmod 2e. \tag{5.12}$$

Applying this criterion to the SOC insulator phase with $j_z = (-1/2, 1/2)$ valence states at Γ and K [see again Tabs. 5.1.2 and 5.4.4 and Figs. 5.1.1 (b) and 5.3.1] yields $\mathbf{P} = \mathbf{0}$. For the HOTI, the total angular momentum at K is instead $j_z = (-1/2, -3/2)$ and the bulk polarization is $\mathbf{P} = 2e(1/3, 2/3)$. This is consistent with our analysis in Sec. 5.4, where the valence band localizes at B$= (2/3, 1/3)$, as the dipole moment is the vector pointing from the displaced electronic charge to the atomic cation ($\mathbf{d} = -\mathrm{B} \equiv \mathrm{A}$). Of course, this holds also in the spinless case, the valence bands with $m = -1$ at K localize at B and induce $\mathbf{P} = 2e(1/3, 2/3)$.

Further the in-plane quadrupole moment Q_{12} of an isolated band can be calculated from symmetry indicators, which is given for class AI by [158]

$$Q_{12} = \frac{2e}{3}[K_1^3] \bmod e, \tag{5.13}$$

and for class AII by

$$Q_{12} = \frac{2e}{3}[K_2^3] \bmod e. \tag{5.14}$$

Hence the HOTI phase has quadrupole moment of $Q_{12} = \frac{2}{3}e$ for $p_\pm$-type valence bands at K. It should be noted, that the terminology *quadrupole* moment refers to the second moment of the electric charge density expressed in terms of the Bravais vectors. However in C_3-symmetric systems, this is reflected by a *hexapole* pattern with alternating charge density on the A and B sites [see for instance Fig. 3.2.1 (a)]. Further a finite dipole moment violates necessarily C_2- and σ_v-symmetry, hence the dipole moment must vanish in C_6-symmetric geometries [147].

To conclude, the symmetry analysis of the valence bands of the $\mathbb{Z}_2$-trivial phases has unveiled their fundamental topological distinction. It is encoded in the real-space localization, which can promote quantized electric multipoles. We will discuss the bulk-boundary correspondence promoted surface states for the minimal model in Secs. 5.6 and 5.7 and for an *ab initio* simulated triangular adsorbate in Sec. 6.3. As introduced in Sec 3.3 and shown here, the relevant key ingredients for real-space obstruction on the triangular lattice are vertical reflection symmetry breaking, which induces chiral wave functions at the valley momenta.

5.6. Finite-Size Geometries and Edge States

We will turn now to the analysis of 1D finite-size geometries, where the $\nu = 1$-phases are expected to host spin-momentum-locked helical edge states. Further, we will also discuss the impact of the bulk polarization for the $\mathbb{Z}_2$-trivial phases.

Fig. 5.6.1 (a) shows the two canonical edge-terminations and the conventional unit-cell of the triangular lattice. The sites at the edges are arranged in a flat-geometry for terminations parallel to a primitive lattice vector. Thus we dub this termination the *flat edge*, which has the bulk mirror reflection plane σ_d normal to the edge. However, if the edge is defined by a vector through the diagonal of the unit cell, the edge is terminated by two different triangular lattice sites which gives rise to a *zigzag edge*. As illustrated by the orange and green empty circles on the A and B voids, respectively, H^{ϕ_v} renders opposed edges of the flat termination inequivalent. This is different for the zigzag edge, where the A and B sites contribute equally. Opposed zigzag edges can be mapped onto each other by a σ_d mirror or a glide-mirror operation, depending on the slab thickness. In addition, the red arrow in Fig. 5.6.1 (a) illustrates the electronic charge displacement arising from an obstructed Wannier center on the B site, which promotes an electric dipole moment normal to the flat and parallel to the zigzag edge. Further, the sketched A/B bipartite honeycomb lattice denotes the edge orientation of Kane-Mele-type systems. The honeycomb zigzag edge corresponds to the flat triangular edge, while the arm-chair termination has the same Bravais lattice orientation as the triangular zigzag edge.

Focusing on momentum-space, the reduced dimensionality of 1D slab geometries implies the projection of the 2D high-symmetry points of the bulk onto the corresponding 1D BZ. This is shown in Fig. 5.6.1 (b) for the primitive, conventional, flat-edge and zigzag-edge geometry. For the flat edge, the valley momenta are projected onto 2/3 of $\overline{\Gamma}$-$\overline{X}$ and M is projected onto $\overline{X}$ and $\overline{\Gamma}$. Whereas for the zigzag edge, K and M are projected onto $\overline{\Gamma}$ and $\overline{Y}$, respectively. The presence of σ_d [see also dashed green lines in Fig. 2.4.2 (b)] guarantees, that pairs of mirror symmetry-protected bulk momenta are backfolded onto the same momenta of the BZ of the zigzag edge, hence all bands must come in two-fold degenerate bands. For the flat edge, this holds if σ_v is preserved.

The band structures of representatives of the four insulating phases are shown in Fig. 5.6.2 for the flat- and zigzag-termination in the top and bottom row, respectively. The bands of the flat geometry are non-degenerate, owed to a small H^{ϕ_v}-interaction, while the zigzag edge has σ_d-protected two-fold degenerate bands. Both canonical terminations of the SOC insulator (I) have insulating edges. This is different for the real-space obstructed HOTI (IV), where the bulk dipole moment [see red arrow in Fig 5.6.2 (a)] is parallel to the zigzag and normal to the flat edge. The former gives rise to insulating edge states, while the latter favors metallic edges. The bulk dipole moment arising from the valence band WCC localized at the B-site promotes negative charge at the B- and positive charge at the A-terminated edge, which is

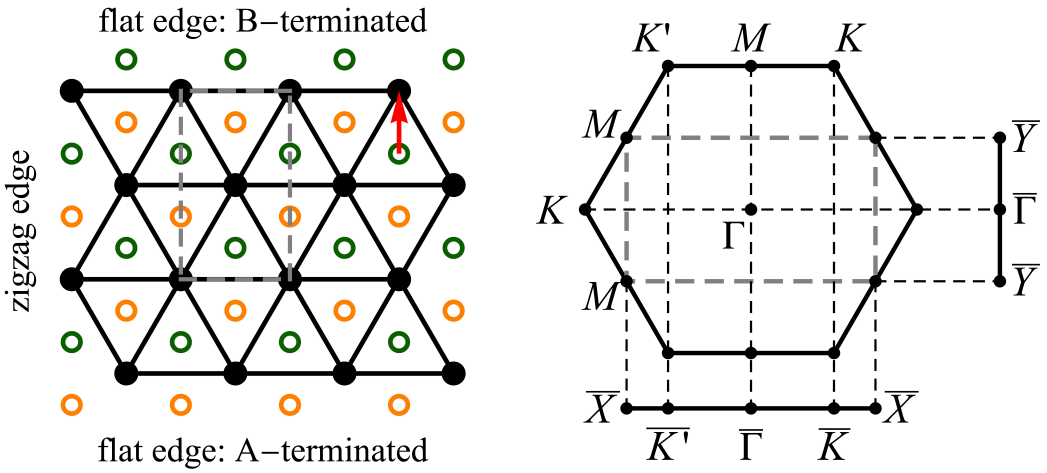

(a) (b)

Figure 5.6.1.: (a) Conventional unit cell (gray dashed lines) and fundamental edge geometries of the triangular lattice. The empty orange and green circles represent the A and B sites, respectively, which render opposed flat edges inequivalent. The red arrow indicates the displacement vector of the electronic charge for the real-space obstructed phase with the valence band Wannier center on the B site. (b) 2D hexagonal and conventional (gray dashed lines) BZ and back-folding of the high-symmetry momenta onto the 1D BZs of the slab-geometries. Reprinted and adopted figures with permission from Eck, P. *et al.* "Real-space obstruction in quantum spin Hall insulators". *Physical Review B* **106,** 195143 (2022). © 2022 by the American Physical Society.

reflected in the B-type valence edge-states. However, the degenerate (quadratic, in the limit of vanishing SOC) touching point at $\overline{\Gamma}$ arising from spatially separated edge states is not protected by a non-trivial $\mathbb{Z}_2$-invariant and can be gapped by a staggered potential discriminating A/B terminations. This is indeed the case for realistic edge potentials and will be discussed in Secs. 6.2.5 and 6.3.3. Instead the $\nu = 1$ phases possess topologically protected helical edge states on both fundamental terminations. For the zigzag edge, the band structures of the $\not{\phi}_h$ QSHI (II) and $\not{\phi}_v$ QSHI (III) are qualitatively identical with four-fold-degenerate edge-states at $\overline{\Gamma}$. The flat termination promotes instead only for the $\not{\phi}_h$ QSHI an edge state-crossing at $\overline{\Gamma}$, the $\not{\phi}_v$ QSHI has two linear crossings in the proximity of the projected valley momenta. Hence, both non-trivial phases posses qualitatively different surface states for the flat termination compared to the Kane-Mele model (see Fig. A.1.2). The corresponding zigzag edge states of the honeycomb traverse the Fermi level at the BZ boundary.

For completeness, the spin and OAM polarization of the flat and the zigzag terminations are shown in the appendix in Figs. A.7.1 and A.7.2. The interplay of OAM induced by symmetry breaking and SOC results in spin and OAM canting of the edge

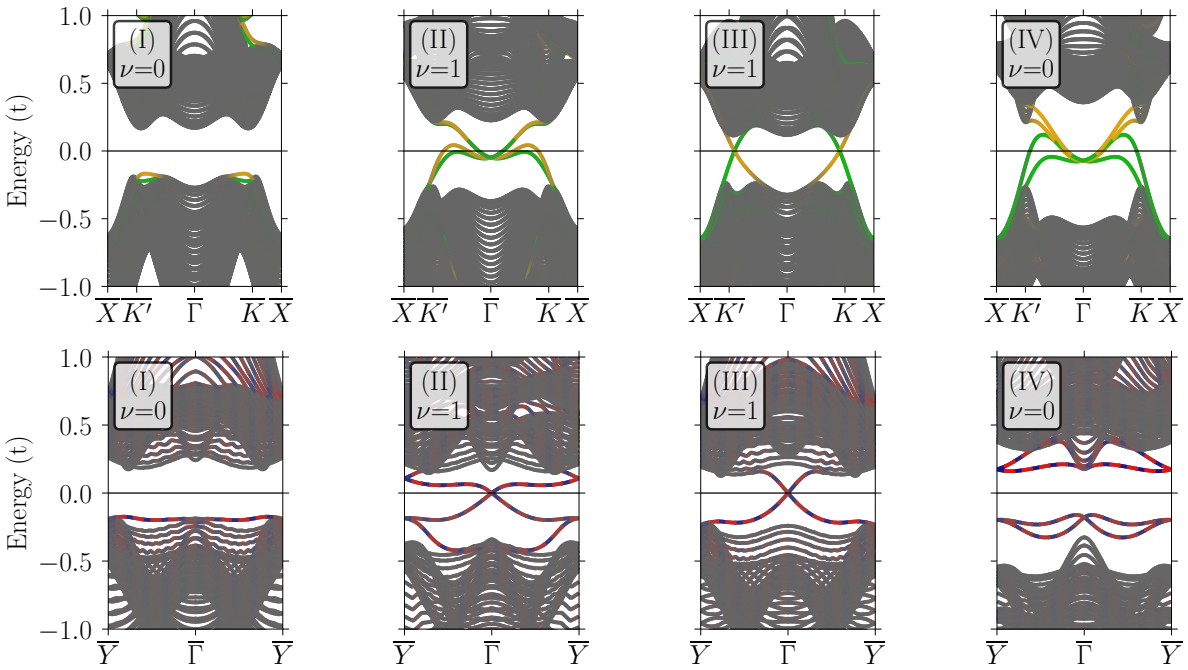

Figure 5.6.2.: Band structures and edge localization of finite size calculations of representatives of the phases illustrated in Fig. 5.1.1. The flat and the zigzag termination is shown in the top and bottom row, respectively, for ribbons of size of 30 conventional UCs. The color code denotes the edge localization with orange and green colors for the A- and B-terminated edges, respectively. The dashed red-blue bands show the alternating projection onto the Kramers-degenerate states of the zigzag geometry. To enlarge the bulk gap, the scaling factors of H^{SOC}, H^{ϕ_h} and H^{ϕ_v} have been chosen twice as large as in Tab. 5.1.1.

states with a total angular momentum perpendicular to the direction of propagation. For the flat edge, the total angular momentum vector is located in the yz-plane, while the symmetries of the zigzag edge confine the polarization to be along x.

5.7. Symmetry-Breaking stabilized HOTI phase

The analysis in the two preceding sections has highlighted the topological distinction of the tow $\mathbb{Z}_2$-trivial insulating phases. They can be discriminated on the level of the bulk polarization. Further, their edge states are insulating or can be gapped by introducing an appropriate edge potential. Here we will show for layer group p3m1, that a strong vertical and horizontal reflection symmetry breaking can stabilize a second-order topological insulator: a system with insulating 1D edges and metallic, i.e., fractionally-filled, 0D in-gap corner states. However, a finite bulk dipole moment can promote edge

charge, which has profound implications, as will be discussed below. These results have been obtained in collaboration with Yuan Fang[6] and Jennifer Cano[7]. This led to a design principle for a HOTI phase in triangular adsorbates which will be presented in Sec. 6.3 and has been published in Ref. [4].

An elegant approach towards higher-order topology in solid state Physics is the idea of *quantized electric multipole insulators*: their bulk polarization stabilizes topologically protected corner and hinge states, as introduced by Benalcazar and coworkers [65, 66]. The total corner charge is called *filling anomaly* η, i.e., the charge difference of the finite system from being insulating [4, 147, 154, 156]. This may be regarded as the electron filling of the corner states. For a C_n symmetric 0D flake it obeys

$$\eta = (\#\text{ions} - \#\text{electrons}) \mod n. \tag{5.15}$$

It is a consequence of the bulk quadrupole moment Q_{12}, which is promoted by the real-space obstruction

$$\eta = Q_{12} \cdot \#\text{sectors}. \tag{5.16}$$

Here we imagine to divide the finite size slab into sectors instead of corners, which accounts for a subtle but important detail [147, 159]: generic 0D geometries can be created from C_n-symmetric bulk unit cells with finite bulk quadrupole moment. However corner charges are only well-defined in sectors which comply with the bulk rotational symmetry. To give a concrete example, for a C_3-symmetric HOTI phase, each corner of a triangular flake forms a sector. Instead for a hexagonal flake, the C_3 symmetry of the bulk Hamiltonian reduces the symmetry of the flake to C_3. Hence, it can only be divided in three equivalent sectors and each sector must comprise two corners.

In the following, we will discuss the corner charge in the aforementioned flake geometries. Figure 5.7.1 shows the spectrum and the localization of the corner states of the HOTI with zigzag termination. In the triangular geometry [panel (a)], the in-gap states are six-fold degenerate with a total filling of two electrons. The filling anomaly $\eta = 2$ is in line with $Q_{12} = \frac{2}{3}e$ obtained in previous section. The exponential localization of the low-energy corner states is shown in Fig. 5.7.2 (a). The hexagonal flake in (b) exhibits also six-fold degenerate corner states with a total filling of two electrons. These states localize on every second corner, which reflects the C_3-symmetry of the bulk Hamiltonian. As shown in panel (b), the corners are constituted by two triangular sites which give rise to a flat-edge geometry [see again Fig 5.6.1 (a)]. Hence the corners are either terminated by an A or B triangle [see also Fig. 5.6.1 (a)]. These systems show all characteristics associated to the bulk-boundary correspondence of a second-order topological insulator: 0D metallic in-gap corner states located in a global gap of the 2D bulk and 1D edges.

[6]Stonybrook university, New York, USA.

[7]Stonybrook university, New York, USA and Center for Computational Quantum Physics, Flatiron Institute, New York, USA.

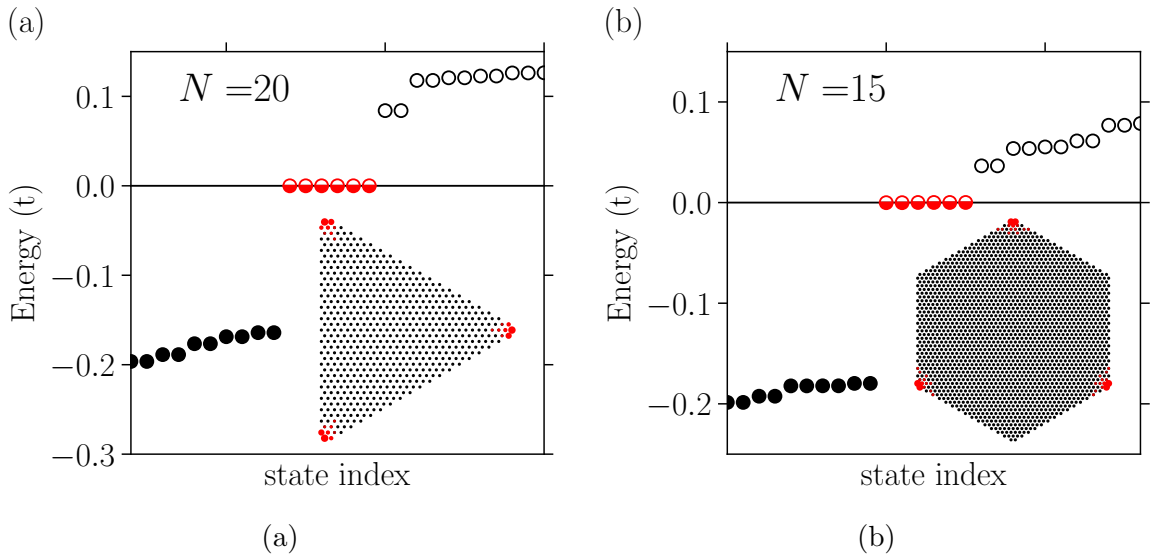

Figure 5.7.1.: Spectrum and charge localization of zig-zag terminated triangular (a) and hexagonal (b) flakes of the HOTI phase with an edge length of N-conventional unit cells. Black empty and filled circles indicate conduction and valence states, respectively. The half-filled red circles denote the six-fold degenerate metallic corner states with a total occupation of two electrons at neutral filling. The inset shows the real-space charge localization of the corner states shown by the size of the red points. To increase the bulk gap, λ_{ϕ_h} has been chosen twice as large as in Tab. 5.1.1.

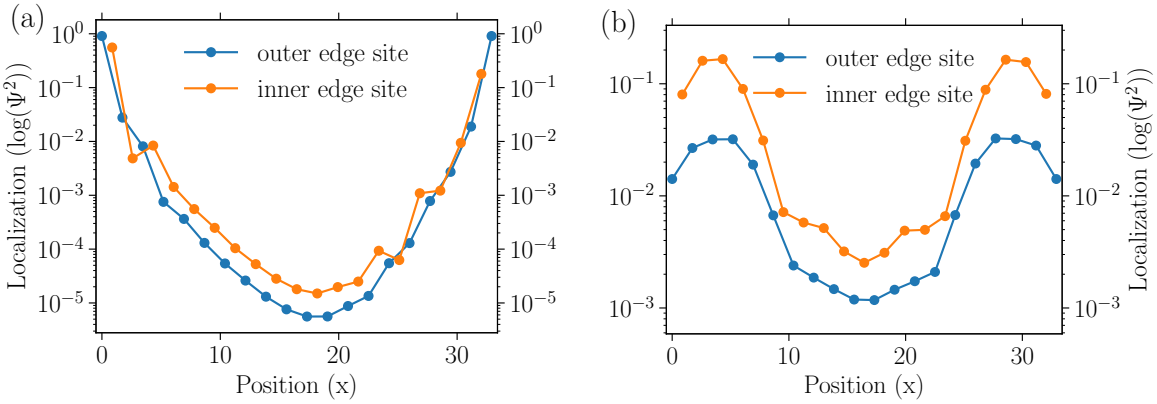

Figure 5.7.2.: Edge localization of the low-energy states of the HOTI (a) and SOC insulator (b) of the red marked states in Figs. 5.7.1 (a) and 5.7.3 (a), respectively. The blue and orange plots illustrate the squared wave function amplitude on the outer and inner zigzag edge site on logarithmic scale .

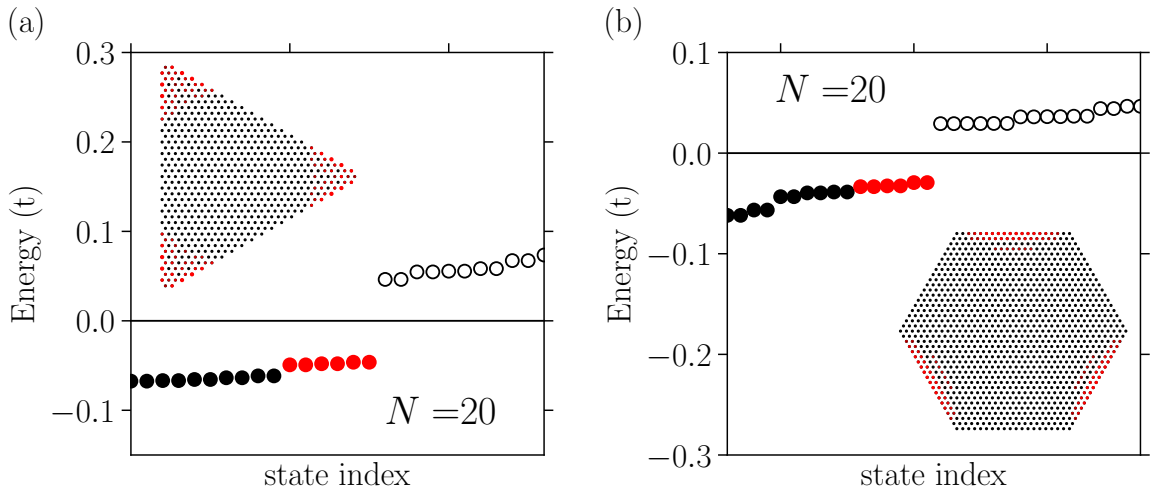

Figure 5.7.3.: Spectrum and charge localization of zig-zag terminated triangular (a) and flat terminated hexagonal (b) flakes of the SOC insulator with an edge length of N-conventional unit cells. Empty and filled circles denote conduction and valence states, respectively, at neutral filling. The inset shows the real-space charge localization of the red-marked valence states.

For comparison, Fig. 5.7.3 illustrates the spectrum and low-energy charge localization in the $\mathbb{Z}_2$-trivial SOC insulator phase for a triangular flake with zigzag- (a) and a hexagonal flake with flat-termination (b). In both cases, the spectrum is insulating. The first six valence states show a weak localization at the triangular corners and at every second hexagon edge, a consequence of a small $\hat{H}^{\not\sigma_v}$-interaction. However, the low-energy states are not exponentially localized at the triangular corners. Instead they favor the inner edge site and possess sizable weights along the edges as shown in Fig. 5.7.2 (b). This and the insulating slab geometries are in perfect agreement with the expected behavior for a trivial atomic limit, as it is the case for the SOC insulator.

We will turn now to the HOTI phase with flat-edge termination. As discussed in Secs 5.5 and 5.6, the bulk dipole moment normal to the edges favors metallic surface states. As the edge states are not protected by a non-trivial $\mathbb{Z}_2$-index they can be gapped by a local potential with opposite sign at the A and B termination. Starting with a triangular flake, as shown in Fig. 5.7.4, all three edges are either A- or B-type. The total edge charge is given by the sum over the edge charge. It is related the dipole moment normal to the edge $p_{\text{normal}} = \mathbf{P} \cdot \hat{e}_{\text{normal}}$ and reads for a triangular flake with edge length of N conventional unit cells [91, 93, 147, 155, 156, 158]:

$$Q_{\text{edge}} = p_{\text{normal}} \cdot \#\text{edge unit cells} \tag{5.17}$$

$$= \text{sgn}(p_{\text{normal}}) \cdot \frac{2e}{3} \cdot 3(N-1) \tag{5.18}$$

$$= \text{sgn}(p_{\text{normal}}) \cdot 2(N-1)e. \tag{5.19}$$

Fractionally in-gap states can be stabilized by accounting for the edge charge as shown

in Fig. 5.7.4 (a). In this calculation, the system is doped by $-Q_{\text{edge}}$ and an edge potential of $9\lambda_{\not\sigma_v} \cdot \text{sgn}(p_{\text{normal}})$ is applied. This results in a filling anomaly of $\eta = 2$ for the edge-charge corrected system. An intrinsic compensation of the edge charge is accomplished in hexagonal geometries, as illustrated in panel (b), where opposed edges have a complementary termination. Further, such a flake has C_{3v} symmetry with three vertical reflection planes normal to the flat edges (see also symmetry discussion in Sec. 5.6). The mirror operation maps neighboring corners onto each other resulting in a twelve-fold degenerate corner state with $\eta = 2$. Again, an edge potential[8] of $9\lambda_{\not\sigma_v} \cdot \text{sgn}(p_{\text{normal}})$ has been applied to open a gap at the energies of the corner states.

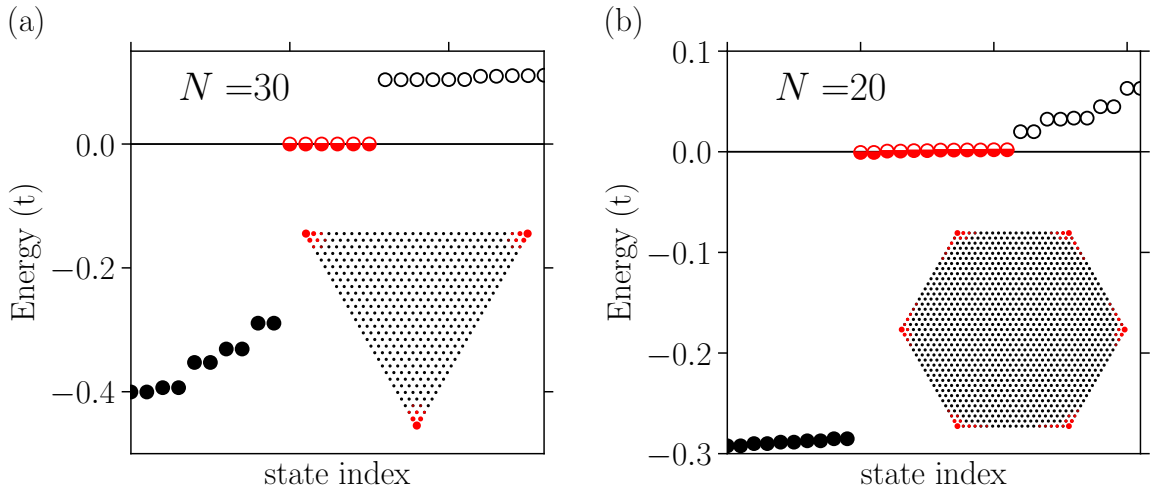

Figure 5.7.4.: Spectrum and charge localization of flat-terminated triangular (a) and hexagonal (b) flakes of the HOTI phase with an edge length of N-conventional unit cells. Black empty and filled circles indicate conduction and valence states, respectively. The half-filled red circles denote the six- (a) and twelve-fold (b) degenerate metallic corner states with a total occupation of two and four electrons, respectively. For the triangular flake, the total occupation has been corrected by the edge charge, the hexagonal flake has neutral filling. The inset shows the real-space charge localization of the corner states. To increase the bulk gap, $\lambda_{\not\sigma_h}$ has been chosen twice as large as in Tab. 5.1.1. A local edge potential of size $9\lambda_{\not\sigma_v}$ has been applied for both geometries to remove the edge states from the corner state energies.

To conclude, the analysis of the finite size geometries unveiled indeed the presence of 0D in-gap states in the real-space obstructed insulating phase of our model. It should be recalled that both mirror symmetry-breaking terms dominate over SOC in the HOTI phase, which necessarily requires layer group p3m1. In agreement with the condition of the filling anomaly in Eq. 5.16, all triangular and hexagonal flakes have $\eta = 2$ with

[8]The alternating A/B termination of neighboring edges is taken into account by $\text{sgn}(p_{\text{normal}})$. The edge charge of both terminations follows the relation $p_{\text{normal}}(\text{A}) = -p_{\text{normal}}(\text{B})$.

a fractional corner charge of $2/3e$ per sector. Considering also the preceding analysis in Secs. 5.4 and 5.5, this phase represents a second-order topological insulator, whose non-trivial topology is encoded in the electric polarization. Importantly, the energy region of the topologically promoted 0D corner states may be *contaminated* by edge states arising from a finite dipole moment. Nevertheless, fractionally corner states can be stabilized by choosing uncharged edge geometries or by edge charge compensation. Further it should be noted, that fractionally filled 0D in-gap corner states are less protected than metallic boundary states of QSHI, which traverse through the bulk gap energies. Therefore they are robust against doping as long as the chemical potential remains in the bulk gap. However, this "weakness" is intrinsic to the dimensionality and the symmetry-promoted fractional-filled 0D corner states in $2D$.

5.8. OAM-Driven Real-Space Obstruction

After having discussed the symmetry-breaking driven electric polarization based on symmetry indicators, this section is devoted to motivate the real-space obstruction from the wave function chirality in the whole BZ. It will serve as a preparatory work to extend the concept of real-space obstruction to the QSHI phases.

For non-obstructed atomic insulators, there must exist a local basis τ_i centered at the atomic sites, which has a positive definite overlap matrix $S_{ij}(\mathbf{k})$ in the whole BZ

$$S_{ij}(\mathbf{k}) = \langle \tau_i | \hat{\mathcal{P}}(\mathbf{k}) | \tau_j \rangle \,, \tag{5.20}$$

with the Bloch wave function of the occupied bands

$$\hat{\mathcal{P}}(\mathbf{k}) = \sum_{n}^{N} |\Psi_{n\mathbf{k}}\rangle \langle \Psi_{n\mathbf{k}}| \,. \tag{5.21}$$

We will argue for the triangular p-shell model, that symmetry-breaking promoted local OAM results in vanishing overlap for projection basis sets on the triangular lattice site. It can be regarded as the microscopic driving force of the real-space obstruction.

The OAM polarization of the valence band of the spinless HOTI model is illustrated in Fig. 5.8.1 (a) (see also Fig. 5.3.1) It reveals a counter-clock-wise winding of its in-plane component around the Γ-point with purely out-of plane polarization at the valley momenta. Hence, one may be tempted to argue that the OAM vector visits all positions of the unit sphere and carries a non-trivial Pontryagin index[9], as it has been observed for non-centrosymmetric Weyl semimetals [150]. In such a case, it would be obvious, that there cannot exist a single local orbital on the atomic site with non-vanishing

[9] This can be excluded from topological arguments and the presence of time-reversal symmetry. A non-trivial winding number would indicate the absence of a Wannier representation at all, indicating a spinless Chern insulator.

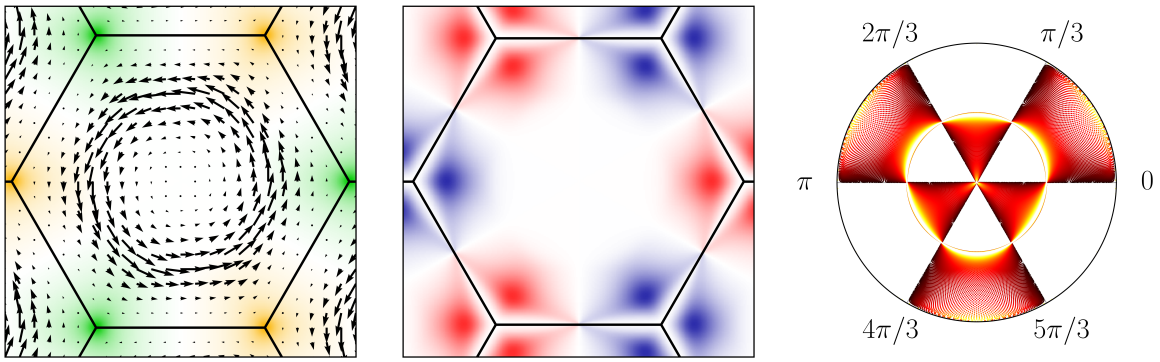

(a) (b) (c)

Figure 5.8.1.: OAM polarization of the valence band in the HOTI phase. (a) in-plane and out-of plane polarization shown by a vector field and color plot, respectively, where green (orange) denotes positive (negative) values. (b) Curvature of the OAM-field (see also Eq. 5.22), where blue (red) indicate positive (negative) values. (c) Polar plot of the OAM-field, where the distance to the origin reflects the spherical polar angle in the interval $[0, \pi]$. The color code visualizes the radial component, bright colors indicate a strong OAM polarization, i.e., OAM eigenstates.

overlaps with all **L**-orientations. To investigate the OAM winding, we calculate the Pontryagin index by integrating over the curvature

$$S = \frac{1}{4\pi} \int_{\mathrm{BZ}} \mathbf{n} \cdot \left[\frac{\partial \mathbf{n}}{\partial x} \times \frac{\partial \mathbf{n}}{\partial y} \right] \mathrm{d}x\mathrm{d}y, \tag{5.22}$$

where $\mathbf{n}$ is the normalized OAM field and the integral is taken over the full BZ. The curvature of the OAM is shown in Fig. 5.8.1 (b) with large values around the valley momenta. However, time-reversal symmetry enforces antisymmetry with respect to $\mathbf{k} \mapsto -\mathbf{k}$ and the Pontryagin index is $S = 0$. The trivial winding can be further understood from the polar plot of the OAM vector field shown in Fig. 5.8.1 (c). It unveils three important qualitative features: (1) the vector visits only half of the unit sphere, (2) has maximum polarization, i.e., it is an OAM eigenstate at the two poles and along a line wiggling around the equator and (3) a vanishing polarization at other momenta. Combining the latter two, namely the presence of a full $l = 1$ OAM eigenbasis set $m = \{-1, 0, 1\}$ with maximum in-plane and out-of plane polarization is a clear indication for the real-space obstruction. Any local orbital choice cannot have finite overlaps with all acquired OAM eigenstates of the Bloch wave function.

To extend this analysis to spinfull models, we will consider in the following the OAM summed over the two valence bands as shown in Fig. 5.8.2[10]. The OAM of the SOC insulator in panel (a) possesses only a weak polarization, as H^{SOC} promotes degenerate

[10] A map plot in the full BZ of the OAM polarization of the valence bands can be found in Fig. A.6.1.

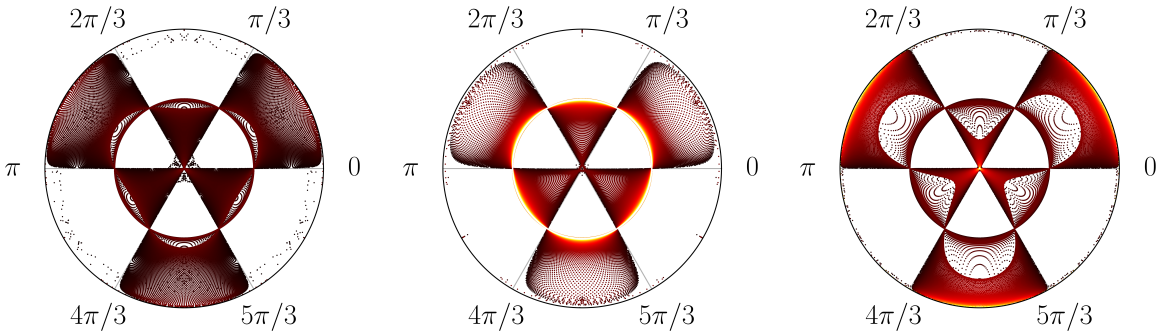

Figure 5.8.2.: Polar plot of the total OAM-field of the valence bands of the SOC insulator (a), the $\not\phi_h$ QSHI (b) and the $\not\phi_v$ QSHI (c). The distance to the origin denotes the spherical polar angle in the interval $[0, \pi]$ and the color code visualizes the radial component, bright colors indicate a strong OAM polarization, i.e., OAM eigenstates. Only the $\not\phi_h$ QSHI and the $\not\phi_v$ QSHI posses OAM eigenstates with out-of and in-plane orientation, respectively.

eigenstates with anti-parallel OAM polarization. This is qualitatively different for the $\not\phi_h$- and $\not\phi_v$-QSHI phases illustrated in panels (b) and (c), respectively. This results for the former in a strong in-plane and for the latter in a dominating out-of plane OAM polarization. Hence the simple obstruction argument derived for the HOTI can not directly applied, as the OAM vector does not visit the poles and the equator for both phases. However, by recalling that the local basis set τ_i must reflect the site-symmetry group (see also Sec. 2.4.2.2), the rotational symmetry around the z-axis of the triangular lattice defines also the OAM quantization axis of the projection basis. Under this consideration, it is evident that the OAM eigenstates in the valence bands of the aforementioned QSHIs enforce vanishing overlaps with basis functions that respect the site-symmetry of the triangular lattice site. Hence this is a first indication of a real-space obstruction for the two QSHI phases.

To conclude, the OAM polarization of the valence bands has been identified as the microscopic origin of real-space obstruction in the triangular p-shell model. This is also suggestive for an extension of real-space obstruction to $\mathbb{Z}_2$-non-trivial bands. Here symmetry indicators do not exist as QSHI phases lack EBRs *per se*.

5.9. Real-Space Obstructed QSHIs

Motivated by the first hints towards real-space obstruction in the two triangular QSHI phases in the previous section, we will construct Wannier basis sets to determine the charge center localization. The local orbital symmetry will be chosen based on

the valence band representations discussed in Sec. 5.4. However the wannierization of a $\mathbb{Z}_2$ non-trivial subspace of bands can be only achieved upon releasing the fundamental protecting symmetry, i.e., time-reversal symmetry. This has been shown by A. Soluyanov and D. Vanderbilt [73] for the Kane-Mele model, which is not real-space obstructed. We will follow their concept to extend the notion of real-space obstruction to QSHI phases.

phase	trial basis	$\mathcal{T}$-symmetric	real-space obstructed	label
SOC insulator	$\|J, J_z\rangle = \|1/2, +1/2\rangle$, $\|J, J_z\rangle = \|1/2, -1/2\rangle$	True	False	$J_{1/2}$
$\not{\sigma}_h$ QSHI	$\|A, \uparrow_x\rangle = \frac{1}{\sqrt{2}}(\|s\rangle + \|p_z\rangle) \otimes \|\uparrow_x\rangle$, $\|B, \downarrow_x\rangle = \frac{1}{\sqrt{2}}(\|s\rangle + \|p_z\rangle) \otimes \|\downarrow_x\rangle$	False	True	AB$\overline{\mathcal{T}}$
$\not{\sigma}_v$ QSHI	$\|B, \uparrow_z\rangle = \frac{1}{\sqrt{2}}(\|s\rangle + \|p_z\rangle) \otimes \|\uparrow_z\rangle$, $\|B, \downarrow_z\rangle = \frac{1}{\sqrt{2}}(\|s\rangle - \|p_z\rangle) \otimes \|\downarrow_z\rangle$	False	True	BB$\overline{\mathcal{T}}$
HOTI	$\|B, \uparrow_z\rangle = \frac{1}{\sqrt{2}}(\|s\rangle + \|p_z\rangle) \otimes \|\uparrow_z\rangle$, $\|B, \downarrow_z\rangle = \frac{1}{\sqrt{2}}(\|s\rangle + \|p_z\rangle) \otimes \|\downarrow_z\rangle$	True	True	BB

Table 5.9.1.: Overview on the trial basis sets. The first column denotes the model from whose valence band symmetries the basis set has been derived. As shown in Figs. 5.9.1 and A.8.1, the symmetry adopted one is indeed a valid valence band representation of the corresponding model. The last column specifies the labeling used in Figs. 5.9.1 and A.8.1.

To verify our approach, we will also consider the $\mathbb{Z}_2$-trivial phases. As the valence band has p_z and in-plane contributions in all four insulating regimes, any trial basis must be a liner combination of σ_h symmetric and anti-symmetric orbitals. Further, as derived in Sec. 3.4 the in-plane orbitals on the triangular site will transform into s-type orbitals on the honeycomb site at the valley momenta. For the SOC insulator, the EBR analysis suggests a $J = 1/2$ trial basis on the triangular site. The valence bands of the HOTI can be described by a $J_z = \pm 1/2$ (or a $m = 0$ spinless) representation on only one of the A or B sites, a sp_z-hybrid orbital will be considered. Focusing on the QSHIs, A. Soluyanov and D. Vanderbilt proposed for the Kane-Mele model [73] the following pair of time-reversal symmetry-breaking trial functions, which is indicated by $\overline{\mathcal{T}}$ in Tab 5.9.1,

$$|\tau_i\rangle = \{|\ \mathrm{A}, \uparrow_x\rangle, |\mathrm{B}, \downarrow_x\rangle\}. \tag{5.23}$$

They are localized on the A/B honeycomb Wyckoff positions with an in-plane spin-

alignment in x-direction[11]. Similarly, to account for the (almost) preserved σ_v symmetry, we will choose for the $\not{\sigma}_h$-QSHI the real-space obstructed trial basis:

$$|\mathrm{A},\uparrow_x\rangle = \frac{1}{\sqrt{2}}(|s\rangle + |p_z\rangle) \otimes |\uparrow_x\rangle\,, \quad |\mathrm{B},\downarrow_x\rangle = \frac{1}{\sqrt{2}}(|s\rangle + |p_z\rangle) \otimes |\downarrow_x\rangle\,. \tag{5.24}$$

This basis is appropriate for positive valued $\lambda_{\not{\sigma}_h}$, otherwise the antisymmetric hybrid-orbital formulation must be chosen. Turning to the $\not{\sigma}_v$ QSHI, its valence band representation is suggestive for $J_z = \pm 1/2$-type orbitals on the B site. To account for the almost preserved σ_h symmetry, the trial basis must contain a symmetric and an antisymmetric sp_z orbital:

$$|B,\uparrow_z\rangle = \frac{1}{\sqrt{2}}(|s\rangle + |p_z\rangle) \otimes |\uparrow_z\rangle\,, \quad |B,\downarrow_z\rangle = \frac{1}{\sqrt{2}}(|s\rangle - |p_z\rangle) \otimes |\downarrow_z\rangle\,. \tag{5.25}$$

Here, the spin polarization can be chosen in z-direction as the valence bands at both valleys carry the same sublattice character. A summary of the four proposed trial basis sets can be found in Tab. 5.9.1 and the details on the calculation of the non-local overlap matrix are given in App. 5.9.

To test, whether the proposed trial basis sets can describe the valence bands of the four topological phases in the full BZ, the overlap matrix given in Eq. 5.20 needs to be inspected. Its determinant will unveil vanishing eigenvalues. This examination is shown for the four proposed trial basis sets in Fig. 5.9.1, where solid and dashed lines indicate basis sets with non-vanishing and vanishing overlaps, respectively. It confirms the wannierizability of all four phases: for each model, only the trial basis set, that complies with the valence band symmetry, has finite overlaps in the entire BZ. Starting with the non obstructed SOC insulator, the determinant of the $J_{1/2}$ basis peaks, as expected, at the SOC-opened p_z-p_r nodal-line and the valley Dirac momenta. All other projection basis sets have a vanishing overlap at at least one of the aforementioned momenta. The other $\mathbb{Z}_2$-trivial phase, the HOTI, has instead finite overlaps with the sp_z time-reversal symmetric basis on the B site, which confirms the real-space obstruction. Focusing on the $\mathbb{Z}_2$-non-trivial phases, the honeycomb-type $\mathcal{T}$-breaking orbitals describe the occupied bands of the $\not{\sigma}_h$ QSHI. This confirms not only the real-space obstruction, but highlights also the equivalence with the Kane-Mele model. For the $\not{\sigma}_v$ QSHI instead, the valence states can be wannierized by a triangular basis located on the B site. A map plot of the determinants of all considered models and projection basis sets can be found in Supp. A.8.1.

Before concluding this section, let us briefly discuss the unambiguousness of the chosen trial basis sets and the derived real-space obstruction. All applied basis sets comply on the level of the orbital degrees of freedom with the site-symmetry group

[11] The in-plane alignment is necessary, as the valence bands at K and K' acquire in both sublattice orbitals maximum positive and negative out-of-plane spin polarization (see also Sec. 2.1.3). An S_z-trial basis would have maximum overlap at one valley and vanishing overlap at the other.

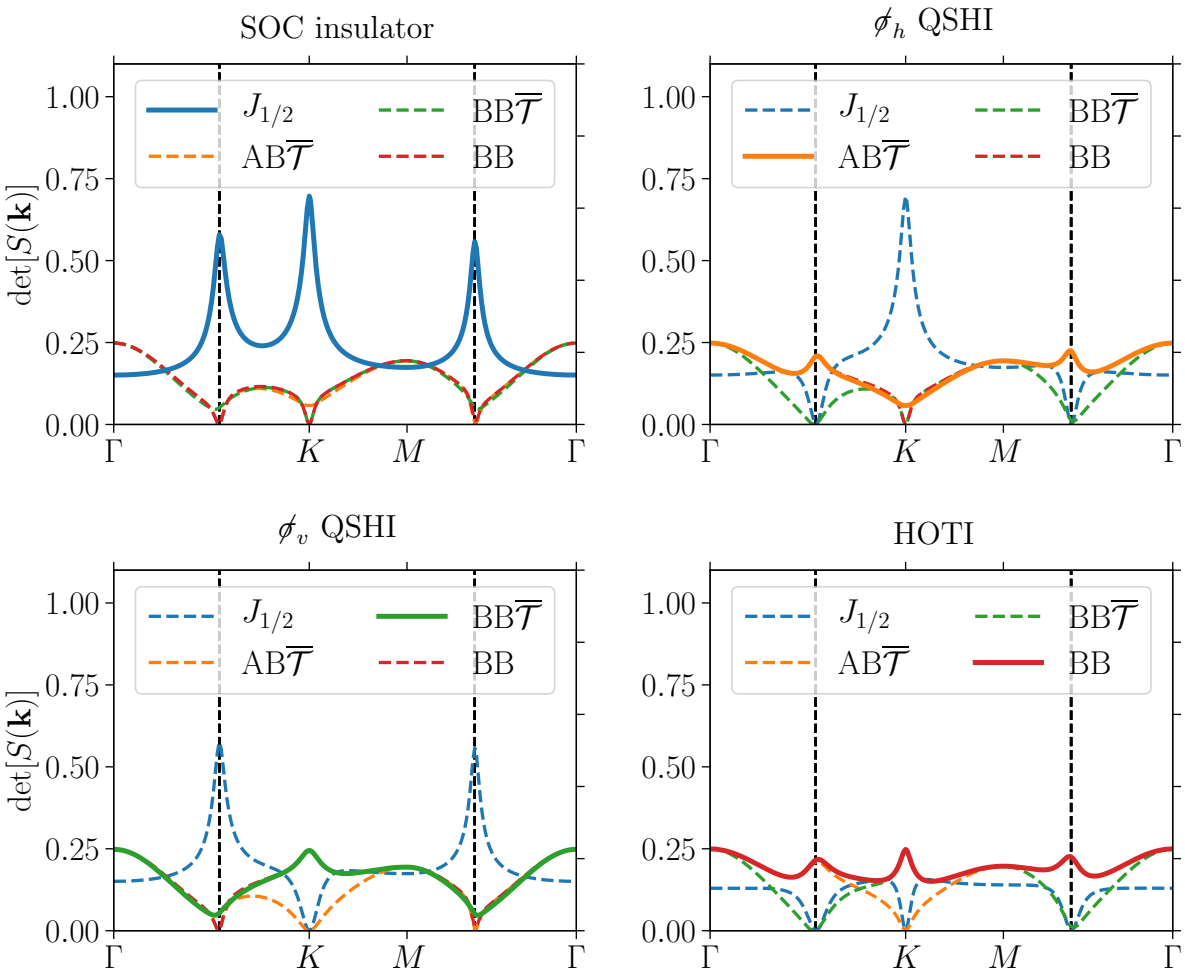

Figure 5.9.1.: Analysis of the overlap matrix $S(\mathbf{k})$ of the trial basis sets given in Tab. 5.9.1 for the four topologically different phases shown in Fig. 5.1.1 (b). Dashed(solid) lines indicate (non-)vanishing overlap eigenvalues along the chosen path, which is representative for the whole BZ (see also Fig. A.8.1). The vertical dashed lines indicate the momenta of the avoided crossing at the p_z-p_r nodal ring.

of the triangular $1a$ and A/B Wyckoff position[12]. The symmetry constraints reduce significantly the space of allowed basis sets. Nevertheless, a criterion indicating the presented trial basis sets as the only valid choice is missing. However, in combination with the inspection of the OAM-texture in Sec. 5.8, the real-space obstruction in the QSHI phases is proven and the basis sets allow for a first interpretation of the localization of the charge centers. Further it should be noted, that the overlap eigenvalues of the presented basis sets can be optimized by constructing maximally localized Wannier

[12]For the $\mathcal{T}$-breaking basis of symmetric and antisymmetric sp_z orbitals on the B site (BB$\overline{\mathcal{T}}$), invariance under σ_h can be achieved by building s- and p_z- orbitals from linear combinations of the Wannier basis states.

functions [34, 119–121, 128] (see also Sec. 2.3.2).

To conclude, by inspecting the overlap of the valence bands of the triangular p-shell model with trial local basis sets, the two $\nu = 1$ phases have been identified as being real-space obstructed. This extends the concept of real-space obstruction to QSHIs, which motivates for future research to investigate the presence of surface, hinge and corner charges in finite size geometries or in $\mathbb{Z}_2$-non-trivial heterostructures. The here presented triangular phases, where one of them has been already realized in indenene [2–4, 61], in combination with the Kane-Mele model [18, 24] and bismuthene [52, 160, 161] could serve as perfect candidates for theoretical and experimental studies.

5.10. Graphene-like QSHI on the Triangular Lattice

We will conclude the discussion on the topological phases by a direct comparison of the $\not{\phi}_h$ QSHI with the Kane-Mele model. Recent experiments have proven that this phase can be indeed realized in a triangular monolayer of indium on SiC [2, 3, 61], where the underlying substrate results in a strong horizontal mirror reflection breaking ($\lambda_{\not{\phi}_h} \gg \lambda_{\mathrm{SOC}}$). This puts forward the technological relevance and realizability of the here conceived model. A closer inspection of the two systems unveils not only the equivalence of their Dirac fermions (see also Chap. 3), but also of their valence bands in the entire BZ as shown in the previous section. An even more rigorous equivalence can be established on the level of the valence band representation: the valence bands of the Kane-Mele transform either under $\overline{\Gamma}_8, \overline{M}_5$ and $\overline{K}_4\overline{K}_5$ or $\overline{\Gamma}_9, \overline{M}_5$ and $\overline{K}_6$ in layer group p6mm (see also Fig. S4 in the supplemental material to Ref. [44]). The latter is exactly the valence band representation of the $\not{\phi}_h$ QSHI shown in Fig. 5.4.2, hence the two models host valence bands with identical symmetries. However, away from the high-symmetry momenta, qualitative differences can be expected and will be discussed in the following.

To compare the two models, the nearest neighbor hopping amplitude, the second nearest neighbor SOC strength and the vertical reflection breaking staggered potential of the Kane-Mele model were extracted from the valley Hamiltonian of the corresponding triangular p-shell model and the details can be found in App. A.5.3. Further, we choose for the triangular model $\lambda_{\not{\phi}_h} = 0.3t$ to gap-out the nodal ring, which leaves the Dirac fermions in a sizable global gap. The resulting band structures and the projected A/B sublattice DOS is shown in Fig. 5.10.1 for the $\nu = 0$ and $\nu = 1$ phase. As discussed in Chap. 5 and Sec. 5.7, the Dirac cone of the trivial bands, i.e., the HOTI, is gapped by a strong $\hat{H}^{\not{\phi}_v}$-interaction which promotes valence bands with identical OAM polarization. This in turn results in a constructive interference at only one of the honeycomb sites and promotes real-space obstruction. Upon reducing the vertical reflection symmetry breaking or increasing the SOC interaction, a $\nu = 1$ phase is stabilized, where the presence of both sublattice flavors in the valence doublet indicates

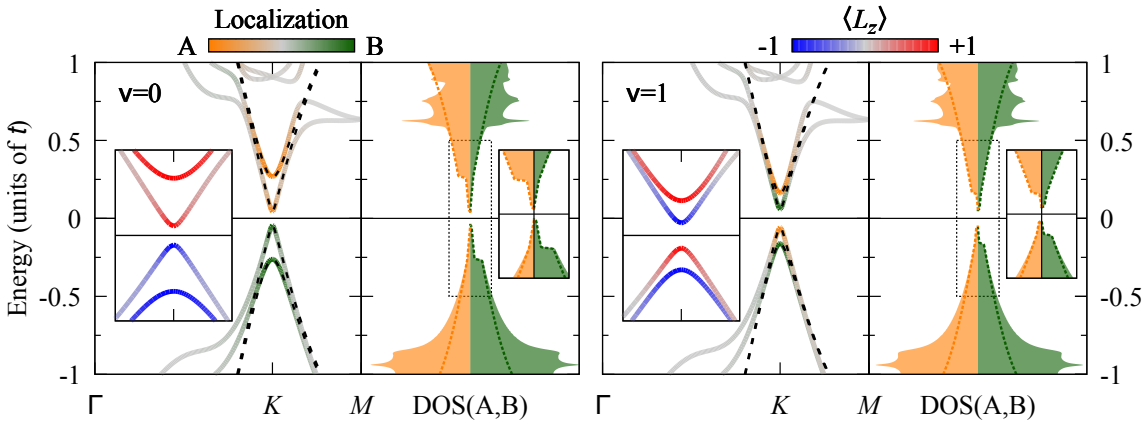

Figure 5.10.1.: Comparison between the triangular p-shell and the Kane-Mele model at the level of the band structure and of the imbalance in the sublattice-projected density of states, denoted as Δ_{AB}DOS for the two different $\mathbb{Z}_2$-phases. The solid lines/filled curve correspond to the triangular lattice, whereas the dashed lines relate to the Kane-Mele model. The blue-red color code in the insets indicates the OAM character, while the green-orange one encodes the A/B sublattice localization. Left: σ_v-breaking-dominated trivial insulator (HOTI): H^{ϕ_v} promotes the same L_z-polarization and A/B localization for the valence bands. Right: SOC-dominated topologically non-trivial phase: both OAM eigenstates are present in valence and correspondingly, the occupied bands localize at the A and B sites giving rise to the emergent honeycomb lattice. To open a large hybridization gap at the p_r-p_z nodal line, the following SOC and symmetry-breaking strengths have been chosen: $\lambda_{\mathrm{SOC}} = 0.2$ and $\lambda_{\phi_h} = 0.3$ and $\lambda_{\phi_v} = 0.03(0.01)$ in the $\nu = 0(1)$ phase. Details on the calculation of the sublattice character in the triangular basis set can be found in App. 5.9. The details on the construction of the Kane-Mele model for the given triangular lattice tight-binding parameters is given in App. A.5.3.

the non-adiabatic connectivity to the atomic limit[13]. In Sec. 6.2.2, we will exploit this charge localization pattern to detect the non-trivial $\mathbb{Z}_2$-phase in a recently synthesized QSHI [2, 3, 61]. The comparison with the "valley-equivalent" Kane-Mele models shows a good agreement also in the vicinity of K. However significant differences can be seen in valence along Γ-K, when the hybridization with the p_z-bands becomes dominant. Further it should be noticed, that particle-hole symmetry is inherently broken in the

[13]The $\mathbb{Z}_2$-invariant in the $\lambda_{\phi_h} \ll \lambda_{\mathrm{SOC}}$ regime is solely determined by the gap at the valley momenta, as the low-energy bands in the remaining BZ are gapped by pure orbital (spin-independent) hybridizations. An adiabatic connection to the atomic limit can only be established, if the Dirac cone is also gapped by H^{ϕ_v} instead of SOC.

in-plane subspace of the triangular model[14] [see also Fig. 4.1.2 (a) and Sec. 6.2.1], which reduces the valence band velocity compared to the Kane-Mele model. This non-linearity is further reflected in an enhanced sublattice DOS in the occupied states, where the hybridization with the p_z-band gives also rise to a van-Hove singularity. Hence, the chosen tight-binding parameters are in support of a strong valence band sublattice polarization exceeding the one of the Kane-Mele model. This helps to overcome the phase decoherence of the triangular chiral wave functions at the honeycomb sites, as discussed in Sec. 3.5.

Before concluding, we extend the comparison to finite size geometries by recalling Sec. 5.6 to highlight the consequences of the interplay of atomic SOC and symmetry-breaking terms: as shown in Figs. A.7.1 and A.7.2 their interplay results in a strong OAM- and spin polarization of the edge states. In particular, the flat-termination hosts edge states which experience a spin canting into the yz-plane owed to the σ_h-breaking promoted in-plane OAM. For the zigzag edge instead, the OAM and spin polarization is purely in-plane. Therefore, also the edge states of the triangular model differ significantly from the ones of the spin-diagonal Kane-Mele model [18, 24].

In summary, although sharing identical valence band symmetries at the high symmetry momenta, the QSHI phase on the triangular and on the honeycomb lattice differ qualitatively in their microscopic interactions, which in turn is reflected in the orbital and spin polarization. The local multi-orbital basis on the triangular lattice profits from an intrinsically strong SOC interaction, while the symmetry-breaking terms allow for a finite OAM polarization in all three spatial components. In these aspects, the triangular QSHI exceeds the Kane-Mele model as its multi-orbital basis allows for a larger tunability.

5.11. Summary

The here discussed triangular lattice Hamiltonian can host four topologically distinct phases, which are stabilized by the interplay of atomic SOC and chiral wave functions from reflection symmetry-breaking (see again Tab. 5.1.2). To be specific, the topology is defined by the gapping nature of the low-energy Dirac fermions at the valleys and the p_r-p_z nodal ring. Two disconnected atomically insulating phases can be found either in high-symmetric or strongly mirror symmetry broken systems. However, the valence band representation of the latter ones localizes on one of the void positions in the triangular lattice indicating this phase as being real-space obstructed. The associated bulk polarization gives rise to topologically-stabilized 0D fractionally filled in-gap corner states. This phase is a higher-order topological insulator. Further we have extended the concept of real-space obstruction to QSHIs. Both $\mathbb{Z}_2$-non-trivial

[14] Particle-hole symmetry in the in-plane subspace is achieved under the condition $V^\sigma = -V^\pi$, where the degeneracy at Γ and the valley Dirac fermions are located at the same energy.

phases have time-reversal violating Wannier representations, which localize either in a Kane-Mele-type honeycomb geometry or on only one of the voids of the triangular lattice. In particular, the real-space obstruction substantiates from the local OAM polarization, which in turn is a consequence of the reflection symmetry breaking.

For spinless models, the analysis of the electronic band representations in the four relevant layer groups allows for a comprehensive understanding of the symmetry promoted gappings and bands degeneracies. However in the presence of SOC, the gapping-type of the p_r-p_z nodal ring is not reflected in the irreps at the high-symmetry momenta. Hence the $\mathbb{Z}_2$-invariant and the electric polarization cannot be solely determined from symmetry indicators. This makes the Wilson-Loop analysis indispensable for space groups lacking horizontal reflection symmetry.

From a more fundamental point of view, the here presented QSHIs are outstanding as they require the absence of inversion symmetry. Indeed, the non-local ISB terms act as the desired antagonist to the atomic SOC. This is a paradigm change in the haunt for new material concepts for stabilizing $\nu = 1$ phases. This deviates from symmetry based approaches, which rely on the presence of inversion symmetry [41, 162, 163] or on spatial symmetry indicators [44–47]. These schemes suggest for the search in high-symmetric space groups. Furthermore, the inherently strong atomic SOC make the material representatives of the triangular model potential candidates for room temperature applications. To be precise, the valence band physics of *the* hexagonal QSHI system, the Kane-Mele model, can be realized on the triangular lattice. However, the Dirac fermion splitting arises from a weak, since non-local, symmetry-breaking and a sizable atomic SOC term.

As a critical note, the stabilization of the four topologically distinct insulating ground states requires well adjusted tight-binding parameters as the Dirac fermions and the p_r-p_z nodal ring are not inherently located in a global energy gap. Nevertheless, the here presented band structures are not only a theoretical edifice. Their occurrence in first material proposals and experiments based on triangular adsorbates will be discussed in the following chapter. Further, the simplicity of the triangular lattice and the vast abundance of substrates is suggestive for the existence of a large plethora of suitable material realizations.

6. Symmetry-Breaking and Topology in Adatom Monolayers

This chapter is devoted to realistic studies of adsorbate monolayers on the surfaces of technologically relevant zincblende- and diamond-type substrates. The layer group of their (111) surface is p3m1 and any adatom on the three high-symmetric adsorbate positions (Wyckoff positions $1a, 1b$ and $1c$, site-symmetry group $3m$) is exposed to a horizontal and vertical reflection symmetry-breaking environment, an ideal situation to validate the theoretical predictions made in Chaps. 3, 4 and 5. This chapter profits from strong and inspiring collaborations between theory and experiment, which prove the relevance of the proposed concepts and can be seen as a first step towards application. In particular, the Angle-Resolved Photoemission Spectroscopy (ARPES) and Scanning Tunneling Spectroscopy (STS) performed in the groups of EP IV and EP VII of the physics department of the university of Würzburg have contributed to gain insights in the wave function symmetry, e.g., symmetry breaking-induced chirality and real-space localization.

The discussion is organized as follows: we will start from the binary honeycomb lattice AgTe on Ag. The low-energy physics of the Te p-shell is governed by a strong SOC and horizontal mirror reflection breaking, which gives rise to the *orbital-driven Rashba effect* [1]. Then we will focus on Group III adsorbates on SiC (0001). We will introduce the first real-space obstructed QSHI based on a triangular layer of indium atoms, *indenene*, a realization of the $\not{\sigma}_h$ QSHI phase discussed in Chap. 5 and published in Refs. [2, 3, 61]. Upon reducing the SOC strength by going to lighter adatoms such as B, Al and Ga the HOTI phase introduced in Chap. 5 can be stabilized. This will be proven on the level of symmetry indicators and finite size calculations [4]. As an outlook, beyond topology and symmetry-breaking effects, Sb on SiC will be considered, which can be regarded as a n-doped version of the Group III adsorbates. This yields pure p_{xy} low-energy physics. Further, it hosts a compensated Fermi surface, which might promote correlation driven electronic ordered phases mediated by orbital symmetries.

6.1. Orbital-Driven Rashba Effect in AgTe

The works of Dresselhaus [164] and Rashba and Bychkov [165] have inspired the search for spin-polarized states, originating from the interplay of inversion-symmetry-breaking and SOC even in non-magnetic, time-reversal symmetric systems. Besides the intrinsic interest in these phenomena [166], with the beginning of the era of topological materials attention in ISB-driven spin-splittings arose. These mechanisms are fundamentally present in non-centrosymmetric Weyl semi-metals [150, 167] and spin-momentum locked surface states of topological materials [19, 49, 168]. This chapter will elucidate on the fundamental interplay of orbital symmetries and symmetry breaking at surfaces, which gives rise to sizable and band-dependent spin-splittings in materials with strong SOC.

The Rashba-Bychkov model [165]

$$\hat{H}^{\mathrm{R}} = \alpha_{\mathrm{R}} \boldsymbol{\sigma} \left(\boldsymbol{e}_z \times \mathbf{k} \right), \tag{6.1}$$

allows for a qualitative description by assuming an electron's motion perpendicular to a (surface) potential gradient $\alpha_{\mathrm{R}} \propto \partial V / \partial z$, but the underlying microscopic nature remains unspecified. Further, it cannot explain band-dependent splittings and the sizable magnitude of experimentally observed Rashba parameters up-to the order of $\mathcal{O}(\mathrm{eV\AA})$[1] [38]. Instead, the large interaction strength can be motivated upon the formation of local orbital angular momentum arising from a mirror symmetry-breaking interaction, which in turn couples to the atomic SOC $\propto \lambda_{\mathrm{SOC}} \hat{\boldsymbol{L}} \cdot \hat{\boldsymbol{S}}$ [169–172]. Hence, Rashba systems are perfectly suited for investigating the impact of the σ_h-breaking term introduced in Chap. 4, which promotes in-plane OAM arising from states of the form of $|p_{\pm^{\mathrm{inp}}}\rangle \propto \alpha |p_r\rangle \pm i\beta |p_z\rangle$ ($\alpha, \beta \in \mathbb{R}^+$).

Here we will focus on the Rashba splitting in the Te p shell in the binary AgTe honeycomb layer on Ag(111) [1]. The results emerged from a fruitful experiment-theory collaboration with the group of EP VII. The joint study profits from the sample preparation and ARPES experiments carried out by Maximilian Ünzelmann as well as from minimal model calculations and *ab initio* theory. The structure is shown in Fig. 6.1.1. Considering only the honeycomb layer on a homogeneous substrate, the layer group is p3m1 and has the symmetries of the tight-binding model introduced in Chap. 4. As illustrated in the left panel of Fig. 6.1.1, the Ag atoms of the binary honeycomb break the σ_v. In addition, the first substrate layer breaks the remaining vertical reflection σ_d with respect to the Te atom. This reduces the layer group down to p3 and the Te site-symmetry group is reduced from 3m to 3. As we will see in the following, the lowered symmetry to p3 has only a minor impact on the orbital polarization of the Te bands, because the system is *almost* p3m1 symmetric.

[1] Realistic *ab initio* work function calculations suggest Rashba parameters of the order of $\mathcal{O}(10^{-6}\mathrm{eV\AA})$ [38].

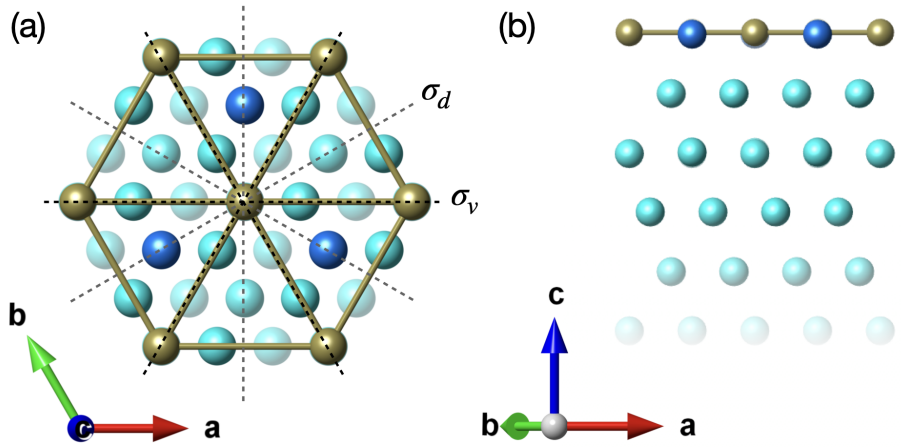

Figure 6.1.1.: Top (a) and side view (b) on the surface geometry of the binary honeycomb compound AgTe on Ag(111). Te and Ag atoms are denoted by golden and turquoise spheres, respectively. The Ag atom of the honeycomb layer is illustrated by a dark blue color. The vertical and diagonal reflection planes with respect to the Te lattice are given by black and gray dashed lines, respectively.

6.1.1. Orbital Polarization and Band-Dependent Rashba-Splitting

The *ab initio* band structure is shown in Fig. 6.1.2 (a). It is characterized by the two Te in-plane bands in valence (labeled by α and β), which are energetically separated by SOC at Γ. The Ag-s-Te-p_z-type conduction band is labeled by (γ) (see also Fig. S2 of the supplement to Ref. [1]), which makes this compound a perfect template for a qualitative comparison with the p-shell tight-binding model. The Ag substrate contributes metallic states at the BZ boundary and parabolic electron-type quantum well states at Γ with minima at $\approx -1.5\,\mathrm{eV}$ and $\approx -0.2\,\mathrm{eV}$. Despite of the underestimation of the gap, the band structure is in excellent agreement with ARPES and two-photon photoemission experiments in panel (b). The α- and β/γ-bands exhibit a negligible and sizable spin-splitting, respectively. A detailed analysis of the momentum-dependence of the splitting around Γ is illustrated in panel (c). Bands β and γ possess a linear splitting with comparable splitting strength, α exhibits instead a cubic relation. This qualitative difference is also reflected in the orbital symmetry [see Fig 6.1.2 (a)] as α possesses tangential in-plane polarization, while β is radially aligned. The latter allows for a hybridization with the Ag-s-Te-p_z conduction band via $\hat{H}^{\phi_h}$ under the formation of in-plane OAM (see also Sec. 4.3). Further, this interaction scales linearly with momentum as derived in Eq. 4.27 explaining the observed momentum-dependence. In turn the cubic scaling of the α-band indicates higher-order processes as the source of its weak Rashba-splitting.

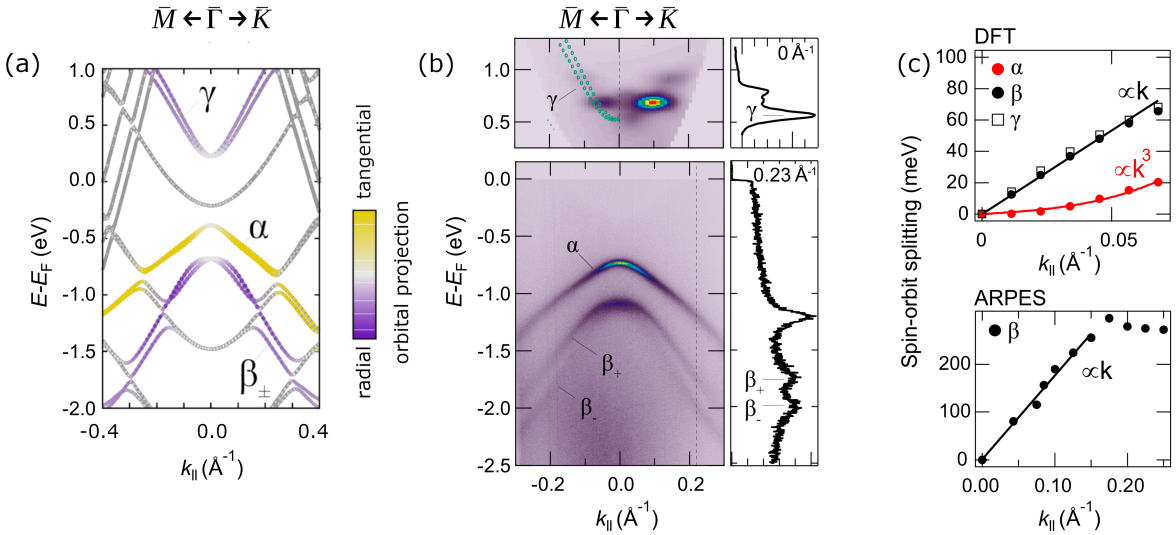

Figure 6.1.2.: (a) DFT band structure of AgTe on seven layers of Ag(111). The color code denotes the Te atom projected orbital contributions. (b) ARPES and two-photon photoemission data and energy distribution curves taken at momenta indicated by the dashed vertical lines. (c) DFT and experimental spin-splittings in the vicinity of Γ in the top and bottom panel, respectively, of the three features labeled in (a) and (b). Reprinted figures with permission from Ünzelmann, M. *et al.* "Orbital-Driven Rashba Effect in a Binary Honeycomb Monolayer AgTe". *Physical Review Letters* **124** (2020). © 2020 by the American Physical Society.

6.1.2. Inversion Symmetry-Breaking Promoted OAM Polarization

Having established the band-dependent Rashba splitting in AgTe, we will confirm in the following the initial hypothesis: symmetry-breaking promoted OAM formation which in combination with SOC gives rise to the sizable spin-splittings. We turn first to the discussion of the OAM polarization around Γ for a spinless calculation shown in Fig. 6.1.3 (for the band structure see also Fig. 6.1.6) calculated from an atomic-like Wannier projection: α has a vanishing in-plane OAM while γ and β posses a clock and anti-clockwise in-plane polarization, respectively. However, the mainly $p_{\pm}$-derived bands α and β have also a C_3-symmetric out-of-plane polarization. This is indicative for $\hat{H}^{\phi_v}$, which is intrinsic to the bipartite AgTe honeycomb. Hence, the *ab initio* calculation unveils AgTe as a perfect template for the investigation of a p-shell in the presence of σ_h-(resulting from the out-of-plane ISB of the substrate) and σ_v-breaking (mainly originating from the C_3-symmetry of the binary honeycomb). They promote a sizable in-plane and out-of-plane OAM polarization.

Upon considering SOC, a gap of size 0.3 eV is opened at the former $p_{\pm}$-degeneracy

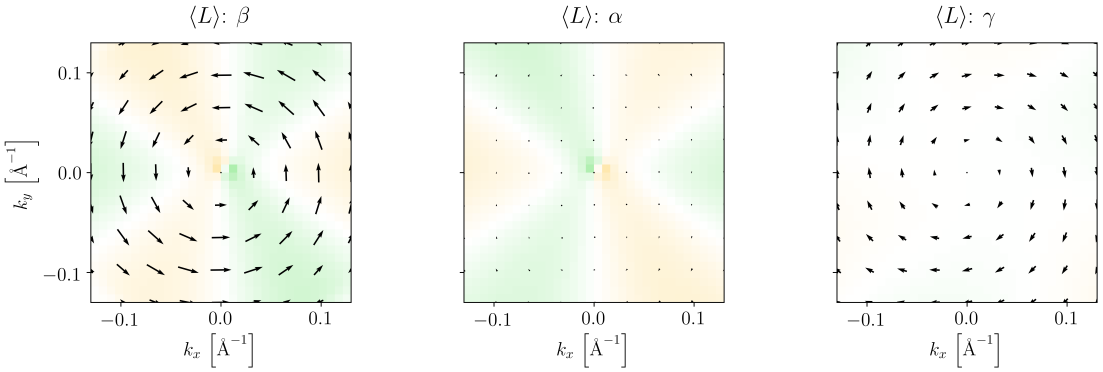

Figure 6.1.3.: OAM texture of the low-energy AgTe bands around Γ in the absence of SOC. The color code and the vector field denote the out-of plane and in-plane components, respectively. The color range of the color scale is $[-0.5, 0.5]$ in units of $\hbar$ (maximal coloring see Fig. 6.1.4).

at Γ, which splits-up into $J_z = \pm 1/2$ and $\pm 3/2$ Kramer's pairs [2]. The low-energy physics at Γ is governed by $\hat{H}^{\mathrm{SOC}}$ and the symmetry-breaking terms can be regarded as perturbative corrections. Instead at larger $\mathbf{k}$, the non-local orbital hybridization terms dominate and the interplay of OAM and SOC introduces the spin-splitting. A detailed OAM and spin polarization analysis in the SOC-dominated vicinity of Γ is shown in Fig. 6.1.4 and a comparison with a minimal p-shell model is presented in Figs. A.9.1 and A.9.2. The features $\alpha_\pm$ ($j_z = \pm 3/2$, $\overline{\Gamma}_4\overline{\Gamma}_5$ irrep assuming p3m1 symmetry, see also Tab. 5.4.2) exhibit a dominant out-of-plane spin and OAM polarization. The latter is enhanced by the SOC interaction compared to the values of the spinless calculation in Fig. 6.1.3. In addition the C_3-symmetric pattern can be associated to $\hat{H}^{\phi_v}$ (compare with Fig. 4.2.1). At larger distances to Γ, the bands accumulate a radial OAM and spin polarization at the hybridization gaps with the substrate quantum well states (see Figs. A.9.1 and A.9.2), which is absent in the p3m1 symmetric tight-binding model. These features are hints of the σ_d-breaking via the first Ag(111) substrate layer. The bands $\beta_\pm$ and $\gamma_\pm$ transform under the $\overline{\Gamma}_6(2)$ irrep and a qualitatively similar behavior for the two bands in the vicinity of Γ can be expected. Their tangential OAM polarization increases with $\mathbf{k}$, which in turn yields a dominant in-plane spin orientation. However, the feature β_- has a reduced in-plane OAM around Γ and reaches only at large $\mathbf{k}$ a parallel alignment with β_+ (see also Fig. A.9.1). This is due to the dominant SOC driven mixing of the in-plane bands at Γ. Instead for the energetically well separated features $\gamma_\pm$, both bands have an almost identical OAM polarization (the one of γ_- is slightly reduced).

[2] See also Fig. 6.1.6 (a,d) and the absence of p_r/p_t polarization due to orbital mixing in Fig. 6.1.2 (a).

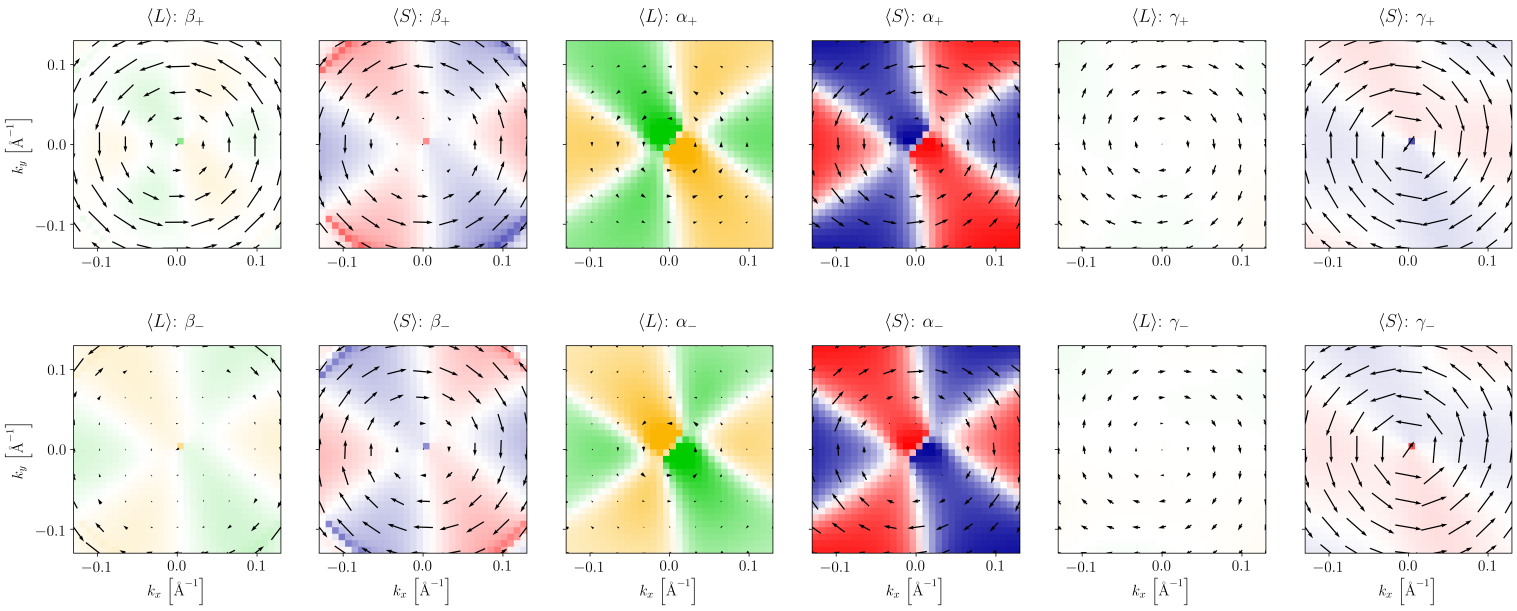

Figure 6.1.4.: OAM and Spin texture of the low-energy bands of the Te p-shell around Γ. The color code and the vector field denote the out-of plane and in-plane components, respectively. The energetically higher (lower) spin-band is labeled with a "+" ("-") subscript [see also Fig. 6.1.2 (b)]. The imperfect C_3 symmetry (considerably visible for $\alpha_\pm$) arises from a small asymmetry of the Wannier Hamiltonian which becomes dominant at band degeneracies, at larger momentum distances to Γ the symmetry is restored. The color range of both color scales is $[-0.5, 0.5]$ in units of $\hbar$.

6.1.3. Band Symmetries from Polarized Light ARPES

Having demonstrated the wave function symmetries from *ab initio* methods and from theoretical concepts introduced in Chap. 4, we will establish in the following an experimental detection of the OAM polarization based on linearly-polarized light ARPES. The measurements have been performed by Maximilian Ünzelmann and coworkers at the chair of EP VII of the University of Würzburg. A detailed discussion on the underlying theory and the hereinafter presented experimental data can be found in the dissertation of Maximilian Ünzelmann [173].

In the electric dipole approximation, the photoemission transition matrix element is given by [174]

$$T_{i\mapsto f} = \langle \Psi_f | \mathbf{E} \cdot \mathbf{r} | \Psi_i \rangle. \tag{6.2}$$

Under the assumption of an even-parity final state Ψ_f, the matrix element is determined by the symmetry of the product of the dipole and the initial state. As shown

in Fig. 6.1.5 (a) for p-orbitals and a light incidence in the xy plane, s-polarized light described by an electric field vector $\mathbf{E}_s = (0, \mathcal{E}_y, 0)$ allows to address orbitals with odd character under the mirror operation $y \mapsto -y$. In particular along the cartesian momentum axes $(k_x, 0)$ and $(0, k_y)$ bands arising from the tangential and radial p-orbitals, respectively, can be measured. Instead p-polarized light with $\mathbf{E}_p = (\mathcal{E}_x, 0, \mathcal{E}_z)$ interacts with states odd under $x \mapsto -x$, i.e., the p_r- along k_x- and the p_t-band along k_y-axis. As the incident angle defines the ratio of $\mathcal{E}_x$ and $\mathcal{E}_z$, the sensitivity to the p_z-states can be controlled. Maximum in-plane contributions can be achieved under normal incidence [175]. A profound discussion can be found in Ref. [173].

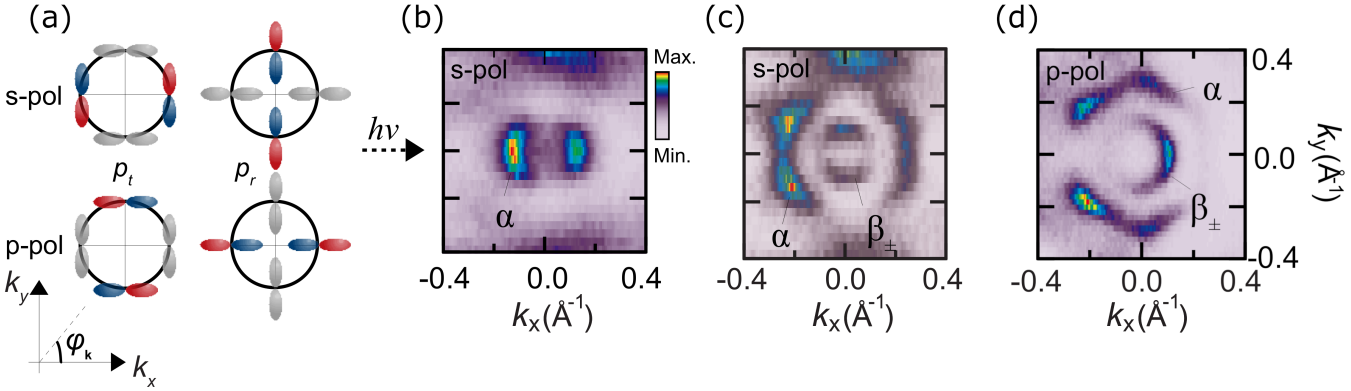

Figure 6.1.5.: Orbital decomposition from linearly polarized light ARPES with a photon energy of $h\nu = 25\,\text{eV}$ for a light incidence in the xy plane and azimuthal angle φ_k.(a) Schematic radial and tangential orbital response for s- and p-polarized light.(b-d) Constant energy cuts taken at $E - E_F = -950\,\text{meV}$ (b) and -1300 meV (c) with s-polarized light and at -1300 meV with p-polarized light (d).Reprinted figures with permission from Ünzelmann, M. *et al.* "Orbital-Driven Rashba Effect in a Binary Honeycomb Monolayer AgTe". *Physical Review Letters* **124** (2020). © 2020 by the American Physical Society.

At binding energies of 950 meV [see also Fig. 6.1.2 (a)], only the band α appears in the corresponding constant energy cut. The respective ARPES data set taken with s-polarized light is shown in Fig.6.1.5 (b). The intensity is suppressed along k_y, but sizable along the k_x-axis and indicates the tangential orbital alignment. This is further confirmed at higher binding energies [1300 meV, panel (c)]. Also the feature β is present at this energy: it has predominantly spectral weight along the k_y-axis, which signals its radial symmetry. For p-polarized light instead [panel (d)], the features α and β are suppressed along k_x and k_y, respectively. This is in agreement with the inferred orbital symmetries. However the spectral weight associated to β has a strong left-right asymmetry, which is less pronounced for α. We will come back to this point later on when discussing the linear dichroism.

To quantify the momentum-dependent orbital character polarization from the ARPES

measurement, the azimuthal asymmetry parameter has been proposed [175, 176]

$$\lambda(\mathbf{k}_\parallel) = \frac{I_0 - I_{\pi/2}}{I_0 + I_{\pi/2}}, \tag{6.3}$$

for a wave vector $\mathbf{k}_\parallel$ (in the following $\mathbf{k}_\parallel = (k_x, 0)$) with azimuthal angles $\varphi_k = 0$ and $\pi/2$ [see also Fig. 6.1.5 (a)]. For s-polarized light, this parameter is expected to be positive for p_t-derived bands and negative for p_r-symmetric bands [175, 176]. The result is shown in Fig. 6.1.6 (a), which is in perfect agreement with the orbital polarization of the *ab initio* calculation in Fig. 6.1.2 (a). Both bands have a vanishing polarization at Γ, which increases with momentum distance and saturates around ±0.2 Å, the overall sign reflects the expected behavior. Hence, this analysis has also experimentally unveiled the momentum-dependent orbital polarization formation in the low-energy bands of AgTe, which includes also the important prerequisite for the orbital Rashba effect: the presence of a radial in-plane band. However the confirmation of OAM-polarized wave functions, which couple to SOC, is still missing.

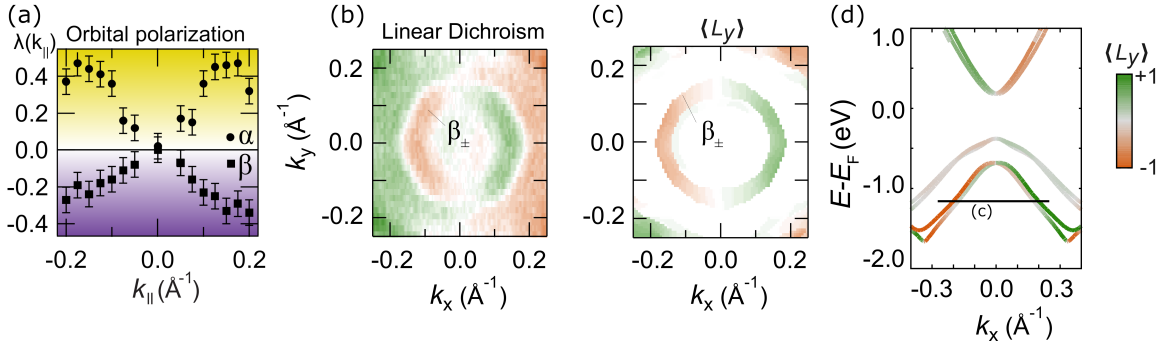

Figure 6.1.6.: (a) Orbital polarization parameter $\lambda(\mathbf{k}_\parallel)$ extracted from the s-polarized ARPES data. (b) Linear Dichroism of the constant energy cut shown in Fig. 6.1.5. (c) $\langle L_y \rangle$ polarization at the constant energy shown in (d). (d) $\langle L_y \rangle$ polarization of a minimal Te p and Ag s Wannier model. Reprinted figures with permission from Ünzelmann, M. *et al.* "Orbital-Driven Rashba Effect in a Binary Honeycomb Monolayer AgTe". *Physical Review Letters* **124** (2020). © 2020 by the American Physical Society.

The OAM polarization can be experimentally addressed with circularly polarized light and results in a finite circular dichroism signal [39, 149, 170, 171, 177, 178]. Sensitivity to $\langle L_y \rangle$ is achieved by an electric field polarization of $\mathbf{E}_\pm = (\mathcal{E}_x, 0, \pm i\mathcal{E}_z)$. The circular dichroism is proportional to

$$CD(k_x, k_y) = I_R(k_x, k_y) - I_L(k_x, k_y) \propto \Im\left(T_x^*(k_x, k_y) T_z(k_x, k_y)\right), \tag{6.4}$$

where T_i is the contribution to the matrix element in Eq. 6.2 of component i of the dipole operator. A direct connection can be drawn to the conducted p-polarized light

measurements at an incident angle of 45° where the electric field reads $\mathbf{E} = (\mathcal{E}, 0, \mathcal{E})$. With the definition of the linear dichroism [1]

$$LD(k_x, k_y) = I(k_x, k_y) - I(-k_x, k_y) \propto \Re\left(T_x(k_x, k_y) T_z^*(k_x, k_y)\right), \tag{6.5}$$

i.e., the difference in the intensities I at momenta, which are mapped onto each other under $k_x \mapsto -k_x$. This comparison makes evident that both, circular and linear dichroism are sensitive to p_z-p_r hybrid states (here $p_r = p_x$) for a light incidence in the xz-plane as they correlate in-plane and out-of-plane orbital contributions. This analysis is shown for the feature β in Fig. 6.1.6 (b), obtained from the data in Fig. 6.1.5 (d). A careful analysis in Ref. [1] (see also supplemental material Sec. VII) allows us to assign the dichroism to the initial state symmetry, which is in perfect agreement with the calculated $\langle L_y \rangle$ polarization shown for the corresponding constant energy cuts in Fig. 6.1.6 (c) and for the band structure in panel (d). It should be noted, that the simple dipole picture expressed in Eq. 6.2 yields a purely imaginary value of $T_x T_z^*$ for an L_y eigenstate and hence a vanishing LD signal. However, final state effects can introduce relative phase shifts between T_x and T_z. Therefore it is reasonable to assume that OAM eigenstates will promote finite LD signals. A detailed analysis combined with a pedagogical explanation on the final state effects in AgTe can be found in Ref [179], while an extensive study on various materials is given in Ref. [173].

6.1.4. Conclusion and Outlook

To conclude this first section, the binary honeycomb compound AgTe on Ag(111) hosts Te p-type in-plane valence bands, which possess fundamentally different Rashba-splittings. The band at lower energies inherits a radial symmetry from the trigonal lattice structure. This, in the presence of horizontal mirror reflection breaking, results in a predominant in-plane OAM polarization. In combination with SOC, this activates the sizable orbital-driven Rashba-splitting whose order of magnitude can be directly related to the SOC strength. Instead, for the upper valence band, its tangential orbital symmetry prevents the formation of in-plane OAM and suppresses significantly the spin-splitting. The joint *ab initio* and experimental investigation allows not only for a profound quantitative analysis of the underlying mechanism, but also highlights the importance of wave function symmetry-sensitive approaches in light of SOC- and symmetry-breaking driven phenomena.

6.2. Indenene on SiC

Since the seminal prediction of the quantum spin Hall effect in graphene by Kane and Mele [18, 24], $\mathbb{Z}_2$-topology in hexagonal and trigonal monolayers is indissociably linked to the honeycomb geometry and its symmetry-promoted Dirac cones at the

valley momenta. In practice, graphene and its heavier representatives suffer from an inherently weak non-local SOC interaction, which can be increased via structural optimization up to the order of $\mathcal{O}(100)$ meV [55, 56, 180, 181]. Instead bismuthene on SiC has proven that substrate-induced symmetry-breaking and atomic SOC of a local multi orbital basis give rise to a sizable inverted band gap of 0.8 eV [52, 161]. However, as discussed in Chap. 3, the Dirac physics is intrinsic to the space group symmetry. Hence one may ask if a hexagonal QSHI with local SOC and similar complexity as graphene, i.e., with a two orbital basis description, can exist. Here we propose the triangular lattice, which is obtained by removing one of the sublattices of the honeycomb. Indeed, in the presence of dominant σ_h-breaking, as elaborated in Chaps. 4 and 5, graphene-like low-energy Dirac bands from p-orbitals can be realized in an otherwise globally gapped band structure. As illustrated in Fig. 6.2.1 (a) the $\mathbb{Z}_2$-invariant is encoded in the sublattice polarization of the Dirac states. Equivalently to the Kane-Mele model, SOC favors a non-trivial phase and σ_v-breaking acts in the opposite direction. While the sublattice polarization of the Dirac states can be easily understood from a honeycomb basis, this arises on the triangular lattice from an interference effect driven by the chirality of the $p_\pm$-orbitals and the Bloch phase as shown in Fig. 6.2.1 (b) (see also Chap. 3 for details). Upon extending the analysis to the whole BZ, the detachment of the corresponding Wannier centers from the atomic basis positions indicates the triangular QSHI phase as being real-space obstructed, which is in contrast to the Kane-Mele model and, likely, to bismuthene[3]. Therefore, such a triangular QSHI would not only constitute *"another QSHI system"*, though benefiting from the simple geometry, but enriches also the scientific perspective, as it extends the concept of real-space obstruction to $\mathbb{Z}_2$-non-trivial phases.

Such a QSHI has been designed in collaboration with the group of Experimentelle Physik IV of the University of Würzburg, which we dubbed *"indenene"*: a triangular monolayer of indium atoms on SiC. The results have been published in Refs. [2–4, 61]. Based on *ab initio* calculations as well as on ARPES and STM experiments conducted by Maximilian Bauernfeind and Jonas Erhardt, theoretical aspects, such as the emergent honeycomb localization at the valley momenta, the real-space obstruction and its edge states introduced in Chaps. 3 and 5 will be discussed hereafter.

6.2.1. Unit Cell Characterization and Electronic Structure

The unit cell is illustrated in Fig. 6.2.2 (a,b), the indium atoms adsorb in a 1×1 geometry on the T1 position, i.e., on top of the Si atom of the Si-terminated 4H-SiC(0001) surface. Both experiment (X-ray standing wave photoemission) and DFT confirm the In-Si distance being $d_{\mathrm{In-Si}} = 2.68$ Å. The mere presence of the SiC substrate breaks the horizontal reflection symmetry. In addition, the vertical reflection symmetry is also

[3]Currently under investigation by Markus Feld (AG Sangiovanni), preliminary results are in favor of a non real-space obstructed QSHI phase for bismuthene. To appear in his master thesis.

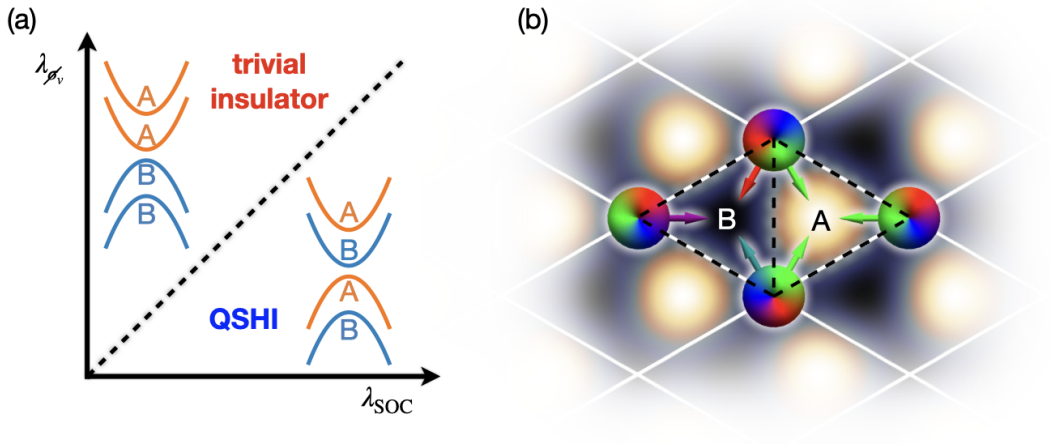

Figure 6.2.1.: (a) Schematic $\mathbb{Z}_2$-phase diagram of a triangular p-shell in the presence of a dominant σ_h-breaking. The gap-topology and the sublattice polarization (A, B) of the valley Dirac states (insets) is dictated by the competition of SOC(λ_{SOC}) and vertical reflection symmetry-breaking ($\lambda_{\not\sigma_v}$) as it was introduced in Chap. 3. (b) Sublattice localization of $p_\pm$-derived Bloch wave functions at the valley momenta. The interference of the local orbital phase (tori on the triangular lattice) and the Bloch phase results in a constructive and destructive interference at the A/B sites, as indicated by the dark-bright color plot of the associated charge density. The panel shows the specific example of a p_+ orbital at $K = (1/3, 1/3)$ and the color of the tori and the arrows denotes the total phase (for details see also Chap. 3 and Fig. 3.2.1). Reprinted figures have been taken and adopted from Bauernfeind, M. *et al.* "Design and realization of topological Dirac fermions on a triangular lattice". *Nature Communications* **12,** 5396 (2021). CC BY 4.0. For consistency, the A/B labeling follows the notation introduced in Chap. 3.

broken, as the C-atom of the first SiC layer renders the A/B positions inequivalent [see Fig. 6.2.2 (b) and c.f. Fig. 5.1.1 (a) for a schematic illustration of the symmetry breaking via the substrate]. Hence the site-symmetry group of the In atom is C_{3v} and the layer group is p3m1, which in principle could host any of the four topologically distinct phases discussed in Chap. 5. However, as the In atom is located on top of the Si atom, a sizable $\hat{H}^{\not\sigma_h}$ term can be expected. The STM apparent height profile shown in Fig. 6.2.2 (c) along the path through the diagonal of the unit cell displays a clear inequivalence of the A and B sites, confirming the non-negligible $\hat{H}^{\not\sigma_v}$ breaking interaction. The top panel confirms the 1×1 surface reconstruction by comparing the lattice constants measured on the initially hydrogen passivated and the In-terminated SiC substrate.

Based on the symmetry analysis, indium on SiC is a potential candidate for the realization of the $\not\sigma_h$ QSHI introduced in Chap. 5. Indeed, as shown by the *ab initio* band

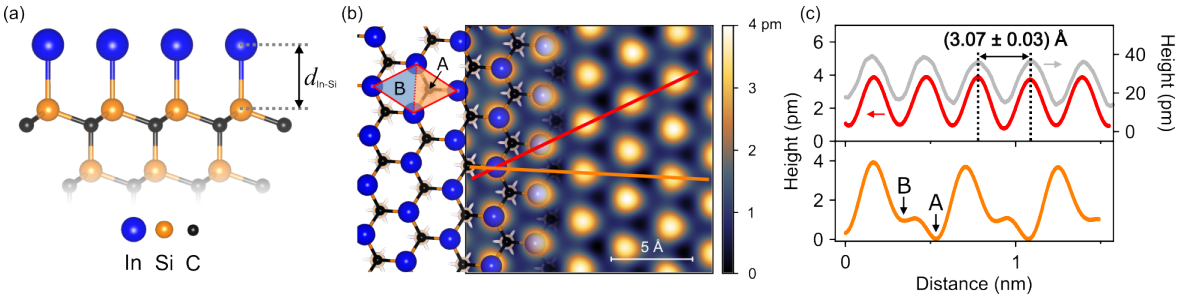

Figure 6.2.2.: Adsorption geometry of indenene on SiC(0001) and experimental indications of non-negligible vertical reflection symmetry breaking. (a) Side view and In-Si bonding distance $d_{\text{In}-\text{Si}}$. (b) Top view and STM topography image [constant current mode, $V_{\text{set}} = 1.5\,\text{V}$ and $I_{\text{set}} = 50\,\text{pA}$, sensitive to the In p_z states, see also Figs. 6.2.3 (a) and 6.2.6 (a,b)] showing the associated triangular lattice geometry. The vertical reflection symmetry breaking via the C-atom in the surface layer of the substrate is schematically illustrated by the blue and orange coloring for one unit cell on the left side of the panel. (c) STM line profiles along the paths with the same color in (b). The comparison with the initially hydrogen terminated SiC substrate (gray line, scale is on the right) confirms the 1×1 construction (top panel). The inequivalent apparent heights at the A and B site (bottom panel) indicate the impact of the vertical reflection symmetry breaking on the electronic structure of the In p-bands. Reprinted figures have been taken and adopted from Bauernfeind, M. *et al.* "Design and realization of topological Dirac fermions on a triangular lattice". *Nature Communications* **12,** 5396 (2021). CC BY 4.0. For consistency, the A/B labeling follows the notation introduced in Chap. 3.

structure in Fig 6.2.3, the system is insulating with an In p-type valence band characterized by a predominant p_z character at Γ and an in-plane-derived Dirac cone at the valley momenta, i.e., the band structure exhibits all relevant orbital symmetry features introduced in Chap. 5. Further, the horizontal mirror reflection symmetry breaking opens a sizable hybridization gap between the radial in-plane and the p_z-orbital and promotes Rashba-type spin-splittings along the paths Γ-M and Γ-K (see also Sec. 6.1). Moreover the Kramers degeneracy is lifted at the valley momenta, a consequence of the vertical reflection symmetry breaking. Nevertheless, SOC dominates, as indicated by the presence of both L_z eigenvalues in valence (conduction) as shown in Fig 6.2.3 (b). The Wilson-loop analysis in Ref. [3] confirms the non-trivial $\mathbb{Z}_2$-topology ($\nu = 1$). Further, the effective filling of two electrons in the In p derived bands can be understood from the covalent bonding of the In p_z-orbital to the sp_z-type dangling bond of the SiC substrate, which shifts the Fermi energy into the global gap.

As illustrated in Fig. 6.2.4, the band structure of the *ab initio* simulation is in excellent agreement with the ARPES experiment, which shows a Dirac feature at the

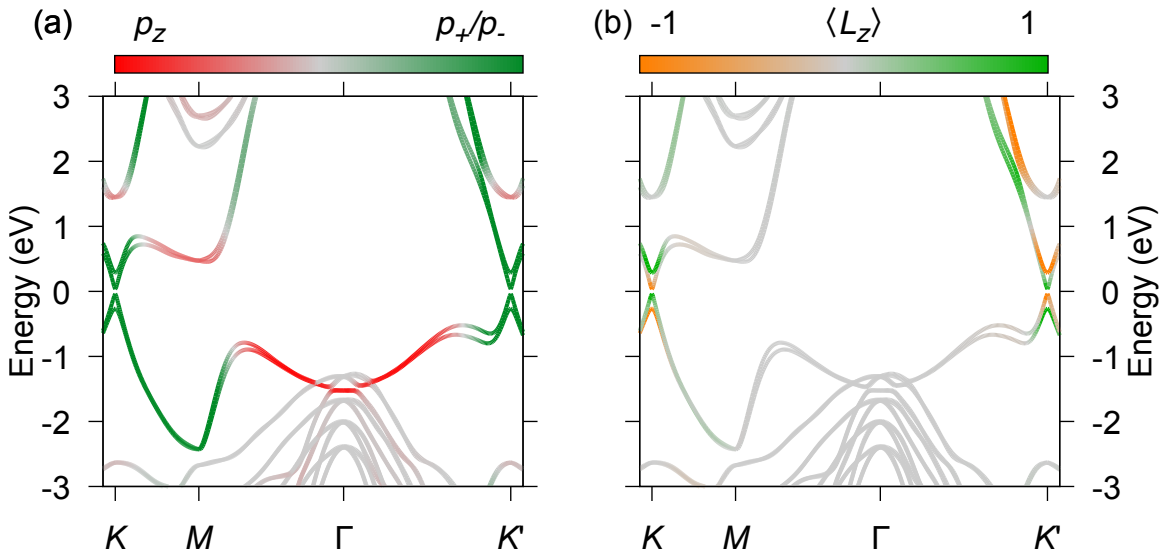

Figure 6.2.3.: Orbital (a) and out-of plane OAM (b) polarization in indenene on SiC calculated from a $\{s, p\}$ Wannier projection on the In, Si and C sites obtained from a HSE06 hybrid functional calculation. Reprinted figures of the supplemental material from Bauernfeind, M. *et al.* "Design and realization of topological Dirac fermions on a triangular lattice". *Nature Communications* **12,** 5396 (2021). CC BY 4.0.

valley momenta. The overall band dispersion fits well with the In p valence band, which hybridizes at Γ with the SiC substrate states. Along the paths Γ-M and Γ-K the ARPES signal broadens in energy at momenta, where DFT predicts sizable Rashba splittings. However the heavily n-doped SiC substrate shifts the chemical potential by $\approx 250\,\text{meV}$ into the conduction states of the Dirac cone, the DFT bands have been aligned upon introducing a rigid energy shift. First calculations with the PBE functional yielded a reduced gap at M, because the p_z-band was predicted to be located at energies between the two conduction bands of the Dirac cone [see also Fig. 6.2.7 (a)]. A better agreement with ARPES and STM can be obtained with the HSE06 functional, which has been chosen for the bulk characterization. A detailed discussion on the impact of the DFT-functional can be found in Sec. 6.2.4.

Focusing on the valley momenta, the energy distribution curve fits illustrated by orange dots in Fig. 6.2.4 (b) indicate a gap of $\mathcal{O}(100)\,\text{meV}$, which is in reasonable agreement with the DFT calculation yielding a gap of 70 meV. Panel (c) shows the band velocities resulting in a Fermi velocity of the Dirac cone of $\approx 0.03\,\text{c}$, which is comparable to graphene [182, 183]. Further, the valence-conduction asymmetry indicates the broken particle-hole symmetry in this Dirac system. A similarity to graphene

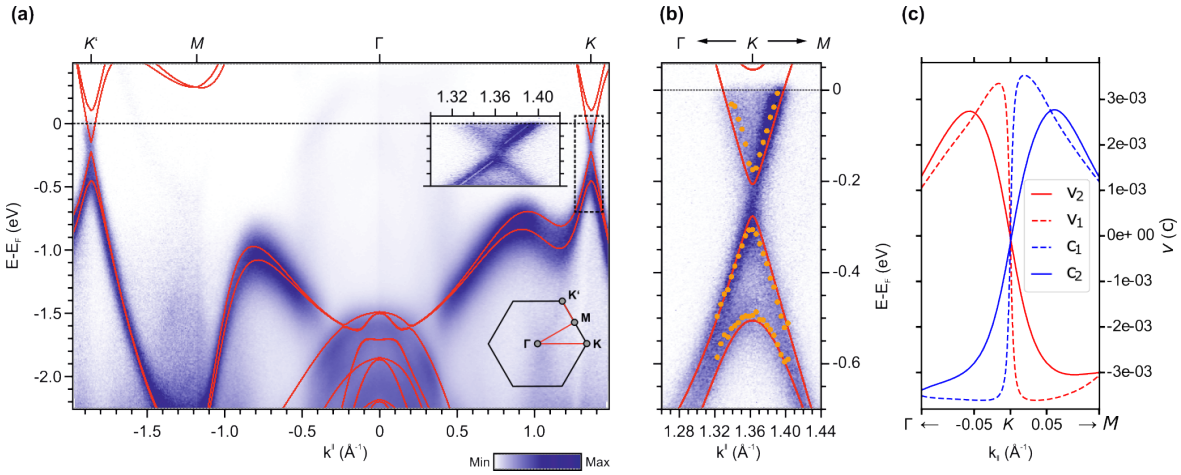

Figure 6.2.4.: (a) Comparison of ARPES (taken at $\approx 20\,\mathrm{K}$ and $h\nu = 21.2\,\mathrm{eV}$) and DFT band structure (red) and BZ schematics for the probed high symmetry cuts. The inset highlights the band situation at the valley momenta and shows a strong asymmetry in the spectral weight of the Dirac bands. (b) Zoom-in of the data shown in (a) at the valley momentum K, the orange dots indicate the maxima of the energy distribution curve fits (for details see Ref. [3]). (c) Band velocity v in units of the speed of light c of the Dirac states. Valence(conduction) bands are indicated by v(c), the index starts counting the states from the Dirac point. Reprinted figures in (a) and (b) from Bauernfeind, M. *et al.* "Design and realization of topological Dirac fermions on a triangular lattice". *Nature Communications* **12,** 5396 (2021). CC BY 4.0.

may be seen in the ARPES intensity distribution[4] shown in panel (b). The upwards dispersing states give rise to a strong signal, while the other bands are suppressed. Such an intensity modulation is well established in graphene and promotes a horse-shoe-shaped intensity around the valley momenta [184–189]. The mirror reflection planes intersecting at K [see again Fig. 2.4.1 (b)] enforce even and odd mirror reflection symmetry eigenvalues for the Dirac bands. In graphene, these symmetries are promoted by a non-local sublattice interference of the Bloch phase. As a result, both sublattices interfere destructively for the anti-symmetric state, which suppresses the ARPES intensity for the odd band. In indenene, this translates into radial and tangential polarization of the in-plane p-orbitals and the latter is suppressed. As a subtle detail, the vertical reflection symmetry breaking and SOC interaction in indenene on SiC mix radial and tangential orbital degrees of freedom. Hence, the radial-tangential polarization vanishes at the valley momenta[5]. This effect is also expected to occur in

[4] Under current investigation by Jonas Erhardt and Simon Moser. Emerged from a discussion on the orbital symmetry of the triangular in-plane bands discussed in Chaps. 4.1 and 6.1.

[5] See also the suppression of p_r and p_t polarization in the valence bands of AgTe in the presence of SOC in Fig. 6.1.2 (a).

transition-metal dichalcogenides, which profit from an even stronger inversion symmetry breaking [152, 190]. At larger momentum distances from K, the wave function is expected to recover the radial-tangential polarization, which will enforce the intensity modulation. This is subject to current investigation.

6.2.2. $\mathbb{Z}_2$-classification

The excellent agreement between theory and experiment in the structural properties and the band dispersion hints towards a non-trivial ground state. Nevertheless the analysis presented so far still lacks a bullet-proof indication of the topology. However, as introduced in Chap. 3 and illustrated in Fig. 6.2.1, chiral Dirac fermions on the triangular lattice interfere constructively on one of the A/B honeycomb sublattice sites. Upon embedding them in a global hybridization gap (see also Sec. 5.10), the $\mathbb{Z}_2$-index is encoded in the sublattice-projected DOS. Therefore, this suggests an energy- and real-space resolved analysis of the Dirac fermion charge density. Further, the lifted Kramers degeneracy will allow to probe the individual spinor contributions by varying the energy. While the analysis in Chaps. 3 and 5 focuses on a qualitative symmetry-based description, the *ab initio* and STM constant height $\mathrm{d}I/\mathrm{d}V$ data, presented in the following, unveils also the quantitative real-space wave function localization. The corresponding analysis is shown in Fig. 6.2.5. Addressing the p_z-dominated conduction states allows to determine the In atom lattice position [panel (a), 300 mV]. An energy sweep through the Dirac bands yields maxima at the A/B honeycomb positions: starting at a STM bias voltage of -400(-150) mV, where only the first valence(conduction) band contributes as illustrated in panel (b), the signal peaks at the A(B) site. At a voltage of -550(190) mV the second valence(conduction) band is expected to dominate [see again Fig. 6.2.4 (b)]. Indeed, at these energies, the charge maximum has switched position to the other sublattice site indicating $\nu = 1$. To confirm this sublattice polarization over the full-energy range of the Dirac cone, the difference in the local density of states at the A and B sites from DFT and STS measurement is shown in 6.2.5 (c,d). It complements the perfect agreement between theory and experiment: both possess a non-trivial localization pattern which switches with the onset of the second valence(conduction) band. Small deviations can be seen at STS voltages between -200 to 0 mV arising from a zero-bias anomaly, not present in the DFT calculations. As this is in general related to the STS measurement [191], i.e., it is not an intrinsic feature of the electronic ground state [192], it does not conflict with the assertions drawn on the $\mathbb{Z}_2$-topology (for details see [3] and supplemental material to Ref. [3]). Obviously, present $\mathbb{Z}_2$-classification depicts the topology of the subspace of bands in the whole BZ below the Dirac point energy[6]. Owed to the shift of the chemical potential to the Dirac cone conduction states induced by the SiC substrate, the experimental

[6] As the SiC substrate is a well-established trivial insulator and all other In-derived bands are either deep in the valence or conduction states, they are expected to be trivial. Hence, the $\mathbb{Z}_2$-topology of the low-energy bands determines the topology of the full system.

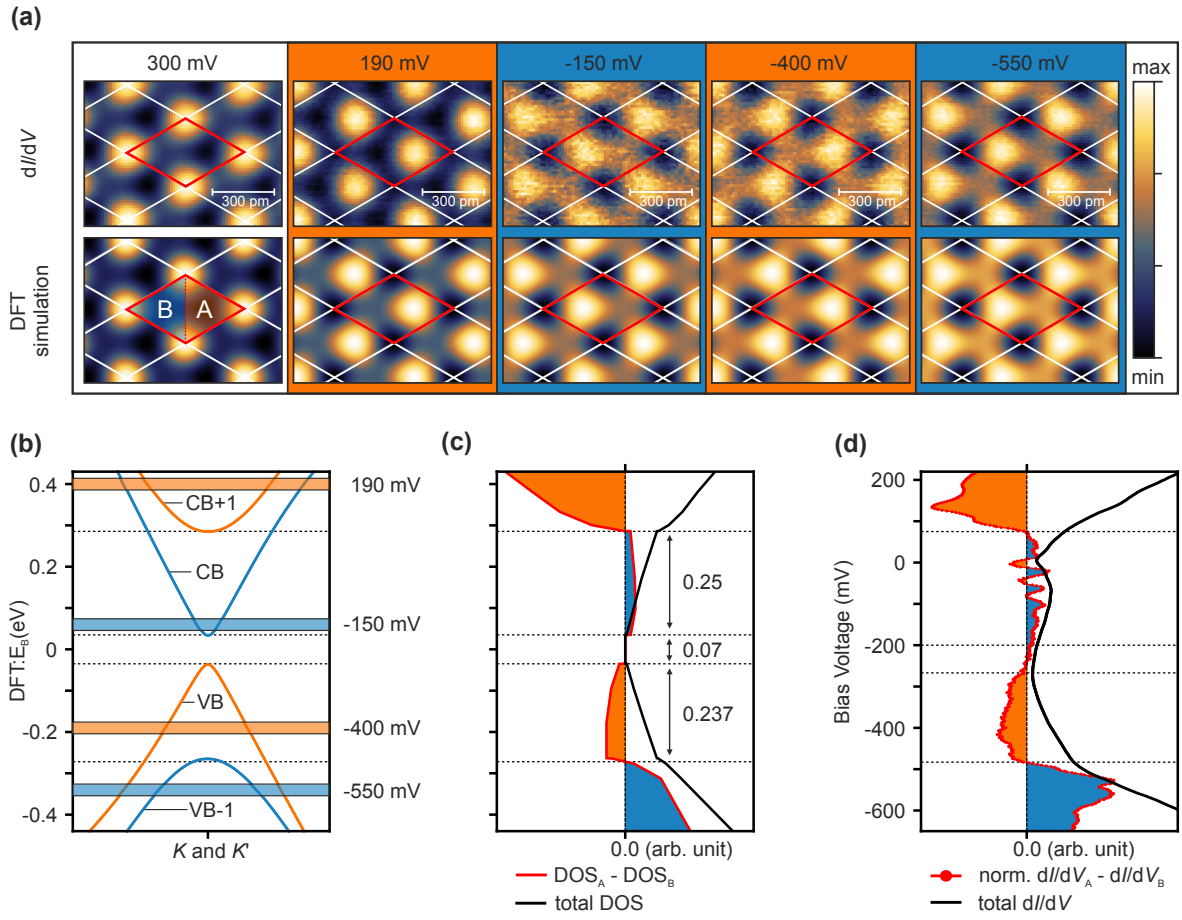

Figure 6.2.5.: $\mathbb{Z}_2$-classification of indenene from the valley charge localization. (a) Comparison of atomically resolved constant height $\mathrm{d}I/\mathrm{d}V$ maps and DFT charge density. The In lattice position is calibrated by addressing the In p_z states at a bias voltage of 300 mV. At the Dirac cone energies, the charge density exhibits a band dependent localization either at the A or B site. The particular switching pattern is assigned to the non-trivial $\mathbb{Z}_2$-topology. (b) Dirac cone band structure and conversion between DFT energy (given with respect to the Fermi level at neutral filling) and the applied STM bias voltage. Blue and orange colors denote the sublattice polarization of the bands, the horizontal bars depict voltage modulation ranges of the measurements shown in (a). (c) Total DOS (black line) and difference in the LDOS (red line) at the A/B sites. The blue and orange areas correspond to the dominant sublattice in the charge localization. The arrows and the numbers indicate the energy spacing in eV of the Dirac band maxima. (d) UC-integrated differential conductance (black line) and normalized difference of the $\mathrm{d}I/\mathrm{d}V$ spectra taken at the A/B sites. The noisy behavior at small negative bias voltages is attributed to the zero-bias anomaly (for details see supplemental material to Ref. [3]). Reprinted figures have been taken and adopted from Bauernfeind, M. *et al.* "Design and realization of topological Dirac fermions on a triangular lattice". *Nature Communications* **12,** 5396 (2021). CC BY 4.0.

realization may be regarded as a degenerately n-doped QSHI.

6.2.3. Orbital Symmetry as an Indicator for Real-Space Obstruction

As it has been discussed in Sec. 5.9 for a minimal indenene-like model ($\not{\sigma}_h$ QSHI), not only the valence Dirac states localize on the A/B sites, but also the time-reversal symmetry-breaking Wannier functions of the occupied bands are located at the honeycomb positions. Hence, it is interesting to investigate the real-space obstruction nature of indenene. However as an experimental analogue to the time-reversal violating Wannier construction (see Sec. 5.9) is missing, we will identify the real-space obstruction based on the band symmetries. In Chap. 5 the following key requirements have been identified: (I) a SOC opened in-plane Dirac cone at the valley momenta, (II) a p_z-type valence band around the BZ center and (III) a σ_h symmetry-breaking gapped nodal line (see also Fig. 6.2.3).

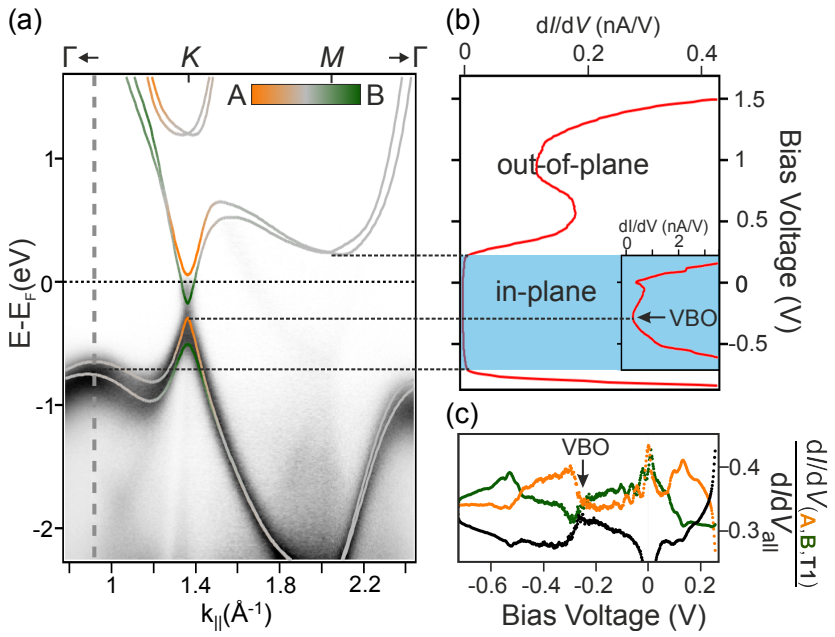

Figure 6.2.6.: (a) Comparison of the ARPES and G_0W_0 band structure, the sublattice DOS has been calculated according to Eq. A.29 in App. A.5. (b) STS spectra taken at tip-to-sample distances z_0 and $z_1 = z_0 - 7.8\,\text{Å}$ (inset) to tune the sensitivity to in-plane and out-of-plane wave functions. (c) $\mathrm{d}I/\mathrm{d}V$ spectrum measured at A (orange), B (green) and the T1 position (black line). Reprinted figures with permission from Eck, P. *et al.* "Real-space obstruction in quantum spin Hall insulators". *Physical Review B* **106,** 195143 (2022). © 2022 by the American Physical Society.

To this aim, Fig. 6.2.6 (a-c) presents a combined *ab initio*, ARPES and STS study

with the focus on the band symmetries. Panel (a) shows the comparison of the band structure and the ARPES results revealing a perfect agreement between theory and experiment. As also the conduction states will be addressed in the following, G_0W_0 calculations have been performed by Armando Consiglio[7] for a more accurate description of the hybridization gaps (for details see Ref. [2]). To tune the sensitivity of the STS experiment to the in-plane and out-of plane orbitals the tip-to-sample distance was varied. For large distances, the contribution of the in-plane bands to the STS signal can be expected to decay faster than the one of the out-of plane orbitals [193]. Such a result is shown in the main plot in (b), which shows a strongly suppressed signal at the energies of the Dirac bands. Pronounced shoulders can be seen at the energies of the valence band maximum along Γ-K and of the conduction band minimum at M. This indicates the presence of out-of plane bands at these energies [see again Fig. 6.2.3 (a)] and proves (II). Upon approaching the tip to the sample, the sensitivity to the in-plane bands is increased [inset to (b)]. In this setup, STS reveals the presence of electronic states in the p_z-gap indicating the Dirac cone in the ARPES measurement as being of in-plane type. Further, we can infer that the valence band character changes from p_z- to in-plane-type along Γ-K and Γ-M, which is indicative of a hybridization gap opened by mirror symmetry breaking (III). As experiment and theory reveal this gap to be significantly larger than the SOC-induced splitting, e.g., the Rashba splittings inside the BZ and the splitting at the valley momenta, it is evident that the horizontal reflection symmetry breaking dominates over SOC ($\lambda_{\not\sigma_h} \gg \lambda_{\mathrm{SOC}}$) (III). To further inspect the symmetry of the Dirac states, LDOS measurements on the three high-symmetry positions of the SiC surface are shown in Fig. 6.2.3 (c). At the Dirac band energies, the charge localization alternates for each band onset/offset between the A or the B site and indicates the SOC-opened gap (I), as discussed in the previous section. At higher bias voltages $> 0.2\,\mathrm{V}$, the spectral weight measured on the indium position T1 increases dominantly, which confirms the onset of the p_z minimum at M. Hence this analysis confirms the presence of all key features (I+II+III) of the $\not\sigma_h$ QSHI model, i.e., it puts forward indenene as the first experimentally realized real-space obstructed QSHI [2].

6.2.4. DFT-Functional and Structural Details

We will conclude the discussion on the bulk properties of indenene on SiC by quantifying the impact of the DFT functional and the adsorption site on the electronic band structure. The latter should not only be regarded as a confirmation of the structural model introduced in 6.2.1, but highlights also the qualitative differences of the three high-symmetry sites of the (111) and (0001) surfaces for future studies. For completeness, also C-terminated SiC will be considered.

The band structures for a generalized gradient approximation functional (PBE), a

[7] Theoretische Physik I, University of Würzburg.

hybrid functional (HSE06) and the G_0W_0 approximation[8] are shown in Fig. 6.2.7 (a) for the unit cell relaxed with HSE06. Focusing on the In valence bands, PBE and G_0W_0 are in reasonable agreement, while HSE06 yields significantly lower eigenvalues at Γ. In conduction, G_0W_0 and HSE06 are almost on top of each other and the PBE bands are at lower energies along K-M in this energy range. The minimum nearby M is below the second conduction band of the Dirac cone. At the valley momenta, the gap and average spin-splittings in the valence and conduction bands are in meV for PBE (gap, splitting)=(13, 248), HSE06 (70, 240) and G_0W_0 (73, 223). The Wilson loop reveals $\nu = 1$ for all calculations. Hence, the three functionals are in qualitative agreement, however the quantitative band energies are strongly sensitive to the chosen functional. Further, for a fixed reference unit cell, PBE results in the largest $\not{\sigma}_v$-splitting and the smallest valley gap. Based on the comparison with the experiment (see again Figs. 6.2.4 and 6.2.7), HSE06 and G_0W_0 result in the best description of indenene on SiC, which indicates the importance of the electron screening via the substrate. To address the edge states in finite size geometries in the next section, we will fall back to PBE due to the extensive computational demand of the other two functionals. However the results need to be interpreted in the light of the present discussion. Their quantitative description may change significantly with more sophisticated methods.

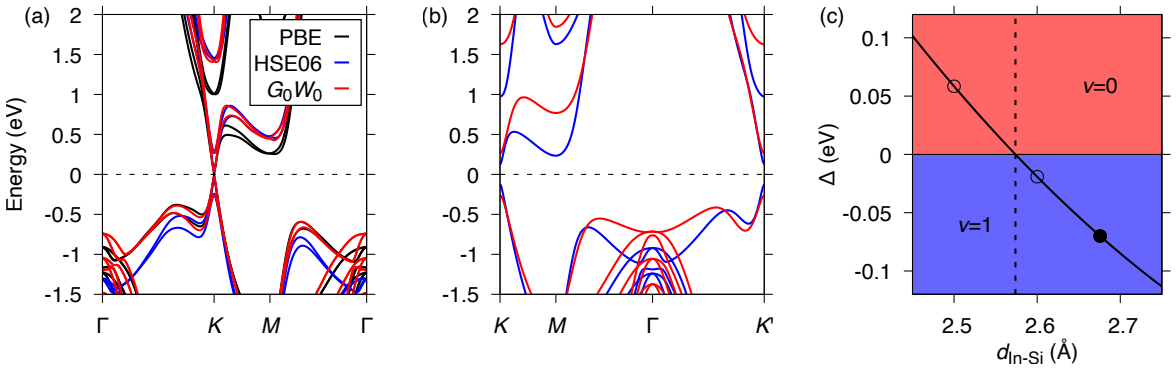

Figure 6.2.7.: (a) Investigation of the dependency of the band structure on the DFT functional. The HSE06-relaxed UC has been used for all functionals. (b) Impact of the bonding distance on the spinless band structures obtained with PBE. The blue and the red lines correspond to the equilibrium bonding distance and a bonding distance reduced by −0.4 Å, respectively. (c) Valley gap Δ and $\mathbb{Z}_2$-invariant ν as a function of the distance of the In atom to the Si atom at the SiC surface. The filled circle indicates the equilibrium distance, empty circles depict further data points and the black line illustrates a fit of the HSE06 obtained data set. The dashed vertical line illustrates the critical distance $d_{\text{crit}} = 2.57$ Å. The positions of the substrate sites have been kept fixed in all calculations shown in (b) and (c).

[8]The gap at the valley momenta has been obtained upon extrapolating to an infinitely dense k-grid, for details see Ref. [2].

Continuing with the structural details, the In-substrate bonding distance is the crucial parameter, as it mediates the horizontal and vertical reflection symmetry breaking. If both dominate over SOC, the considered subset of bands is $\mathbb{Z}_2$-trivial (see also Chap. 5). Further it should be noted that the freestanding In layer is metallic. This also explains the huge experimental and theoretical effort in the structural classification, which is also of importance for the ongoing capping and intercalation studies at the chair of EP IV. To this purpose Fig. 6.2.7 (b) shows the spinless band structure at the equilibrium bonding distance (blue lines). Upon approaching In to the substrate (red bands), the vertical reflection symmetry breaking opened gap of the in-plane Dirac cone increases, which favors $\nu = 0$. Further the p_z-type band at K and around Γ is pushed to higher energies. In addition, the gapping between the radial in-plane and the p_z-band via the horizontal reflection breaking is enhanced. Considering also SOC, panel (c) shows the dependency of the valley gap on the bonding distance. For HSE06 the topological phase transition occurs at $d_{\mathrm{crit}} = 2.57\,\text{Å}$ and the first derivative of the gap function at the equilibrium distance yields a slope of $-0.63\,\mathrm{eV\AA}^{-1}$.

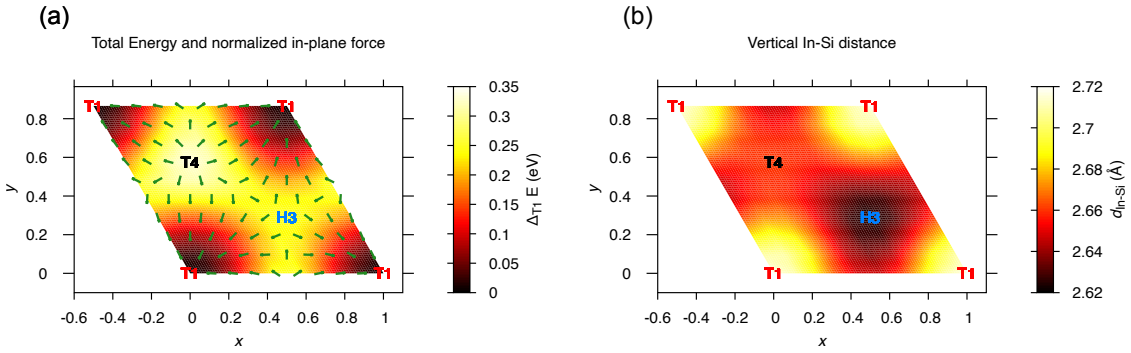

Figure 6.2.8.: Adsorption study of In on the Si-terminated 1×1 SiC(0001) surface calculated with PBE. (a) Total energy with respect to its global minimum for adsorption on the T1 site and normalized in-plane force (vector field plot). (b) Vertical distance between indium and surface silicon, yielding a maximum for indium adsorption at T1. The in-plane x and y coordinate are given in units of the lattice constant. Reprinted figures of the supplemental material from Bauernfeind, M. *et al.* "Design and realization of topological Dirac fermions on a triangular lattice". *Nature Communications* **12,** 5396 (2021). CC BY 4.0.

Considering adsorption not only on the T1 site, Fig. 6.2.8 shows an in-plane coordinate dependent study of the total energy landscape and the in-plane forces as well as the In-Si distance obtained with PBE. The total energy has a saddle point at H3 and a global maximum at the T4 site with values of 245 and 340 meV, respectively, larger compared to the T1 position. This confirms from theory the adsorption of the indium atom at the T1 site. Further the In-Si distance $d_{\mathrm{In-Si}}$ [see panel (b)] is largest for the T1 site, which implies an increased vertical reflection symmetry breaking on the H3

and T4 position owed to the reduced distance to the substrate surface.

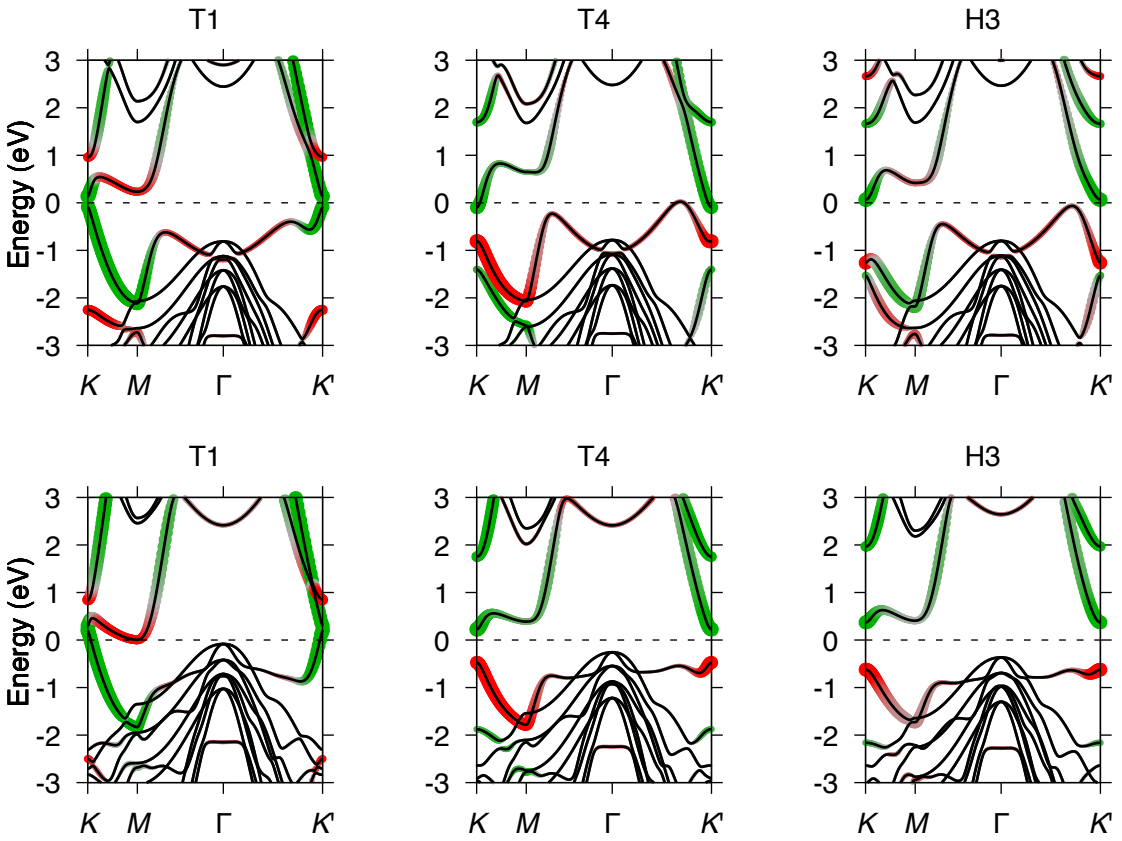

Figure 6.2.9.: Band structures of In adsorbed on the high symmetry positions of the Si- and C-terminated SiC(0001) surface in the top and bottom row, respectively. The point size denotes the total In character, while the color code depicts the $s + p_z$ (red) and $p_\pm$ (green) orbital contribution. All plots show spinless calculations obtained with the PBE functional.

This is also reflected in the band structure (without SOC) shown in Fig. 6.2.9, where the splitting of the in-plane bands at the valley momenta is orders of magnitude larger compared to the T1 position. These unit cells lack a narrow-gap Dirac cone feature. For T4, the In s-type valence band is located in the in-plane gap at the valley momenta and the p_z-band is pushed into the conduction states, the overall band structure is metallic. H3 yields instead an insulating band structure, which is rendered metallic if SOC is considered (see also supplementary material to Ref. [3], Fig. 10). As the hybridization gaps, opened by symmetry breaking, are much larger than the SOC interaction, these systems are $\mathbb{Z}_2$-trivial. The strong vertical reflection symmetry breaking might stabilize a finite quadrupole moment (assuming a global gap), however as these configurations are metallic in the presence of SOC and as they have not been realized in experiment, this analysis has not been pursued further.

Although having the same layer group, adsorption on the C-terminated surface is expected to yield quantitatively different results owed to the large electronegativity of carbon. This is also reflected in the reduced vertical bonding distances between the In atom and the C atom of the surface layer, which are 2.28, 2.20 and 2.08 Å for the T1, T4 and H3 position, respectively. Similarly to the Si-terminated surface, the total energy is minimized on T1 and increased by 495 meV on T4 and by 325 meV on H3. The corresponding band structures are shown in the lower row of Fig. 6.2.9. Adsorption on T1 promotes a band ordering and orbital character similar to the one obtained on the Si-terminated surface, albeit being metallic. T4 and H3 are instead insulating with a predominant sp_z-type band in valence, which hints towards a $\mathbb{Z}_2$-trivial ground state with vanishing bulk quadrupole moment.

6.2.5. Edge States

Having established the bulk properties of indenene on SiC, we will discuss in the following its topologically protected edge states in finite size geometries. As this requires large lateral UCs, we will reduce the substrate to one layer of SiC and employ the PBE functional, to keep the numerical effort within controllable limits. Hence, the results have to be interpreted by considering also the discussion of the previous section, e.g., the underestimation of the hybridization gaps. On the other hand, the *ab initio* treatment takes into account the edge potential self-consistently, in contrast to finite-size calculations based on the bulk tight-binding parameters as analyzed in Sec. 5.6. We account for this by considering a 2D SiC substrate with 1D indenene structures as shown in Figs. 6.2.10 and 6.2.12. To avoid metallic dangling bonds, hydrogen passivation is applied to the non-indium occupied Si sites.

Starting with the flat edge as shown in Fig. 6.2.10, a UC with eleven In sites is considered which corresponds to a terrace width of 26.6 Å. The in-plane spacing between periodic indenene slab replicas is 16.0 Å. Its band structure possesses four metallic exponentially localized edge states connecting the insulating valence and conduction bulk states, a consequence of the non-trivial topology. The vertical mirror reflection parallel to the edge is broken via the presence of the C atom, which renders the left and the right edge inequivalent. This lifts the degeneracy of the edge states located on opposed terminations. The associated charge density at $\overline{\Gamma}$ shows that the edge state is not solely in-plane derived, but has also a sizable p_z contribution. Albeit the low-energy Dirac physics in the bulk arises from the in-plane orbitals, the p_z-orbital is at play in the edge state. As discussed in Sec. 5.6, this allows for the formation of in-plane OAM which cants also the spin alignment from out-of plane towards in-plane.

A detailed analysis of the localization and spin-alignment of the edge states is presented in Fig. 6.2.11. Panel (a) shows the squared amplitude of the wave function over the slab $|\Psi(y)|^2$ at $\overline{\Gamma}$ in the plane of the indium atoms. Additionally, an exponential

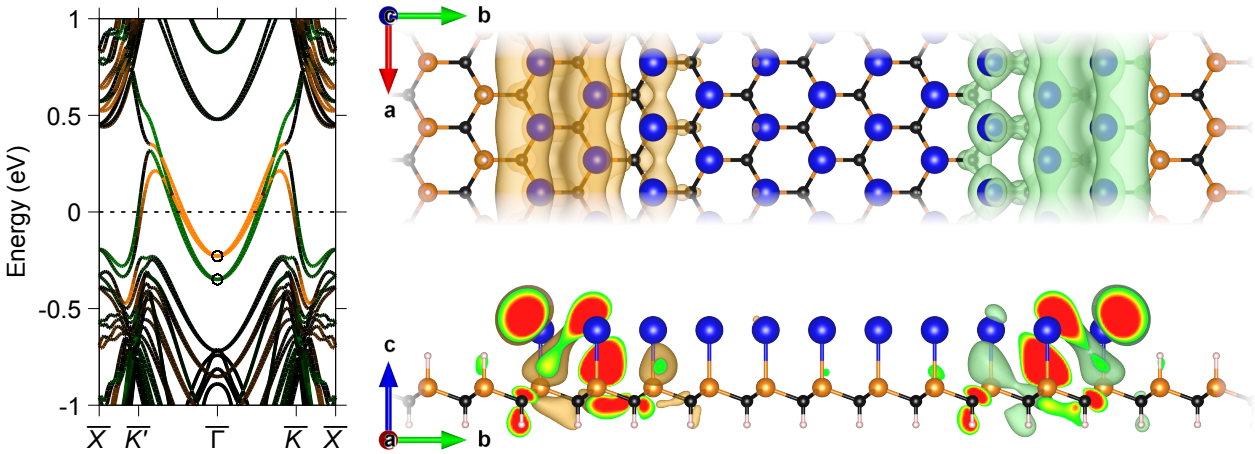

Figure 6.2.10.: Band structure and charge localization of the edge states at $\overline{\Gamma}$ (indicated by the open circles in the band structure plot). The orange and green color denotes the projection onto the left and the right edge, respectively.

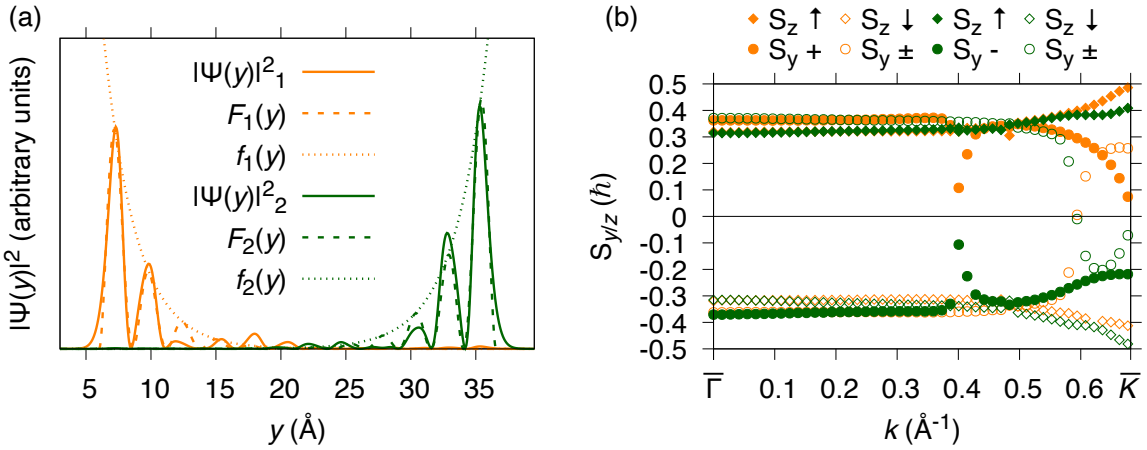

Figure 6.2.11.: (a) Exponentially localized wave package fit of the edge states. The colors denote the edges following the scheme of Fig. 6.2.10, the details of the fit are given in the text. (b) Spin polarization of the edge states. The color denotes the edge as in Fig. 6.2.10. For each edge, filled(empty) symbols are used for the band with dominating positive(negative) S_z polarization. The y and z spin components are given by diamonds and circles, respectively. As indicated by the empty circles, the sign of the S_y component switches at $0.6\,\text{Å}^{-1}$ for bands with negative spin down polarization.

fit for determining the bulk penetration length is presented:

$$F(y) = f(y) \cdot \sin(b \cdot y + c)^2, \quad f(y) = A^2 \cdot \exp(-2R \cdot y). \tag{6.6}$$

Assuming a massive Dirac system with mass m and Fermi velocity v_F [16, 19], the wave function has the real space parametrization in the non-periodic direction

$$\Psi(y) \propto \exp\left(-\int_0^y dy' m(y')/v_F\right). \tag{6.7}$$

This allows an estimation of the bulk gap, which damps the decay into the bulk. The edge states have a decay constant of $|R| \approx 0.2\,\text{Å}^{-1}$ and a Fermi velocity of $v_F \approx 1\,\text{eVÅ}$ for a linearized dispersion throughout the whole gap. Assuming a constant mass parameter yields $m \approx 0.2\,\text{eV}$, which is twice as large as the bulk gap at the valley momenta. However this is not the relevant energy scale, as the exponential damping of the edge states is mediated by the bulk gap at the given slab crystal momentum [74]. At $\overline{\Gamma}$ the projected bulk gap onto the 1D BZ is much larger than the global gap, since it is defined by the hybridization gap of the back-folded bulk states along Γ-M, which is 0.85 eV in PBE. Further, this approximation neglects spatial variations of the mass parameter. Therefore it cannot account for sizable hybridization gaps at the edges opened by the broken lattice periodicity and the edge potential. However, due to the relatively small slab width, separate fits for the edge and the bulk region are out of reach.

The non-zero components of the spin polarization are shown in Fig. 6.2.11 (b). The S_y and S_z components are almost of similar size and remain constant until the edge state approaches the projected valley momentum. S_y deviates from this behavior around $0.4\,\text{Å}^{-1}$, where two edge states cross. Close to $\overline{K}$, the S_y component switches for bands with predominant S_z-down character [see description to Fig. 6.2.11 (b)]. At $\overline{K}$ all states possess a dominant S_z polarization. The spin canting from out-of plane towards in-plane is a clear indicator of the formation of in-plane OAM, which arises from the horizontal reflection symmetry breaking. Away from the projected valley momenta, mirror symmetry breaking dominates over SOC. This results in a dominant OAM polarization for states located at the same edge. SOC acts as a weak perturbation and promotes an anti-parallel spin-alignment. Approaching $\overline{K}$, the SOC-opened gap in the in-plane subspace takes over, which is reflected in the abandonment of the anti-parallel spin alignment until out-of plane polarization is reached.

We will turn now to the other fundamental termination of the triangular lattice, namely the zigzag edge. As shown in Fig. 6.2.12, we consider a 35.3 Å wide terrace (corresponding to twelve repetitions of the conventional bulk unit cell), periodic in-plane replicas are separated by a distance of 10.8 Å. The presence of the C atom in the substrate breaks reflections on a plane normal to the edge. Further, as the UC contains an integer repetition of the conventional unit cell, it is not inversion symmetric and lacks a diagonal reflection σ_d parallel to the edge[9]. Its band structure and the charge localization of the low-energy valence state at $\overline{Y}$ are shown in Fig. 6.2.12. This geometry is insulating with strongly edge localized low-energy states at the BZ bound-

[9]Inversion and σ_d is only preserved in $n+1/2$ repetitions of the bulk UC, i.e., upon adding/removing one vertical line of In atoms at the edge.

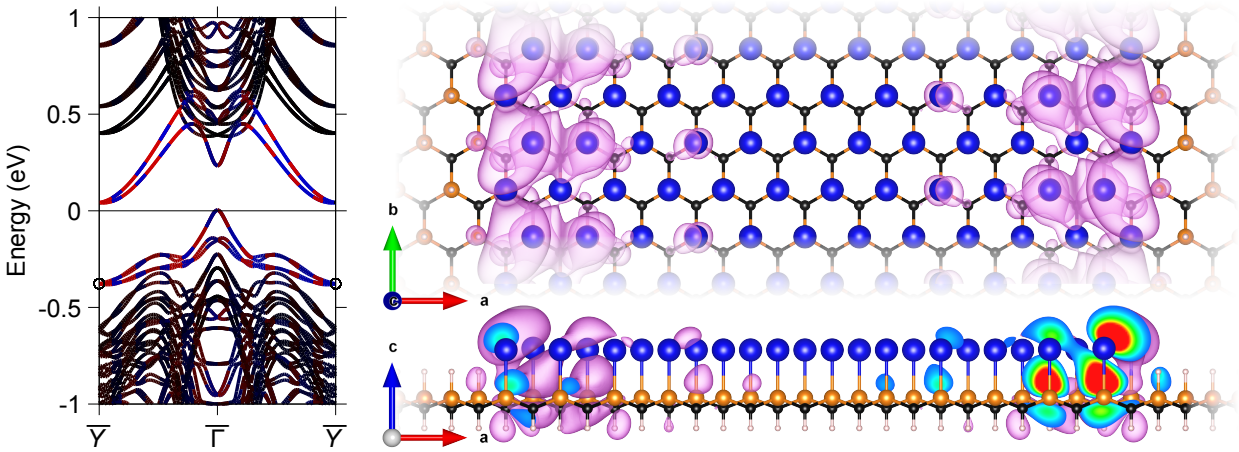

Figure 6.2.12.: Band structure and charge localization of the edge states at $\overline{Y}$ (indicated by the empty circles in the band structure plot). The red and blue color denotes the projection onto the left and the right edge, respectively. For an improved visualization, the edge character is plotted by projecting alternatingly on the opposed edges.

ary. They are almost degenerate, but spin-splittings are visible in valence along $\overline{\Gamma}$-$\overline{Y}$, owed to the absence of inversion. Instead referring to Sec. 5.6, a Dirac-type edge state crossing at $\overline{\Gamma}$ is expected in the thick slab limit. In the shown geometry, the weights obtained from projection onto the edge sites declines around $\overline{\Gamma}$, which indicates an increased localization across the indenene flake (see also Fig. 6.2.13). This opens a hybridization gap between the edge states, the flake width is insufficient to disentangle states located at opposed edges. A similar behavior is observed for graphene [182, 194], whose arm-chair edge corresponds to the zigzag termination of the triangular lattice. This behavior can be understood from the mapping of 2D bulk momenta onto the 1D slab BZ (see also Fig. 5.6.1). For the flat termination, the edge states occur at momenta where the projected bulk band structure has a wide gap, i.e., it can be interpreted as a SSH model [17] in its dimerizing phase [74]. Instead for the zigzag edge, the narrow gapped Dirac fermions at K and K' are mapped onto $\overline{\Gamma}$. Hence, the edge states live in a very small bulk gap, which allows them to deeply penetrate into the bulk. In turn, the intra-bulk hybridization of the edge states is sizable and promotes a gapped edge states. In agreement with the minimal model calculations (see also Fig. A.7.1) and in contrast to the flat edge, the spin polarization is solely in-plane oriented as the out-of plane component vanishes as shown in Fig. 6.2.13.

Focusing on the charge distribution of the four-fold degenerate valence state at the TRIM $\overline{Y}$, as shown in Fig. 6.2.12, its wave function is heavily edge localized. The in-plane charge distribution unveils the absence of inversion symmetry: the vertical reflection symmetry breaking driven by the C atom promotes a strong asymmetry with respect to reflection planes normal to the edge ($y \mapsto -y$). Further, the edge

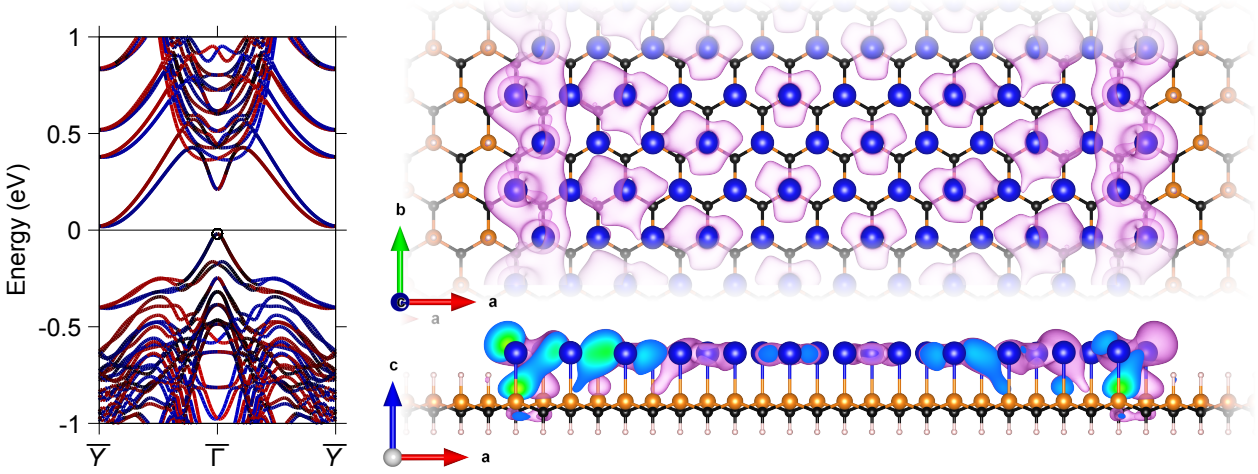

Figure 6.2.13.: Tangential spin polarization (S_x) in the left panel. Positive and negative values are denoted by blue and red colors, respectively. The empty circle highlights the state, for which the charge localization is shown at the right.

charge density is invariant under a diagonal reflection onto the other edge followed by a fractional translation of half a lattice constant parallel to the edge. Again, the side view unveils the importance of the p_z-orbital in indenene, as the edge state exhibits also a strong out-of plane character. The hybridization of the edge states via the bulk at $\overline{\Gamma}$ is shown in Fig. 6.2.13. This gives rise to a $\sqrt{3}\times\sqrt{3}$ reconstruction, which has been also reported and attributed to the inter-valley coupling in graphene supercells [195]. For a quantitative comparison of the edge localization, the squared wave function amplitude over the slab at $\overline{Y}$ and $\overline{\Gamma}$ is shown in Fig. 6.2.14. The edge state decays fast into the bulk at $\overline{Y}$ in (a). A wave packet fit introduced in Eq. 6.6 yields $|R| \approx 0.1\,\text{Å}^{-1}$. At $\overline{\Gamma}$ [panel (b)], the periodicity of the edge state changes when penetrating into the bulk. This makes a fit with the aforementioned parametrization challenging. Nonetheless, the enveloping function $f(x)$ describes reasonably well the maxima of the squared wave function, the decay constant is $|R| \approx 0.04\,\text{Å}^{-1}$. This value is one order of magnitude smaller compared to the flat-edge geometry. It reflects on a quantitative level the weak damping of the edge state penetration due to the small projected bulk gap at $\overline{\Gamma}$. While this *ab initio*-derived trend is expected to be robust on the qualitative level, the absolute numbers need to be conceived with care owed to the fitting procedure, the relatively small flake widths, the thin single layer substrate and the treatment within the PBE functional (see also Sec. 6.2.4).

The comparison of the two fundamental edge geometries has unveiled qualitative differences in the edge localization and spin polarization of the edge states. Similar to other trigonal and hexagonal systems, the edge states penetrate deeply into the bulk if they happen to occur at the projected bulk Dirac momenta. In contrast to graphene

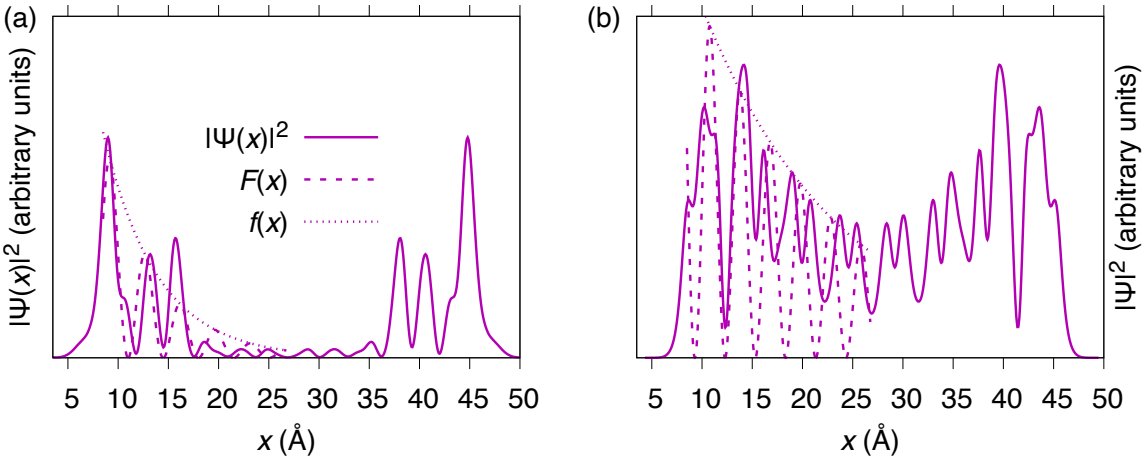

Figure 6.2.14.: Exponentially localized wave package fit of the edge state at $\overline{Y}$ and $\overline{\Gamma}$ in (a) and (b), respectively. The corresponding illustration of the associated charge density can be found in Figs. 6.2.12 and 6.2.13. The fitting details are given in the text and the fit functions are defined in Eq. 6.6.

and bismuthene, in-plane *and* out-of-plane orbital degrees of freedom participate in the edge states, which tilts the spin polarization from out-of-plane towards in-plane for the flat edge. Instead for the zigzag edge, the spin alignment is purely in-plane.

6.2.6. Conclusion and Outlook

In close collaboration with the experiment, indenene on SiC has been put forward as the first real-space obstructed triangular monolayer QSHI. Its trigonal (almost hexagonal) symmetry promotes a SOC-gapped Dirac cone. It is located in a sizable hybridization gap in the p-bands, opened by the horizontal reflection symmetry breaking via the substrate. Indenene has been unambiguously classified as $\mathbb{Z}_2$-non-trivial upon addressing the real-space localization of the bulk Dirac bands, i.e., without searching for the topology-promoted quantized features in its transport properties.

A detailed analysis of the wave function symmetry in the whole BZ from theory and experiment has classified indenene as being real-space obstructed. The time-reversal symmetry-breaking valence band Wannier centers localize on the honeycomb positions in the voids of the triangular lattice. This extends the concept of real-space obstruction to the $\nu = 1$ regime and calls immediately for the investigation of edge and corner states in heterostructures involving no or differently obstructed QSHIs. In particular, interfacing indenene with the other large gap QSHI on the same SiC substrate, bismuthene, could be highly promising.

Indenene's edge states are qualitatively comparable to graphene's, as the flat edge

hosts strongly localized states, while the zigzag edge (corresponds to the honeycomb's armchair edge) allows for a sizable bulk penetration length. However a fundamental difference can be seen in the orbital composition, as the full p shell is involved in the formation of the edge states. In the flat geometry this promotes in-plane and out-of plane spin and OAM polarization, which makes them particularly interesting for transport applications relying on electrons with strongly coupled orbital and spin degrees of freedom.

6.3. HOTIs on SiC, the Lightweight Siblings of Indenene

Inspired by the discovery of indenene on SiC and based on the profound symmetry analysis presented in Sec. 2.4 and Chap. 5, a design principle for higher-order topology in triangular monolayer adsorbates will be conceived. The results have been obtained in a highly enjoyable and productive collaboration with with Yuan Fang[10] and Jennifer Cano[11]. As highlighted in Chap. 5, a HOTI phase can be stabilized by a p-shell on the triangular lattice, if vertical and horizontal reflection symmetry breaking dominate over SOC, especially if SOC vanishes. As discussed for indenene on SiC (see again Sec. 6.2.1), adsorption on the high symmetry sites of the (111) surfaces of zinc-blende- and diamond-type insulating substrates, such as SiC, Si, GaAs, InSb, etc., results in layer group p3m1, which is exactly the symmetry, where the HOTI phase is expected to occur (see also Sec. 5.7). However the sizable SOC renders indenene a real-space obstructed QSHI, which forbids a time-reversal symmetric Wannier construction. Hence, to achieve a $\mathbb{Z}_2$-trivial ground state with insulating edges it is instructive to inspect lighter Group III atoms on the T1 position on SiC(0001). In the following, we will propose triangular adatom layers of boron, aluminum and gallium as potential candidates for the experimental realization of the triangular HOTI phase [4]. As a paradigmatic example for corner states in Group III adsorbates, the bulk and finite size properties of the Al adsorbate will be discussed in detail.

6.3.1. Unit Cell and Bulk Electronic Structure

Equivalently to indenene on SiC, we will consider in the following adsorption on the T1 position as shown in Fig. 6.3.2 [see also Fig. 6.2.2 (a,b)]. This provides three important key ingredients: (I) structural stabilization of a triangular adsorbate monolayer; (II) symmetry breaking across the horizontal mirror plane to open a hybridization gap ($\hat{H}^{\phi_h}$) between the in-plane and out-of-plane orbitals; and (III) symmetry breaking

[10] Stonybrook university, New York, USA.
[11] Stonybrook university, New York, USA and Center for Computational Quantum Physics, Flatiron Institute, New York, USA.

LG	ν	SOC vs $\not\sigma_h$	SOC vs $\not\sigma_v$	IRREPs Γ	IRREPs K	$\mathbf{P} = (P_1, P_2)$	Q_{12}
p3m1	0	$\lambda_{\mathrm{SOC}} \ll \lambda_{\not\sigma_h}$	$\lambda_{\mathrm{SOC}} \ll \lambda_{\not\sigma_v}$	$\overline{\Gamma}_6(2)$	$\overline{K}_4(1) \oplus \overline{K}_6(1)$	$(\frac{2}{3}, \frac{1}{3})$ mod 2	$\frac{2}{3}$ mod 1

Table 6.3.1.: Summary of the triangular HOTI phase of the Group III adsorbates on SiC(0001). The UC symmetries stabilize a $\mathbb{Z}_2$-trivial band structure with finite dipole and quadrupole moment, which is determined by the irreps of the valence bands at Γ and K. Reprinted table of the supplemental material with permission from Eck, P. *et al.* "Recipe for higher order topology on the triangular lattice". *Phys. Rev. B* **107,** 115130 (2023). © 2022 by the American Physical Society.

across the vertical mirror planes ($\hat{H}^{\not\sigma_v}$) via the presence of the C atom in the SiC surface layer to gap the Dirac states by inducing a finite bulk quadrupole moment[12] [4] (see also Tab. 6.3.1). A relaxation of B, Al, and Ga with the PBE functional yields bonding distances to the Si-atom of the size of $d_{\mathrm{B}} = 2.03\,\text{Å}$, $d_{\mathrm{Al}} = 2.53\,\text{Å}$ and $d_{\mathrm{Ga}} = 2.51\,\text{Å}$.

As shown in Fig. 6.3.1, all three adsorbates give rise to an insulating band structure. The valence bands have a predominant p_z character around Γ and in-plane character at the BZ boundary. The impact of the horizontal reflection symmetry breaking can be seen along Γ-M and Γ-K. The change in the valence band orbital character from p_z to radial in-plane alignment is accompanied by a large hybridization gap around the Fermi energy [see Fig. 6.3.2 (a,c) for orbital symmetry]. Further, the vertical reflection symmetry breaking gaps the in-plane Dirac cones at the valley momenta by $\Delta_{\mathrm{B}} = 0.49\,\text{eV}$, $\Delta_{\mathrm{Al}} = 0.24\,\text{eV}$ and $\Delta_{\mathrm{Ga}} = 0.22\,\text{eV}$. The spin splitting resulting from the SOC interaction is 1, 12 and 81 meV for B, Al and Ga, respectively. Focusing on characteristic differences, the p_z state is strongly bound to the adatom in the case of B. This results in a small bandwidth and a weak hybridization with the SiC quantum well states at Γ. For Al and Ga, the p_z state is more dispersive and hybridizes strongly with the SiC states [see also Fig. 6.3.2 (a)]. However for Ga and B, the p_z state at M is located in the Dirac cone gap, which results in global indirect band gaps of 0.18 and 0.27 eV, respectively. As it has been discussed for indenene in Sec. 6.2.4, the relative alignment of the low-energy band extrema is expected to be highly DFT-functional dependent.

[12] Further details can be found in Secs. 5.5 and 5.7.

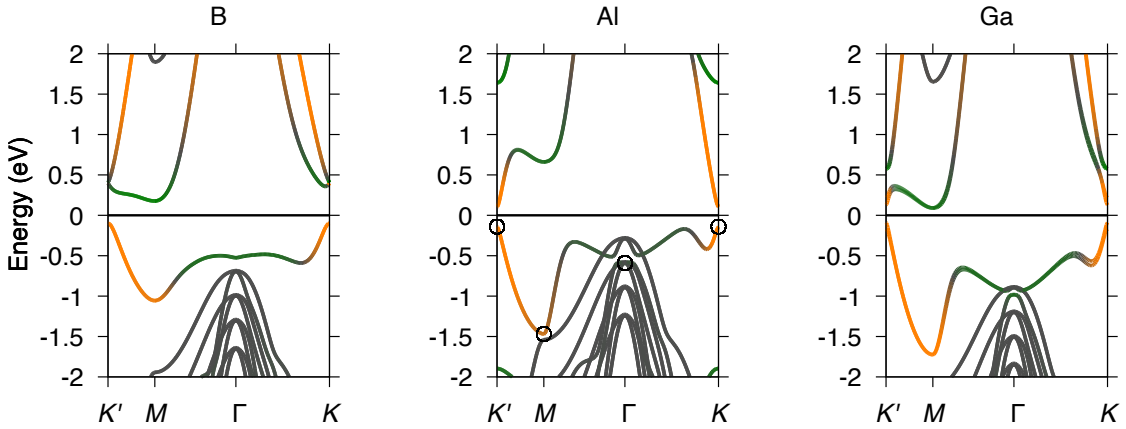

Figure 6.3.1.: Bulk band structure of the three triangular adsorbates on the T1 position of four layers SiC(0001). The green and orange color code denotes the $s+p_z$- and the $p_\pm$-character, respectively. The empty circles in (b) depict the states for which the real-space squared amplitude is illustrated in Fig. 6.3.2. Reprinted figure taken and adopted from the supplemental material with permission from Eck, P. *et al.* "Recipe for higher order topology on the triangular lattice". *Phys. Rev. B* **107,** 115130 (2023). © 2022 by the American Physical Society.

6.3.2. Band Symmetry Driven Electronic Multipoles

All band structures are insulating and $\mathbb{Z}_2$-trivial as the valence band doublet localizes on the same sublattice positions [see Fig. 6.3.2 (b) and Sec. 6.2.2 for argumentation]. Therefore the position of the bulk Wannier centers and the resulting electronic bulk multipoles can be calculated from symmetry indicators. For all three configurations, the highest adsorbate valence band transforms under the $\overline{\Gamma}_6(2)$, $\overline{M}_3\overline{M}_4(2)$ and $\overline{K}_4(1)\oplus\overline{K}_6(1)$ irreps. This is an elementary band representation of Wyckoff position $1b$, which corresponds to the H3= $(1/3, 2/3)$ position [A site in Fig. 6.2.2 (b), see also panel (d) of Fig. 6.3.2]. Hence the electronic dipole moment is $\mathbf{P} = 2e(2/3, 1/3)$ and the quadrupole moment is $Q_{12} = 2e/3$ (see also Tab. 6.3.1). Similarly, this can be also derived from the C_3 rotation eigenvalues at Γ and K which arise from the total angular momentum $j_z = \{-1/2, 1/2\}$ and $j_z = \{1/2, 3/2\}$, respectively, and recalling Eqs. 5.12 and 5.14. The real-space obstruction is illustrated in Fig. 6.3.2 by showing the squared wave function amplitude at the high symmetry momenta. At Γ (a) the adatom centered p_z-type wave function penetrates deep into the substrate and has maxima along the vertical bonds. This is different for K (b) and M (c), where the wave function has a node on the triangular lattice site and its maximum is located in the void space. The high-symmetry momenta integrated wave function (d), which may be qualitatively

regarded as the valence band Wannier function[13], is centered on the H3 site. This illustrates the finite electronic dipole and qadrupole moment of the unit cell. However it should be noted, that this quantitative analysis depends strongly on the radial scaling of the wave function, because its maximum is not necessarily centered on H3. Boron for instance has a strongly bound $2p$ states, which result in maxima centered in between the H3 and the adatom position. Nevertheless, as the localization argument is solely band symmetry based, the corresponding valence band Wannier function is centered at H3.

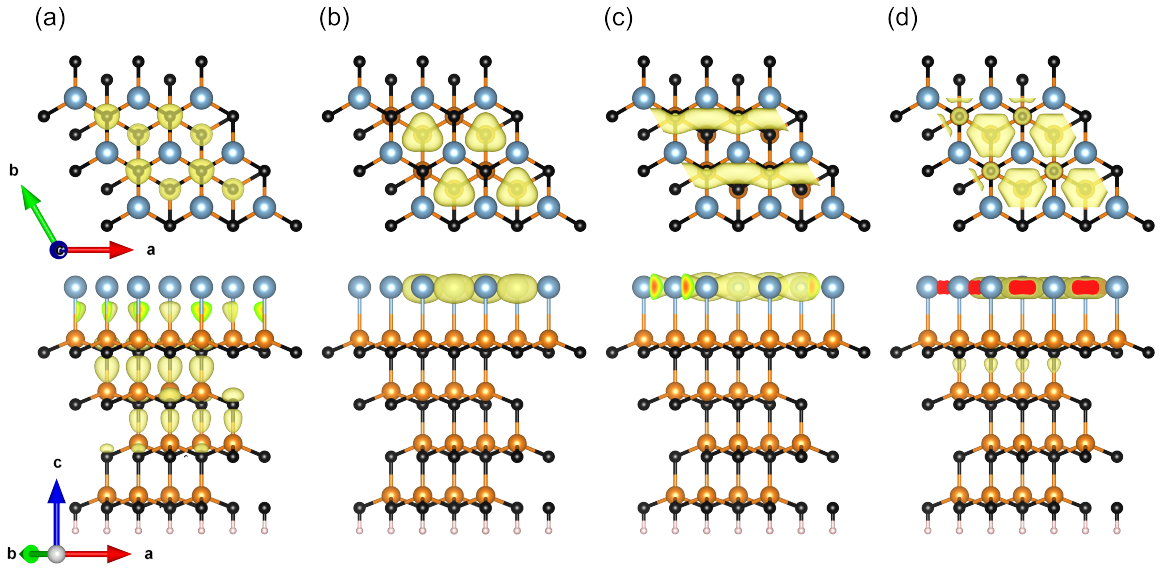

Figure 6.3.2.: Qualitative construction of a Wannier function for Al on SiC(0001). Panels (a-c) show the squared wave function of the Al-derived valence band at Γ (a), K (b) and $M = (0, k_y)$ (c). The corresponding states are highlighted by empty circles in Fig. 6.3.1 (b). (d) presents the over all six high symmetry momenta (Γ, K, K' and $3M$) summed squared amplitude, which can be regarded as a qualitative representation of the valence band Wannier function. The isosurface value in (d) is four times larger than in (a-c). The color scheme of the atoms follows Fig. 6.2.2, Al is depicted by light-blue colors.

6.3.3. Edge States of Al

To observe metallic in-gap states at the corners, it is important to stabilize an insulating gap at the 1D edges. Here, we will briefly discuss the edge states of Al on SiC, which can be regarded as the $\mathbb{Z}_2$-trivial analogues of the indenene edge states presented

[13]This is only a qualitative argument as the construction of the Wannier function requires the integration over the full BZ (see Eq. 2.52). The high-symmetry momenta do not constitute an appropriate sampling grid.

in Sec. 6.2.5. As it has been demonstrated for the minimal model in Sec. 5.6, the finite bulk dipole results in polar flat edges, which favor metallicity. The DFT calculation shown in Fig. 6.3.3 (a) shows that this also the case for Al. For the tight-binding model [see again Fig. 5.6.2 (IV)] states living on opposite edges are degenerate at $\overline{\Gamma}$. Instead, the realistic treatment of the edge potential in the *ab initio* calculation gaps the edge states at $\overline{\Gamma}$ resulting in metallic edge state crossings along $\overline{\Gamma}$-$\overline{K}$, i.e. it enforces a metallic slab band structure. The lifted degeneracy at can be understood from an inspection of the edge geometry (see again Fig. 6.2.10): the C-atom renders opposite edges inequivalent. However the determination of the sign and, of course, the absolute strength of this mass term requires *ab initio* methods. Hence, 0D geometries with flat edge terminations are unsuitable for the direct observation of in-gap corner states and a passivation to compensate the edge charge and the edge potential is required (see again Sec. 5.7). By contrast the zigzag edge offers perfect conditions as it has an insulating band structure as shown in Fig. 6.3.3 (b). Similar to indenene, the bulk penetration increases as the edge states approach $\overline{\Gamma}$. However, as the bulk gap is trivial, it is reasonable to assume that the chosen slab width yields a valid gap even though the hybridization via the bulk is still at play. Further, σ_d (+glide-shift) maps opposed edges onto each other [see again Fig. 5.6.1 (a)]. Hence their edge potentials must be of same strength and a metallic tendency, as for the flat edge, can be excluded. The qualitative band structure is also supported by tight-binding models with a size of 30 conventional UC repetitions, where the edge states possess a similar localization [see again Fig. 5.6.2 (IV)]. Further it should be noted, that in corner regions, where two edges meet, the inter edge hybridization via the bulk will be relevant.

6.3.4. Quadrupole Promoted Corner Charge

Having understood the formation of the electronic bulk polarization and being equipped with the knowledge of the presence of insulating 1D edges allows us to predict potential hosts of in-gap corner states: the touching points of zigzag edges. However, as the system lacks chiral symmetry, the in-gap position of the corner states is not symmetry protected and will hence depend on a proper edge potential [147, 196–199].

For a triangular flake with zigzag termination, the UC and the corresponding electronic spectrum and charge localization of the zero-energy states is shown in Fig. 6.3.4. To correctly incorporate the edge potential, a 2D SiC substrate is considered with H-passivated surface and bottom dangling bonds (b, c). At neutral filling, its electronic spectrum possesses a six-fold degenerate[14] state located in the bulk gap (a). This state localizes at the corners and has a total filling of 2 electrons. Hence, it exhibits the filling anomaly associated to the quadrupole moment given in Eq. 5.16. Focusing on its real-space symmetries (b, c), out-of plane and in-plane degrees of freedom participate

[14]The sixfold degeneracy is slightly lifted as the rectangular substrate UC of the calculation does not comply with the C_3 symmetry of the triangular flake.

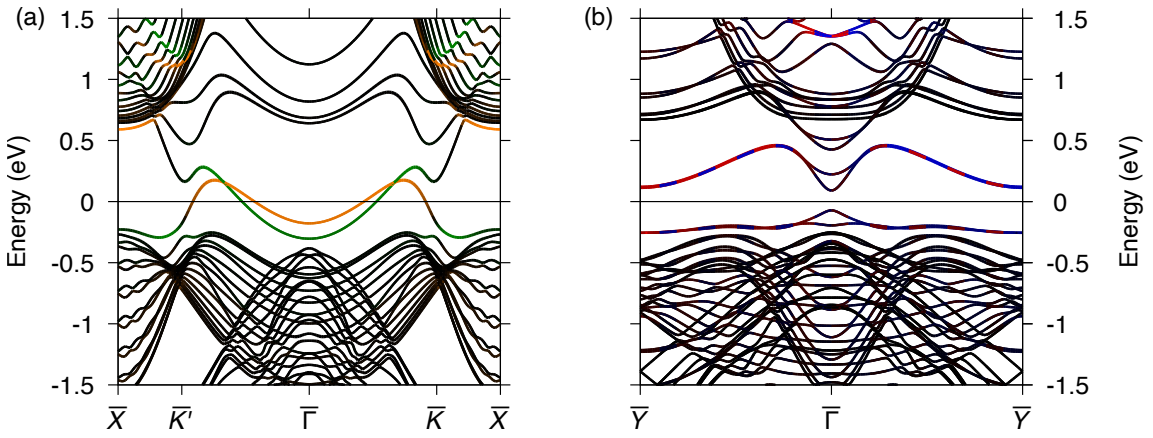

Figure 6.3.3.: Band structures with SOC and edge projection of flat- (a) and zigzag-edge (b) terminated Al slabs with terrace widths of 39.9Å (7 conventional UCs) and 36.9Å (11.5 conventional UCs), respectively. The color code follows the schemes of Figs. 6.2.10 and 6.2.12. Reprinted figure in (b) is taken and adopted from the supplemental material with permission from Eck, P. *et al.* "Recipe for higher order topology on the triangular lattice". *Phys. Rev. B* **107,** 115130 (2023). © 2022 by the American Physical Society.

in the formation of the tightly bound corner state. Furthermore, it is almost perfectly symmetric with respect to the three vertical mirror reflections σ_d of the bulk, even though these symmetries are broken at the edges of the flake [4]. It is also interesting to note that the local symmetry of the corner state [see Fig 6.3.4 (b)] has strong similarity with the indenene edge states shown in Figs 6.2.10 and 6.2.12, namely a p_z-p_t symmetry which forms a bonding state with the neighboring p_z state. This highlights again the importance of the hybridization of the in-plane and out-of-plane subspaces via horizontal reflection symmetry breaking.

Having established the existence of fractionally filled in-gap corner states in zigzag terminated flakes, we will turn now to the flat edge termination. This is also of importance for future experimental investigations, as for indenene [3, 61] the flake termination can be controlled via the SiC substrate terrace geometry. We will address this in the following in a qualitative study for a freestanding triangular flake. At neutral filling, the chemical potential is located in the bulk continuum Fig. 6.3.5 (a). However, the energy spectrum possesses a gap of size 0.25 eV at 0.7 eV. The first six "valence" states[15] of this gap are strongly corner localized. As explained in Sec. 5.7 and 6.3.3 the metallicity[16] of this geometry can be expected from its polar edges. Upon compensating the edge charge for a dipole moment of $p_{\text{edge}} = 2/3e$ according to Eq. 5.19, the

[15]The quadratic DFT UC breaks the C_3 symmetry, which lifts the six-fold degeneracy of the states.
[16]The chemical potential is in a gap of the spectrum shown in Fig. 6.3.5, which is expected to vanish or at least to exponentially seize with increasing flake size.

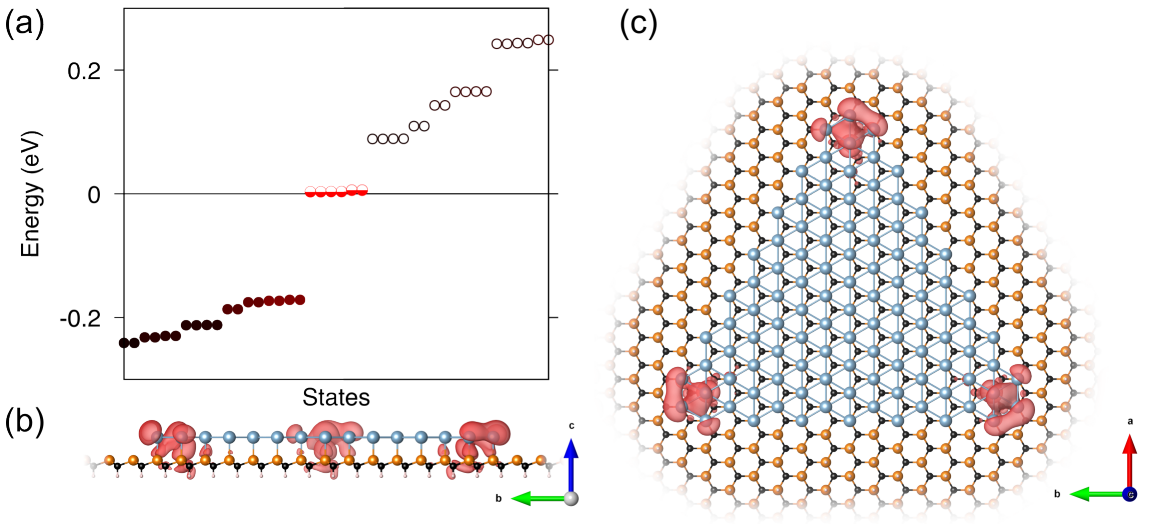

Figure 6.3.4.: (a) Energy spectrum of a zigzag terminated triangular flake of Al on SiC, truncated as shown in (b, c). The red color code denotes the corner character of the state: the six-fold degenerate in-gap states are completely localized on the corners. Top and side view of the in-gap state are shown in panels (b) and (c), respectively. To improve visualization in (b), the illustration of the H-passivation of the pristine region of the top SiC surface is omitted. The color scheme of the atoms follows Fig. 6.2.2, Al is depicted by light-blue colors. Reprinted figures in (a) and (b) are taken and adopted with permission from Eck, P. *et al.* "Recipe for higher order topology on the triangular lattice". *Phys. Rev. B* **107,** 115130 (2023). © 2022 by the American Physical Society.

corrected chemical potential promotes indeed a filling of two electrons in the corner state, as shown by the dashed line in panel (a). Focusing on the real-space symmetries (b, c), the edge state and the flake are symmetric with respect to the vertical reflection σ_d. The side view unveils again the presence of in-plane and out-of plane degrees of freedom, the overall charge distribution is similar to states living on corners, where two zigzag edges meet.

6.3.5. Conclusion and Outlook

Based on symmetry considerations combined with the experience gained on indenene on SiC, the "light" Group III elements B, Al and Ga have been identified as real-space obstructed 2D HOTI candidates which can host fractionally filled in-gap corner states. As they have not only a finite quadrupole, but also a non-vanishing dipole moment,

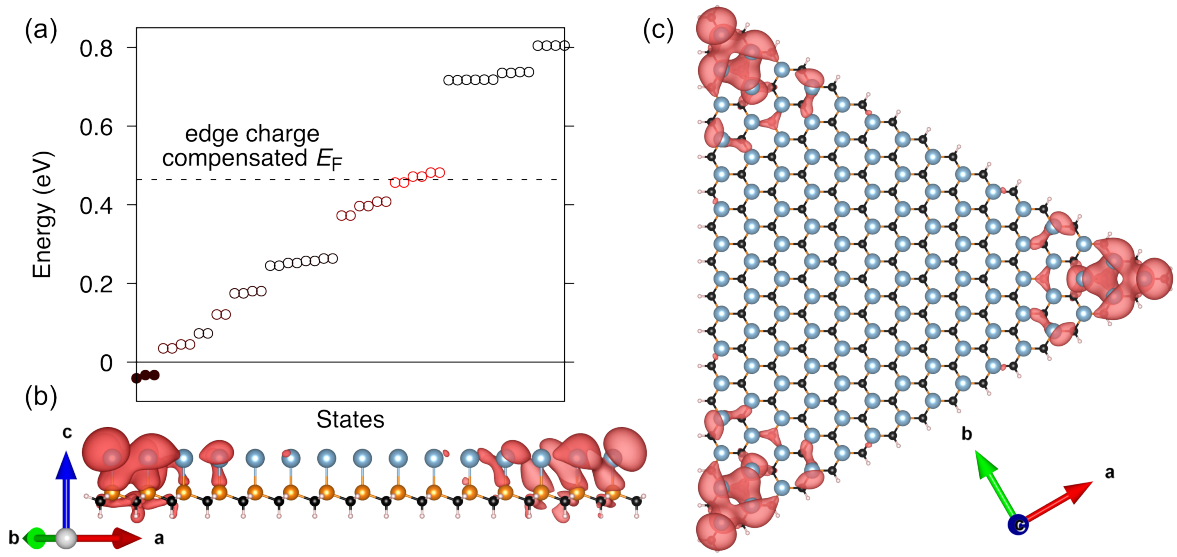

Figure 6.3.5.: (a) Energy spectrum of a flat terminated triangular flake of Al on SiC, with $N = 15$ sites per edge as shown in (b,c). The red color code denotes the corner character of the state, which unveils a strongly corner localized sixfold degenerate state in conduction. The dashed line shows the chemical potential for a doping by $Q_{\text{edge}} = 28e$, which compensates the edge charge. The edge charge is a consequence of the dipole moment $p_{\text{edge}} = 2/3e$ normal to the edge (see Eq. 5.19). Top and side view of the corner state are shown in panels (b) and (c), respectively. The color scheme of the atoms follows Fig. 6.2.2, Al is depicted by light-blue colors.

insulating edges, a necessary prerequisite for the observation of in-gap states, exist only for the zigzag termination. For this geometry, the *ab initio* calculations reveal for a triangular flake a sixfold degenerate corner state with a total occupation of 2 electrons. For the chosen flat edge geometry instead, the dipole moment promotes an edge charge that pushes the corner state to conduction. If the edge charge is compensated, the fractional filling of $2/3e$ per corner is restored. Hence, in-gap states at neutral filling might be achieved by a suitable passivation. On a more general perspective, the results of the *ab initio* calculations for Al are highly promising, as they highlight also, that the self-consistently obtained corner potential is of appropriate magnitude to stabilize the corner state in the bulk gap. This is an important detail, as the bulk quadrupole moment guarantees only for the presence of corner charge. However the in-gap energy position of the corner state in the considered unit cells is not protected owed to the absence of chiral symmetry [147, 196–199].

6.4. The Generically Compensated Fermi Surface of Group V Adsorbates on SiC

We will conclude the chapter on triangular adsorbates by giving a perspective beyond spatial symmetry breaking. Namely by investigating the compensated Fermi surface of antimony on SiC in the light of nesting properties, which may give rise to electron-electron- and electron-phonon-coupling driven phases. This work has been inspired by experiments of Tim Wagner and Bing Liu (both EP IV, university of Würzburg), who have found structural indications for a triangular antimony monolayer on a 1×1 SiC(0001) substrate, while STM measurements hint towards a 2×2 electronic reconstruction. We will consider the 1×1 UC where moving to Group V adatoms can be regarded as the $+2e^-$-doped versions of indenene. In particular, this section will be devoted to the discussion of the low-energy band structure of Sb on SiC, which can be however regarded as generical to Group V adsorbates. Their compensated Fermi surface consists of a Γ-centered hole pocket and electron pockets at the valley momenta. The orbital symmetries of these features are dictated by the mirror reflection symmetries of the triangular lattice. Further, a minimal tight-binding Hamiltonian based on a $\{p_x, p_y\}$ basis is developed. This model serves as an *ab initio* derived starting point for obtaining the Lindhard function and functional renormalization group calculations. The latter are currently performed by Lennart Klebl (Universität Hamburg), with the aim to address multi-orbital long-range correlation physics. Finally, by considering also phosphorus and bismuth, *ab initio* theory unveils that this particular Fermi surface topography is not specific to antimony, but instead generic to Group V adsorbates.

6.4.1. Unit Cell and Electronic Structure

Similarly to Secs. 6.2 and 6.3, we will consider in the following the Sb atom on the T1 position [see Figs. 6.2.2 (a,b) and 6.3.2]. Hence this UC belongs to layer group p$3m1$ and the site symmetry group of the Sb site is $3m$. An *ab initio* treatment with PBE yields a bonding distance of $d_{\mathrm{Sb-Si}} = 3.27\,\text{Å}$. The corresponding spinless band structure is shown in Fig. 6.4.1, the bands at the Fermi level have strong Sb in-plane p character and develop a momentum-dependent radial and tangential alignment with respect to the nearest Γ point. Their valley Dirac cone is located at $-3.7\,\mathrm{eV}$, which is gapped by $0.26\,\mathrm{eV}$, a signature of the vertical reflection symmetry breaking. This gap is reopened in the presence of SOC by $68\,\mathrm{meV}$ (the band structure with SOC can be found in Fig. 6.4.5). However, as it is deep in valence and the overall band structure is metallic, a profound discussion on $\mathbb{Z}_2$-topological properties is inappropriate. Another distinction to the Group III adsorbates is also reflected in the out-of-plane degree of freedom, because the Sb p_z state is in valence in the whole BZ. It hybridizes strongly with the substrate quantum well states at Γ and forms a relatively flat band around

−2 eV at the BZ boundary, e.g., along M-K in Fig. 6.4.1 (a).

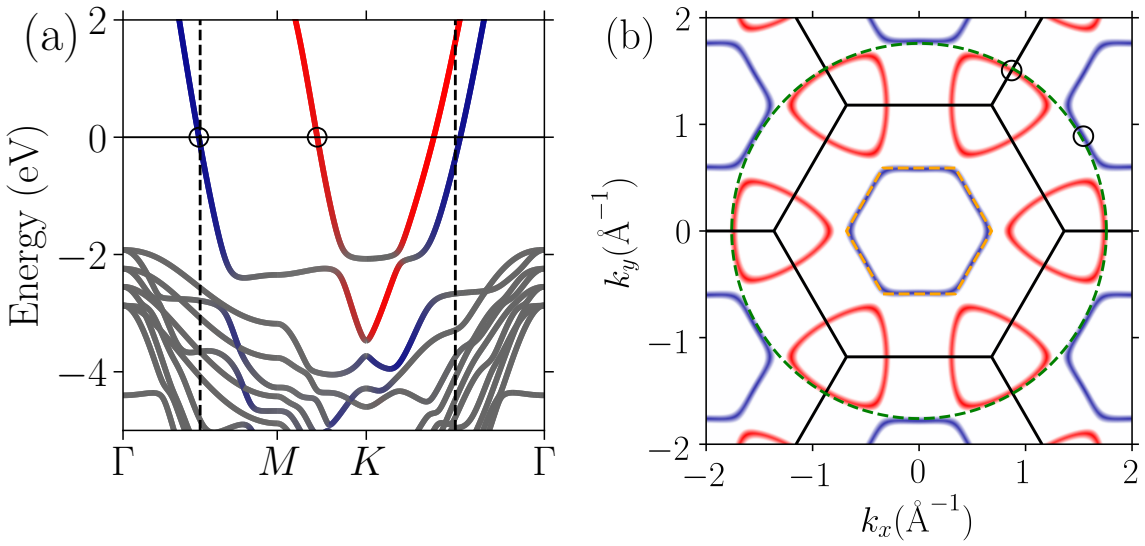

Figure 6.4.1.: (a) Spinless band structure of Sb on four layers of SiC(0001). The blue and red color code denotes the radial and the tangential character, respectively, of the Sb in-plane bands. The vertical dashed lines highlight the boundary and the corner of the 2×2 BZ. (b) Corresponding orbital projected Fermi surface to (a). The dashed orange hexagon illustrates the 2×2 BZ and the dashed green circle corresponds to a free electron parabola with $|\mathbf{k}_{\mathrm{Fermi}}| = 1.76\,\text{Å}^{-1}$ centered at Γ of the first BZ. The empty black circles in (a) and (b) depict representatives of the momenta, for which the Fermi velocity and the effective mass have been determined (see text for details). The orbital character has been calculated from a $\mathbf{k}$-dependent basis rotation of a Wannier Hamiltonian into a radial (blue) and tangential (red) in-plane basis as introduced for the minimal p shell model in Chap. 4 in Eq. 4.9 and shown in Fig. 4.1.1. It should be noted, that the $\{p_x, p_y\}$ orbital character changes continuously along the Fermi surface features.

As shown in Fig. 6.4.1 (b), the filling of two electrons in the in-plane bands gives rise to a compensated Fermi surface formed by a hole and two electron pockets of compensating area: the radial polarized band (even under vertical reflections) forms a hexagonal hole pocket centered around Γ. It coincides well with the 2×2 BZ as indicated by the dashed orange line. This constitutes ideal nesting conditions as momenta along opposed sites are connected by half of a reciprocal lattice vector. Instead the tangential in-plane band promotes a triangular shaped electron pocket at the valley momenta. As their sides are parallel to the next nearest triangles, this may result in an enhanced scattering between the valley momenta states. The metallic band structure of the in-plane orbitals can be understood from the $5p^3$ valence configuration of antimony. However, the formation of a Fermi surface with parallel aligned features

that favor nesting is surprising and will be subject of the next section. The important key ingredient is already illustrated in Fig. 6.4.1 (b) by the comparison with the Fermi surface of a free-electron parabola assigned to the first BZ (green dashed circle). It describes well the Fermi surface of the in-plane bands in the second BZ. As expected, deviations can be seen at gaps between the electron and hole pockets. The symmetry character of the free electron state with respect to Γ of the first BZ is even under vertical reflections, which is supported by the alternating radial and tangential character given with respect to the nearest Γ point. A quantitative analysis of the corresponding free electron state yields for the momenta depicted by empty circles in Fig. 6.4.1 with $|\mathbf{k}_{\mathrm{Fermi}}| = 1.74$ and $1.78\,\text{Å}^{-1}$ a Fermi velocity of $\approx 0.006\,c$ and an effective band mass of $\approx 0.11\,m_{el}$.

6.4.2. Minimal Tight-Binding Hamiltonian

As the low-energy bands have predominantly in-plane character, we will proceed with the construction of a minimal $\{p_x, p_y\}$ model. This serves not only as an *ab initio* derived starting point for ongoing functional renormalization group calculations, but unveils also the importance of long-range hoppings for the Fermi surface features discussed in the previous section. From a *VASP+Wannier90* $\{p_x, p_y\}$ model, created by Domenico Di Sante, the V^{σ} and V^{π} Slater-Koster integrals up to third nearest neighbors can be immediately extracted along x and y direction from the diagonal elements of $H(\mathbf{R})$ (see also Sec. 2.3), with their values given in Tab. 6.4.1. Interestingly, the σ-bonding contribution is larger for third than for second nearest neighbors. Finally, n-th order tight-binding models can be constructed from these parameters[17] (for details see Sec. 2.3.1). They are inherently p6/mmm symmetric, vertical reflection symmetry breaking will be neglected in the following as its impact is negligible at the Fermi level (see again Fig. 6.4.1), though it could be extracted from the off-diagonal elements of the Hamiltonian or by fitting the gap at the valley momenta.

$V^{\sigma\prime}$	$V^{\pi\prime}$	$V^{\sigma\prime\prime}$	$V^{\pi\prime\prime}$	$V^{\sigma\prime\prime\prime}$	$V^{\pi\prime\prime\prime}$
1.721	0.195	-0.179	0.044	0.294	-0.031

Table 6.4.1.: First, second and third neighbor Slater-Koster parameters in eV of a minimal $\{p_x, p_y\}$ Hamiltonian for Sb on SiC.

[17] This approach may appear cumbersome at first glance, however the creation of tight-binding Hamiltonians from extracted Slater-Koster integral values guarantees for the correct incorporation of the lattice symmetries. They can be spoiled in *VASP+Wannier90* generated Hamiltonians as the optimization bases solely on the Wannier function spread irrespective of the lattice symmetry [200]. Hence, the truncation of such a Wannier Hamiltonian may result in inaccurate eigenstate symmetries. See also Fig. 6.1.4 for an example of weak symmetry breaking in a *VASP+Wannier90* created Hamiltonian.

The band structures of the initial Wannier model and of the n-th order tight-binding Hamiltonians are shown in Fig. 6.4.2 (a). While the band dispersion and the intersection points with the Fermi energy along the high symmetry lines are already well described by a first neighbor Hamiltonian, the agreement at the TRIMs Γ and M requires long-range hoppings. In particular, the van Hove singularities at the band minimum and saddle point at M require third-nearest neighbor interactions. The corresponding constant energy cuts at the Fermi level are shown in Fig. 6.4.2 (b). A reasonable description along the edges and the corners of the hexagonal and triangular features requires long-range hoppings. This is consistent with the previous paragraph, where the Fermi surface topography has been assigned to a free electron alike dispersion.

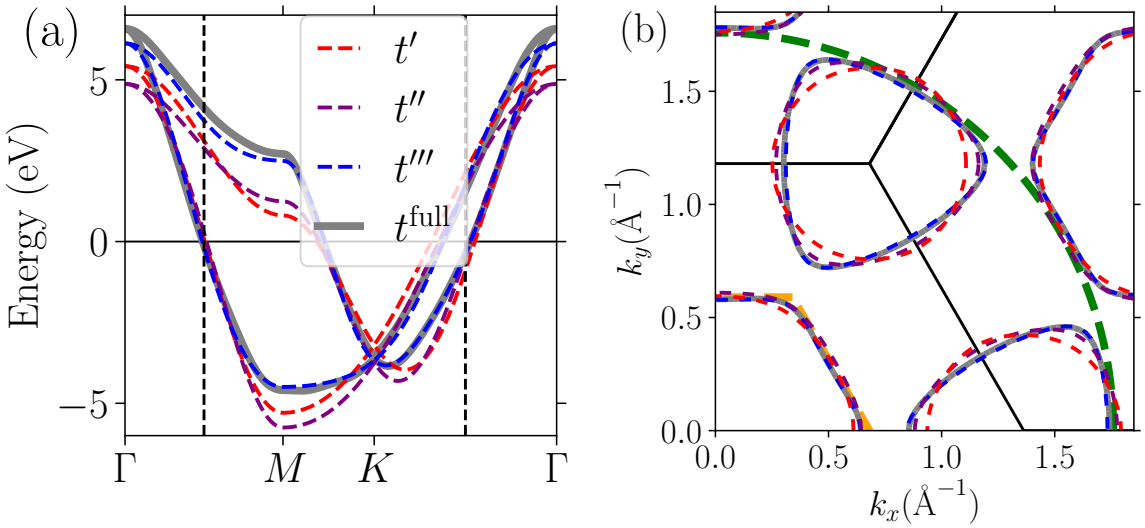

Figure 6.4.2.: (a) Band structures of the *ab initio* derived Wannier model (t^{full}) and the constructed p6/*mmm* symmetric n-th order tight-binding Hamiltonians (see text for details). (b) Corresponding Fermi surfaces to the models shown in (a). The line style and coloring follows the legend in (a), while the dashed orange and green line denote the 2×2 BZ and the fitted free electron parabola, respectively, similarly to Fig. 6.4.1 (b).

6.4.3. Static Electronic Susceptibility

Having established a minimal third-order tight-binding model, which describes well the Fermi surface of Sb on SiC, we will address in the following the nesting prerequisites by inspecting the static electronic susceptibility χ^{ij} for a momentum transfer of $\mathbf{q}$

$$\chi^{ij}(\mathbf{q}) = -\frac{1}{N_k}\sum_{\mathbf{k}\mu\nu} a_{\mu i}(\mathbf{k})a^*_{\mu i}(\mathbf{k})a_{\nu j}(\mathbf{k}+\mathbf{q})a^*_{\nu j}(\mathbf{k}+\mathbf{q})\frac{n_F(E_\mu(\mathbf{k})) - n_F(E_\nu(\mathbf{k}+\mathbf{q}))}{E_\mu(\mathbf{k}) - E_\nu(\mathbf{k}+\mathbf{q})}. \quad (6.8)$$

Latin and Greek indices denote the orbital degrees of freedom[18] and the band index, respectively, and $n_F(E)$ is the Fermi distribution (here for $T = 0$). A detailed analysis is illustrated in Fig. 6.4.3. To assign the main features to the Fermi surface characteristics, we will focus at first on the band resolved susceptibility shown in panels (a-c). The lower band (a), which is associated to the hexagonal Fermi surface centered around Γ, has an enhanced susceptibility at M favoring a 2×2 reconstruction. The upper band (b), responsible for the triangular Fermi surface feature around K and K' gives rise to a triangular shaped feature around the valley momenta of the scattering BZ. It is particularly sizable at the intersection points of neighboring triangles. Inter-band scattering is shown in (c) and peaks around the valley momenta, i.e., when the scattering vector $\mathbf{q}$ aligns parallel sides of the hexagonal and triangular Fermi surface feature.

The $\{p_x, p_y\}$ orbital resolved susceptibility is shown in panels (d-f) of Fig. 6.4.3. The feature at M can be clearly assigned to a scattering between states even under a vertical reflection normal to the momentum transfer $\mathbf{q}$ as it is present in the p_x-p_x channel (d) for momenta with $q_x \neq 0$ and in the p_y-p_y channel (e) at $q_x = 0$. The same holds also for the enhanced susceptibility arising from the triangular feature around the valley momenta. It is pronounced for p_x-p_x scattering along $q_y = 0$. The inter-band response (triangular shaped enlarged susceptibility at the valley momenta) is instead odd under vertical reflections normal to the momentum transfer. It is predominant in the p_y-p_y (e) and suppressed in the p_x-p_x susceptibility (d) along $q_y = 0$. The inter-orbital p_x-p_y susceptibility is shown in panel (f), which is in support of our analysis. It peaks for the triangular feature around K at momenta, where the previously discussed pairing symmetry requires a linear combination of both in-plane basis states. However, it does not show new features, which would indicate an enhanced susceptibility for initial and final states with different in-plane symmetry.

Based on this analysis, the Fermi surface and the corresponding electronic response of the low energy bands of Sb on SiC hint towards the emergence of non-local correlation effects mediated by the orbital symmetries. The existence of such phases requires however still theoretical confirmation from many-body theory as well as a profound experimental investigation.

Before concluding this section, we will briefly analyze the susceptibilities for a doping to the van Hove singularities at the M points [see Fig. 6.4.2 (a)]. They are under current investigation in kagome systems [201–205], which are spanned by a three site atomic basis on a hexagonal lattice. Following the argumentation given in Chap. 3 the Kagome and the triangular lattice belong to the same space group and have identical irreps. Hence, there must be a mapping between the Bloch wave functions derived from the two different local basis sets. Further we can infer that the mirror planes σ_v and σ_d [see again Fig. 2.4.2 (b)] will dictate the wave function symmetry. Therefore the associated

[18] For the sake of simplicity, only orbital diagonal elements at $\mathbf{k}$ and $\mathbf{k}+\mathbf{q}$ are considered. This reduces the number of independent orbital indices from four to two.

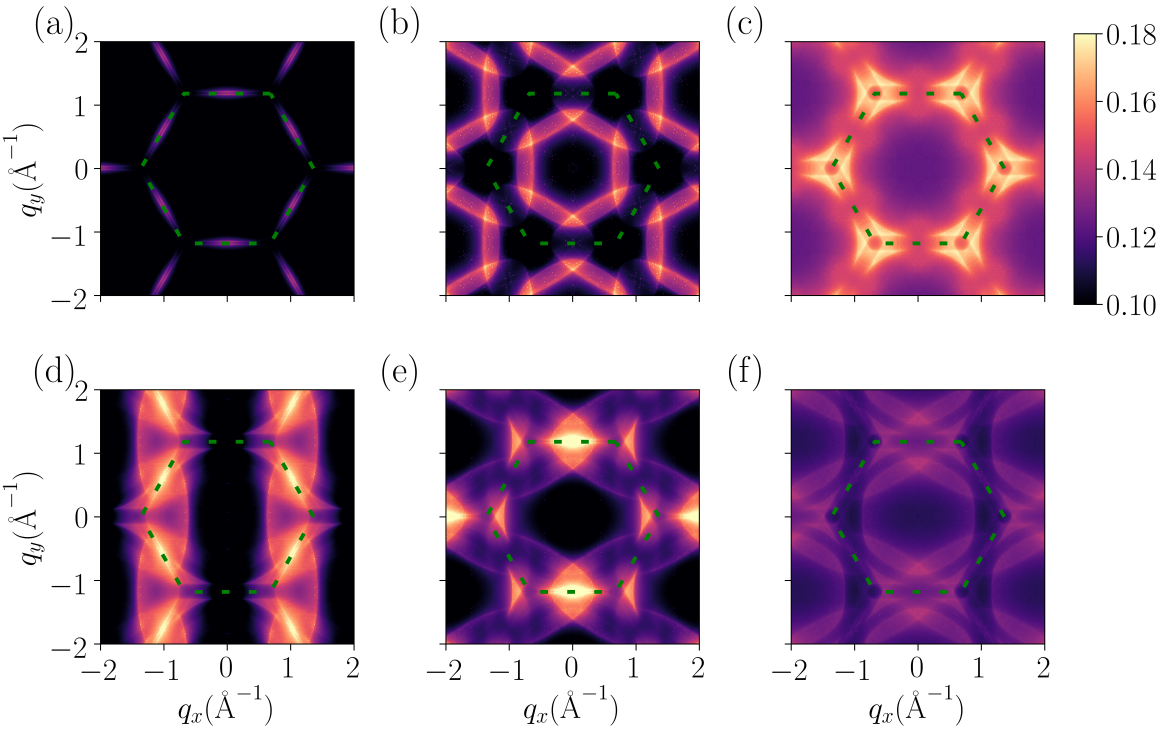

Figure 6.4.3.: (a-c) Contributions to the static susceptibilities from the first (a) and second (b) band and inter-band (c) response. (d-f) Orbital resolved susceptibility $\chi^{p_x p_x}$ (d), $\chi^{p_y p_y}$ (e) and $\chi^{p_x p_y}$ (f). The dashed green line depicts the first BZ.

van Hove singularities at M of the two lattices may be regarded as equivalent partners in the single-particle picture. However, in contrast to the topological arguments given for the Dirac fermion mapping, strong differences may arise at the many-body level, as the wave function symmetry in the remaining BZ and the Coulomb repulsion tensor are expected to live in completely different parameter regimes for multi-orbital monopartite and single orbital tripartite systems.

Turning to the electronic susceptibility, it is important to note, that the broken particle-hole symmetry renders the two van Hove singularities inequivalent [see again Fig. 6.4.2 (a)]. The one in conduction constitutes a saddle point and transforms under the M_3^- irrep[19], while the lower one (M_4^-) represents the band minimum with the Dirac cone at the valley momenta nearby in energy. This is also reflected in the response functions shown in Fig 6.4.4, which possess a larger background for the Fermi level at the energy of the van Hove in conduction (d-f). For a Fermi energy at the van Hove in valence (a-c), the electronic response peaks around Γ and possesses slightly weaker features at M (scattering between states from neighboring M points). They result

[19]For irrep classification in the presence of vertical and horizontal reflection symmetry breaking see Sec. 5.4 and Fig. 5.4.1.

from a scattering of states odd under a mirror reflection at the momentum transfer plane (only p_x-p_x along $q_x = 0$, while the p_y-p_y contribution vanishes). This analysis is less clear in conduction (d-f) owed to the sizable background. Nevertheless, the intense features along $q_x = 0$ for the p_y-p_y channel and the suppressed response in p_x-p_x along the same scattering momenta indicate an even symmetry under a mirror reflection normal to $\mathbf{q}$. In contrast to the Fermi level at the van Hove in valence, the p_x-p_y susceptibility is enhanced along the whole BZ boundary and displays sharp line-shape features connecting Γ with the BZ boundary. This can be attributed to the plethora of states in this energy region.

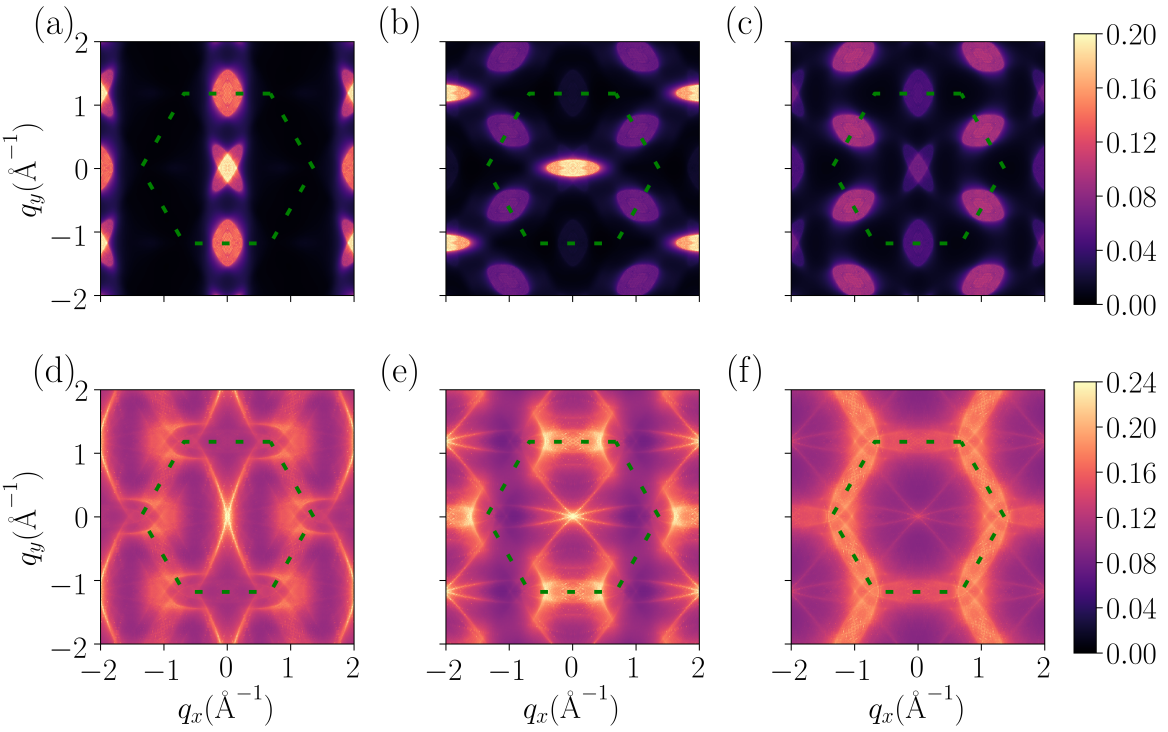

Figure 6.4.4.: Static electronic susceptibilities for the chemical potential at the energy of the van Hove singularities at M in valence (a-c) and in conduction (d-f). The $\chi^{p_x-p_x}$,$\chi^{p_y-p_y}$ and $\chi^{p_x-p_y}$ channel are shown in (a,d), (b,e) and (c,f), respectively. The dashed green line depicts the first BZ.

To summarize, the analysis of the electronic response function has unveiled a tendency towards orbital symmetry mediated long-range ordering at neutral filling, where the compensated Fermi surface is at play. Upon doping to the van Hove singularities at M, the susceptibility has its maximum at Γ. Non-local contributions are sizable, especially in the case of the van Hove in conduction. The strength of the Lindhard function in the orbital channels can be controlled via the symmetry of the initial state, i.e., by the mirror symmetry character of the corresponding irrep at M. In contrast to honeycomb systems, which often have the tendency to be *more* particle-hole symmetric, the calculations presented in Chap. 6 reveal a strong asymmetry. This is in favor

of tuning the chemical potential towards the van Hove singularities at M, e.g., making them accessible via degenerate doping and strain. As also shown in this section, this may activate further response channels.

6.4.4. Robustness of the Compensated Fermi Surface

We will conclude this section upon testing the low-energy band structure against different Group V adatoms and a DFT hybrid functional approach. Relaxing also phosphorus and bismuth on the T1 position of the SiC(0001) surface results in bonding distances of 2.29 Å (P) and 2.73 Å (Bi) with PBE. As shown in Fig. 6.4.5, their overall band structure is qualitatively similar to that of Sb. Minor differences can be observed with increasing adatom size: the enhanced SOC promotes a significant Rashba splitting of the p_z-band and a non-trivial gapping of the Dirac cone. In addition, both the p_z-band and the Dirac cone are shifted to lower energies. For all three adatom species, the in-plane bands cross the Fermi energy at similar momenta along Γ-M and Γ-K. Hence, the Fermi surface discussed for Sb may be regarded as intrinsic to Group V adatoms on T1 position on SiC(0001).

The robustness of the Fermi surface is further investigated by a HSE06 calculation for Sb shown by dashed orange lines in Fig. 6.4.5. Compared to PBE, the band width and gaps are slightly increased and the p_z-band is shifted to lower energies. Nevertheless, the intersection points with the Fermi energy are DFT functional invariant. This confirms not only the preceding Fermi surface discussion on the level of the functional choice, but highlights also its robustness against variations in the electron-electron screening.

6.4.5. Conclusion and Outlook

The *ab initio* study has unveiled a compensated Fermi surface arising from the in-plane bands of Group V adatoms on the T1 position of SiC(0001). It is formed by a hexagonal Γ-centered hole pocket of the size of the 2×2 BZ and a triangular shaped electron pocket at the valley momenta. The overall topography can be understood from an almost free-electron-like dispersion at the Fermi energy. A minimal p6/mmm symmetric tight-binding model has been constructed for antimony, which is currently used as input for functional renormalization group calculations. A first analysis highlights indeed an elevated electronic susceptibility at scattering momenta, which favor a 2×2 reconstruction, but unveils also sizable features nearby the valley momenta of the momentum transfer BZ. Further, the susceptibility has been investigated for a doping to the van Hove singularities at M. For such a doping, the response function is highly influenced by the symmetry of the predominantly contributing irreducible band representation at M. In addition, the the relative positions in energy of the Dirac cone

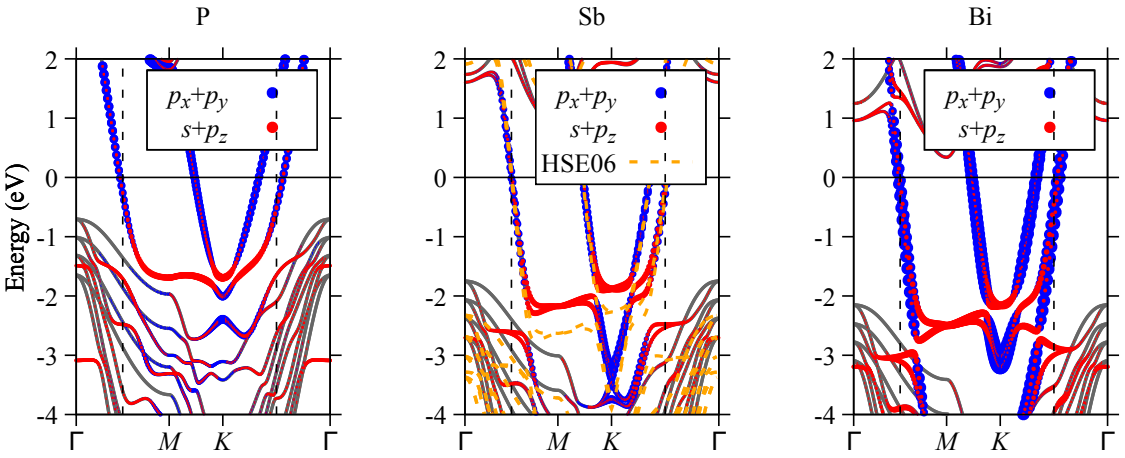

Figure 6.4.5.: Orbital resolved PBE band structures with SOC for Group V adatoms on T1 position on four layers of SiC(0001). The unit cell is illustrated in Fig. 6.2.2 (a,b). In addition, the band structure obtained with HSE06 is shown by dashed orange lines for Sb. The vertical dashed lines depict the boundary and the corner of the 2×2 BZ.

and of the two-fold band degeneracy at Γ are important. Upon switching to phosphorus or bismuth, a qualitatively similar compensated Fermi surface can be stabilized by varying the SOC parameter. Albeit the work presented here constitutes only a preliminary theory study towards multi orbital correlation physics in triangular monolayer adatom systems, the robustness of the Fermi surface across all considered Group V elements raises significantly the chance for the structural realization and experiments on its low-energy physics. On a broader scale, the combination of various adatom species and trigonal substrate surfaces gives rise to a huge tunability of the electronic properties by controlling the Coulomb interaction, SOC, the band width and band symmetries (also by symmetry breaking), electron filling and the involved orbital degrees of freedom (d-shell of transition metals and f-orbitals in rare earths). Of course, it remains to be seen, if similar compensated Fermi surfaces can be stabilized in other adatom-substrate combinations. On the other hand, the contemporary scientific focus on correlation physics arising from van Hove singularities in kagome lattices [201–205] may also profit from the investigation of their symmetry equivalent representations on the fundamental hexagonal lattice.

6.5. Summary and Outlook

The here presented work on triangular adsorbate systems on (111) surfaces of diamond- and zincblende-type substrates has unveiled a rich plethora of interesting physical phenomena driven by the interplay of lattice symmetries, mirror reflection symmetry

breaking and SOC. All fundamental effects discussed in Chaps. 3, 4 and 5 have been addressed with *ab initio* methods in appropriate surface geometries: (I) chiral wave functions promoted by inversion symmetry breaking and their Rashba-splitting in the presence of SOC. (II) The honeycomb connectivity of Dirac fermions on the triangular lattice. (III) Real-space obstruction in $\nu = 0$ and $\nu = 1$ insulating phases. (IV) Lattice symmetry imposed wave function symmetry and its effect on the Lindhard function. Further it should be noted that all presented systems have been either inspired by or jointly investigated in close collaboration with the experiment, which underlines their realizability.

As a paradigmatic Rashba system, AgTe on Ag(111) shows a sizable band-dependent Rashba splitting in the low-energy Te p in-plane bands. This can be clearly associated from theory and experiment to an orbital-symmetry-dependent OAM formation. The chiral wave functions promoted by inversion symmetry breaking are split by the SOC interaction. This gives rise to the *orbital-driven Rashba effect* [1]. From the methodological point of view, the combination of an *ab initio* band symmetry analysis and polarized light dichroism in ARPES measurements has allowed to identify the impact of mirror reflection symmetry breaking and the formation of chiral wave functions. In the context of classifying experimentally topological materials, this approach has been theoretically suggested to probe the Berry curvature [149, 206], recently also the local OAM has been identified with circular dichroism as the winding property at the Weyl points in the non-centrosymmetric Weyl semimetal TaAs [150].

The formation of chiral wave functions promoted by symmetry-breaking plays also a decisive role in one of the main findings of this work, in the triangular QSHI indenene on SiC [3]. The stabilization of the non-trivial ground state requires dominant horizontal mirror reflection symmetry breaking to open a global gap at the energy of the in-plane Dirac bands at the valley momenta. The presence of a weak vertical mirror reflection breaking lifts their Kramers degeneracy and allows for a band-resolved measurement of the associated charge localization: the two valence bands of the Dirac cone establish a honeycomb connectivity as their charges center in the voids of the triangular lattice. This real-space symmetry classifies the bulk wave functions of indenene unambiguously as $\mathbb{Z}_2$-non-trivial without relying on transport experiments. Upon addressing indenene's wave function symmetries in the whole BZ, it has been identified as a real-space obstructed because its valence bands are symmetry equivalent to graphene: the occupied bands localize not only at the valley momenta on the honeycomb positions, but also the time-reversal symmetry breaking Wannier functions of the valence bands are centered in the void positions [2]. This has extended the concept of real-space obstruction to QSHI phases and the consequences resulting from the bulk polarization are subject for future research, e.g., in indenene-bismuthene heterostructures. Similarly to AgTe [1], circular polarized light ARPES measurements could unveil the particular OAM polarization (see also Fig. A.6.1), which serves also an unambiguous identifier of the $\mathbb{Z}_2$-topology. Further its importance for the real-space obstruction has been highlighted in Sec. 5.8.

Stimulated by the success of indenene and based on dominant inversion symmetry breaking, a recipe for higher-order topology in triangular adsorbate systems has been developed and verified for lightweight Group III elements (B, Al, Ga) on 4H-SiC (0001) [4]. A detailed study of aluminum has revealed the real-space obstruction and the associated electronic dipole and quadrupole moment. DFT calculations confirm insulating zigzag and metallic flat edges as predicted from the minimal model in Sec. 5.6. Upon considering triangular flakes, the zigzag termination hosts a fractionally filled in-gap state, whose filling-anomaly is in agreement with the bulk quadrupole moment. It should be noted, that the in-gap energy position of the corner state is not symmetry protected, still *ab initio* theory yields an edge and corner potential which is appropriate for the stabilization of in-gap states. Even for flat-edge terminated flakes, an energetically isolated corner state has been observed. By compensating the edge charge, the fractional filling of the corner state driven by the quadrupole moment is restored. As boron and gallium have identical bulk valence band symmetries as aluminum, they are also potential candidates for realizing a HOTI state. Further, as their bands are $\mathbb{Z}_2$-trivial since the Dirac cone is gapped by a strong vertical reflection symmetry-breaking, they allow for a direct comparison with indenene, e.g., on the level of the charge localization (STM) and wave function chirality (CD ARPES).

We conclude the chapter with an outlook beyond topology in triangular adsorbates by discussing the compensated Fermi surface in Group V adsorbates (P, Sb, Bi) on 4H-SiC (0001) in the light of possible multi-orbital correlation driven phenomena on the triangular lattice. The doping by $+2e^-$ compared to Group III shifts the chemical potential deep into the in-plane bands. They disperse at these energies like nearly free electron states, which gives rise to a compensated Fermi surface. Based on a minimal $\{p_x, p_y\}$ model for antimony, the static susceptibility reveals indeed a tendency towards long-range instabilities. By tuning the Fermi energy to the van Hove singularities at the M-point, the vertical mirror reflection symmetry of the involved states is decisive for the susceptibility. These results should be regarded as inspiration and motivation for further theoretical studies involving full many-body approaches and experimental investigations. As this particular Fermi surface is generic for the considered Group V elements, the chance of its experimental realization is high and the variation of the adsorbate atom allows for a tuning of Coulomb and SOC interaction. In a broader perspective, triangular systems constitute the fundamental hexagonal lattice realization of the van Hove singularities in kagome systems [201–205]. Hence the mutual comparison may substantially stimulate the research in this intensely investigated field of research.

7. Conclusion and Outlook

Let us conclude by taking up the general motivation pointed out in the introduction, i.e., the intrinsic scientific interest in the topology of electronic band structures and the potential long-term implications of its application in electronic devices. Focusing on a multi-orbital basis on the triangular lattice, this work has revealed a plethora of topological insulating phases. They are driven by the intricate interplay of lattice symmetry, mirror symmetry-breaking and SOC. In particular, ISB has been identified as the desired non-local antagonist to the atomic SOC: the presence of both interactions can induce a non-trivial geometrical phase stabilizing a QSHI. Based on a broad spectrum of methods ranging from symmetry considerations over minimal modeling to *ab initio* simulations, a profound knowledge on the underlying mechanisms has been gained. This constitutes a first step towards technological relevance, which is underlined by the realization of the first triangular QSHI *indenene* [2, 3, 61] as well as by the proposal for a higher-order topological insulating state in light Group III adsorbates on SiC [4]. Fundamental insights on the impact of non-local mirror-symmetry breaking and atomic SOC on band symmetry [1] and topology of the triangular lattice has been gained from the inspection of the local OAM polarization and the application of symmetry indicators. The latter highlights also the equivalence and difference to the "drosophila" of topological phases in hexagonal and trigonal space groups, the honeycomb lattice, i.e., it puts forward the triangular lattice as an equally important setup. Further, by invoking the approach of Soluyanov and Vanderbilt [73], the concept of real-space obstruction has been extended to $\mathbb{Z}_2$-non-trivial insulators, and indenene has been classified as the first real-space obstructed QSHI [2].

In preparation for the discussion of the topological phases on the triangular lattice, a group theoretical analysis has unveiled the impact of vertical reflection symmetry breaking which reduces the rotational symmetry from six- to three-fold. It lifts the symmetry protection of the honeycomb Wyckoff position, i.e., the void sites in the triangular lattice are rendered inequivalent. This is an indispensable key mechanism for stabilizing the real-space obstructed HOTI phase [4], as the Wannier center of the valence band can dissociate from the triangular lattice position, which allows it to shift to the void sites. At the valley momenta, vertical reflection symmetry breaking gaps the Dirac fermions by promoting chiral wave functions. This mass term counteracts SOC, which favors a valence charge localization on both void sites. A formal mapping between bipartite honeycomb and multi-orbital triangular basis sets unveils also a change in the locality of the mass terms: the non-local Kane-Mele SOC transforms into a local SOC in the triangular basis [2, 18, 24]. By contrast, the reflection symmetry-

breaking term, local on the honeycomb, is momentum-dependent for a multi-orbital basis on the triangular lattice. The sizable local SOC and the weak symmetry-breaking term, because of its non-locality, represents a first but decisive result in favor of QSHIs based on triangular Dirac fermions. The SOC interaction is commonly the gap-limiting factor in material realizations.

Upon considering a full p-shell, a lattice periodic tight-binding Hamiltonian has been derived. The low-energy features of the valence band comprise in-plane Dirac fermions at the valley momenta and a nodal ring centered around the Γ-point, which is formed by the intersection of an in-plane and the out-of-plane band. These metallic crossings can be either gapped by atomic SOC or by mirror symmetry breaking via the formation of chiral wave functions. This gives rise to four topologically distinct insulating phases as summarized in Fig. 5.1.1. Trivial bands are realized in the presence of inversion symmetry breaking and in the highly symmetric regime dominated by SOC. They can be discriminated at the level of their valence charge localization: only the phase dominated by ISB is indeed real-space obstructed with a valence band charge center on one of the void positions of the triangular lattice. Its finite electric quadrupole moment can stabilize in-gap corner states, however only the zigzag edge geometry is insulating thanks to a finite dipole moment. QSHI phases are realized if *exactly* one of the reflection symmetry-breaking terms dominates over SOC. For an indenene-type QSHI with a SOC-opened gap at the valley momenta, the nodal ring must be rendered insulating by a sizable horizontal reflection symmetry breaking. The other QSHI is obtained if SOC dominates at the nodal line and vertical reflection symmetry breaking opens a gap at the valley momenta. Hence, these QSHI phases can only be stabilized in the absence of inversion symmetry and under the condition that one of the mirror reflections is (almost) preserved. Further, the absence of the horizontal reflection symmetry impedes the classification within the framework of *topological quantum chemistry* [44]: Non-trivial bands are mistakenly indicated as trivial (false-trivials), if band inversions occur at non-high symmetry momenta. Nevertheless, it gives profound insights on the relation between real-space and band symmetry. In combination with a Wilson-loop analysis, the electric polarization can be determined. In particular, the atomic OAM polarization at the nodal ring and at the valley momenta is a sufficient indicator for $\mathbb{Z}_2$-topology as well as for the real-space obstruction of the considered triangular systems.

Inspired by the discrimination of the two disconnected $\mathbb{Z}_2$-trivial phases at the level of their charge localization, the concept of real-space obstruction has been extended to QSHIs. This intriguing step is conceptually not straightforward, as their non-trivial bands lack a time-reversal-symmetric Wannier representation by definition. Based on non-Kramers degenerate Wannier constructions [73], both $\mathbb{Z}_2$-non-trivial phases are classified as real-space obstructed. Again, the vertical reflection symmetry defines the charge localization, a strong symmetry-breaking term shifts the Wannier centers to only one of the void positions, while the indenene-type QSHI possesses charge centers on both honeycomb sites. In combination with the symmetry analysis, this eluci-

dates the full extent of the similarities and differences of this system with respect to a Kane-Mele-type QSHI. Both QSHI phases are classified by an identical valence band representation, i.e., their wave functions are equivalent at the level of their symmetries. However, the SOC and vertical reflection symmetry breaking interaction have a different locality in both systems and the triangular basis set promotes a real-space obstructed ground state.

The relevance of these theoretical findings is corroborated by state-of-the-art first principles calculations and experiments on trigonal monolayer adsorbate systems. In the spirit of this thesis, the focus is on wave function symmetry, SOC, reflection symmetry-breaking and topology. As a perfect example for the interplay of band symmetry, inversion symmetry breaking and SOC, the *orbital-driven* Rashba effect in AgTe on Ag(111) is discussed based on DFT simulations and LD in ARPES measurements. The vertical mirror reflections of the triangular lattice promote an even and an odd Te in-plane p-band. In combination with the horizontal reflection-symmetry breaking due to the presence of the substrate, only the even band hybridizes with p_z state by forming in-plane OAM-polarized states. In turn, the local OAM couples to SOC, which gives rise to a band-dependent Rashba splitting in the Te bands at the Γ point. Key to these results is the joint theory-experiment wave function symmetry analysis, which has been also proven to be a particularly powerful tool for the investigation of topological states such as the Fermi arcs and the Weyl points in the TaP/TaAs Weyl semi-metal family [150, 168].

The deep understanding of the interplay of symmetry-breaking and SOC in triangular adsorbates has lead to the the major result of this work: the design of a triangular QSHI, *indenene* on SiC [2, 3, 61], where the low-energy physics of the In $5p$ bands is well-described by the p-shell Hamiltonian established in Chaps. 4 and 5. A strong horizontal reflection symmetry breaking gaps out the nodal ring formed by the in-plane and p_z-band inducing a pinning of the Dirac point to the Fermi level. Its mass term determines the band topology. The substrate, however, breaks also the vertical reflection symmetry, which would favor a trivial ground state. A thorough analysis of the valley states by DFT and STM reveals a valence charge localization on both honeycomb sublattice sites [3]. As discussed in the general theory part, this is indicative of a SOC-opened gap and classifies indenene as $\mathbb{Z}_2$-non-trivial. Remarkably, our theory analysis allows us to base these conclusions on the topological character of indenene, analyzing its bulk wave function symmetries rather than transport features. Upon extending the valence band symmetry analysis to the full BZ, indenene is put forward as the first real-space obstructed QSHI, with non-Kramers-degenerate Wannier charge centers on the honeycomb Wyckoff positions [2]. Its valence bands constitute a realization of a Kane-Mele-type QSHI on the triangular lattice. Furthermore the surface states for both fundamental edge terminations of the triangular lattice have been investigated. For the "flat" termination, the edge states are located in a sizable bulk gap, which results in a strong edge localization. Instead, for the "zigzag" termination (equivalent to the graphene's armchair edge) the bulk Dirac cone is projected onto the edge

state. In turn, the relatively small bulk gap at these momenta allows for a deep bulk penetration of the surface state, which may impede its detectability in experiment.

Motivated by the discovery of indenene, another topological triangular adsorbate monolayer has been predicted upon lowering the SOC strength by considering lightweight Group III adsorbates (B, Al, Ga) on SiC. The gapping of the Dirac cone is opened by a sizable vertical reflection symmetry-breaking term and the $\mathbb{Z}_2$-trivial valence bands localize on only one of the honeycomb Wyckoff positions. This real-space obstructed atomic limit possesses a finite quadrupole moment and DFT predicts for triangular flakes with zigzag termination a HOTI state with insulating 1D edges and fractionally filled in-gap corner states [4]. As it has been shown for the minimal p-shell model, the band topology and the real-space obstruction is encoded in the OAM-texture in the full BZ. Hence, in combination with the QSHI indenene, these systems offer a perfect platform for conducting experiments sensitive to the wave function chirality, e.g., circularly polarized light ARPES. This has been put forward as a potential measurement for addressing the Berry curvature and the orbital magnetization [149]. In the spirit of topological quantum chemistry [44], the band topology may be derived by measuring the band symmetries at all avoided band crossings. These are the nodal ring and the Dirac fermions for the triangular p-shell model.

As an outlook towards multi-orbital long-range electronic correlations on the triangular lattice, the Lindhard function of the compensated Fermi surface of Group V adsorbates (P, Sb, Bi) on SiC has been investigated. The additional valence charge of $2e^-$ with respect to the Group III elements shifts the Fermi energy to the in-plane bands. Their free electron-type dispersion gives rise to two characteristic Fermi surface features of compensating size: a hexagonal hole pocket centered around Γ, which favors a 2×2 reconstruction, and a triangular electron pocket at the valley momenta. Similar to AgTe, the vertical reflection symmetry of the triangular lattice dictates the orbital character of the Fermi surface features. In turn, the band symmetry mediates the contributions of the orbital channels to the Lindhard function, possible electronic instabilities are subject of current investigation.

From a general perspective, the analysis presented on lattice symmetry and symmetry-breaking induced wave functions, topology and possible correlation effects may induce a paradigm shift from hexagonal and trigonal multi-site systems, such as the honeycomb and the kagome lattice, to multi-orbital basis sets on the triangular lattice. The investigation of a p-shell basis has revealed four topological distinct insulating phases, one of which has already been observed in indenene, while the HOTI phase has been proposed by DFT. Their existence relativizes also an intrinsic weakness of the triangular lattice Hamiltonian, compared to the Kane-Mele model: the non-particle-hole symmetric band structure, which requires fine-tuned parameters for the stabilization of a global gap. The other triangular QSHI phase, which is characterized by a dominant vertical reflection symmetry breaking, might occur in crystal systems similar to the non-inversion symmetric H-phase of monolayer transition-metal dichalcogenides.

Considering higher angular momentum shells, e. g., d- and f-orbitals would also constitute an intriguing but complex further step, as it would introduce multiple Dirac cones at the valley momenta. Additional sources of Berry curvature like nodal lines can occur. Hence, higher angular momentum shells might host HOTI phases with vanishing dipole moment resulting in an insulating band structure on all fundamental edge terminations. Due to the strong localization of the higher angular momentum shells, small bandwidths, sizable SOC and dominant Coulomb interactions are expected.

Additionally, the role of the substrate for topological monolayers has been conceptually broadened. For Kane-Mele-type QSHIs, a weak interaction with the substrate is desirable [57]. Instead, the strong bonding of bismuthene to the SiC substrate filters out the p_z degree of freedom from the low-energy physics [52]. However, the systems presented in this thesis profit from an intermediate substrate interaction: the full p-shell participates in the valence band structure and the symmetry breaking opens intermediate-sized hybridization gaps compared to the bandwidth. Inversion symmetry breaking is indispensable for the discussed $\mathbb{Z}_2$-non-trivial insulators, a requirement which impedes their detection with symmetry indicators in high-throughput studies. Hence, a sizable number of hitherto undiscovered QSHIs is expected to exist in the almost infinite phase space spanned by the combination of triangular adatom species and insulating trigonal substrate surfaces. These systems may be straightforwardly applicable for transport measurements and functionalization. The limiting factor of the flake size of indenene on SiC is the terrace width of the substrate, thanks to the particularly simple 1×1 reconstruction. Also stability under air exposure seems to be at reach via graphene intercalation [207–209].

More fundamentally, the extension of the concept of real-space obstruction to QSHIs raises conceptional questions, which require further investigation. How does the real-space obstruction manifest in finite size-geometries? Will there be metallic states at the interface of two differently real-space obstructed QSHIs? In particular, do fractionally filled in-gap corner states exist in an inverted gap? How does the electronic multipole moment from time-reversal violating Wannier centers translate into the properties of the corner states? To address these questions, heterostructures of indenene and bismuthene on SiC may serve as perfect material templates. Also the other triangular QSHI phase, which is characterized by a strong vertical reflection breaking, should be considered.

A. Appendix

A.1. Kane-Mele model

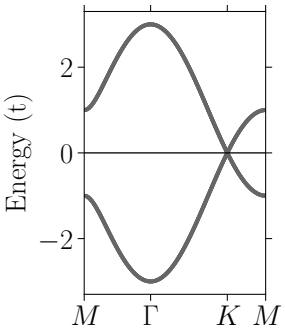

Figure A.1.1.: Band structure of the Kane-Mele model in the absence of SOC and ISB. The lattice symmetry promotes massless Dirac cones at the valley momenta.

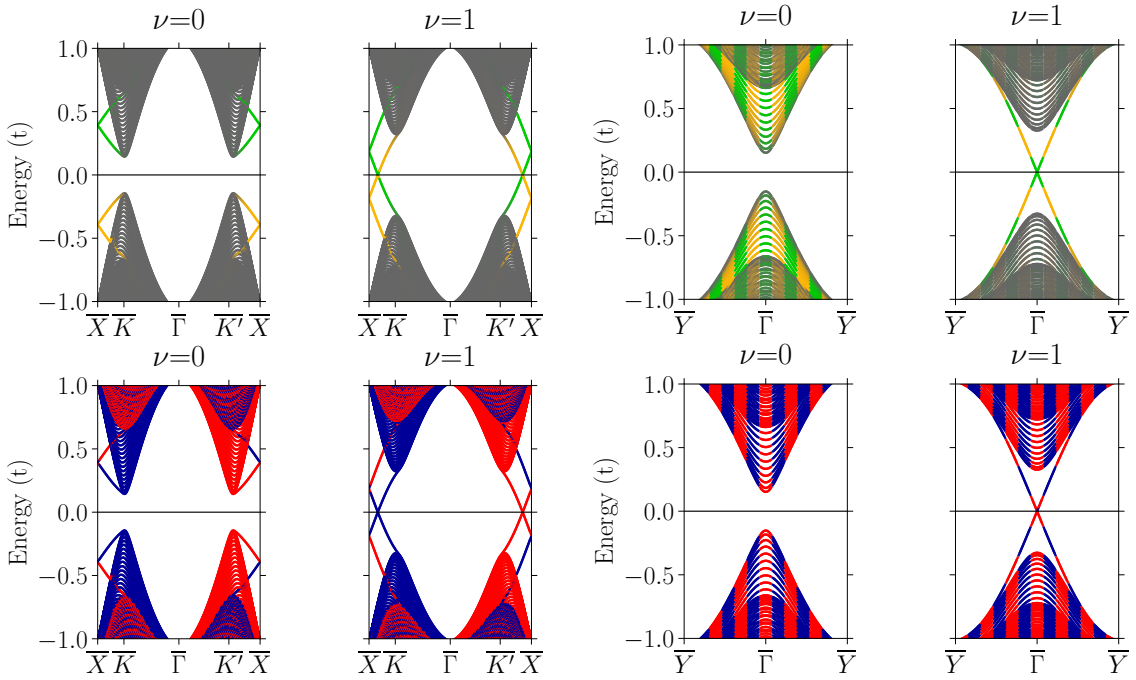

Figure A.1.2.: (a) Edge localization (top row) and $\langle S_z \rangle$ polarization (bottom row) in zigzag and armchair terminated ribbons shown in (a) and (b), respectively, for slab sizes of 40 conventional UCs. For an improved visualization in (b), the expectation values are shown by projecting alternatingly onto Kramers partners. The corresponding bulk band structures and parameters can be found in Fig. 2.1.1. An illustration of the conventional UC and the slab BZs is given in Fig. 5.6.1.

A.2. Coulomb-Sturmians

Here we introduce briefly the Coulomb-Sturmians as they form a complete basis set in $\mathbb{R}^3$ with atomic-like spherical-symmetries. They have been studied in the context of atomic and molecule spectra [146, 210–214]. In the following, they will be used to prove the existence of a complete basis set transformation for the valley Bloch wave function on the hexagonal lattice in Sec. 3.4.

The Coulomb Sturmians are defined as the isoenergetic solutions for a weighted potential. Starting from the Schrödinger equation in atomic units for a particle in a radial symmetric potential $V(r)$ [146]

$$\left[-\frac{1}{2}\nabla^2 - E\right]\Psi(\mathbf{r}) = V(r)\Psi(\mathbf{r}), \tag{A.1}$$

and defining $E = -k^2/2$ and $V(r) = nk/r$, we arrive at the generating equation of the Coulomb-Sturmians $\chi_{nlm}(\mathbf{r})$:

$$\left[-\frac{1}{2}\nabla^2 + \frac{1}{2}k^2\right]\chi_{nlm}(\mathbf{r}) = \frac{nk}{r}\chi_{nlm}(\mathbf{r}), \tag{A.2}$$

where $\{n, l, m\}$ are atomic-like quantum numbers and k defines the isoenergy of the basis set. Upon replacing $k \to Z/n$, the hydrogen-like solutions for the Schrödinger equation are obtained [146, 213]. Similarly to the hydrogen-like solutions, the Coulomb-Sturmians can be written as

$$\chi_{nlm}(\mathbf{r}) = R_{nl}(r)Y_{lm}(\theta, \varphi). \tag{A.3}$$

With the spherical harmonic $Y_{lm}(\theta, \varphi)$ and the radial wave function R_{nl}

$$R_{nl}(r) = N_{nl}(2kr)^l e^{-kr} F(l + 1 - n|2l + 2|2kr), \tag{A.4}$$

where N_{nl} is a normalizing factor and $F(a|b|c)$ is a confluent hypergeometric function. For details, the interested reader is referred to references [146, 213]

Further, the Coulomb-Sturmians obey the potential-weighted orthonormality relation

$$\int \mathrm{d}^3\mathbf{r}\chi^*_{n'l'm'}(\mathbf{r})\frac{1}{r}\chi_{nlm}(\mathbf{r}) = \frac{k}{n}\delta_{n'n}\delta_{l'l}\delta_{m'm}, \tag{A.5}$$

and form a full basis in $\mathbb{R}^3$. This allows us to represent any localized "tight-binding" orbital basis sets in Coulomb-Sturmians

$$|\phi\rangle = \sum_{nlm} |\chi_{nlm}\rangle \langle\chi_{nlm}|\phi\rangle \tag{A.6}$$

$$= \sum_{nlm} \alpha_{nlm} |\chi_{nlm}\rangle . \tag{A.7}$$

It will be proven in Chap. 3 by symmetry arguments, that certain Bloch wave functions can be represented in more than one local basis set on different basis positions $\boldsymbol{\tau}$. We will use the Coulomb-Sturmians to derive a formal mapping between equivalent local basis sets in App. A.3.

$$|\psi_{n\mathbf{k}}\rangle = \sum_{\mathbf{R}} e^{i\mathbf{k}\cdot(\mathbf{R}+\boldsymbol{\tau})} |\phi_n\rangle = \sum_{\mathbf{R}} e^{i\mathbf{k}\cdot(\mathbf{R}+\tilde{\boldsymbol{\tau}})} |\tilde{\phi}_n\rangle \,. \tag{A.8}$$

This basis transformation $\phi_n \rightarrow \tilde{\phi}_n$ involves orbitals, which are located at different Wyckoff positions separated by the displacement vector $\mathbf{x}$. Hence, this involves complicated overlap-integrals. As we only intend to prove the existence of such a basis mapping, we will refrain from their explicit evaluation. For completeness, these so-called Shibuya-Wulfman integrals are defined as [210]

$$k^2 S_{n'l'm',nlm}(\mathbf{x}) = \int \mathrm{d}^3\mathbf{r} \chi^*_{n'l'm'}(\mathbf{r}-\mathbf{x}) \left[-\frac{1}{2}\nabla^2 + \frac{1}{2}k^2\right] \chi_{nlm}(\mathbf{r}). \tag{A.9}$$

Equation A.9 is obtained by plugging Eq. A.2 into A.5. As the evaluation of the integrals is challenging, a Fock mapping onto the 4-D hypersphere has been proposed [210].

A.3. Coulomb-Sturmians based Transformation between Honeycomb and Triangular Lattice Basis Set

The following is a direct citation of APPENDIX A to Ref. [2]. It describes a formal derivation of a complete basis transformation of the valley Bloch wave function between triangular and honeycomb basis sets.

> Here we demonstrate the equivalence of a pair of chiral orbitals on the triangular lattice and a bipartite basis on the honeycomb lattice by deriving a complete basis transformation at the valley momenta. Its existence can be proven by projecting the Bloch wave function onto Coulomb Sturmians [215], a full basis in the $\mathcal{R}^3$ which are given by
>
> $$\chi_\tau(\mathbf{x}) = R_{nl}(r) Y_l^m(\theta,\varphi), \tag{A.10}$$
>
> defined by a set of atomic-like quantum numbers $\tau = [n,l,m]$ centered around $\mathbf{r}_0$ with the distance vector $\mathbf{r} = \mathbf{x} - \mathbf{r}_0$. For the sake of simplicity, we will neglect in the following the radial part R_{nl} and consider only the spherical harmonics Y_l^m. First, we express the initial orbital at $\mathbf{r}_0$ in Coulomb Sturmians $|w_{R_n}\rangle = \sum_\tau c_\tau |\chi_\tau\rangle$. The transformed orbital $|w_{n'}\rangle$ centered at site $\mathbf{r}'_0$ is given by the projection of the Bloch wave function onto

the Coulomb Sturmian basis $|\chi_{\tau'}\rangle$ in the home unit cell.

$$|w_{n'}\rangle = \sum_{\tau'} |\chi_{\tau'}\rangle\langle\chi_{\tau'}|\Psi\rangle \tag{A.11}$$

$$= \sum_{\mathbf{R},\tau,\tau'} c_\tau e^{i\mathbf{k}\cdot\mathbf{R}} |\chi_{\tau'}\rangle\langle\chi_{\tau'}|\chi_\tau(\mathbf{R})\rangle \tag{A.12}$$

$$\propto \sum_{\mathbf{R},\tau,\tau'} e^{i\mathbf{k}\cdot\mathbf{R}} c_\tau |Y_{\tau'}\rangle\langle Y_{\tau'}|Y_\tau(\mathbf{R})\rangle. \tag{A.13}$$

The spherical harmonics are parameterized by $Y_l^m = P_l^m(\theta)e^{im\varphi}$ with the Legendre polynomial P_l^m and the spherical coordinates (θ, φ). When transforming from position $1a$ to one of the A/B sites, all neighbors of the same order come in triangular triplets t, the complex phase transforms as

$$\frac{1}{3}\sum_{\mathbf{R}\in t,} e^{i\mathbf{k}\cdot\mathbf{R}}\langle Y_{\tau'}|Y_\tau(\mathbf{R})\rangle \tag{A.14}$$

$$\overset{\mathbf{k}=\mathrm{K/K'}}{\propto} \frac{1}{3}\sum_{n}^{3} e^{i\frac{2\pi}{3}n\left(\tilde{m}_{\mathrm{K/K'}}-m'+m\right)} \tag{A.15}$$

$$= \delta_{(m'-m)\mathrm{mod}(3),\tilde{m}_{\mathrm{K/K'}}}, \tag{A.16}$$

where the Bloch lattice phase enters at K/K' with $\tilde{m}_{\mathrm{K/K'}} = \{\pm 1, \mp 1\}$ at $\{\mathrm{A,B}\}$. Akin to the Bloch localization in Eq. 3.17, this relates m and $-m$:

$$A\text{:}\quad \begin{cases} \mathbf{k} = K, & \text{if } (m'-m) \mod 3 = -1 \\ \mathbf{k} = K', & \text{if } (m'-m) \mod 3 = +1 \end{cases},$$

$$B\text{:}\quad \begin{cases} \mathbf{k} = K, & \text{if } (m'-m) \mod 3 = +1 \\ \mathbf{k} = K', & \text{if } (m'-m) \mod 3 = -1 \end{cases}.$$

A further constraint arises from the symmetry of the Legendre polynomials requiring that P_m^l and $P_{m'}^{l'}$ are both even or odd with respect to horizontal reflection

$$|\langle P_{m'}^{l'}|P_m^l(\mathbf{R})\rangle| \begin{cases} > 0, & \text{if } (l-m+l'-m') \bmod 2 = 0 \\ = 0, & \text{if } (l-m+l'-m') \bmod 2 = 1 \end{cases}.$$

This shows indeed, that the valley Bloch function of a chiral triangular doublet $|\pm m\rangle$ with $m \bmod 3 \neq 0$ can be mapped onto a bipartite honeycomb basis whose magnetic quantum numbers are constrained to $m' \bmod 3 = 0$. For example a $\{p_+, p_-\}$ basis can be mapped onto a $\{s_\mathrm{A}, s_\mathrm{B}\}$-like honeycomb basis located on the sublattice sites A and B. Consequently, a triangular $\{d_+, d_-\}$ basis (odd under reflections at the horizontal reflection plane) transforms into a p_z-like graphene basis. The concrete basis transformation involves the elaborate evaluation of the overlap of Coulomb-Sturmians, so-called Shibuya-Wulfman integrals [213].

A.4. Berry curvature of Dirac Fermions and Nodal lines in 2D

Here, we derive the Berry charge of the low-energy features of the triangular lattice model discussed in Chaps. 4 and 5. A spin-diagonal basis can be chosen locally in momentum space, which allows for a comprehensive analysis in terms of Berry curvature instead of spin-Berry curvature.

Without loss of generality, any avoided band crossing in 2D can be approximated locally in momentum space by the generic Hamiltonian

$$H(\mathbf{k}) = d_x(\mathbf{k})\sigma_x + d_y(\mathbf{k})\sigma_y + m\sigma_z, \tag{A.17}$$

with mass parameter m. With the gauge-invariant definition of the Berry curvature [74],

$$\Omega_k^n(\mathbf{k}) = -\Im \sum_{m\neq n} \frac{\epsilon_{ijk}\langle n(\mathbf{k})|\partial_{k_i}H(\mathbf{k})|m(\mathbf{k})\rangle\langle m(\mathbf{k})|\partial_{k_j}H(\mathbf{k})|n(\mathbf{k})\rangle}{(E_m(\mathbf{k}) - E_n(\mathbf{k}))^2}, \tag{A.18}$$

its calculation from the eigenstates and eigenenergies of Eq. A.17 is straightforward, also the derivative of the Hamiltonian is well-defined. Further, only $\Omega_z^n(\mathbf{k})$ is non-vanishing in 2D. Hence the Berry charge of an avoided low-energy crossing is given by

$$\gamma = \int \mathrm{d}^2\mathbf{k}\Omega_z^n(\mathbf{k}). \tag{A.19}$$

A.4.1. Berry Charge of a Dirac Cone

Upon considering a rotationally-symmetric Dirac dispersion, as it is the case at the valley momenta of the hexagonal BZ, Eq. A.17 reads[1]

$$H(\mathbf{k}) = k_x\sigma_x + k_y\sigma_y + m\sigma_z. \tag{A.20}$$

Hence the radial momentum dependence of the Berry curvature can be directly calculated from the eigenstates given in Sec. 3.5 in Eq. 3.26

$$\Omega_z^{\pm}(k_r) = \pm\frac{m}{2(k_r^2 + m^2)^{3/2}}, \tag{A.21}$$

and the associated Berry charge is

$$\gamma = \int_0^{2\pi}\int_0^{\infty} k_r \mathrm{d}\varphi \mathrm{d}k_r \Omega_z^{\pm}(k_r) = \pm\pi. \tag{A.22}$$

[1]The group velocity has been set to 1 for simplicity.

The Berry charge of a single Dirac cone in 2D violates obviously the Chern theorem $2\pi C = \gamma$. This is however reconciled by the fact, that Dirac cones must come in multiples of two in 2D. The total Berry charge of a pair of Dirac cones obeys the Chern theorem.

A.4.2. Berry Charge of a Nodal Ring

A low-energy description of the nodal ring formed by the p_r-p_z crossing is more subtle, as the mass term, i.e., the orientation of the OAM polarization, varies. However, the nodal ring may be considered as being generated from a continuous rotation of a Dirac cone around the center of the ring. Hence the Berry charge is given by

$$\gamma = \lim_{r\to\infty} \int_0^{2\pi} \int_{-r}^{\infty} k_r \mathrm{d}\varphi \mathrm{d}k_r \Omega_z^{\pm}(k_r) = \pm 2\pi, \tag{A.23}$$

where the integral over the radial momentum is evaluated from the center of the ring with radius r over the Dirac point at $k_r = 0$ to ∞. Upon taking the radius of the nodal ring to ∞, the integral yields a quantized Berry charge of $\pm 2\pi$. Again, as mentioned in Sec. 5.2, in a periodic lattice model, higher-order terms in the dispersion will guarantee for a quantization of the Berry charge in a BZ with finite size.

As a concluding remark, it should be noted that the p_r-p_z nodal ring collapses to a quadratic band touching at Γ, if the in-plane and out-of plane bands are shifted in energy against each other (see for instance Fig. 4.1.2). Hence such a massive quadratic band touching must also possess a Berry charge of $\pm 2\pi$. Consequently, this applies also to the SOC gapped in-plane bands at Γ. This feature is in conduction for the discussed models, therefore it is not relevant for their $\mathbb{Z}_2$-topology. It may be considered in future investigations with different tight-binding parameters and an adjusted electron filling.

A.5. Sublattice Polarization and Non-Local Overlap Matrix

Let us recall the definition of the Bloch wave function given in Eq. 2.34 for an atomic-like orbital $|\phi_{j\mathbf{R}}\rangle$,

$$|\psi_j(\mathbf{k})\rangle = \sum_{\mathbf{R}} e^{i\mathbf{k}\cdot\mathbf{R}} |\phi_{j\mathbf{R}}\rangle \,. \tag{A.24}$$

In the following, we assume that the orbital is located on the triangular basis position (0,0,0) of the UC at Bravais vector $\mathbf{R}$.

A.5.1. Honeycomb Sublattice Polarization

Hence, the real-space representation of the Bloch wave function reads at the honeycomb sublattice sites A=(1/3,2/3) and B=(2/3,1/3)

$$\langle \mathbf{r} = \{\mathrm{A,B}\} | \psi_j(\mathbf{k}) \rangle = \sum_{\mathbf{R}} e^{i\mathbf{k}\cdot\mathbf{R}} \langle \mathbf{r} | \phi_{j\mathbf{R}} \rangle \,. \tag{A.25}$$

Despite of the summation over all triangular lattice sites $\mathbf{R}$, its calculation requires also a real-space parametrization of the local orbital φ_j. Under the assumption[2], that the orbital is sufficiently localized, we consider only the three nearest neighbor lattice sites $\mathbf{R}_i$ shown in Fig. 3.2.1

$$\langle \mathbf{r} = \{\mathrm{A,B}\} | \psi_j(\mathbf{k}) \rangle = \sum_{n=0}^{2} e^{i\mathbf{k}\cdot\mathbf{R}_i} \langle \mathbf{r} | \phi_{j\mathbf{R}_i} \rangle \,. \tag{A.26}$$

Further, we neglect the radial part of φ_j and take only its spherical contribution into account

$$\langle \mathbf{r} | \phi_j \rangle \equiv \langle \mathbf{r} = (r, \varphi) | Y_{lm} \rangle = e^{i\varphi m}, \tag{A.27}$$

where l and m are the total and the magnetic quantum number of ϕ_j, respectively. For a given Bloch state of the Hamiltonian

$$|\Psi(\mathbf{k})\rangle = \sum_{\mathbf{R}j} e^{i\mathbf{k}\cdot\mathbf{R}} c_{\mathbf{k}j} \, |\phi_{\mathbf{R},j}\rangle \,, \tag{A.28}$$

we define the sublattice polarization [2]

$$X_{\mathrm{A,B}}(\mathbf{k}) = |\, \langle \mathbf{r} | \Psi(\mathbf{k}) \rangle \,|^2 = \left| \frac{1}{3} \sum_{i=0}^{2} e^{i\mathbf{k}\cdot\mathbf{R}_i} \sum_j c_{\mathbf{k}j} e^{i\frac{2\pi}{3} n \hat{L}_z} \, |\phi_j\rangle \right|^2 . \tag{A.29}$$

Here, we exploit that all three nearest neighbors can be mapped onto each other by $C_3^n = e^{i\frac{2\pi}{3} n \hat{L}_z}$. Hence the main prerequisite for the calculation of the sublattice polarization is a proper definition of $\hat{L}_z$ in the tight-binding basis φ_j.

A.5.2. Non-Local Overlap Matrix

In Sec. 5.9, the overlap matrix from a projection onto atomic-like orbitals τ_j

$$S_{ij}(\mathbf{k}) = \langle \tau_i | \hat{\mathcal{P}}(\mathbf{k}) | \tau_j \rangle \,, \tag{A.30}$$

[2]Further arguments in support of this approximation can be found in Chap. 3.3.

is calculated with the projection operator of the occupied states

$$\hat{\mathcal{P}}(\mathbf{k}) = \sum_{n}^{N} |\Psi_{n\mathbf{k}}\rangle \langle \Psi_{n\mathbf{k}}| \,. \tag{A.31}$$

In cases, where the trial basis is displaced from the atomic lattice position, non local contributions must be taken into account. Similarly to the sublattice polarization, we consider only overlaps with orbitals on the three nearest neighbor triangular sites.

$$\langle \phi_i(\mathbf{r} = (r, \varphi))|\tau_j\rangle = \langle Y_{l'm'}(r, \phi)|Y_{lm}\rangle = e^{i\varphi(m-m')}\delta_{(l-l')\bmod 2,(m-m')\bmod 2}, \tag{A.32}$$

The symmetry of the local orbitals with respect to horizontal mirror reflection symmetry σ_h is incorporated by taking into account the angular quantum number l and the magnetic quantum number m also. Hence, the overlap matrix reads

$$S_{ij}(\mathbf{k}) = \frac{1}{9} \sum_{\mathbf{R}_i\mathbf{R}_j} e^{i\mathbf{k}(\mathbf{R}_i - \mathbf{R}_j)} \sum_{\alpha} |c_{\mathbf{k}\alpha}|^2 \langle \tau_i|\phi_\alpha(\mathbf{R}_i)\rangle \langle \phi_\alpha(\mathbf{R}_j)|\tau_j\rangle \,. \tag{A.33}$$

While the relative phases between the A and B site can be neglected in the sublattice polarization in Eq. A.29, they are relevant for the off-diagonal elements of S_{ij}.

A.5.3. Valley Expansion of the Triangular and the Kane-Mele Model

In Sec. 5.10 the p-shell triangular lattice and the Kane-Mele model with identical valley Hamiltonians are compared. Here we will derive their Dirac Hamiltonians. This allows for a direct relation between the tight-binding parameters of the two models. In the following, the lattice constant will be the unit of length and the scaling factor of 2π between real and reciprocal space is set to 1.

The Hamiltonian of the $\{p_x, p_y\}$ subspace on the triangular lattice reads

$$\begin{aligned} H(\mathbf{k}) =& (V^\sigma + V^\pi) \cdot [\cos(k_1) + \cos(k_2) + \cos(k_1 + k_2)]\, \tau_0 \otimes \sigma_0 \\ &+ \frac{\sqrt{3}}{2}(V^\sigma - V^\pi) \cdot [-\cos(k_2) + \cos(k_1 + k_2)]\, \tau_x \otimes \sigma_0 \\ &+ \frac{\lambda_{\phi_v}}{3\sqrt{3}} \cdot [\sin(k_1) + \sin(k_2) - \sin(k_1 + k_2)]\, \tau_y \otimes \sigma_0 \\ &+ \frac{1}{2}(V^\sigma - V^\pi) \cdot [2\cos(k_1) - \cos(k_2) - \cos(k_1 + k_2)]\, \tau_z \otimes \sigma_0 \\ &+ \frac{\lambda_{\mathrm{SOC}}}{2} \cdot \tau_y \otimes \sigma_z, \end{aligned} \tag{A.34}$$

where τ_i and σ_i are Pauli matrices acting on the orbital and spin degrees of freedom, respectively. The expansion of the Hamiltonian up to first order around $K = (2/3, -1/3)$ with $\mathbf{k} = \mathbf{k}' - K$ is given by

$$H_K^{\mathrm{triang}}(\mathbf{k}) = H(\mathrm{K}) + \nabla_{\mathbf{k}'} H(\mathbf{k}')\big|_{\mathbf{k}'=K} \cdot \mathbf{k} + \mathcal{O}(\mathbf{k}^2)$$

$$\begin{aligned}
&\approx -\frac{3}{2}(V^\sigma + V^\pi)\cdot\tau_0\otimes\sigma_0 + \tau_y\otimes\left(\lambda_{\phi_\mathrm{v}}\sigma_0 + \frac{\lambda_\mathrm{SOC}}{2}\sigma_z\right)\\
&\quad + (V^\sigma - V^\pi)\left[-\frac{3}{4}(k_1+2k_2)\,\tau_x + \frac{3\sqrt{3}}{4}k_1\tau_z\right]\otimes\sigma_0 \qquad \text{(A.35)}\\
&\approx -\frac{3}{2}(V^\sigma + V^\pi)\cdot\tau_0\otimes\sigma_0 + \tau_y\otimes\left(\lambda_{\phi_\mathrm{v}}\sigma_0 + \frac{\lambda_\mathrm{SOC}}{2}\sigma_z\right)\\
&\quad + \frac{3\sqrt{3}}{4}(V^\sigma - V^\pi)\,(-k_y\tau_x + k_x\tau_z)\otimes\sigma_0. \qquad \text{(A.36)}
\end{aligned}$$

The Hamiltonian of the Kane-Mele model in the {A,B} basis given in Eq. 2.7 reads in momentum space in Bloch-gauge

$$\begin{aligned}
H^\mathrm{KM}(\mathbf{k}) =& t\left[(1+\cos(k_1)+\cos(k_2))\,\tau_x + (\sin(k_1)-\sin(k_2))\,\tau_y\right]\\
&+ \frac{\lambda^\mathrm{KM}_\mathrm{SOC}}{3\sqrt{3}}\cdot\left[\sin(k_1)+\sin(k_2)-\sin(k_1+k_2)\right]\tau_z\otimes\sigma_z \qquad \text{(A.37)}\\
&+ \lambda_\mathrm{ISB}\tau_z\otimes\sigma_0.
\end{aligned}$$

Its expansion up to first order at $K = (2/3, -1/3)$ yields

$$\begin{aligned}
H^\mathrm{KM}_\mathrm{K}(\mathbf{k}) \approx& t\left[\frac{\sqrt{3}}{2}(k_1+k_2)\,\tau_x + \frac{1}{2}(k_1-k_2)\,\tau_y\right]\otimes\sigma_0 + \tau_z\otimes\left(\lambda^\mathrm{KM}_\mathrm{SOC}\sigma_z + \lambda_\mathrm{ISB}\sigma_0\right) \qquad \text{(A.38)}\\
\approx& \frac{\sqrt{3}}{2}t\left[\left(\frac{1}{2}k_x + \frac{\sqrt{3}}{2}k_y\right)\tau_x + \left(\frac{\sqrt{3}}{2}k_x - \frac{1}{2}k_y\right)\tau_y\right]\otimes\sigma_0 + \tau_z\left(\lambda^\mathrm{KM}_\mathrm{SOC}\sigma_z + \lambda_\mathrm{ISB}\sigma_0\right).
\end{aligned}$$

Hence we find the relations $2t = 3(V^\sigma - V^\pi)$, $\lambda_\mathrm{ISB} = \lambda_{\phi_v}$ and $2\lambda^\mathrm{KM}_\mathrm{SOC} = \lambda_\mathrm{SOC}$. The factor of 2 in the SOC strength arises from the different definitions in the two models. In the triangular lattice Hamiltonian, it corresponds to the atomic SOC parameter, while it reflects directly the mass parameter of the Dirac fermions in the Kane-Mele model. As discussed in Sec. 4.4, the energy splitting between the in-plane bands and the p_z-state will rescale the effective SOC splitting of the Dirac cone. For the Kane-Mele model shown in Fig. 5.10.1 this is taken into account by fitting its SOC parameter to the splitting of the Dirac bands of the triangular model.

A.6. Bulk OAM Polarization

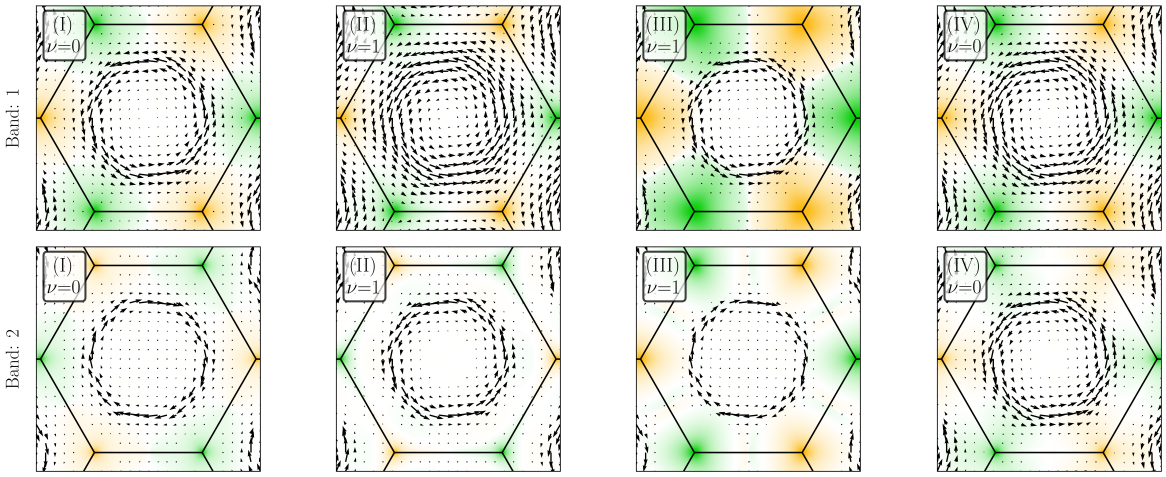

Figure A.6.1.: OAM polarization of the valence bands of the models shown in Fig. 4.3.1. The in-plane component is illustrated by a vector field plot and the color plot denotes the out-of-plane polarization. Green and orange colors denote positive and negative values, respectively.

A.7. OAM and Spin Polarization in Finite Size Geometries

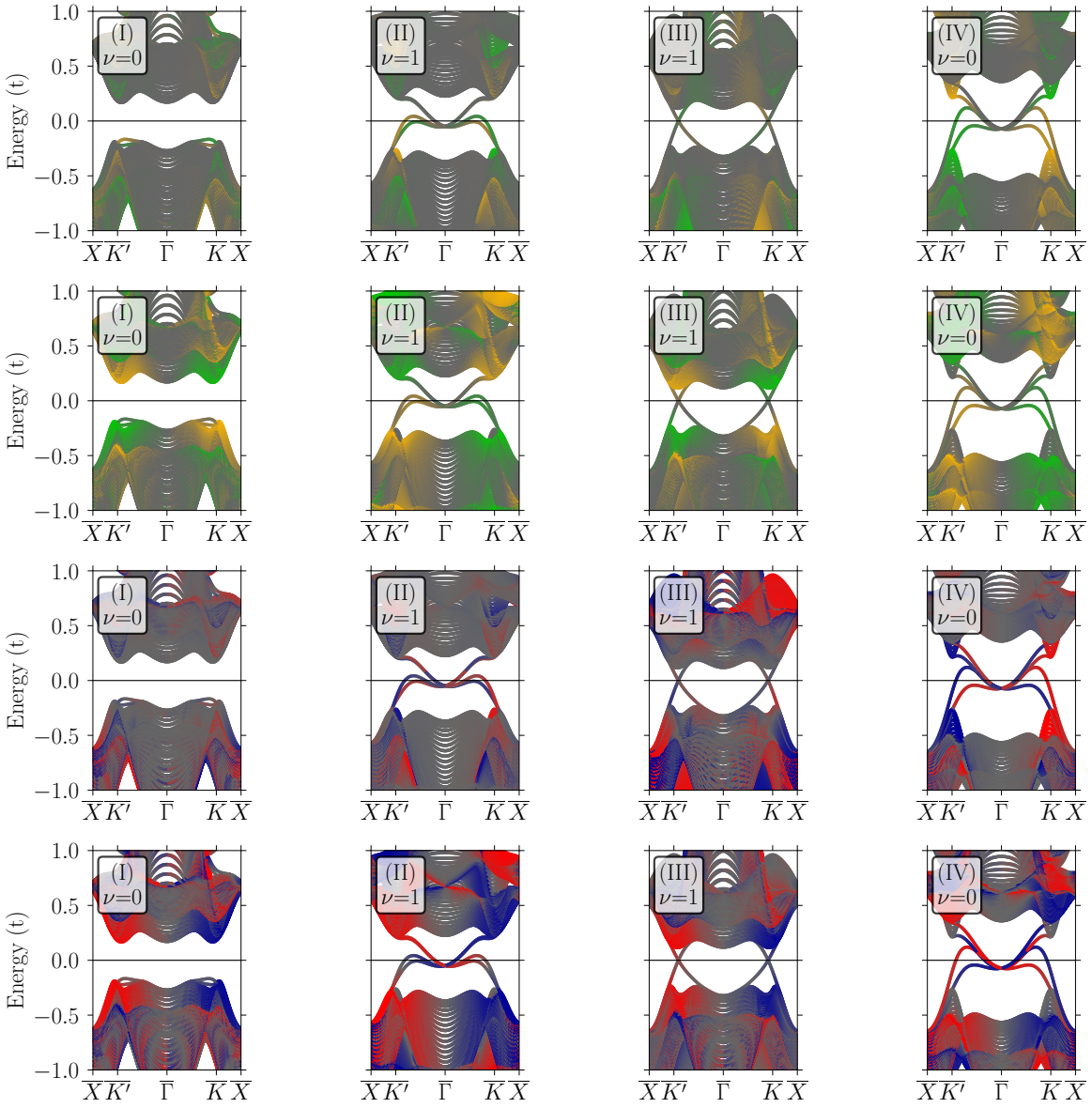

Figure A.7.1.: OAM and Spin polarization in ribbon geometries with *flat* termination for ribbons constituted of 30 conventional UCs for representatives of the models shown in Fig. 4.3.1. The rows show from top to bottom $\langle L_z \rangle, \langle L_y \rangle, \langle S_z \rangle$ and $\langle S_y \rangle$. Green/blue and orange/red denote positive and negative values, respectively. To enlarge the bulk gap, the scaling factors of $H^{\mathrm{SOC}}, H^{\phi_h}$ and H^{ϕ_v} have been chosen twice as large as in Tab. 5.1.1.

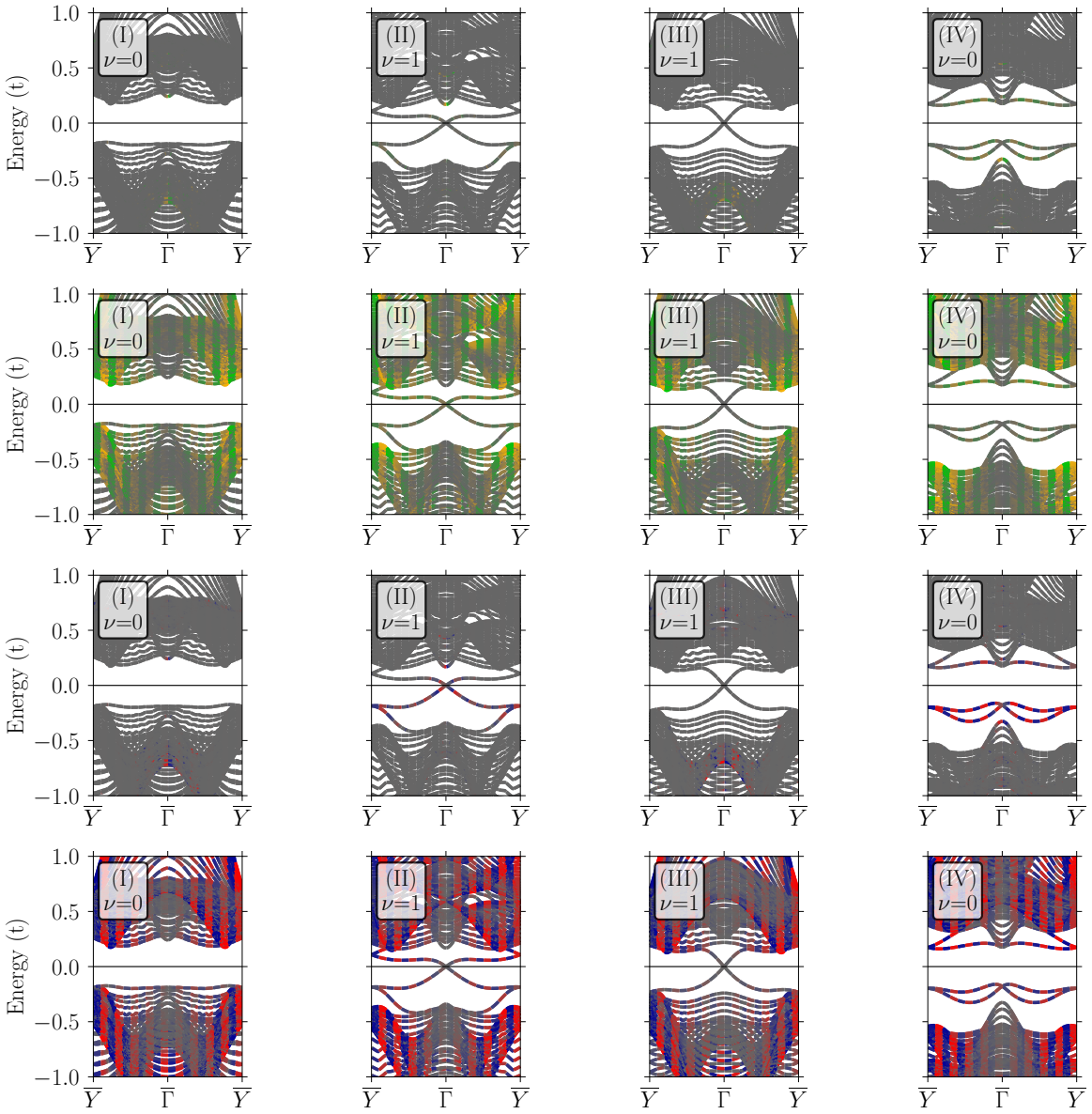

Figure A.7.2.: OAM and Spin polarization in ribbon geometries with *zigzag* termination for ribbons constituted of 30 conventional UCs for representatives of the models shown in Fig. 4.3.1. The rows show from top to bottom $\langle L_z \rangle, \langle L_x \rangle, \langle S_z \rangle$ and $\langle S_x \rangle$. In contrast to the flat edge (see Fig. A.7.1), both z-components are vanishing, the total angular momentum polarization is purely in x-direction Green/blue and orange/red denote positive and negative values, respectively. As the bands are two-fold degenerate, the plots show alternatingly the projection onto one of the Kramers partners. To enlarge the bulk gap, the scaling factors of $H^{\mathrm{SOC}}, H^{\phi_h}$ and H^{ϕ_v} have been chosen twice as large as in Tab. 5.1.1. A small $\hat{S}_z = \mathcal{O}(10^{-5})$-term has been added to make the spin a good quantum number. This promotes a weak $\langle L_z \rangle$- and $\langle S_z \rangle$-polarization around Γ.

A.8. Trial Basis Overlaps

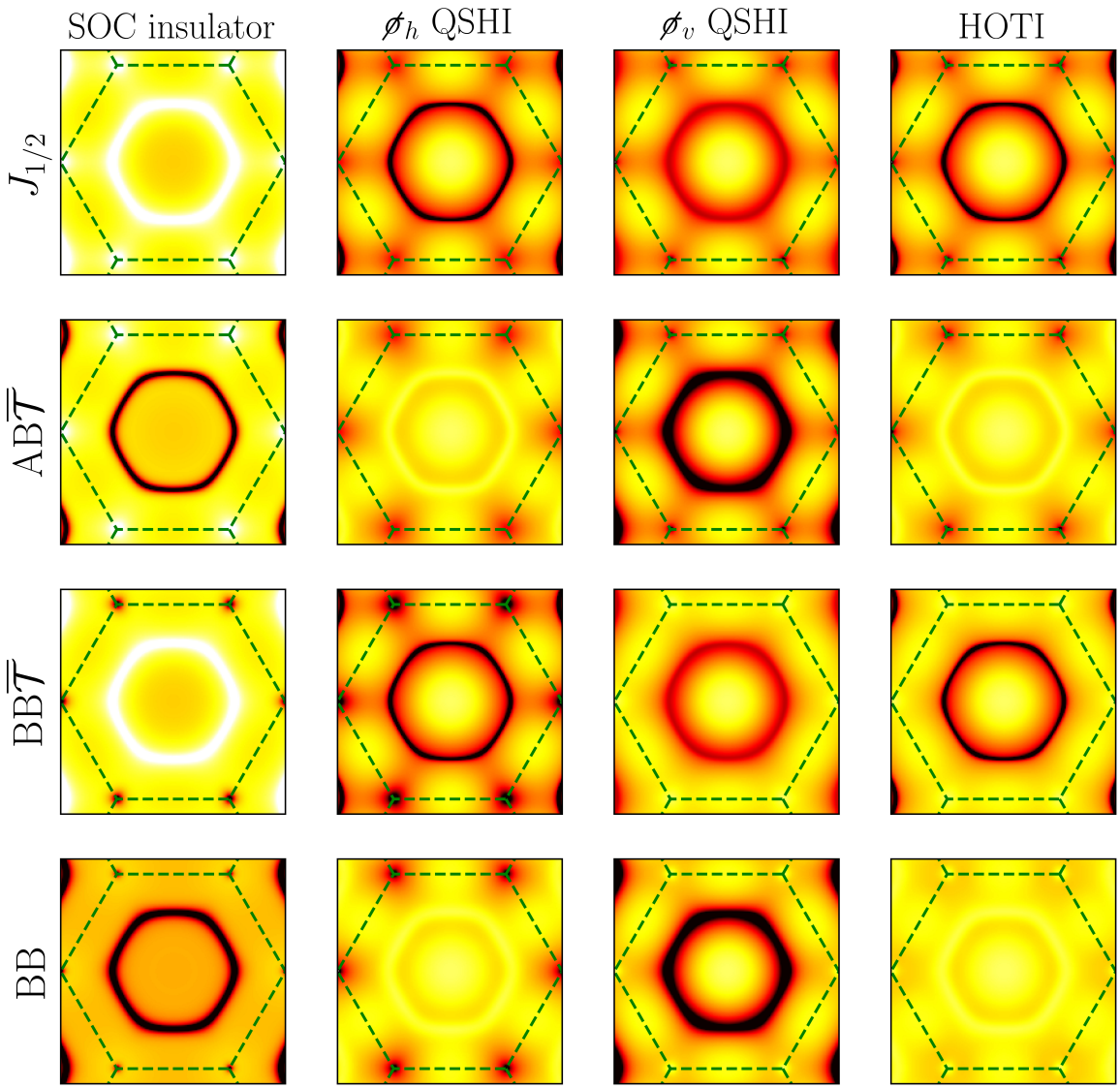

Figure A.8.1.: Logarithmic plot of $\det[S(\mathbf{k})]$ for the valence bands of representatives of the four topologically distinct phases and the trial basis sets given in Tab 5.9.1. The range of the color code is identical in all panels and dark colors denote vanishing overlap eigenvalues. The green dashed lines indicate the first BZ. The diagonal of the figure denotes the tuple of the model and projection basis, for which the overlap is finite in the full BZ, i.e. the valence states are a band representation of that trial basis. The tight-binding parameters of the models can be found in Tab. 5.1.1.

A.9. AgTe: Comparison of the Minimal Tight-Binding Model and DFT

To obtain a qualitative model description of the low-energy in-plane Te p-physics on Ag (111), we invoke the minimal triangular Hamiltonian introduced in Chap. 4 with the tight-binding parameters given in Tab. A.9.1. The band structure with OAM and spin polarization is shown in the top rows of Figs. A.9.1 and A.9.2, respectively. To describe the Ag s band, the triangular p_z-orbital (on the Te site) is borrowed, which results in a reasonable qualitative agreement. However, a closer inspection reveals a deviation in the $\beta_\pm$ feature: while the DFT model possesses a weak OAM polarization in β_- (lower β band), β_+ has a reduced polarization for the minimal model. The correct pattern is reproduced, if the p_z-band is shifted below the in-plane bands at Γ. This is in fact also the case in the DFT calculations, where the Te p_z-band hybridizes with the Ag-substrate quantum well states in valence [see also Fig. S2(d) of the supplemental material of Ref. [1]].

E_z	V^σ	V^π	$V^\pi_{p_z}$	λ_{ϕ_h}	λ_{ϕ_v}	λ_{SOC}
5.7	0.45	0.15	-0.5	0.2	0.1	0.3

Table A.9.1.: Parameters for the qualitative tight-binding model in units of the hopping parameter t (the unit set to eV in Figs. A.9.1 and A.9.2).

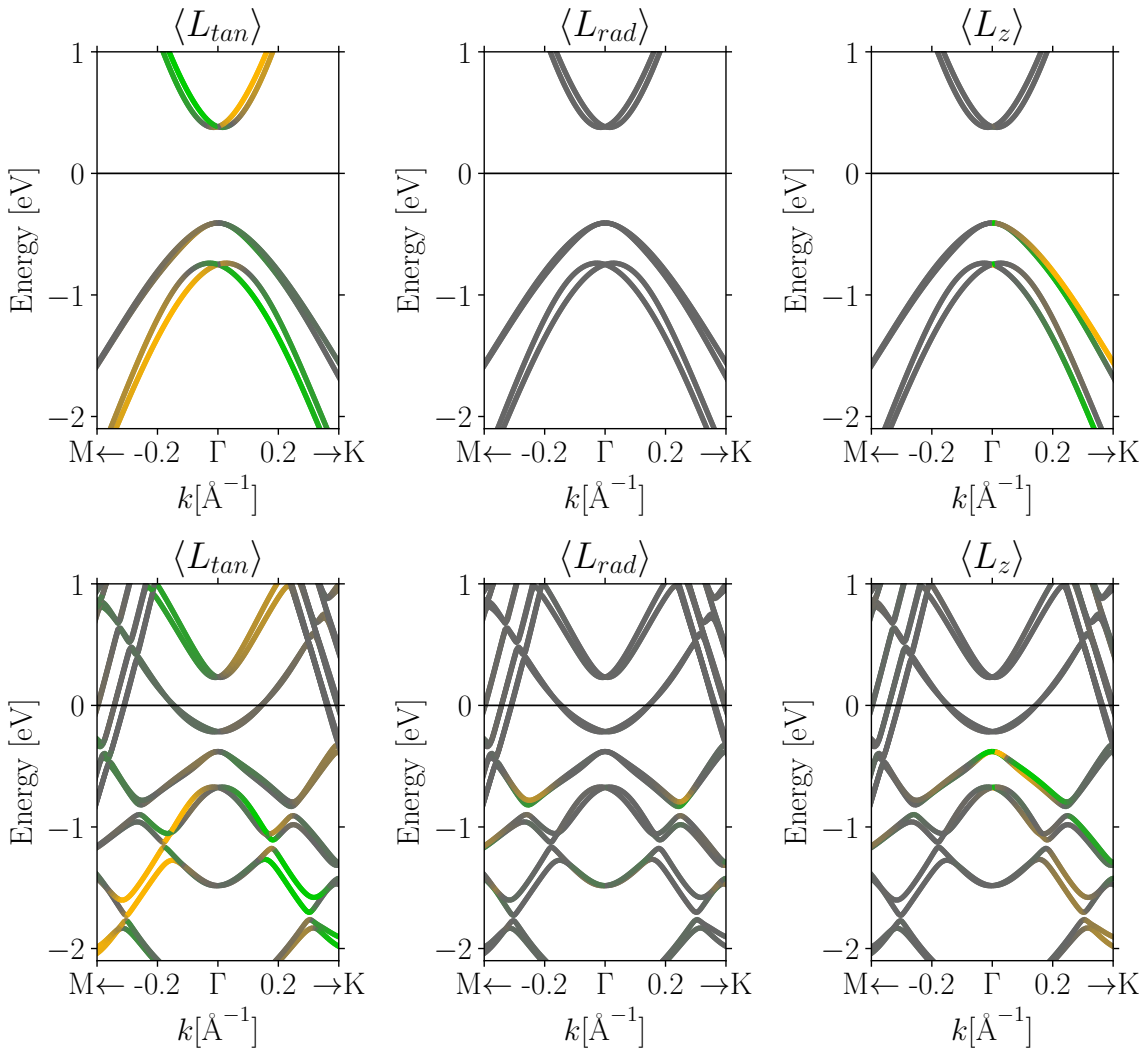

Figure A.9.1.: OAM polarization in the minimal p-shell model and the AgTe-projected one of the *ab initio*-derived Wannier model in the top and bottom row, respectively.

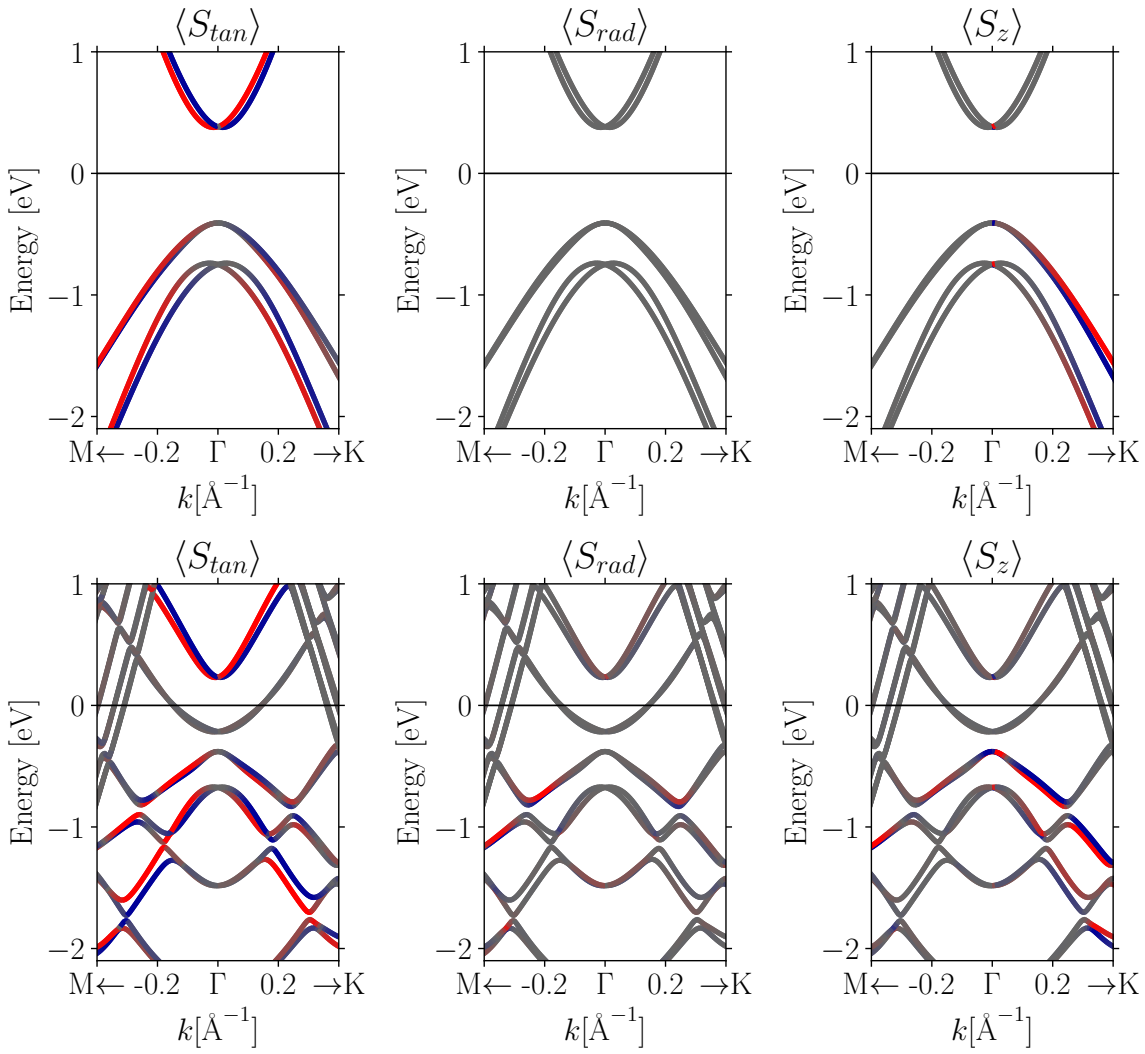

Figure A.9.2.: Spin polarization in the minimal p-shell model and the AgTe-projected one of the *ab initio*-derived Wannier model in the top and bottom row, respectively.

Bibliography

1. Ünzelmann, M., Bentmann, H., Eck, P., Kißlinger, T., Geldiyev, B., Rieger, J., Moser, S., Vidal, R. C., Kißner, K., Hammer, L., Schneider, M. A., Fauster, T., Sangiovanni, G., Di Sante, D. & Reinert, F. "Orbital-Driven Rashba Effect in a Binary Honeycomb Monolayer AgTe". *Physical Review Letters* **124** (2020).
2. Eck, P., Ortix, C., Consiglio, A., Erhardt, J., Bauernfeind, M., Moser, S., Claessen, R., Di Sante, D. & Sangiovanni, G. "Real-space obstruction in quantum spin Hall insulators". *Physical Review B* **106,** 195143 (2022).
3. Bauernfeind, M., Erhardt, J., Eck, P., Thakur, P. K., Gabel, J., Lee, T. L., Schäfer, J., Moser, S., Di Sante, D., Claessen, R. & Sangiovanni, G. "Design and realization of topological Dirac fermions on a triangular lattice". *Nature Communications* **12,** 5396 (2021).
4. Eck, P., Fang, Y., Di Sante, D., Sangiovanni, G. & Cano, J. "Recipe for higher order topology on the triangular lattice". *Phys. Rev. B* **107,** 115130 (2023).
5. Bloch, F. "Über die Quantenmechanik der Elektronen in Kristallgittern". *Zeitschrift für Physik* **52,** 555–600 (1929).
6. Slater, J. C. & Koster, G. F. "Simplified LCAO method for the periodic potential problem". *Physical Review* **94,** 1498–1524 (1954).
7. Hohenberg, P. & Kohn, W. "Inhomogeneous Electron Gas". *Physical Review* **136,** B864–B871 (1964).
8. Kohn, W. & Sham, L. J. "Self-Consistent Equations Including Exchange and Correlation Effects". *Physical Review* **140,** A1133–A1138 (1965).
9. Czochralski, J. "Ein neues Verfahren zur Messung der Kristallisationsgeschwindigkeit der Metalle". *Zeitschrift für Physikalische Chemie* **92U,** 219–221 (1918).
10. Günther, K. G. "Aufdampfschichten aus halbleitenden III-V-Verbindungen". *Zeitschrift für Naturforschung A* **13,** 1081–1089 (1958).
11. Willson, C. G., Dammel, R. R. & Reiser, A. *Photoresist materials: a historical perspective.* in *Advances in Resist Technology and Processing XIV* (ed Tarascon-Auriol, R. G.) **3049** (SPIE, 1997), 28–41.
12. Binnig, G. & Rohrer, H. "Scanning tunneling microscopy". *Surface Science* **126,** 236–244 (1983).
13. Eigler, D. M. & Schweizer, E. K. "Positioning single atoms with a scanning tunnelling microscope". *Nature* **344,** 524–526 (1990).

14. Zhang, H., Pincelli, T., Jozwiak, C., Kondo, T., Ernstorfer, R., Sato, T. & Zhou, S. "Angle-resolved photoemission spectroscopy". *Nature Reviews Methods Primers* **2,** 54 (2022).

15. Wen, X.-G. "Topological orders and edge excitations in fractional quantum Hall states". *Advances in Physics* **44,** 405–473 (1995).

16. Jackiw, R. & Rebbi, C. "Solitons with fermion number $\frac{1}{2}$". *Physical Review D* **13,** 3398–3409 (1976).

17. Su, W. P., Schrieffer, J. R. & Heeger, A. J. "Solitons in Polyacetylene". *Physical Review Letters* **42,** 1698–1701 (1979).

18. Kane, C. L. & Mele, E. J. "Quantum Spin hall effect in graphene". *Physical Review Letters* **95** (2005).

19. Hasan, M. Z. & Kane, C. L. "Colloquium : Topological insulators". *Reviews of Modern Physics* **82,** 3045–3067 (2010).

20. Bansil, A, Lin, H. & Das, T. "Colloquium: Topological band theory". *Reviews of Modern Physics* **88,** 21004 (2016).

21. Brouder, C., Panati, G., Calandra, M., Mourougane, C. & Marzari, N. "Exponential Localization of Wannier Functions in Insulators". *Physical Review Letters* **98,** 46402 (2007).

22. Panati, G. "Triviality of Bloch and Bloch–Dirac Bundles". *Annales Henri Poincaré* **8,** 995–1011 (2007).

23. Altland, A. & Zirnbauer, M. R. "Nonstandard symmetry classes in mesoscopic normal-superconducting hybrid structures". *Physical Review B* **55,** 1142–1161 (1997).

24. Kane, C. L. & Mele, E. J. "Z2 topological order and the quantum spin hall effect". *Physical Review Letters* **95,** 146802 (2005).

25. Moore, J. E. & Balents, L. "Topological invariants of time-reversal-invariant band structures". *Physical Review B* **75,** 121306 (2007).

26. Bernevig, B. A. & Zhang, S.-C. "Quantum Spin Hall Effect". *Physical Review Letters* **96,** 106802 (2006).

27. Bernevig, B. A., Hughes, T. L. & Zhang, S.-C. "Quantum Spin Hall Effect and Topological Phase Transition in HgTe Quantum Wells". *Science* **314,** 1757–1761 (2006).

28. Kitaev, A. "Fault-tolerant quantum computation by anyons". *Annals of Physics* **303,** 2–30 (2003).

29. Murakami, S. "Quantum spin hall effect and enhanced magnetic response by spin-orbit coupling". *Physical Review Letters* **97,** 236805 (2006).

30. Fu, L. & Kane, C. L. "Superconducting Proximity Effect and Majorana Fermions at the Surface of a Topological Insulator". *Physical Review Letters* **100,** 96407 (2008).

31. Xia, Y., Qian, D., Hsieh, D., Wray, L., Pal, A., Lin, H., Bansil, A., Grauer, D., Hor, Y. S., Cava, R. J. & Hasan, M. Z. "Observation of a large-gap topological-insulator class with a single Dirac cone on the surface". *Nature Physics* **5,** 398–402 (2009).

32. Thouless, D. J. "Wannier functions for magnetic sub-bands". *Journal of Physics C: Solid State Physics* **17,** L325 (1984).

33. Thonhauser, T. & Vanderbilt, D. "Insulator/Chern-insulator transition in the Haldane model". *Physical Review B* **74,** 235111 (2006).

34. Marzari, N., Mostofi, A. A., Yates, J. R., Souza, I. & Vanderbilt, D. "Maximally localized Wannier functions: Theory and applications". *Reviews of Modern Physics* **84,** 1419–1475 (2012).

35. Thouless, D. J., Kohmoto, M., Nightingale, M. P. & den Nijs, M. "Quantized Hall Conductance in a Two-Dimensional Periodic Potential". *Physical Review Letters* **49,** 405–408 (1982).

36. Berry, M. V. "Quantal phase factors accompanying adiabatic changes". *Proceedings of the Royal Society of London. A. Mathematical and Physical Sciences* **392,** 45–57 (1984).

37. Kramers, H. A. *Théorie générale de la rotation paramagnétique dans les cristaux.* in *Proceedings of the Royal Netherlands Academy of Arts and Sciences* **33** (1930), 959.

38. Park, S. R., Kim, C. H., Yu, J., Han, J. H. & Kim, C. "Orbital-Angular-Momentum Based Origin of Rashba-Type Surface Band Splitting". *Physical Review Letters* **107,** 156803 (2011).

39. Sunko, V., Rosner, H., Kushwaha, P., Khim, S., Mazzola, F., Bawden, L., Clark, O. J., Riley, J. M., Kasinathan, D., Haverkort, M. W., Kim, T. K., Hoesch, M., Fujii, J., Vobornik, I., Mackenzie, A. P. & King, P. D. C. "Maximal Rashba-like spin splitting via kinetic-energy-coupled inversion-symmetry breaking". *Nature* **549,** 492–496 (2017).

40. Fu, L. & Kane, C. L. "Time reversal polarization and a Z_2 adiabatic spin pump". *Physical Review B* **74,** 195312 (2006).

41. Fu, L. & Kane, C. L. "Topological insulators with inversion symmetry". *Physical Review B* **76,** 45302 (2007).

42. Soluyanov, A. A. & Vanderbilt, D. "Computing topological invariants without inversion symmetry". *Physical Review B* **83,** 235401 (2011).

43. Yu, R., Qi, X. L., Bernevig, A., Fang, Z. & Dai, X. "Equivalent expression of Z2 topological invariant for band insulators using the non-Abelian Berry connection". *Physical Review B* **84,** 75119 (2011).

44. Bradlyn, B., Elcoro, L., Cano, J., Vergniory, M. G., Wang, Z., Felser, C., Aroyo, M. I. & Bernevig, B. A. "Topological quantum chemistry". *Nature* **547,** 298–305 (2017).

45. Kruthoff, J., de Boer, J., van Wezel, J., Kane, C. L. & Slager, R.-J. "Topological Classification of Crystalline Insulators through Band Structure Combinatorics". *Physical Review X* **7,** 41069 (2017).

46. Po, H. C., Vishwanath, A. & Watanabe, H. "Symmetry-based indicators of band topology in the 230 space groups". *Nature Communications* **8,** 50 (2017).

47. Cano, J., Bradlyn, B., Wang, Z., Elcoro, L., Vergniory, M. G., Felser, C., Aroyo, M. I. & Bernevig, B. A. "Building blocks of topological quantum chemistry: Elementary band representations". *Physical Review B* **97,** 035139 (2018).

48. Guo, H.-M. & Franz, M. "Topological insulator on the kagome lattice". *Physical Review B* **80,** 113102 (2009).

49. König, M., Wiedmann, S., Brüne, C., Roth, A., Buhmann, H., Molenkamp, L. W., Qi, X.-L. & Zhang, S.-C. "Quantum Spin Hall Insulator State in HgTe Quantum Wells". *Science* **318,** 766–770 (2007).

50. Hsieh, D., Qian, D., Wray, L., Xia, Y., Hor, Y. S., Cava, R. J. & Hasan, M. Z. "A topological Dirac insulator in a quantum spin Hall phase". *Nature* **452,** 970–974 (2008).

51. Zhang, H., Liu, C.-X., Qi, X.-L., Dai, X., Fang, Z. & Zhang, S.-C. "Topological insulators in Bi2Se3, Bi2Te3 and Sb2Te3 with a single Dirac cone on the surface". *Nature Physics* **5,** 438–442 (2009).

52. Reis, F., Li, G., Dudy, L., Bauernfeind, M., Glass, S., Hanke, W., Thomale, R., Schäfer, J. & Claessen, R. "Bismuthene on a SiC substrate: A candidate for a high-temperature quantum spin Hall material". *Science* **357,** 287–290 (2017).

53. Haldane, F. D. "Model for a quantum hall effect without landau levels: Condensed-matter realization of the "parity anomaly"". *Physical Review Letters* **61,** 2015–2018 (1988).

54. Yao, Y., Ye, F., Qi, X.-L., Zhang, S.-C. & Fang, Z. "Spin-Orbit Gap of Graphene: First-Principles Calculations". *Physical Review B* **75,** 41401 (2007).

55. Liu, C. C., Jiang, H. & Yao, Y. "Low-energy effective Hamiltonian involving spin-orbit coupling in silicene and two-dimensional germanium and tin". *Physical Review B* **84,** 195430 (2011).

56. Molle, A., Goldberger, J., Houssa, M., Xu, Y., Zhang, S.-C. & Akinwande, D. "Buckled two-dimensional Xene sheets". *Nature Materials* **16,** 163–169 (2017).

57. Di Sante, D., Eck, P., Bauernfeind, M., Will, M., Thomale, R., Schäfer, J., Claessen, R. & Sangiovanni, G. "Towards topological quasifreestanding stanene via substrate engineering". *Physical Review B* **99** (2019).

58. Ortiz, B. R., Teicher, S. M. L., Hu, Y., Zuo, J. L., Sarte, P. M., Schueller, E. C., Abeykoon, A. M. M., Krogstad, M. J., Rosenkranz, S., Osborn, R., Seshadri, R., Balents, L., He, J. & Wilson, S. D. "CsV_3Sb_5: A Z_2 Topological Kagome Metal with a Superconducting Ground State". *Physical Review Letters* **125,** 247002 (2020).

59. Kang, M., Ye, L., Fang, S., You, J.-S., Levitan, A., Han, M., Facio, J. I., Jozwiak, C., Bostwick, A., Rotenberg, E., Chan, M. K., McDonald, R. D., Graf, D., Kaznatcheev, K., Vescovo, E., Bell, D. C., Kaxiras, E., van den Brink, J., Richter, M., Prasad Ghimire, M., Checkelsky, J. G. & Comin, R. "Dirac fermions and flat bands in the ideal kagome metal FeSn". *Nature Materials* **19,** 163–169 (2020).

60. Kang, M., Fang, S., Ye, L., Po, H. C., Denlinger, J., Jozwiak, C., Bostwick, A., Rotenberg, E., Kaxiras, E., Checkelsky, J. G. & Comin, R. "Topological flat bands in frustrated kagome lattice CoSn". *Nature Communications* **11,** 4004 (2020).

61. Erhardt, J., Bauernfeind, M., Eck, P., Kamp, M., Gabel, J., Lee, T.-L., Sangiovanni, G., Moser, S. & Claessen, R. "Indium Epitaxy on SiC(0001): A Roadmap to Large Scale Growth of the Quantum Spin Hall Insulator Indenene". *Journal of Physical Chemistry C* **126,** 16289–16296 (2022).

62. Po, H. C., Watanabe, H., Zaletel, M. P. & Vishwanath, A. "Filling-Enforced Quantum Band Insulators in Spin-Orbit Coupled Crystals". *Science Advances* **2,** e1501782 (2016).

63. Li, G., Xu, Y., Song, Z., Yang, Q., Zhang, Y., Liu, J., Gupta, U., Süβ, V., Sun, Y., Sessi, P., Parkin, S. S. P., Bernevig, B. A. & Felser, C. "Obstructed Surface States as the Descriptor for Predicting Catalytic Active Sites in Inorganic Crystalline Materials". *Advanced Materials* **34,** 2201328 (2022).

64. Xu, Y., Elcoro, L., Song, Z.-D., Vergniory, M., Felser, C., Parkin, S. S., Regnault, N., Mañes, J. L. & Bernevig, B. A. "Filling-Enforced Obstructed Atomic Insulators". *arXiv:2106.10276* (2021).

65. Benalcazar, W. A., Bernevig, B. A. & Hughes, T. L. "Quantized electric multipole insulators". *Science* **357,** 61–66 (2017).

66. Benalcazar, W. A., Bernevig, B. A. & Hughes, T. L. "Electric multipole moments, topological multipole moment pumping, and chiral hinge states in crystalline insulators". *Physical Review B* **96,** 245115 (2017).

67. Langbehn, J., Peng, Y., Trifunovic, L., von Oppen, F. & Brouwer, P. W. "Reflection-Symmetric Second-Order Topological Insulators and Superconductors". *Physical Review Letters* **119,** 246401 (2017).

68. Song, Z., Fang, Z. & Fang, C. "$(d-2)$-Dimensional Edge States of Rotation Symmetry Protected Topological States". *Physical Review Letters* **119,** 246402 (2017).

69. Schindler, F., Cook, A. M., Vergniory, M. G., Wang, Z., Parkin, S. S. P., Bernevig, B. A. & Neupert, T. "Higher-order topological insulators". *Science Advances* **4,** eaat0346 (2018).

70. Schindler, F., Wang, Z., Vergniory, M. G., Cook, A. M., Murani, A., Sengupta, S., Kasumov, A. Y., Deblock, R., Jeon, S., Drozdov, I., Bouchiat, H., Guéron, S., Yazdani, A., Bernevig, B. A. & Neupert, T. "Higher-order topology in bismuth". *Nature Physics* **14,** 918–924 (2018).

71. Van Miert, G. & Ortix, C. "Higher-Order Topological Insulators Protected by Inversion and Rotoinversion Symmetries". *Physical Review B* **98,** 81110 (2018).

72. Van Miert, G. & Ortix, C. "On the topological immunity of corner states in two-dimensional crystalline insulators". *npj Quantum Materials* **5,** 63 (2020).

73. Soluyanov, A. A. & Vanderbilt, D. "Wannier Representation of $\mathbb{Z}_2$ Topological Insulators". *Physical Review B* **83,** 35108 (2011).

74. Bernevig, B. A. & Hughes, T. L. in *Topological Insulators and Topological Superconductors* (Princeton university press, 2013).

75. Vanderbilt, D. *Berry Phases in Electronic Structure Theory: Electric Polarization, Orbital Magnetization and Topological Insulators* (Cambridge University Press, 2018).

76. Klitzing, K. v., Dorda, G. & Pepper, M. "New Method for High-Accuracy Determination of the Fine-Structure Constant Based on Quantized Hall Resistance". *Physical Review Letters* **45,** 494–497 (1980).

77. Goldman, N., Budich, J. C. & Zoller, P. "Topological quantum matter with ultracold gases in optical lattices". *Nature Physics* **12,** 639–645 (2016).

78. Haldane, F. D. & Raghu, S. "Possible Realization of Directional Optical Waveguides in Photonic Crystals with Broken Time-Reversal Symmetry". *Physical Review Letters* **100,** 13904 (2008).

79. Lu, L., Joannopoulos, J. D. & Soljačić, M. "Topological photonics". *Nature Photonics* **8,** 821–829 (2014).

80. Kane, C. L. & Lubensky, T. C. "Topological boundary modes in isostatic lattices". *Nature Physics* **10,** 39–45 (2014).

81. Yang, Z., Gao, F., Shi, X., Lin, X., Gao, Z., Chong, Y. & Zhang, B. "Topological Acoustics". *Physical Review Letters* **114,** 114301 (2015).

82. Ningyuan, J., Owens, C., Sommer, A., Schuster, D. & Simon, J. "Time- and Site-Resolved Dynamics in a Topological Circuit". *Physical Review X* **5,** 21031 (2015).

83. Lee, C. H., Imhof, S., Berger, C., Bayer, F., Brehm, J., Molenkamp, L. W., Kiessling, T. & Thomale, R. "Topolectrical Circuits". *Communications Physics* **1,** 39 (2018).

84. Helbig, T, Hofmann, T, Imhof, S, Abdelghany, M, Kiessling, T, Molenkamp, L. W., Lee, C. H., Szameit, A, Greiter, M & Thomale, R. "Generalized bulk–boundary correspondence in non-Hermitian topolectrical circuits". *Nature Physics* **16,** 747–750 (2020).

85. Ezawa, M. "Higher-Order Topological Insulators and Semimetals on the Breathing Kagome and Pyrochlore Lattices". *Physical Review Letters* **120,** 026801 (2018).

86. Liu, B., Zhao, G., Liu, Z. & Wang, Z. F. "Two-Dimensional Quadrupole Topological Insulator in γ-Graphyne". *Nano Letters* **19,** 6492–6497 (2019).

87. Sheng, X.-L., Chen, C., Liu, H., Chen, Z., Yu, Z.-M., Zhao, Y. X. & Yang, S. A. "Two-Dimensional Second-Order Topological Insulator in Graphdiyne". *Physical Review Letters* **123,** 256402 (2019).

88. Park, M. J., Kim, Y., Cho, G. Y. & Lee, S. B. "Higher-Order Topological Insulator in Twisted Bilayer Graphene". *Physical Review Letters* **123,** 216803 (2019).

89. Lee, E., Kim, R., Ahn, J. & Yang, B.-J. "Two-dimensional higher-order topology in monolayer graphdiyne". *npj Quantum Materials* **5,** 1 (2020).

90. Xue, Y., Huan, H., Zhao, B., Luo, Y., Zhang, Z. & Yang, Z. "Higher-order topological insulators in two-dimensional Dirac materials". *Physical Review Research* **3,** L042044 (2021).

91. Zeng, J., Liu, H., Jiang, H., Sun, Q. F. & Xie, X. C. "Multiorbital model reveals a second-order topological insulator in 1H transition metal dichalcogenides". *Physical Review B* **104,** L161108 (2021).

92. Costa, M., Schleder, G. R., Mera Acosta, C., Padilha, A. C. M., Cerasoli, F., Buongiorno Nardelli, M. & Fazzio, A. "Discovery of higher-order topological insulators using the spin Hall conductivity as a topology signature". *npj Computational Materials* **7,** 49 (2021).

93. Qian, S., Liu, G.-B., Liu, C.-C. & Yao, Y. "C_n-symmetric higher-order topological crystalline insulators in atomically thin transition metal dichalcogenides". *Physical Review B* **105,** 045417 (2022).

94. Semenoff, G. W. "Condensed-Matter Simulation of a Three-Dimensional Anomaly". *Physical Review Letters* **53,** 2449–2452 (1984).

95. Kresse, G & Hafner, J. "Ab initio molecular-dynamics simulation of the liquid-metal–amorphous-semiconductor transition in germanium". *Physical Review B* **49,** 14251–14269 (1994).

96. Kresse, G & Furthmüller, J. "Efficiency of ab-initio total energy calculations for metals and semiconductors using a plane-wave basis set". *Computational Materials Science* **6,** 15–50 (1996).

97. Kresse, G. & Furthmüller, J. "Efficient iterative schemes for ab initio total-energy calculations using a plane-wave basis set". *Physical Review B* **54,** 11169–11186 (1996).

98. Kresse, G. & Joubert, D. "From ultrasoft pseudopotentials to the projector augmented-wave method". *Physical Review B* **59,** 1758–1775 (1999).

99. Grosso, G. & Parravicini, G. P. *Solid State Physics* (Elsevier, San Diego, UNITED KINGDOM, 2000).

100. Martin, R. M. *Electronic Structure: Basic Theory and Practical Methods* 2nd ed. (Cambridge University Press, 2020).

101. Born, M. & Oppenheimer, R. "Zur Quantentheorie der Molekeln". *Annalen der Physik* **389,** 457–484 (1927).

102. Koopmans, T. "Über die Zuordnung von Wellenfunktionen und Eigenwerten zu den Einzelnen Elektronen Eines Atoms". *Physica* **1,** 104–113 (1934).

103. Vidal, J., Zhang, X., Yu, L., Luo, J. W. & Zunger, A. "False-positive and false-negative assignments of topological insulators in density functional theory and hybrids". *Physical Review B* **84,** 41109 (2011).

104. Aguilera, I., Friedrich, C., Bihlmayer, G. & Blügel, S. "*GW* study of topological insulators Bi_2Se_3, Bi_2Te_3, and Sb_2Te_3: Beyond the perturbative one-shot approach". *Physical Review B* **88,** 45206 (2013).

105. Förster, T., Krüger, P. & Rohlfing, M. "*GW* calculations for Bi_2Te_3 and Sb_2Te_3 thin films: Electronic and topological properties". *Physical Review B* **93,** 205442 (2016).

106. Von Barth, U. & Hedin, L. "A local exchange-correlation potential for the spin polarized case: I". *Journal of Physics C: Solid State Physics* **5,** 1629–1642 (1972).

107. Rajagopal, A. K. & Callaway, J. "Inhomogeneous Electron Gas". *Physical Review B* **7,** 1912–1919 (1973).

108. Oliver, G. L. & Perdew, J. P. "Spin-density gradient expansion for the kinetic energy". *Physical Review A* **20,** 397–403 (1979).

109. Langreth, D. C. & Mehl, M. J. "Beyond the local-density approximation in calculations of ground-state electronic properties". *Physical Review B* **28,** 1809–1834 (1983).

110. Becke, A. D. "Density-functional exchange-energy approximation with correct asymptotic behavior". *Physical Review A* **38,** 3098–3100 (1988).

111. Levy, M. & Perdew, J. P. "Hellmann-Feynman, virial, and scaling requisites for the exact universal density functionals. Shape of the correlation potential and diamagnetic susceptibility for atoms". *Physical Review A* **32,** 2010–2021 (1985).

112. Perdew, J. P., Ernzerhof, M. & Burke, K. "Rationale for mixing exact exchange with density functional approximations". *Journal of Chemical Physics* **105,** 9982–9985 (1996).

113. Heyd, J., Scuseria, G. E. & Ernzerhof, M. "Hybrid functionals based on a screened Coulomb potential". *Journal of Chemical Physics* **118,** 8207–8215 (2003).

114. Krukau, A. V., Vydrov, O. A., Izmaylov, A. F. & Scuseria, G. E. "Influence of the exchange screening parameter on the performance of screened hybrid functionals". *The Journal of Chemical Physics* **125,** 224106 (2006).

115. Blöchl, P. E. "Projector augmented-wave method". *Physical Review B* **50,** 17953–17979 (1994).

116. Van Lenthe, E., Baerends, E. J. & Snijders, J. G. "Relativistic regular two-component Hamiltonians". *The Journal of Chemical Physics* **99,** 4597–4610 (1993).

117. Steiner, S., Khmelevskyi, S., Marsmann, M. & Kresse, G. "Calculation of the magnetic anisotropy with projected-augmented-wave methodology and the case study of disordered $Fe_{1-x}Co_x$ alloys". *Physical Review B* **93,** 224425 (2016).

118. Eck, P. *post_wan: a python package for tight-binding calculations.*

119. Marzari, N. & Vanderbilt, D. "Maximally localized generalized Wannier functions for composite energy bands". *Physical Review B* **56,** 12847–12865 (1997).

120. Mostofi, A. A., Yates, J. R., Lee, Y.-S., Souza, I., Vanderbilt, D. & Marzari, N. "wannier90: A tool for obtaining maximally-localised Wannier functions". *Computer Physics Communications* **178,** 685–699 (2008).

121. Mostofi, A. A., Yates, J. R., Pizzi, G., Lee, Y. S., Souza, I., Vanderbilt, D. & Marzari, N. "An updated version of wannier90: A tool for obtaining maximally-localised Wannier functions". *Computer Physics Communications* **185,** 2309–2310 (2014).

122. Papaconstantopoulos, D. A. & Mehl, M. J. "The Slater-Koster tight-binding method: A computationally efficient and accurate approach". *Journal of Physics Condensed Matter* **15,** R413 (2003).

123. Mercer, J. L. & Chou, M. Y. "Tight-binding model with intra-atomic matrix elements". *Physical Review B* **49,** 8506–8509 (1994).

124. Cohen, R. E., Stixrude, L. & Wasserman, E. "Tight-binding computations of elastic anisotropy of Fe, Xe, and Si under compression". *Physical Review B* **56,** 8575–8589 (1997).

125. Wannier, G. H. "The structure of electronic excitation levels in insulating crystals". *Physical Review* **52,** 191–197 (1937).

126. Kohn, W. "Analytic properties of Bloch waves and Wannier functions". *Physical Review* **115,** 809–821 (1959).

127. Cloizeaux, J. D. "Orthogonal orbitals and generalized wannier functions". *Physical Review* **129,** 554–566 (1963).

128. Souza, I., Marzari, N. & Vanderbilt, D. "Maximally localized Wannier functions for entangled energy bands". *Physical Review B* **65,** 1–13 (2002).

129. King-Smith, R. D. & Vanderbilt, D. "Theory of polarization of crystalline solids". *Physical Review B* **47,** 1651–1654 (1993).

130. Resta, R. "Macroscopic polarization in crystalline dielectrics: The geometric phase approach". *Reviews of Modern Physics* **66,** 899–915 (1994).

131. Cloizeaux, J. D. "Energy bands and projection operators in a crystal: Analytic and asymptotic properties". *Physical Review* **135,** A685 (1964).

132. Blount, E. I. in *Solid State Physics - Advances in Research and Applications* C, 305–373 (Elsevier, 1962).

133. Dresselhaus, M. S., Dresselhaus, G. & Jorio, A. *Group theory: application to the physics of condensed matter,* 1–582 (Springer Science & Business Media, 2008).

134. Bradley, C. & Cracknell, A. *The mathematical theory of symmetry in solids: representation theory for point groups and space groups* (Oxford University Press, 2010).

135. Cano, J. & Bradlyn, B. "Band Representations and Topological Quantum Chemistry". *Annual Review of Condensed Matter Physics* **12,** 225–246 (2021).

136. Mañes, J. L. *Group theory in condensed matter: A practical introduction.* Lecture Notes (University of the Basque Country, 2022).

137. Zak, J. "Symmetry Specification of Bands in Solids". *Physical Review Letters* **45,** 1025–1028 (1980).

138. Zak, J. "Band representations and symmetry types of bands in solids". *Physical Review B* **23,** 2824–2835 (1981).

139. Liu, G., Zhang, P., Wang, Z. & Li, S.-S. "Spin Hall effect on the kagome lattice with Rashba spin-orbit interaction". *Physical Review B* **79,** 35323 (2009).

140. Aroyo, M. I., Orobengoa, D., De La Flor, G., Tasci, E. S., Perez-Mato, J. M. & Wondratschek, H. "Brillouin-zone database on the Bilbao Crystallographic Server". *Acta Crystallographica Section A: Foundations and Advances* **70,** 126–137 (2014).

141. Aroyo, M. I., Kirov, A., Capillas, C., Perez-Mato, J. M. & Wondratschek, H. "Bilbao Crystallographic Server. II. Representations of crystallographic point groups and space groups". *Acta Crystallographica Section A: Foundations of Crystallography* **62,** 115–128 (2006).

142. Kochan, D., Irmer, S. & Fabian, J. "Model spin-orbit coupling Hamiltonians for graphene systems". *Physical Review B* **95,** 165415 (2017).

143. Aroyo, M. I., Perez-Mato, J. M., Capillas, C., Kroumova, E., Ivantchev, S., Madariaga, G., Kirov, A. & Wondratschek, H. "Bilbao Crystallographic Server: I. Databases and crystallographic computing programs". *Zeitschrift fur Kristallographie* **221,** 15–27 (2006).

144. Condon, E. U. & Shortley, G. H. *The Theory of Atomic Spectra*. **6,** 383–383 (Cambridge University Press, 1952).

145. Arfken, G. B. & Weber, H. J. in *Mathematical Methods for Physicists (Fourth Edition)* (eds Arfken, G. B. & Weber, H. J.) Fourth Edi, 693–765 (Academic Press, Boston, 1995).

146. Avery, J. S. & Avery, J. E. *Generalized sturmians and atomic spectra,* 1–241 (World Scientific, 2006).

147. Benalcazar, W. A., Li, T. & Hughes, T. L. "Quantization of fractional corner charge in Cn -symmetric higher-order topological crystalline insulators". *Physical Review B* **99,** 245151 (2019).

148. Souza, I. & Vanderbilt, D. "Dichroic f-sum rule and the orbital magnetization of crystals". *Physical Review B* **77,** 54438 (2008).

149. Schüler, M., Giovannini, U. D., Hübener, H., Rubio, A., Sentef, M. A. & Werner, P. "Local Berry curvature signatures in dichroic angle-resolved photoelectron spectroscopy from two-dimensional materials". *Science Advances* **6,** eaay2730 (2020).

150. Ünzelmann, M., Bentmann, H., Figgemeier, T., Eck, P., Neu, J. N., Geldiyev, B., Diekmann, F., Rohlf, S., Buck, J., Hoesch, M., Kalläne, M., Rossnagel, K., Thomale, R., Siegrist, T., Sangiovanni, G., Di Sante, D. & Reinert, F. "Momentum-space signatures of Berry flux monopoles in the Weyl semimetal TaAs". *Nature Communications* **12,** 3650 (2021).

151. Bentmann, H., Maaß, H., Braun, J., Seibel, C., Kokh, K. A., Tereshchenko, O. E., Schreyeck, S., Brunner, K., Molenkamp, L. W., Miyamoto, K., Arita, M., Shimada, K., Okuda, T., Kirschner, J., Tusche, C., Ebert, H., Minár, J. & Reinert, F. "Profiling spin and orbital texture of a topological insulator in full momentum space". *Physical Review B* **103,** L161107 (2021).

152. Cho, S., Park, J.-H., Huh, S., Hong, J., Kyung, W., Park, B.-G., Denlinger, J. D., Shim, J. H., Kim, C. & Park, S. R. "Studying local Berry curvature in 2H-WSe2 by circular dichroism photoemission utilizing crystal mirror plane". *Scientific Reports* **11,** 1684 (2021).

153. Cracknell, A. P. & Davies, B. L. *General introduction and Tables of irreducible representations of space groups* (IFI/Plenum, 1979).

154. Schindler, F., Brzezińska, M., Benalcazar, W. A., Iraola, M., Bouhon, A., Tsirkin, S. S., Vergniory, M. G. & Neupert, T. "Fractional corner charges in spin-orbit coupled crystals". *Physical Review Research* **1,** 033074 (2019).

155. Watanabe, H. & Ono, S. "Corner charge and bulk multipole moment in periodic systems". *Physical Review B* **102,** 165120 (2020).

156. Fang, Y. & Cano, J. "Filling anomaly for general two-and three-dimensional C_4 symmetric lattices". *Physical Review B* **103,** 165109 (2021).

157. Fang, Y. & Cano, J. "Classification of Dirac points with higher-order Fermi arcs". *Physical Review B* **104,** 245101 (2021).

158. Takahashi, R., Zhang, T. & Murakami, S. "General corner charge formula in two-dimensional C_n-symmetric higher-order topological insulators". *Physical Review B* **103,** 205123 (2021).

159. Zhou, Y., Rabe, K. M. & Vanderbilt, D. "Surface polarization and edge charges". *Physical Review B* **92,** 41102 (2015).

160. Dominguez, F., Scharf, B., Li, G., Schäfer, J., Claessen, R., Hanke, W., Thomale, R. & Hankiewicz, E. M. "Testing topological protection of edge states in hexagonal quantum spin Hall candidate materials". *Physical Review B* **94,** 161407 (2018).

161. Li, G., Hanke, W., Hankiewicz, E. M., Reis, F., Schäfer, J., Claessen, R., Wu, C. & Thomale, R. "Theoretical paradigm for the quantum spin Hall effect at high temperatures". *Physical Review B* **98,** 165146 (2018).

162. Fu, L. "Topological Crystalline Insulators". *Physical Review Letters* **106,** 106802 (2011).

163. Hughes, T. L., Prodan, E. & Bernevig, B. A. "Inversion-symmetric topological insulators". *Physical Review B* **83,** 245132 (2011).

164. Dresselhaus, G. "Spin-Orbit Coupling Effects in Zinc Blende Structures". *Physical Review* **100,** 580–586 (1955).

165. Bychkov, Y. A. & Rashba, É. I. "Properties of a 2D electron gas with lifted spectral degeneracy". *JETP lett* **39,** 78 (1984).

166. Manchon, A., Koo, H. C., Nitta, J., Frolov, S. M. & Duine, R. A. "New perspectives for Rashba spin–orbit coupling". *Nature Materials* **14,** 871–882 (2015).

167. Armitage, N. P., Mele, E. J. & Vishwanath, A. "Weyl and Dirac semimetals in three-dimensional solids". *Reviews of Modern Physics* **90,** 15001 (2018).

168. Min, C. H., Bentmann, H., Neu, J. N., Eck, P., Moser, S., Figgemeier, T., Ünzelmann, M., Kissner, K., Lutz, P., Koch, R. J., Jozwiak, C., Bostwick, A., Rotenberg, E., Thomale, R., Sangiovanni, G., Siegrist, T., Di Sante, D. & Reinert, F. "Orbital Fingerprint of Topological Fermi Arcs in the Weyl Semimetal TaP". *Physical Review Letters* **122** (2019).

169. Petersen, L. & Hedegård, P. "Simple tight-binding model of spin-orbit splitting of sp-derived surface states". *Surface Science* **459,** 49–56 (2000).

170. Park, J.-H., Kim, C. H., Rhim, J.-W. & Han, J. H. "Orbital Rashba effect and its detection by circular dichroism angle-resolved photoemission spectroscopy". *Physical Review B* **85,** 195401 (2012).

171. Go, D., Hanke, J.-P., Buhl, P. M., Freimuth, F., Bihlmayer, G., Lee, H.-W., Mokrousov, Y. & Blügel, S. "Toward surface orbitronics: giant orbital magnetism from the orbital Rashba effect at the surface of sp-metals". *Scientific Reports* **7,** 46742 (2017).

172. Jisook, H., Jun-Won, R., Inkyung, S., Changyoung, K., Ryong, P. S. & Hoon, S. J. "Giant Rashba-Type Spin Splitting in Bi/Ag(111) from Asymmetric Interatomic-Hopping". *Journal of the Physical Society of Japan* **88,** 124705 (2019).

173. Ünzelmann, M. *Interplay of Inversion Symmetry Breaking and Spin-Orbit Coupling– From the Rashba Effect to Weyl Semimetals*. PhD thesis (Universität Würzburg, 2022).

174. Fauster, T., Hammer, L., Heinz, K. & Schneider, M. A. in *Surface Physics* (De Gruyter, 2020).

175. Cao, Y., Waugh, J. A., Zhang, X.-W., Luo, J.-W., Wang, Q., Reber, T. J., Mo, S. K., Xu, Z., Yang, A., Schneeloch, J., Gu, G. D., Brahlek, M., Bansal, N., Oh, S., Zunger, A. & Dessau, D. S. "Mapping the orbital wavefunction of the surface states in three-dimensional topological insulators". *Nature Physics* **9,** 499–504 (2013).

176. Bawden, L., Riley, J. M., Kim, C. H., Sankar, R., Monkman, E. J., Shai, D. E., Wei, H. I., Lochocki, E. B., Wells, J. W., Meevasana, W., Kim, T. K., Hoesch, M., Ohtsubo, Y., Fèvre, P. L., Fennie, C. J., Shen, K. M., Chou, F. & King, P. D. C. "Hierarchical spin-orbital polarization of a giant Rashba system". *Science Advances* **1,** e1500495 (2015).

177. Kim, B., Kim, C. H., Kim, P., Jung, W., Kim, Y., Koh, Y., Arita, M., Shimada, K., Namatame, H., Taniguchi, M., Yu, J. & Kim, C. "Spin and orbital angular momentum structure of Cu(111) and Au(111) surface states". *Physical Review B* **85,** 195402 (2012).

178. Park, S. R., Han, J., Kim, C., Koh, Y. Y., Kim, C., Lee, H., Choi, H. J., Han, J. H., Lee, K. D., Hur, N. J., Arita, M., Shimada, K., Namatame, H. & Taniguchi, M. "Chiral Orbital-Angular Momentum in the Surface States of Bi_2Se_3". *Physical Review Letters* **108,** 46805 (2012).

179. Moser, S. "A toy model for dichroism in angle resolved photoemission". *Journal of Electron Spectroscopy and Related Phenomena* **262,** 147278 (2023).

180. Geissler, F., Budich, J. C. & Trauzettel, B. "Group theoretical and topological analysis of the quantum spin Hall effect in silicene". *New Journal of Physics* **15,** 085030 (2013).

181. Xu, Y., Yan, B., Zhang, H.-J., Wang, J., Xu, G., Tang, P., Duan, W. & Zhang, S.-C. "Large-Gap Quantum Spin Hall Insulators in Tin Films". *Physical Review Letters* **111,** 136804 (2013).

182. Castro Neto, A. H., Guinea, F, Peres, N. M. R., Novoselov, K. S. & Geim, A. K. "The electronic properties of graphene". *Reviews of Modern Physics* **81,** 109–162 (2009).

183. Hwang, C., Siegel, D. A., Mo, S.-K., Regan, W., Ismach, A., Zhang, Y., Zettl, A. & Lanzara, A. "Fermi velocity engineering in graphene by substrate modification". *Scientific Reports* **2,** 590 (2012).

184. Shirley, E. L., Terminello, L. J., Santoni, A. & Himpsel, F. J. "Brillouin-zone-selection effects in graphite photoelectron angular distributions". *Physical Review B* **51,** 13614–13622 (1995).

185. Bostwick, A., Ohta, T., Seyller, T., Horn, K. & Rotenberg, E. "Quasiparticle dynamics in graphene". *Nature Physics* **3,** 36–40 (2007).

186. Mucha-Kruczyński, M., Tsyplyatyev, O., Grishin, A., McCann, E., Fal'ko, V. I., Bostwick, A. & Rotenberg, E. "Characterization of graphene through anisotropy of constant-energy maps in angle-resolved photoemission". *Physical Review B* **77,** 195403 (2008).

187. Liu, Y., Bian, G., Miller, T. & Chiang, T. C. "Visualizing Electronic Chirality and Berry Phases in Graphene Systems Using Photoemission with Circularly Polarized Light". *Physical Review Letters* **107,** 166803 (2011).

188. Puschnig, P. & Lüftner, D. "Simulation of angle-resolved photoemission spectra by approximating the final state by a plane wave: From graphene to polycyclic aromatic hydrocarbon molecules". *Journal of Electron Spectroscopy and Related Phenomena* **200,** 193–208 (2015).

189. Moser, S. "An experimentalist's guide to the matrix element in angle resolved photoemission". *Journal of Electron Spectroscopy and Related Phenomena* **214,** 29–52 (2017).

190. Liu, G.-B., Shan, W.-Y., Yao, Y., Yao, W. & Xiao, D. "Three-band tight-binding model for monolayers of group-VIB transition metal dichalcogenides". *Physical Review B* **88,** 85433 (2013).

191. Zhang, Y., Brar, V. W., Wang, F., Girit, C., Yayon, Y., Panlasigui, M., Zettl, A. & Crommie, M. F. "Giant phonon-induced conductance in scanning tunnelling spectroscopy of gate-tunable graphene". *Nature Physics* **4,** 627–630 (2008).

192. Butko, V. Y., DiTusa, J. F. & Adams, P. W. "Coulomb Gap: How a Metal Film Becomes an Insulator". *Physical Review Letters* **84,** 1543–1546 (2000).

193. Feenstra, R. M. "Tunneling spectroscopy of the Si(111)2 × 1 surface". *Physical Review B* **60,** 4478–4480 (1999).

194. Peres, N. M. R. "Colloquium: The transport properties of graphene: An introduction". *Reviews of Modern Physics* **82,** 2673–2700 (2010).

195. Ren, Y., Deng, X., Qiao, Z., Li, C., Jung, J., Zeng, C., Zhang, Z. & Niu, Q. "Single-valley engineering in graphene superlattices". *Physical Review B* **91,** 245415 (2015).

196. Okugawa, R., Hayashi, S. & Nakanishi, T. "Second-order topological phases protected by chiral symmetry". *Physical Review B* **100,** 235302 (2019).

197. Ahn, J., Park, S. & Yang, B.-J. "Failure of Nielsen-Ninomiya Theorem and Fragile Topology in Two-Dimensional Systems with Space-Time Inversion Symmetry: Application to Twisted Bilayer Graphene at Magic Angle". *Physical Review X* **9,** 21013 (2019).

198. Peterson, C. W., Li, T., Benalcazar, W. A., Hughes, T. L. & Bahl, G. "A fractional corner anomaly reveals higher-order topology". *Science* **368,** 1114–1118 (2020).

199. Xie, B., Wang, H.-X., Zhang, X., Zhan, P., Jiang, J.-H., Lu, M. & Chen, Y. "Higher-order band topology". *Nature Reviews Physics* **3,** 520–532 (2021).

200. Gresch, D., Wu, Q., Winkler, G. W., Häuselmann, R., Troyer, M. & Soluyanov, A. A. "Automated construction of symmetrized Wannier-like tight-binding models from ab initio calculations". *Physical Review Materials* **2,** 103805 (2018).

201. Mielke, A. "Exact ground states for the Hubbard model on the Kagome lattice". *Journal of Physics A: Mathematical and General* **25,** 4335 (1992).

202. Yu, S.-L. & Li, J.-X. "Chiral superconducting phase and chiral spin-density-wave phase in a Hubbard model on the kagome lattice". *Physical Review B* **85,** 144402 (2012).

203. Kiesel, M. L., Platt, C. & Thomale, R. "Unconventional Fermi Surface Instabilities in the Kagome Hubbard Model". *Physical Review Letters* **110,** 126405 (2013).

204. Wang, W.-S., Li, Z.-Z., Xiang, Y.-Y. & Wang, Q.-H. "Competing electronic orders on kagome lattices at van Hove filling". *Physical Review B* **87,** 115135 (2013).

205. Kang, M., Fang, S., Kim, J.-K., Ortiz, B. R., Ryu, S. H., Kim, J., Yoo, J., Sangiovanni, G., Di Sante, D., Park, B.-G., Jozwiak, C., Bostwick, A., Rotenberg, E., Kaxiras, E., Wilson, S. D., Park, J.-H. & Comin, R. "Twofold van Hove singularity and origin of charge order in topological kagome superconductor CsV3Sb5". *Nature Physics* **18,** 301–308 (2022).

206. Di Sante, D., Bigi, C., Eck, P., Enzner, S., Consiglio, A., Pokharel, G., Carrara, P., Orgiani, P., Polewczyk, V., Fujii, J., King, P. D. C., Vobornik, I., Rossi, G., Zeljkovic, I., Wilson, S. D., Thomale, R., Sangiovanni, G., Panaccione, G. & Mazzola, F. "Flat band separation and robust spin Berry curvature in bilayer kagome metals". *Nature Physics* (2023).

207. Sforzini, J., Nemec, L., Denig, T., Stadtmüller, B., Lee, T.-L., Kumpf, C., Soubatch, S., Starke, U., Rinke, P., Blum, V., Bocquet, F. C. & Tautz, F. S. "Approaching Truly Freestanding Graphene: The Structure of Hydrogen-Intercalated Graphene on $6H-$SiC(0001)". *Physical Review Letters* **114,** 106804 (2015).

208. Han, Y., Evans, J. W. & Tringides, M. C. "Dy adsorption on and intercalation under graphene on 6H-SiC(0001) surface from first-principles calculations". *Physical Review Materials* **5,** 74004 (2021).

209. Schmitt, C., Erhardt, J., Eck, P., Schmitt, M., Lee, K., Wagner, T., Keßler, P., Kamp, M., Kim, T., Cacho, C. & Others. "Stabilizing an atomically thin quantum spin Hall insulator at ambient conditions: Graphene-intercalation of indenene". *arXiv preprint arXiv:2305.07807* (2023).

210. Shibuya, T.-I. & Wulfman, C. E. "Molecular orbitals in momentum space". *Proceedings of the Royal Society of London. Series A. Mathematical and Physical Sciences* **286,** 376–389 (1965).

211. Gazeau, J. P. & Maquet, A. "A new approach to the two-particle Schrödinger bound state problem". *The Journal of Chemical Physics* **73,** 5147–5154 (1980).

212. Bang, J. M. & Vaagen, J. S. "The sturmian expansion: A well-depth-method for orbitals in a deformed potential". *Zeitschrift für Physik A Atoms and Nuclei* **297,** 223–236 (1980).

213. Avery, J. "Many-center Coulomb Sturmians and Shibuya-Wulfman integrals". *International Journal of Quantum Chemistry* **100,** 121–130 (2004).

214. Aquilanti, V., Cavalli, S. & Coletti, C. "The *d*-dimensional hydrogen atom: hyperspherical harmonics as momentum space orbitals and alternative Sturmian basis sets". *Chemical Physics* **214,** 1–13 (1997).

215. Rotenberg, M. "Application of sturmian functions to the Schroedinger three-body problem: Elastic e^+-H scattering". *Annals of Physics* **19,** 262–278 (1962).

List of Publications

- C. H. Min, H. Bentmann, J. N. Neu, **P. Eck**, S. Moser, T. Figgemeier, M. Ünzelmann, K. Kissner, P. Lutz, R. J. Koch, C. Jozwiak, A. Bostwick, E. Rotenberg, R. Thomale, G. Sangiovanni, T. Siegrist, D. Di Sante, and F. Reinert, "Orbital Fingerprint of Topological Fermi Arcs in the Weyl Semimetal TaP", *Physical Review Letters* **122** (2019).

- M. Ünzelmann, H. Bentmann, **P. Eck**, T. Kißlinger, B. Geldiyev, J. Rieger, S. Moser, R. C. Vidal, K. Kißner, L. Hammer, M. A. Schneider, T. Fauster, G. Sangiovanni, D. Di Sante, and F. Reinert, "Orbital-Driven Rashba Effect in a Binary Honeycomb Monolayer AgTe", *Physical Review Letters* **124** (2020).

- M. Ünzelmann[1], H. Bentmann[1], T. Figgemeier[1], **P. Eck**[1], J. N. Neu, B. Geldiyev, F. Diekmann, S. Rohlf, J. Buck, M. Hoesch, M. Kalläne, K. Rossnagel, R. Thomale, T. Siegrist, G. Sangiovanni, D. Di Sante, and F. Reinert, "Momentum-space signatures of Berry flux monopoles in the Weyl semimetal TaAs", *Nature Communications* **12**, 3650 (2021).

- M. Bauernfeind[1], J. Erhardt[1], **P. Eck**[1], P. K. Thakur, J. Gabel, T. L. Lee, J. Schäfer, S. Moser, D. Di Sante, R. Claessen, and G. Sangiovanni, "Design and realization of topological Dirac fermions on a triangular lattice", *Nature Communications* **12**, 5396 (2021).

- J. Erhardt, M. Bauernfeind, **P. Eck**, M. Kamp, J. Gabel, T.-L. Lee, G. Sangiovanni, S. Moser, and R. Claessen, "Indium Epitaxy on SiC(0001): A Roadmap to Large Scale Growth of the Quantum Spin Hall Insulator Indenene", *Journal of Physical Chemistry C* **126**, 16289–16296 (2022).

- **P. Eck**, C. Ortix, A. Consiglio, J. Erhardt, M. Bauernfeind, S. Moser, R. Claessen, D. Di Sante, and G. Sangiovanni, "Real-space obstruction in quantum spin Hall insulators", *Physical Review B* **106**, 195143 (2022).

- **P. Eck**, Y. Fang, D. Di Sante, G. Sangiovanni, and J. Cano, "Recipe for higher-order topology on the triangular lattice", *Physical Review B* **107**, 115130 (2023).

- B. Liu, T. Wagner, S. Enzner, **P. Eck**, M. Kamp, G. Sangiovanni, and R. Claessen,"Moiré pattern formation in epitaxial growth on a covalent substrate:

[1]These authors contributed equally.

Sb on InSb (111)A", *Nano Letters* **23**, 3189-3195 (2023).

- D. Di Sante, C. Bigi, **P. Eck**, S. Enzner, A. Consiglio, G. Pokharel, P. Carrara, P. Orgiani, V. Polewczyk, J. Fujii, P. D. C. King, I. Vobornik, G. Rossi, I. Zeljkovic, S. D. Wilson, R. Thomale, G. Sangiovanni, G. Panaccione, and F. Mazzola, "Flat band separation and robust spin Berry curvature in bilayer kagome metals", *Nature Physics* (2023).

Acknowledgment

I would like to take this occasion to thank special people, companions and friends on this exceptional journey. Without you, this work and my PhD would not have been possible or at least even harder and definitely less fun.

- First of all I would like to thank my doctoral supervisor **Prof. Dr. Giorgio Sangiovanni** for offering me the possibility of conducting this research, for all the support throughout the project and the trust in my work. Also for granting me highly flexible working conditions during the pandemic and the time beyond. I appreciated immensely your irresistible positive attitude and our inspiring discussions. The stay at the flatiron institute and the conferences in Campello and Amalfi were exceptional experiences. You definitely can claim that you did your best to make the decision on my future career an extremely tough one.

- Secondly, many thanks to my co-supervisor and mentor **Dr. Domenico Di Sante**. I am highly grateful for your introduction to *ab initio* methods, your inspiration for the development of the post_wan package and your persistent skepticism in my code, which was elevating it to the next level. I really enjoyed working with you on all our successful scientific collaborations. After this exciting journey, I am happy to call you a friend. I'm still thankful for your daily support during my COVID quarantine in Manhattan, which included also a birthday basket and a long-distance birthday song by Giulia, Chiara and you. All the best for starting the new chapter in Bologna.

- Special thanks to all the other members of the Sangiovanni group and friends for making this time a pleasant one by creating a friendly and cooperative atmosphere as well as by the italienized social activities after work. In particular, I want to thank my DFT mate **Stefan Enzner** for his inexhaustible stamina and his passion for gigantic graphene, antimony and kagome unit cells, especially for the countless zooms and virtual social time during the lock down. Many thanks also to **Dr. Lorenzo Crippa** for all the inspiring lunch discussions beyond Physics, for the proofreading and the fantastic experience of taming Bernevig's MATBLG model, you can do it! To **Niklas Wagner** for the pleasurable crafting of dozen QM1 and QM2 exercise sheets and exams, and their subsequent correction sessions. To **Armando Consiglio** for the common work on indenene including the usage of beloved python. To **Dr. Andreas Hausoel** for many stimulating debates with and without drinks. To **Severino Adler** for surfing

together the rapidly growing COVID lock down wave via New York, Denver to Aspen in March 2020. To **Max Xylander** and **Markus Feld** for their enthusiasm, I really appreciated supervising your Master projects. And of course to my office colleagues **Alexander Kowalski** and **Max Fischer**.

- I have substantially profited from the collaboration with the triangular lattice enthusiasts from Experimentelle Physik IV. I acknowledge **Prof. Dr. Ralph Claessen, Prof. Dr. Jörg Schäfer, Dr. Simon Moser, Dr. Maximilian Bauernfeind, Jonas Erhardt** and **Cedric Schmitt**. Many ideas presented in this work were inspired or arose from our joint projects. Indispensable was the exceptional work by Max and Jonas, ranging from the sample growth to the characterization of the electronic properties. Surely we all agree that none of the manuscripts would have ever met the high scientific standards for publication without the intervention of our "devil's advocate"from 4D Fock space: Simon. Thank you also for bringing up all the ideas on the expansion of the Bloch wave function in Coulomb Sturmians, these discussions helped me a lot.

- Many thanks to the "TaAs-force" from Experimentelle Physik VII formed by **Prof. Dr. Friedrich Reinert, Prof. Dr. Hendrik Bentmann, Dr. Maximilian Ünzelmann, Dr. Chul-Hee Min, Tim Figgemeier** and **Begmuhammet Geldiyev**. Putting forward the intriguing relation between inversion symmetry breaking, chiral wave functions and in particular the atomic orbital angular momentum polarization and their manifestation in polarized light angle-resolved photoemission has deepened enormously my understanding of band structures and wave function symmetries. They are the key ingredients of the topological phases presented in this thesis. I also want to thank "Mr. Rashba", Max, for all the coffee-discussions. Exchanging personal perspectives on various topics was quite illuminating.

- Working with **Dr. Jennifer Cano** and **Yuan Fang** has broadened significantly my understanding of the connection between symmetries, real-space obstruction and topology. I highly appreciated this collaboration, thanks for being my guide through the stormy sea of irreps, EBRS and real-space obstructed limits.

- Many thanks also to **Dr. Bing Liu, Tim Wagner** and **Dr. Lennart Klebl** for the collaboration on the antimony projects.

- Let me also thank **Dr. Giancarlo Panaccione, Dr. Federico Mazzola, Dr. Chiara Bigi, Dr. Ilija Zeljkovic** and **Dr. Hong Li** for involving me in the inspiring projects on the Kagome systems.

- Further I want to acknowledge **Prof. Dr. Philipp Hansmann, Prof. Dr. Andrea Caviglia, Dr. Carmine Ortix, Dr. Mario Cuoco, Dr. Michael Schmid, Dr. Thierry van Thiel** and **Ulderico Fillippozzi** for their fruitful collaboration in various projects during my PhD not covered in this thesis.

- I thank my family, especially my parents, for all the support not only during my studies and for encouraging me for pursuing my way. Without you, I would not have made it so far.

- To Jana, thank you for your deep love, patience, for your comforting words when needed, for keeping up our relationship even over long distances and for your support. Thanks for everything, I'm looking forward to what lies ahead.